

8-2016

# Studies of Arctic Tropospheric Ozone Depletion Events Through Buoy-Borne Observations and Laboratory Studies

John W. Halfacre  
*Purdue University*

Follow this and additional works at: [https://docs.lib.purdue.edu/open\\_access\\_dissertations](https://docs.lib.purdue.edu/open_access_dissertations)



Part of the [Atmospheric Sciences Commons](#), and the [Chemistry Commons](#)

---

## Recommended Citation

Halfacre, John W., "Studies of Arctic Tropospheric Ozone Depletion Events Through Buoy-Borne Observations and Laboratory Studies" (2016). *Open Access Dissertations*. 767.  
[https://docs.lib.purdue.edu/open\\_access\\_dissertations/767](https://docs.lib.purdue.edu/open_access_dissertations/767)

This document has been made available through Purdue e-Pubs, a service of the Purdue University Libraries. Please contact [epubs@purdue.edu](mailto:epubs@purdue.edu) for additional information.

**PURDUE UNIVERSITY**  
**GRADUATE SCHOOL**  
**Thesis/Dissertation Acceptance**

This is to certify that the thesis/dissertation prepared

By John W. Halfacre

Entitled STUDIES OF ARCTIC TROPOSPHERIC OZONE DEPLETION EVENTS THROUGH  
BUOY-BASED OBSERVATIONS AND LABORATORY STUDIES

For the degree of Doctor of Philosophy

Is approved by the final examining committee:

Paul B. Shepson  
\_\_\_\_\_

Garth J. Simpson  
\_\_\_\_\_

Peter T. Kissinger  
\_\_\_\_\_

Harshvardhan  
\_\_\_\_\_

To the best of my knowledge and as understood by the student in the Thesis/Dissertation Agreement, Publication Delay, and Certification/Disclaimer (Graduate School Form 32), this thesis/dissertation adheres to the provisions of Purdue University's "Policy on Integrity in Research" and the use of copyrighted material.

Paul B. Shepson

Approved by Major Professor(s): \_\_\_\_\_

Approved by: Timothy Zwier

07/18/2016

Head of the Department Graduate Program

Date



STUDIES OF ARCTIC TROPOSPHERIC OZONE DEPLETION EVENTS THROUGH  
BUOY-BASED OBSERVATIONS AND LABORATORY STUDIES

A Dissertation

Submitted to the Faculty

of

Purdue University

by

John W. Halfacre

In Partial Fulfillment of the

Requirements for the Degree

of

Doctor of Philosophy

August 2016

Purdue University

West Lafayette, Indiana

## ACKNOWLEDGEMENTS

I would first like to thank my research advisor, Paul Shepson. Because of his hard work and advising, I was able to see the world and learn how to perform meaningful science. While humoring my numerous career changes over the past six years, his guidance and encouragement kept me on track, and I won't ever be able to convince him of how much I appreciate his support. I am also grateful for the kind support of the folks at the Jonathan Amy Facility for Chemical Instrumentation, the Chemistry Shop, Procurement, and the Business Office. Additionally, I would like to thank members of the Shepson Lab, past and present, for all of their help and guidance. Especially, I would like to thank Allyson Costa, for convincing me to join the group; Maria Cambaliza, just for letting me know her; Chelsea Thompson, for helping me out of my shell and being a darn good office buddy; Kevin McAvey, for helping me learn healthier ways to deal with my own frustration; Joel Rindelaub, for proving to me that I am in control of my life; Kyle Custard, for teaching me empathy and for always having a positive attitude toward his work; Fulizi Xiong, for being my role model and graduate student hero; Olivia Salmon, for our many walks and for helping with my mess of a dog; Tegan Lavoie, for our mutual thesis commiserations and for letting me borrow your stale coffee that one time; and Nate Slade, just for being a really good guy.

I thank my O-Buoy Team collaborators, past and present, for their support and assistance throughout the last several years. In particular, I would need to mention Carlton Rauschenberg, Chris Williams, Paty Matrai, Bill Simpson, Jan Bottenheim, Stoyka Netcheva, Rob Oglesbee, Jim Zimmerman, Phil Wyss, Gernot Friederich, Peter Peterson, Steve Walsh, Mark Carlsen, Mike Everly, Don Perovich, Todd Valentic, and finally Ben Tupper, who taught me that I, too, could be a programmer. In addition, I thank the crew of the Canadian Coast Guard Vessel Louis St Laurent and our Joint Ocean Ice Study collaborators for three enjoyable science cruises, with special recognition to those directly involved with my buoy deployments: helicopter pilots, John Kemp, Leo Rose, Mike Dempsey, Bill Williams, Rick Krishfield, June Marion, Christopher Charles, Geoffrey Oliver, Carpenter Gary, Andy Davies, and Jeff O'Brien.

I would finally like to specifically mention my graduate school “family” with whom I shared many adventures, beers, and laughs: Alex Dow, Karen Olsen, Walter Bosley, Natalya Khanina, Ian Pytlarz, Erik Alberts, Joseph Korn, Rebecca Scott, Dan McMahon, Olivia Kellner, Timothy Berry, Cori Jenkins, and Maggie the Dog.

## TABLE OF CONTENTS

	Page
LIST OF TABLES .....	vii
LIST OF FIGURES .....	viii
ABSTRACT.....	xiii
CHAPTER 1. INTRODUCTION .....	1
1.1 Introduction.....	1
1.2 Oxidation Chemistry within the Boundary Layer.....	1
1.3 Arctic Ozone Depletion .....	11
1.4 Research Objectives.....	30
CHAPTER 2. BUOY-BASED ARCTIC OCEAN OBSERVATIONS OF OZONE: THE O-BUOY PROJECT .....	32
2.1 Introduction.....	32
2.2 Design .....	34
2.2.1 Ozone Instrument.....	40
2.2.2 MAX-DOAS BrO Instrument.....	49
2.2.3 Other Sensors .....	52
2.3 Summary of Deployments and Observations .....	52
2.4 Conclusions.....	65
CHAPTER 3. THE TEMPORAL AND SPATIAL CHARACTERISTICS OF OZONE DEPLETION EVENTS FROM BUOY-BASED MEASUREMENTS IN THE ARCTIC .....	66
3.1 Introduction.....	66
3.2 Methods.....	72
3.2.1 Instrumentation .....	72
3.2.2 ODE Definition.....	78

	Page
3.2.3 Air Mass Trajectory Analysis .....	80
3.2.4 Monte Carlo Experiment.....	84
3.3 Results and Discussion .....	86
3.3.1 Ozone Depletion Timescale.....	86
3.3.2 ODE Spatial Scales.....	100
3.3.3 Temperature and Wind Speed during ODEs .....	108
3.4 Conclusions.....	113
CHAPTER 4. AIR MASS HISTORIES AND METEOROLOGY DURING PERIODS OF OZONE DEPLETION EVENTS FROM ARCTIC OCEAN-BASED MEASUREMENTS .....	115
4.1 Introduction.....	115
4.2 Methods.....	125
4.2.1 Instrumentation .....	125
4.2.2 Air Mass Trajectory Analysis .....	126
4.2.3 Satellite Surface Type Observations.....	126
4.3 Results.....	132
4.3.1 Air Mass History and Surface Composition .....	132
4.3.2 Explaining O <sub>3</sub> Variability .....	136
4.4 Discussion.....	143
4.5 Conclusions.....	153
CHAPTER 5. LABORATORY STUDIES OF OXIDATIVE RELEASE OF MOLECULAR CHLORINE, BROMINE, AND IODINE FROM FROZEN SURFACES .....	155
5.1 Introduction.....	155
5.2 Methods.....	160
5.2.1 Materials .....	160
5.2.2 Flow Tube .....	161
5.2.3 CIMS.....	163
5.3 Results.....	166
5.3.1 Effects of the Hydroxyl Radical .....	168
5.3.2 Effects of O <sub>3</sub> .....	177
5.4 Discussion.....	179
5.5 Summary and Conclusions .....	187



	Page
CHAPTER 6. CONCLUSIONS.....	189
LIST OF REFERENCES.....	192
VITA.....	216
PUBLICATION.....	217

## LIST OF TABLES

Table	Page
2.1 Summary of O-Buoy deployment locations and dates of active operation as of June 2016.....	53
3.1 O-Buoy deployment locations and time periods of continuous measurements relevant to this study.....	72
3.2 Cross sections used in spectral analysis.....	76
3.3 Average BrO mole fractions during periods of O <sub>3</sub> decrease from O-Buoy2 MAX-DOAS .....	92
3.4 Average BrO mole fractions during periods of O <sub>3</sub> decrease from O-Buoy1 at Barrow, AK, MAX-DOAS.....	93
5.1 List of species monitored by chemical ionization mass spectrometry.....	164
5.2 List of experiments performed using an explicit OH source .....	169
5.3 List of experiments performed using an explicit OH source (i.e., HOOH or NO <sub>2</sub> <sup>-</sup> ). Yields represent the integrated totals of halogens 1 hour after turning on the O <sub>3</sub> generator .....	171
5.4 List of experiments performed without using an explicit OH source.....	177
5.5 List of experiments performed without using an explicit OH source (i.e., without HOOH or NO <sub>2</sub> <sup>-</sup> ). Yields represent the integrated totals of halogens 1 hour after turning on the O <sub>3</sub> generator .....	177

## LIST OF FIGURES

Figure	Page
1.1 Vertical profile of earth's atmosphere .....	2
1.2 Visualization of the troposphere and the planetary BL .....	3
1.3 Modeled relationship between normalized boundary-layer height ( $z/h$ ) and normalized eddy diffusivity ( $K_z$ ).....	4
1.4 Hourly time series of $O_3$ at Mauna Loa Observatory during May 1988.....	8
1.5 Whisker plots of $O_3$ at various remote tropospheric sites in the northern hemisphere.....	9
1.6 Annual trends in ozone at remote sites around the northern hemisphere .....	10
1.7 Representative time series of boundary-layer $O_3$ behavior in the Arctic from Barrow, AK .....	12
1.8 Comparison of daily mean ground level $O_3$ and filterable Br concentrations .....	13
1.9 Example model time series simulation of ODEs considering only bromine-based mechanisms .....	18
1.10 Map of Alert, NU, Canada.....	20
1.11 Relationship between $O_3$ and BrO during the Polar Sunrise Experiment 1992 .....	21
1.12 Time series measurements of (top) wind speed, wind direction, (middle) water mole fractions, snowpack and ambient temperature, and (bottom) $O_3$ and BrO mole fractions .....	23
1.13 Example back trajectory during a high BrO event.....	24
1.14 The Global Ozone Monitoring Experiment (GOME) satellite observations of BrO. ....	25

Figure	Page
1.15 Photograph of the drifting schooner TARA (left) and its drift track (right) during its 2007 expedition .....	26
1.16 Time series measurements of O <sub>3</sub> obtained from (top) TARA (the Arctic Ocean), Zeppelin Station, Barrow, and Alert (bottom) .....	27
1.17 Time series of sonde-based vertical profiles of O <sub>3</sub> in Barrow, AK, during Spring of 2009.....	29
2.1 Left – photograph of lifted O-Buoy .....	34
2.2 Schematic drawing of the aluminum O-Buoy hull (left) and instrument tray (right). .....	36
2.3 Schematic drawings of the O-Buoy mast and the collar connecting the mast with the hull. ....	37
2.4 Camera images received from O-Buoy1 (left) and O-Buoy2 (right) during the summer melt. ....	38
2.5 Counter-weight is an aluminum container filled with lead shot, acting as a ballast... ..	39
2.6 Absorption cross sections of ozone at 298K.....	40
2.7 O-Buoy ozone sensor flow schematic representative of those used in O-Buoys 1-4.....	42
2.8 O-Buoy ozone sensor flow schematic representative of those used in O-Buoys 5-15. The primary difference between this schematic in that of 2.8 is the removal of the latching valve. ....	43
2.9 Demonstration of the effect of flow rate on 2B 205 O <sub>3</sub> data .....	44
2.10 Sample laboratory calibration curves for an individual 2B held at room temperature (top) and at -15 °C. ....	45
2.11 Top – flow schematic following sample air from the atmosphere through the O <sub>3</sub> filter holder to the 2B. ....	48
2.12 Schematic drawing of the light path for the MAX-DOAS system used in O-Buoys.....	51
2.13 Summary of the spatial coverage of all deployments. ....	53
2.14 Visualization of temporal data coverage of all O-Buoy deployments.....	54

Figure	Page
2.15 Data representative of O-Buoy O <sub>3</sub> instrument failure.....	57
2.16 O-Buoy 10 O <sub>3</sub> instrument flow rate (top) plotted above O-Buoy 10 power source voltages.....	58
2.17 Time series of O-Buoy 10 ozone (black trace) and its reported flow rate (blue) .....	59
2.18 Schematic diagram of O-Buoy power going from the battery source to the relevant instrument. This schematic is relevant to O-Buoys deployed prior to 2013.....	63
2.19 Schematic diagram of O-Buoy power going from battery source to the relevant instruments. This schematic is relevant to O-Buoys deployed beginning in 2013 ..	64
3.1 Map of locations at which various O-Buoys (abbreviated OB) were deployed between 2009-2011 .....	73
3.2 Example time series of O <sub>3</sub> , BrO, and temperature from O-Buoy2 during its deployment in the Beaufort Sea. ....	74
3.3 a) Example ODE from O-Buoy2 deployment in the Beaufort Sea with ODE definitions illustrated.....	79
3.4 Time lengths of ODEs as defined by the ODE start time and the O <sub>3</sub> decrease stop time.....	81
3.5 Example HYSPLIT backward air mass trajectory.....	82
3.6 Visualization of one iteration out of 2000 of the Monte Carlo experiments .....	85
3.7 a) Histogram of the distribution of calculated O <sub>3</sub> depletion timescales during ODEs .....	87
3.8 Periods of O <sub>3</sub> decrease from O-Buoy1 at Barrow and corresponding 48 hour HYSPLIT backward trajectories .....	95
3.9 Histogram of the O <sub>3</sub> tendency.....	98
3.10 a) Histogram of ODE dimensions for all ODEs. ....	101
3.11 Distribution of ODE sizes utilized in the Monte Carlo experiments .....	103
3.12 Results from Monte Carlo simulation experiment.....	105
3.13 Results from Monte Carlo simulation experiment with three observation sites. ....	106

Figure	Page
3.14 Wind rose plots based on the HYSPLIT backward air mass trajectories .....	107
3.15 Histograms of the average ambient temperature .....	109
3.16 a) Histogram of the average wind speed measured by the O-Buoys. ....	111
3.17 a) Histogram of the average wind speed measured by the O-Buoys during non- ODEs .....	112
4.1 Example of low ozone mole fraction during a temperature inversion.....	119
4.2 Map of O-Buoy drift tracks relevant to this study. ....	120
4.3 Results from the backward air mass analysis by Bottenheim and Chan (2006). ....	122
4.4 Example of an open lead.....	124
4.5 Time series of O-Buoy2 observations and HYSPLIT results. ....	129
4.6 Time series of O-Buoy4 observations and HYSPLIT results. ....	130
4.7 Time series of Icelander 2 observations and HYSPLIT results.....	131
4.8 Cumulative frequencies of ozone concentrations .....	134
4.9 Scatter plots of particles over a surface type (y-axes) against O <sub>3</sub> levels .....	135
4.10 Correlation coefficients calculated between O <sub>3</sub> mole fractions and other explanatory variables.....	137
4.11 Adjusted R <sup>2</sup> values for linear models.....	140
4.12 Adjusted R <sup>2</sup> values from the models represented by Equations 4.3-4.6. ....	141
4.13 For O-Buoy 2, average particle concentrations during periods when O <sub>3</sub> levels fall below 10 nmol mol <sup>-1</sup> . ....	144
4.14 For O-Buoy 4, average particle concentrations and positions during periods when O <sub>3</sub> levels fall below 10 nmol mol <sup>-1</sup> . ....	145
4.15 For Icelander 2, average particle concentrations during periods when O <sub>3</sub> levels fall below 10 nmol mol <sup>-1</sup> . ....	146
4.16 Molecular dynamics simulation demonstrating the thickness of the disordered surface on frozen water based on temperature .....	149

Figure	Page
4.17 Effects of temperature on the concentration and ionic strength in the QBL .....	150
5.1 Experimental schematic representing the majority of experiments.....	162
5.2 Representative experiments.. ..	167
5.3 Absorption coefficients hydrogen peroxide and emission spectrum for General Electric “Cool White” fluorescent bulb.....	170
5.4 HOX signals from experiment IO2.....	184
5.5 HOX signals from experiment SW5. ....	185

## ABSTRACT

Halfacre, John W. Ph.D., Purdue University, August 2016. Studies of Arctic Tropospheric Ozone Depletion Events Through Buoy-Borne Observations and Laboratory Studies. Major Professor: Paul Shepson.

The photochemically-induced destruction of ground-level Arctic ozone in the Arctic occurs at the onset of spring, in concert with polar sunrise. Solar radiation is believed to stimulate a series of reactions that cause the production and release of molecular halogens from frozen, salty surfaces, though this mechanism is not yet well understood. The subsequent photolysis of molecular halogens produces reactive halogen atoms that remove ozone from the atmosphere in these so-called “Ozone Depletion Events” (ODEs). Given that much of the Arctic region is sunlit, meteorologically stable, and covered by saline ice and snow, it is expected that ODEs could be a phenomenon that occurs across the entire Arctic region. Indeed, an ever-growing body of evidence from coastal sites indicates that Arctic air masses devoid of O<sub>3</sub> most often pass over sea ice-covered regions before arriving at an observation site, suggesting ODE chemistry occurs upwind over the frozen Arctic Ocean. However, outside of coastal observations, there exist very few long-term observations from the Arctic Ocean from which quantitative assessments of basic ODE characteristics can be made.

This work presents the interpretation of ODEs through unique chemical and meteorological observations from several ice-tethered buoys deployed around the Arctic



Ocean. These observations include detection of ozone, bromine monoxide, and measurements of temperature, relative humidity, atmospheric pressure, wind speed, and wind direction. To assess whether the O-Buoys were observing locally based depletion chemistry or the transport of ozone-poor air masses, periods of ozone decay were interpreted based on current understanding of ozone depletion kinetics, which are believed to follow a pseudo-first order rate law. In addition, the spatial extents of ODEs were estimated using air mass trajectory modeling to assess whether they are a localized or synoptic phenomenon. Results indicate that current understanding of the responsible chemical mechanisms are lacking, ODEs are observed primarily due to air mass transport (even in the Arctic Ocean), or some combination of both. Air mass trajectory modeling was also used in tandem with remote sensing observations of sea ice to determine the types of surfaces air masses were exposed to before arriving at O-Buoys. The impact of surface exposure was subsequently compared with local meteorology to assess which variables had the most effect on  $O_3$  variability. For two observation sites, the impact of local meteorology was significantly stronger than air mass history, while a third was inconclusive.

Finally, this work tests the viability of the hypothesis that initial production of molecular halogens from frozen saline surfaces results from photolytic production of the hydroxyl radical, and could be enhanced in the presence of  $O_3$ . This investigation was enabled by a custom frozen-walled flow reactor coupled with chemical ionization spectrometry. It was found that hydroxyl radical could indeed promote the production and release of iodine, bromine, and chlorine, and that this production could be enhanced in the presence of ozone.

## CHAPTER 1. INTRODUCTION

### 1.1 Introduction

The continuing increases in global average temperatures has affected no part of the earth more dramatically than the Arctic. While the year 2015 was reported to be the hottest year in recorded history, with a global average surface temperature increase of 1.0°C since the late 19<sup>th</sup> century, temperatures in the Arctic region have increased 2.9°C over the same amount of time (Brown et al., 2016; Overland et al., 2015). The direct consequences of a warming Arctic include drastic reductions in sea ice coverage and volume, which will lead to decreases in the albedo of the planet (Perovich and Polashenski, 2012), and shifts in Arctic wildlife ecosystems (Post et al., 2013). Often less considered are the consequences for the unique chemistry that occurs between frozen surfaces and the Arctic atmosphere. In this thesis, I will briefly describe specifically the chemistry of ozone in the Arctic boundary layer, and new insights gained as a result of my Ph.D. work.

### 1.2 Oxidation Chemistry within the Boundary Layer

The lowest layer of the atmosphere is known as the troposphere (Figure 1.1). Extending vertically from the surface to ~11 km at midlatitudes ( $\leq 10\%$  of the entire vertical scale of the atmosphere), the troposphere is characterized by decreasing

temperatures with height and contains close to 80% of the mass ( $\sim 4.8 \times 10^{18}$  kg), or  $\sim 90\%$  of the molecules, of the atmosphere (Wallace and Hobbs, 2006).

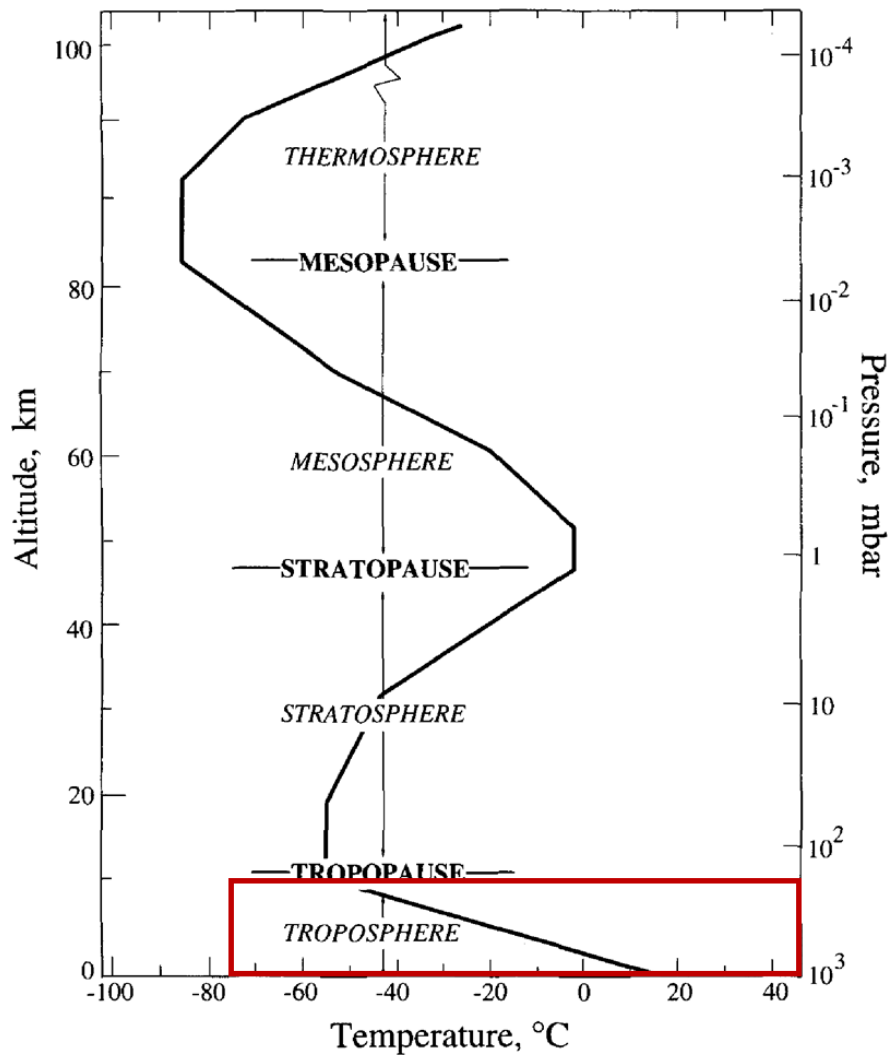


Figure 1.1 Vertical profile of earth's atmosphere, showing temperature changes (x-axis) with respect to altitude (left y-axis) and pressure (right y-axis). Layers are divided based on changes in the temperature gradient with height. The lowest layer of the atmosphere, the troposphere, is outlined in red. Figure repurposed from Seinfeld and Pandis (2012).

Virtually all known life exists in the lowest portion of the troposphere that serves as a boundary between the surface and the rest of the atmosphere: the so-called boundary layer (BL), seen in Figure 1.2.

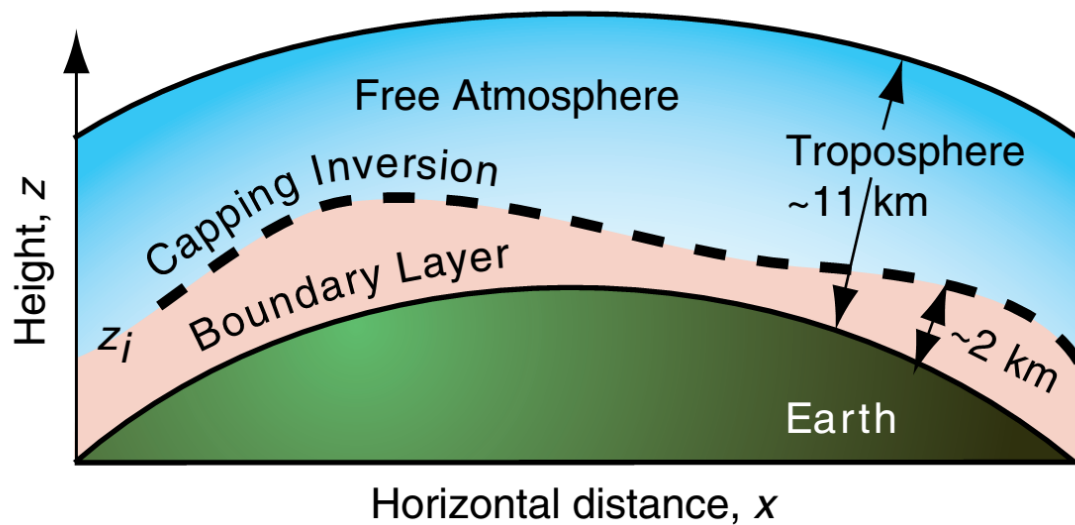


Figure 1.2 Visualization of the troposphere and the planetary BL. The height of the boundary layer, shown here as  $z_i$ , varies throughout the day. Figure taken from Wallace and Hobbs (2006).

The BL is a dynamic system, constantly changing in height (from as low as 200 m to as high as 3 km) as a function of absorbance and emission of radiation from the earth's surface. This heating also in part enables the movement of gases throughout the BL via advection and turbulence (Stull, 1988). The vertical distribution of turbulent activity can be modeled in terms of eddy diffusivity ( $K_z$ ), which parameterizes the diffusion rate in the boundary

layer. One such model is shown by Figure 1.3, which shows how  $K_z$  varies with height above a homogeneous surface (Kumar and Sharan, 2012).

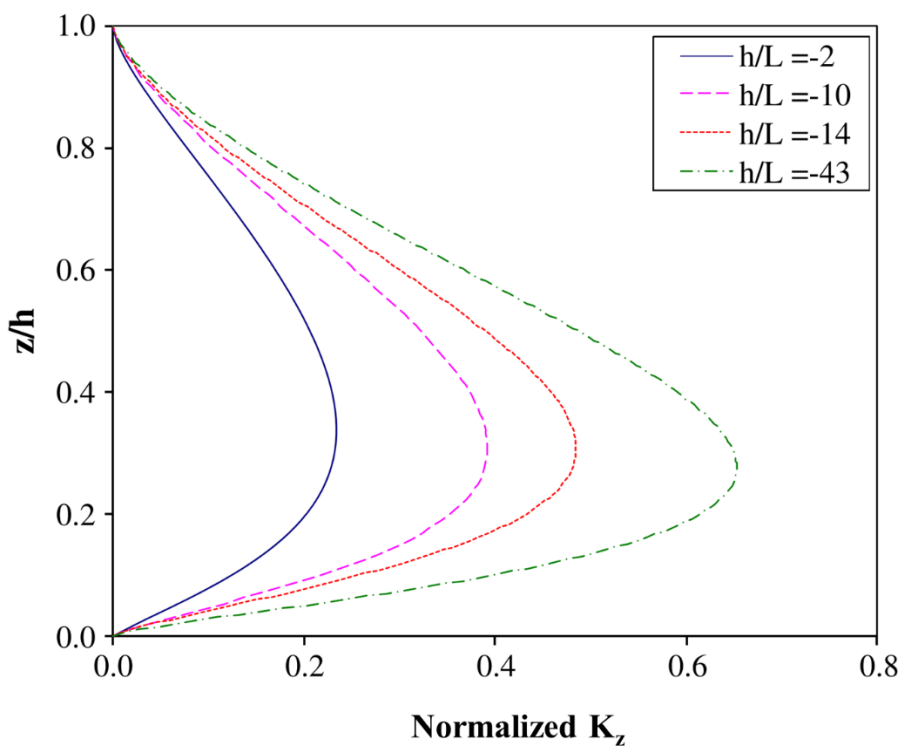


Figure 1.3 Modeled relationship between normalized boundary-layer height ( $z/h$ ) and normalized eddy diffusivity ( $K_z$ ). Here,  $h$  represents the height of the BL, while  $z$  represents altitude.  $K_z$  is modeled here as function of the height at which production of turbulence from buoyancy begins to dominate that produced by wind shearing (i.e., Monin-Obukhov length,  $L$ ). Figure modified from Kumar and Sharan, (2012).

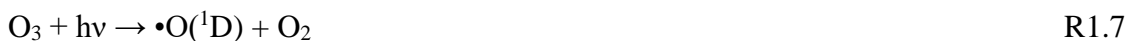
It can be seen here that turbulent mixing increases with altitude until it reaches ~30% of the BL height, and then begins decreasing, converging at  $K_z \approx 0$  at the top of the boundary layer. A “capping” temperature inversion forms at the top of the BL when rising air cools enough to become saturated with water vapor, leading to its condensation as clouds. This

condensation releases latent heat at the top of the boundary layer. When a relatively cooler (more dense) air mass meets the warm air mass (less dense) at this height, further vertical transport of air masses is inhibited (except for especially long-lived, stable compounds). This inversion limits turbulent mixing to the BL, which combined with the high concentration of molecules at the surface ( $2.46 \times 10^{19}$  molecules  $\text{cm}^{-3}$  at 298 K) makes the chemistry within the BL more active than the rest of the troposphere (i.e., the free troposphere, or free atmosphere), which is only intermittently turbulent.

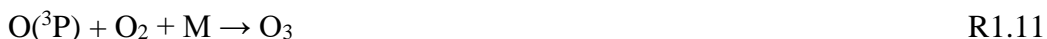
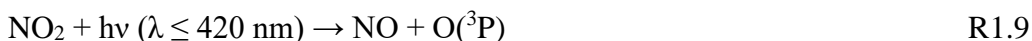
Gaseous pollution released from the surface typically stays in the troposphere until it is either oxidized or permanently removed by depositing onto a surface. Atmospheric oxidation chemistry is controlled by ozone ( $\text{O}_3$ ), which serves as the primary precursor to the atmosphere's primary oxidant, hydroxyl radical ( $\text{OH}$ ) (Thompson, 1992). The hydroxyl radical can react favorably with volatile organic compounds (VOCs) via reactions analogous to R1.1 – R1.6:



Though OH is a critical atmospheric cleansing agent, the oxidation capacity of the atmosphere is actually controlled by its primary precursor, ozone (O<sub>3</sub>) (Thompson, 1992), which forms OH via Reactions R1.7-R1.8.



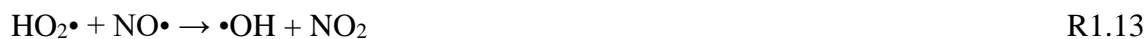
The scientific community is therefore interested in the processes that control ambient production and removal of O<sub>3</sub>. Reactions R1.7-R1.8 are generally thought to dominate O<sub>3</sub> loss processes (~75%) at mid-latitudes and in the marine boundary layer (Horowitz et al., 2003; Read et al., 2008). Additionally, O<sub>3</sub> itself is a potent oxidizer and can efficiently remove alkenes from the atmosphere. Major sources of tropospheric O<sub>3</sub> include the photolysis of NO<sub>2</sub> and the periodic turbulent intrusion of stratospheric air, rich in O<sub>3</sub> formed from the photolysis of oxygen (R1.9-R1.11) (Blacet, 1952; Chapman, 1930; Finlayson-Pitts and Pitts, 2000).



However, O<sub>3</sub> can also react with NO to reproduce NO<sub>2</sub> (R1.12), which essentially makes R1.9-R1.11 a null cycle:



Net O<sub>3</sub> production from NO<sub>2</sub> photolysis therefore only occurs when NO<sub>2</sub> is formed by alternative processes, such as R1.5 or R1.13:



The earliest measurements of surface-level O<sub>3</sub> from the latter half of the 19<sup>th</sup> century at various locations across the world yielded O<sub>3</sub> mole fractions peaking at 10 nmol mol<sup>-1</sup> (Volz and Kley, 1988). Modern O<sub>3</sub> mole fractions can range anywhere between 20-50 nmol mol<sup>-1</sup> in clean, remote air (Marenco et al., 1994), depending on location and time of year. A time series of spring hourly O<sub>3</sub> trends at the remote observatory in Mauna Loa, HI, is seen in Figure 1.4 (Ridley et al., 1992), while monthly average O<sub>3</sub> in remote regions can be found in Figure 1.5 (Oltmans and Levy, 1994). Finally, annual O<sub>3</sub> average trends since (Cooper et al., 2014), and average hourly variations in remote regions can be seen in Figure 1.6.



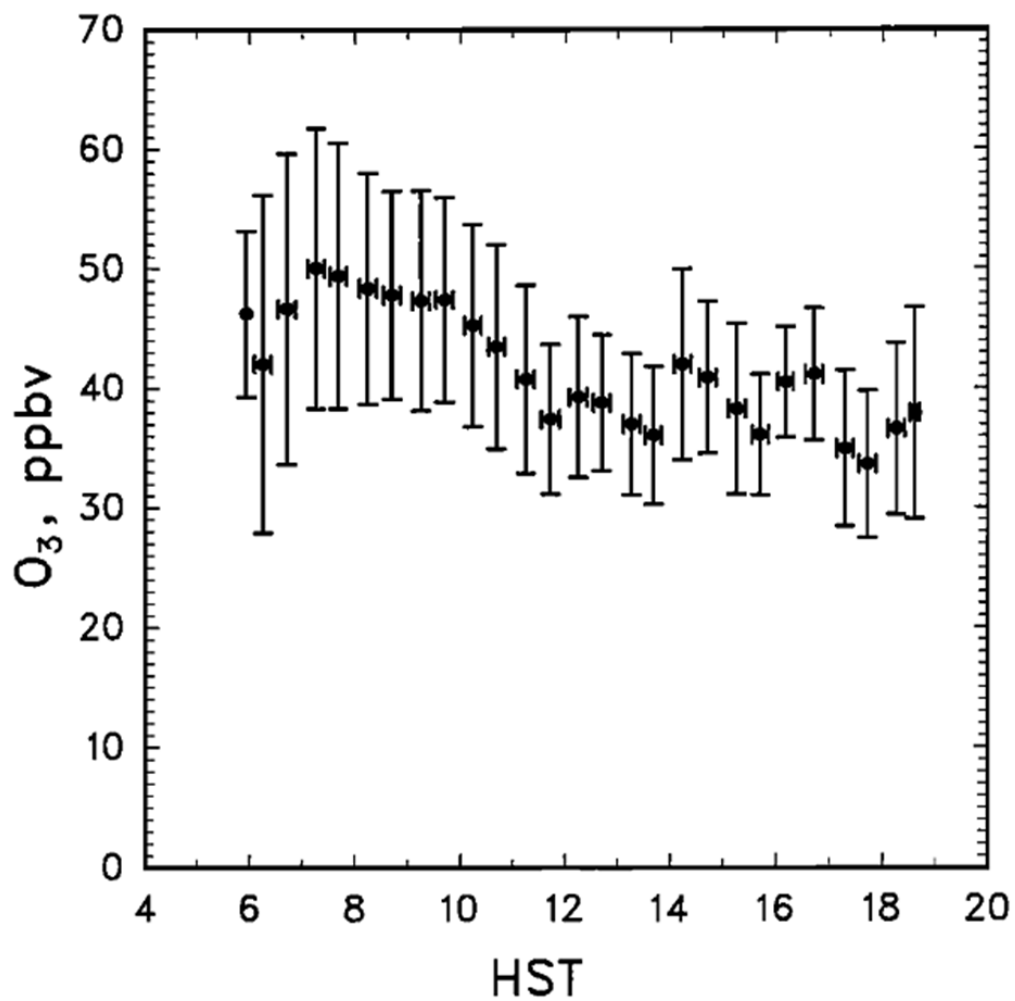


Figure 1.4 Hourly time series of  $O_3$  at Mauna Loa Observatory during May 1988. Figure reproduced from Ridley et al (1992).

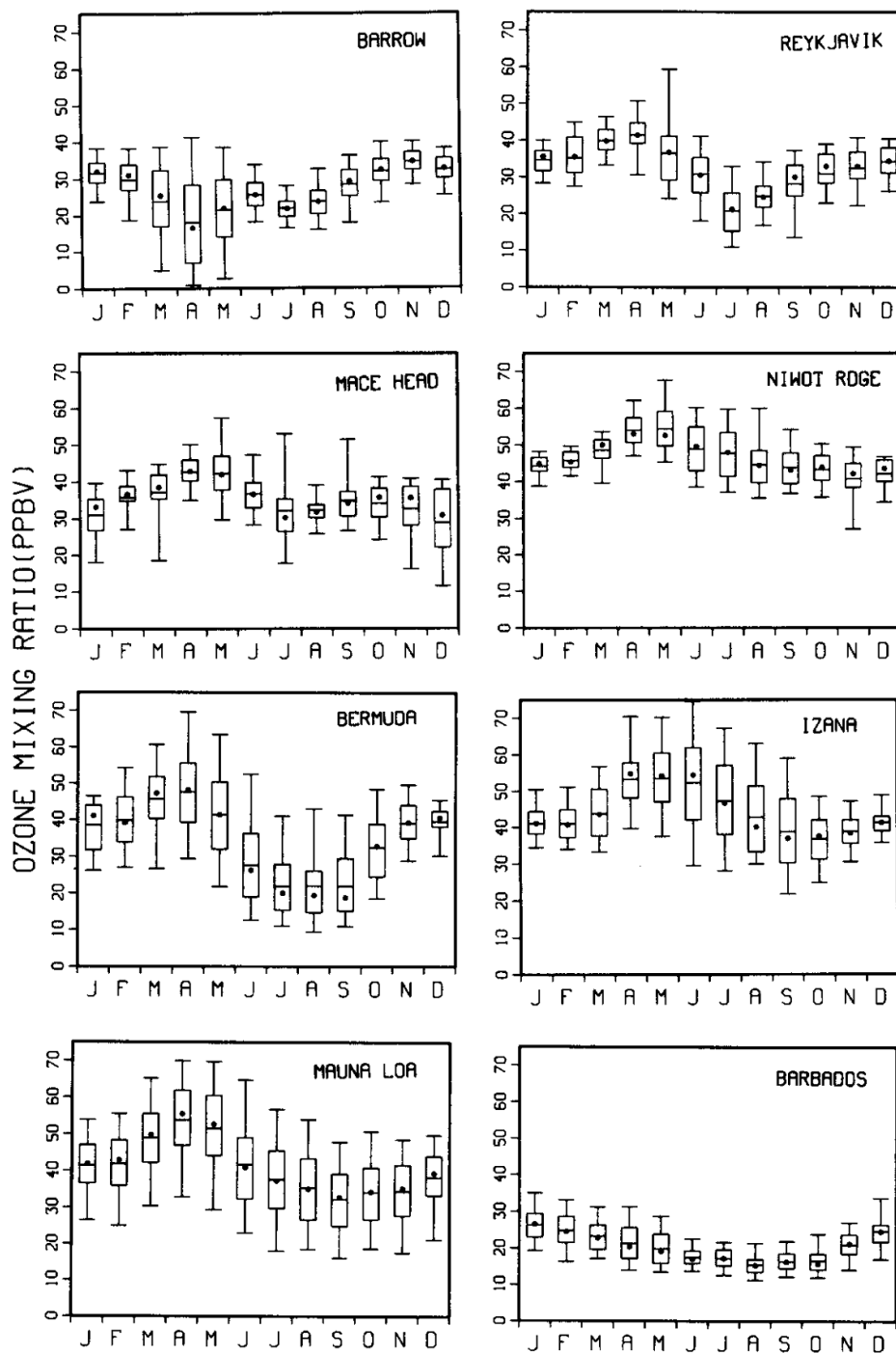


Figure 1.5 Whisker plots of O<sub>3</sub> at various remote tropospheric sites in the northern hemisphere. Central tendencies included are median (dot), mean (bar), inner 50<sup>th</sup> percentile (box), and inner 90<sup>th</sup> percentile (whiskers). Figure reproduced from Oltmans and Levy (1994).

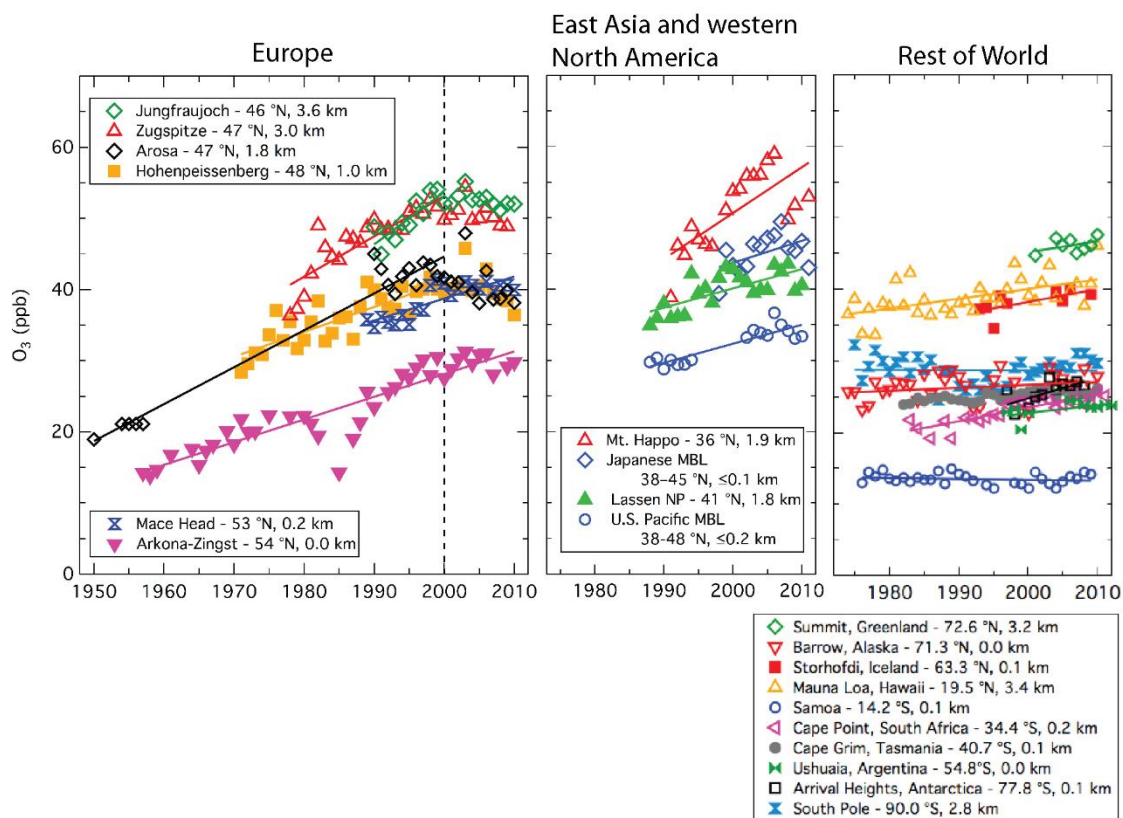


Figure 1.6 Annual trends in ozone at remote sites around the northern hemisphere. Figure taken from Cooper et al. (2014).

While these  $O_3$  levels are not harmful to humans,  $O_3$  can begin to cause respiratory issues and plant damage at levels above  $55 \text{ nmol mol}^{-1}$  (Hewitt et al., 1990; Hubbell et al., 2005). High mole fractions of  $O_3$  are found most often in urban environments, and has even been detected in amounts exceeding  $100 \text{ nmol mol}^{-1}$  in Mexico City (Raga and Raga, 2000), and approaching  $300 \text{ nmol mol}^{-1}$  in Los Angeles, CA, during the 1970s (Parrish and Zhu, 2009). This increase in  $O_3$  levels can be attributed to increasing  $NO_x$  ( $NO_x = NO + NO_2$ ) levels, a perturbation largely resulting from growing anthropogenic use of fossil fuels (Chameides et al., 1992).

### 1.3 Arctic Ozone Depletion

Because O<sub>3</sub> can act as an atmospheric cleaning agent, a greenhouse gas, and a poison to humans, it is of great scientific interest to understand the processes that produce and remove tropospheric ozone (Mickley et al., 1999; Myhre et al., 2013). Modern chemical models are largely able to simulate the major characteristics of the global distribution of O<sub>3</sub> (sources / sink uncertainties ranging from 10-20%), though there remain discrepancies in simulating changes associated with emissions and changes in climate (Solomon et al., 2007). It would then be expected that simulating O<sub>3</sub> in remote, pristine regions (e.g., over oceans) could be done with relatively high accuracy in regions separated from pollution, where the chemistry is expected to be less complex, and O<sub>3</sub> loss would be dominated by photolysis and water vapor.

Until the 1980s, the above reasoning was extended to the polar regions, which are dry and far-removed from local sources of anthropogenic pollution. Interest in studying the atmospheric chemistry of these regions piqued on the discovery of the depletion of stratospheric ozone over Antarctica (Farman et al., 1985). This phenomenon is caused by the reaction of O<sub>3</sub> with reactive chlorine atoms (R1.14), originating from the photolysis of long-lived chlorofluorocarbons (Molina and Rowland, 1974).



The Cl atom in the ClO produced in R1.14 can chemically recycle in a number of ways (both in the gas phase and heterogeneously on the surface of ice crystals), and subsequently catalytically destroy more O<sub>3</sub>. The chemical mechanisms specific to stratospheric ozone

depletion are beyond the scope of this thesis, but the interested reader is referred to the excellent review by Solomon (1999).

Concurrent with investigations of the stratospheric ozone depletion, a mysterious brown “haze” was being studied in the Arctic troposphere during springtime. It was learned that this haze is caused by light scattering off Eurasian pollutants (specifically sulfate aerosol) that travel to the Arctic during the dark winter months, enabled by cold temperatures, a stable boundary layer (i.e., temperatures increase with height, preventing vertical movement), and atmospheric circulation patterns (Barrie et al., 1981, 1989; Worthy et al., 1994).

A serendipitous result of monitoring trace gases in the Arctic was the unexpected discovery that boundary-layer O<sub>3</sub> episodically depletes from “clean,” background mole fractions of 40 nmol mol<sup>-1</sup> to near zero for periods ranging from hours to weeks (Figure 1.7).

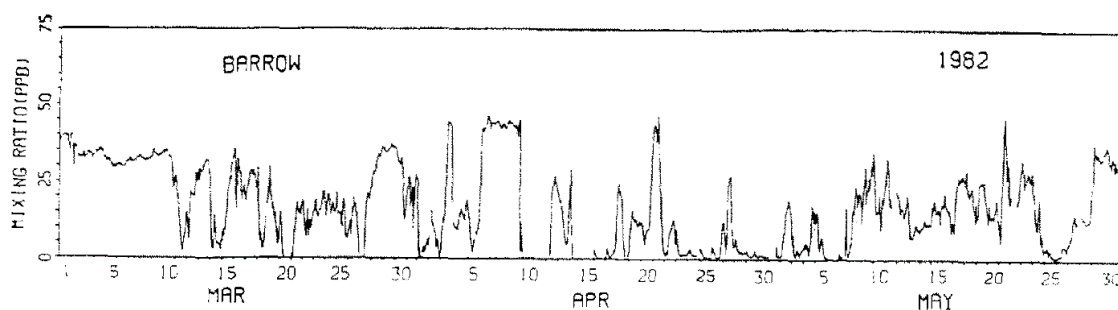


Figure 1.7 Representative time series of boundary-layer O<sub>3</sub> behavior in the Arctic from Barrow, AK. Figure reproduced from Oltmans et al (1989).

As illustrated by Figure 1.7, the gross variability in  $O_3$  mole fractions coincides with the onset of polar sunrise, and typically ceases in late May / early June. It can be seen from Figure 1.5 that the change in  $O_3$  variability during these months at Barrow is considerably more dramatic than other at remote sites. It was also noticed at Alert, NU, another high Arctic observation site, that the behavior of  $O_3$  during these periods was strongly anticorrelated with Br-species collected on filters, as seen in Figure 1.8 (Barrie et al., 1988). This suggests the possible involvement of reactive halogen species in a manner resembling stratospheric ozone depletion, described above.

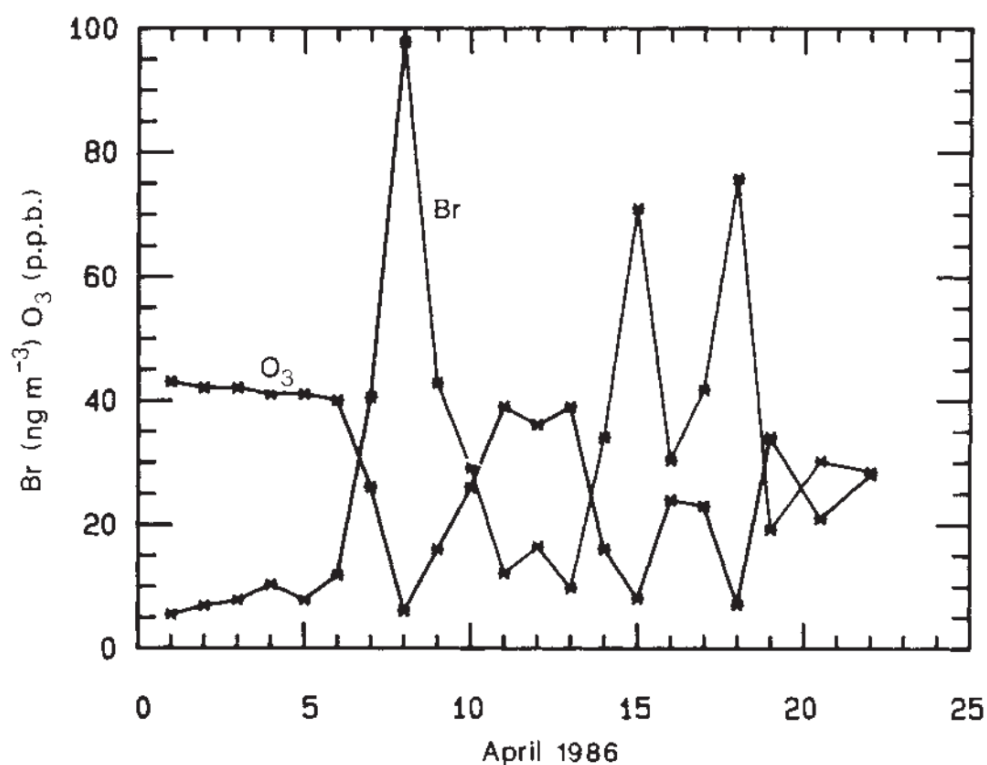


Figure 1.8 Comparison of daily mean ground level  $O_3$  and filterable Br concentrations at Alert, NU, Canada in April 1986.

The discovery of these Ozone Depletion Events (ODEs) inspired intensive scientific studies aimed at elucidating their fundamental characteristics, including the underlying chemistry, the corresponding kinetics, and their spatial extent (i.e., could they be an Arctic-wide phenomenon?). What follows is a brief summary of current knowledge regarding ODEs:

When the sun rises in the Arctic spring, molecular halogens are believed to be produced within a quasi-brine layer (QBL) that exists on frozen, saline surfaces like snow (Cho et al., 2002; Pratt et al., 2013). Once these halogens desorb and enter the boundary layer, they photolyze and react to remove boundary layer O<sub>3</sub> via Reactions R1.15- 1.16 below, where X = Cl, Br, I:

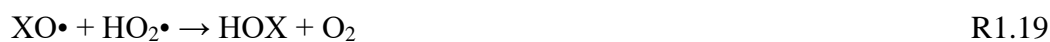


BrO species was the first XO species unambiguously detected by differential optical absorption spectroscopy in the Arctic at Alert during the Polar Sunrise Experiment 1992 (Hausmann and Platt, 1994). XO species are photolabile and can reform O<sub>3</sub> in a null cycle (R1.17, R1.11).



Therefore, O<sub>3</sub> is only truly destroyed when XO reacts with another species (e.g. YO, where Y = Cl, Br, or I; or HO<sub>2</sub>), and not reform O<sub>3</sub>. Ozone-destruction therefore is propagated by

the regeneration of reactive halogen species. In the gas phase, R1.18 has traditionally been believed to be the rate limiting step in O<sub>3</sub> destruction when atmospheric concentrations of XO/YO are high, while R1.19 occurs when they are lower (Hausmann and Platt, 1994; Le Bras and Platt, 1995; Piot and von Glasow, 2008).



Reaction R1.18a directly reproduces reactive halogen radicals that can continue depleting additional O<sub>3</sub>, while the XY and the HOX produced by R1.18b and R1.19 must first undergo photolysis (R1.15, R1.20).



In addition, the nitrogen oxides NO and NO<sub>2</sub> (NO<sub>x</sub>) have been detected in ambient Arctic air at levels between 10 and 100 pmol mol<sup>-1</sup> (Honrath et al., 2002; Ridley et al., 2000), with its primary source originating from photochemistry within the Arctic snowpack (Beine et al., 2002; Honrath et al., 1999; Ridley and Orlando, 2003). The reaction of NO with XO can reproduce X, while NO<sub>2</sub> reacts with XO to produce XONO<sub>2</sub> (R1.21-R1.24) (Cao et al., 2014; Evans et al., 2003; Morin et al., 2007, 2012). XONO<sub>2</sub> is soluble and can enter the QBL of snow surfaces or the aqueous phase on sea salt aerosol (Bartels-Rausch et al., 2014; Koop et al., 2000).





The production of HOX (R1.19 and R1.24) is also the first step in an autocatalytic reaction sequence known generally as the “halogen explosion,” which is believed to be responsible for the exponential buildup of halogen concentrations at high enough levels to enable the efficient destruction of O<sub>3</sub> (Fan and Jacob, 1992; Pratt et al., 2013; Tang and McConnell, 1996; Vogt et al., 1996; Wennberg, 1999a; Wren et al., 2013).



Per R1.25-R1.26, HOX diffuses into the QBL that exists on frozen surfaces and reacts with halides to produce dihalogen species. The dihalogens return to the gas phase (R1.27), photolyze (R1.15), and react with O<sub>3</sub> (R1.16), after which the sequence can reinitialize until some required reagent depletes. A recent modeling study by Thompson et al. (2016) found that most bromine atoms are generated through Br<sub>2</sub> photolysis rather than directly from other reservoirs (i.e., R1.18a, R1.20, R1.21), because XO termination is very effective (Thompson et al., 2016). This suggests, therefore, that the rate limiting steps in O<sub>3</sub>

depletion are actually those steps that produce  $X_2$  or  $XY$ , such as Reactions R1.18 and R1.26.

While Cl-, Br-, and I-related species are all involved with  $O_3$ -depletion chemistry to some degree (Thompson et al., 2015), it has been traditionally expected that Br-species are the most relevant based on relative abundances and kinetic favorability for reactions with  $O_3$  over hydrocarbons. While Cl atoms react most favorably with  $O_3$  (typical conversion time of  $\sim 0.1$  sec) relative to Br or I (typical conversion time of  $\sim 1$  sec), the relatively low concentrations ( $[Cl]$  has been estimated to range from  $4.8 \times 10^4$  to  $1.7 \times 10^5$  molecules  $cm^{-3}$  (Keil and Shepson, 2006)) and slow photolysis rate of  $Cl_2$  (typical spring lifetime of  $\sim 8$  min, while  $Br_2$  lifetime is  $\sim 20$  seconds (Thompson et al., 2015)), combined with the high reactivity of Cl toward the large abundance of tropospheric hydrocarbons mitigates its role in ODEs (Simpson et al., 2007b). For example, at a typical Arctic springtime  $[Br]/[Cl]$  ratio of 550 (Keil and Shepson, 2006), the X=Br version of R1.16 still proceeds at a rate  $\sim 33$  times faster than that for the Cl reaction (Thompson et al., 2015). In addition, even though  $Cl_2$  has recently been observed at mole fractions briefly peaking above  $400 \text{ pmol mol}^{-1}$ , it was still only estimated to account for as much as 21% of the observed  $O_3$  depletion in that study (Liao et al., 2014). Until recently, most evidence for the presence of reactive I-species in the Arctic was based on the springtime peaks in filterable iodine measurements (Sturges and Barrie, 1988), total gaseous iodine (Martinez et al., 1999), and active differential optical absorption spectroscopy observations of IO at levels peaking at  $1 \text{ pmol mol}^{-1}$  (Zielcke, 2015). Most model studies testing our understanding of ODE chemistry have thus been designed considering R1.14-R1.20 in terms of Br and Cl-based chemistry. In these cases,  $O_3$  is expected to deplete from

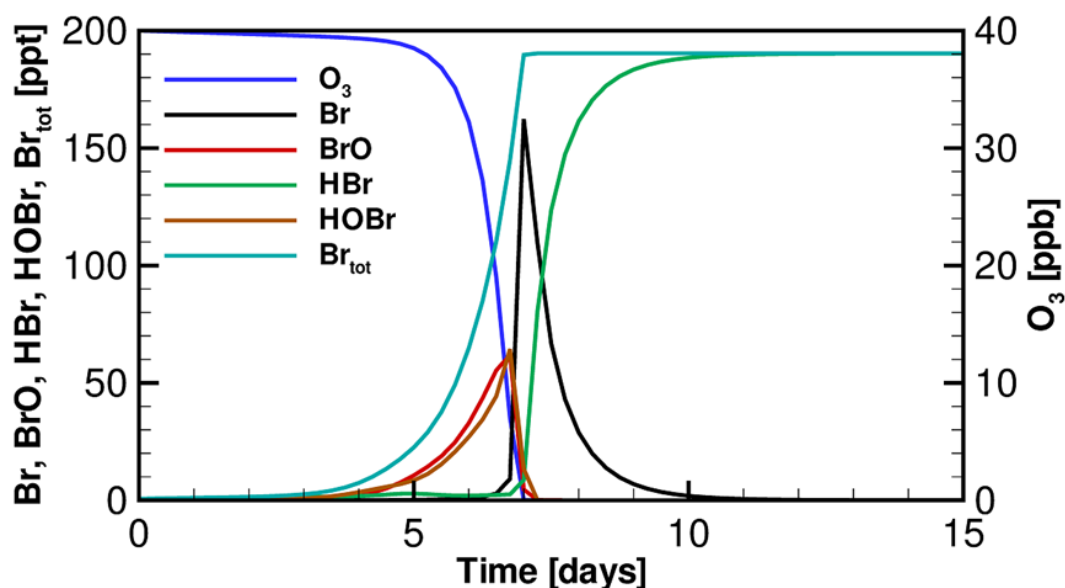


Figure 1.9 Example model time series simulation of ODEs considering only bromine-based mechanisms. In this particular simulation, the bromine compounds originate from aerosol or snowpacks, and are shown to deplete  $40 \text{ nmol mol}^{-1}$  (ppb) of  $\text{O}_3$  to  $0 \text{ nmol mol}^{-1}$  over the course of 7 days. Figure taken from Cao et al. (2014)

background levels to near zero on a timescale on the order of days (e.g., Cao et al., 2014; Hausmann and Platt, 1994) as illustrated by Figure 1.9. In fact, the disappearance of  $\text{O}_3$  within an air mass is usually observed on timescales much faster than 24-hours (Halfacre et al., 2014), which would require the co-observation of  $>30 \text{ pmol mol}^{-1}$  of BrO on average throughout an ODE if it is Reaction R1.16 that limits the chemical rate of  $\text{O}_3$  depletion (discussed in greater detail within Chapter 3). While the largest recorded surface BrO mole fraction is  $41 \text{ pmol mol}^{-1}$  (Pöhler et al., 2010), BrO levels rarely rises above  $30 \text{ pmol mol}^{-1}$  for extended periods of time. When bromine chemistry cannot account for the observed rate of  $\text{O}_3$  depletion, the apparent  $\text{O}_3$  depletion is generally attributed to the transport of an

already O<sub>3</sub>-devoid air mass that chemically depleted upwind. Alert, NU, Canada is an example of where this behavior is believed to occur often.

In 1992, a major effort was made to study ODEs during the Polar Sunrise Experiment (PSE) campaign that occurred near Alert (Barrie et al., 1994c). A map of this area can be seen in Figure 1.10. The surrounding terrain is described as steeply rolling with frequent deep ravines and high cliffs. The observation site (labeled BAPMoN in Figure 1.10) is located on a plateau approximately 200 m above sea level. Hopper and Hart (1994) report that meteorological measurements in this area are difficult because they are significantly affected by the surrounding topography. The prevailing winds are channeled from the surrounding mountains, resulting in predominately southerly winds. However, when winds originated from the north or east (i.e., air that had traveled over the ocean), Hausmann and Platt (1994) noted ODEs and increases in BrO (time series in Figure 1.11).

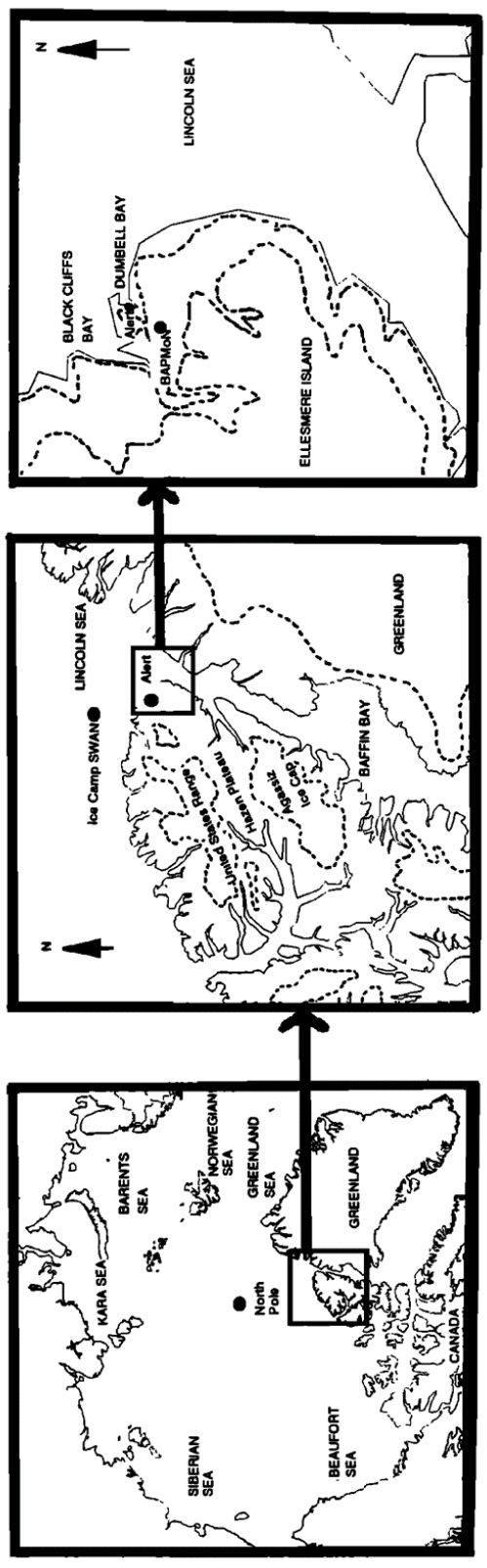


Figure 1.10 Map of Alert, NU, Canada. Left – Arctic Basin. Middle – Northern Ellesmere Island (dashed contours correspond to 1000 m. Right – Alert region (dashed contours correspond to 60 m and 300 m). Figure reproduced from Hopper and Hart (1994).

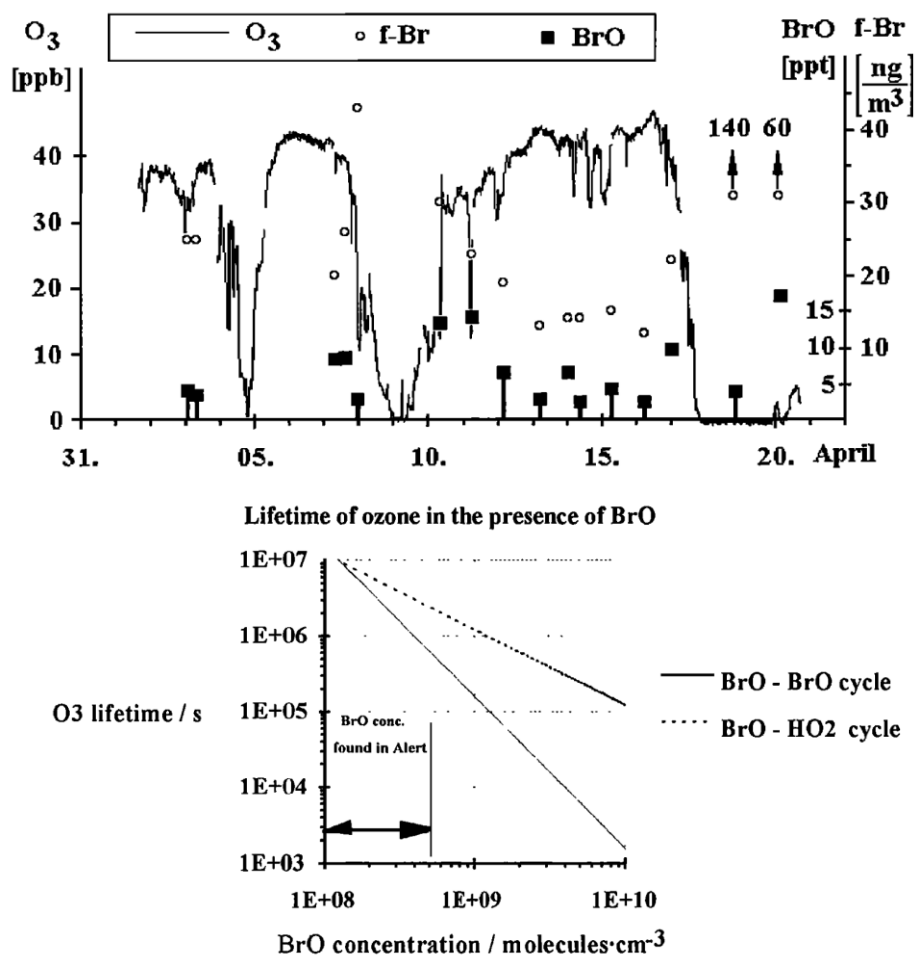


Figure 1.11 Relationship between  $O_3$  and BrO during the Polar Sunrise Experiment 1992. Top – time series between  $O_3$ , BrO, and filterable bromine. Bottom – relationship between the lifetime of  $O_3$  and the  $[BrO]$  required to obtain this lifetime. Figure adapted from Hausmann and Platt (1994).

They also noted rapid changes in  $O_3$  concentrations, corresponding to  $1.5 \text{ nmol mol}^{-1} \text{ hr}^{-1}$  to  $40 \text{ nmol mol}^{-1} \text{ hr}^{-1}$ . In both cases,  $O_3$  can deplete from an upper limit of  $35 \text{ nmol mol}^{-1}$  to near zero in less than 24 hours. Hausmann and Platt (1994) subsequently calculated the relationships between the lifetime of  $O_3$  and the corresponding BrO required to achieve

this Figure 1.11, bottom). If the typical amounts of BrO observed at Alert are considered in this respect ( $1 \times 10^8 - 5 \times 10^8 \text{ cm}^{-3}$ ), the corresponding O<sub>3</sub> lifetimes range between 180 days (if R1.19 is limiting) and 7 days (when R1.18 is limiting). In addition, analyzed periods of O<sub>3</sub> depletion were observed under low wind speeds (< 5 m/s), suggesting a stable boundary layer. A scenario is then developed by which O<sub>3</sub> completely depletes within an airmass upwind over the Arctic Ocean, and the rate of observed O<sub>3</sub> depletion is a function of the spatial extent of the transition range between background O<sub>3</sub> (at the edge of an air mass) and depleted O<sub>3</sub>.

Similarly, a scenario of meteorologically induced O<sub>3</sub> recovery was clearly observed by Morin et al. (2005), which observed sudden variations in O<sub>3</sub> levels were accompanied by similar changes in wind speed and direction, water vapor, concentrations, temperature, and BrO mole fractions (Figure 1.12).

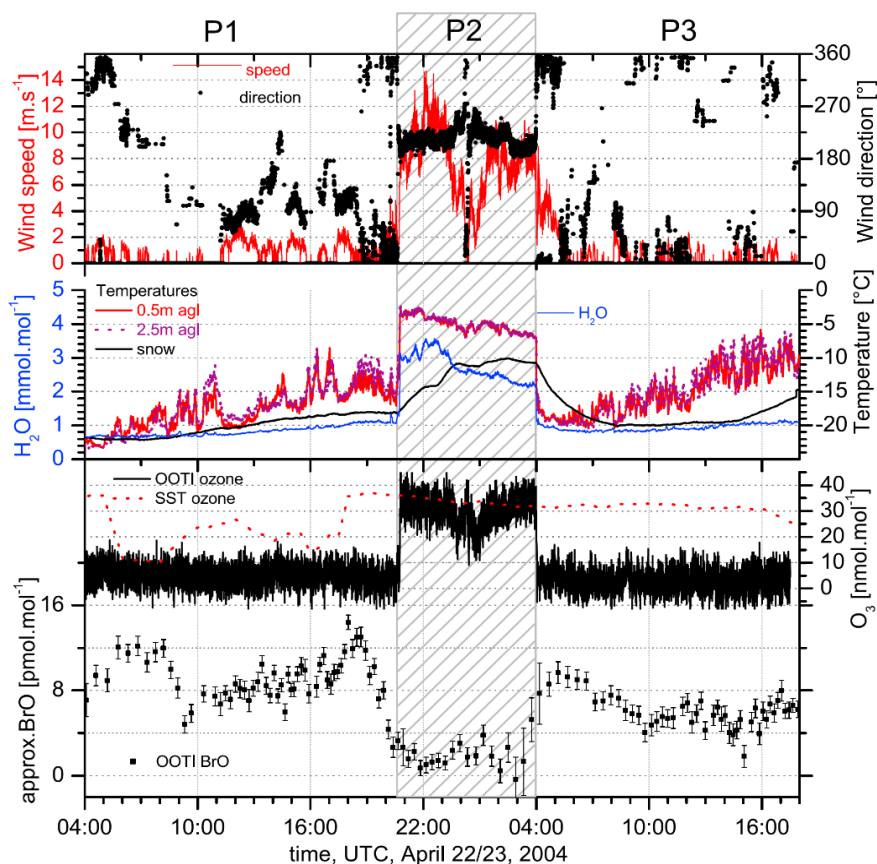


Figure 1.12 Time series measurements of (top) wind speed, wind direction, (middle) water mole fractions, snowpack and ambient temperature, and (bottom)  $\text{O}_3$  and BrO mole fractions. Period (P) 1 shows a period of depleted  $\text{O}_3$  and elevated BrO. In P2, a sudden shift is noted across all variables, indicative of the transport of an air mass with strikingly different composition from that in P1. In P3, variables return to resembling P1. OOTI represents ice-based observations 5 km off the coast of Alert, NU, while SST represents coastal observations from Alert. Figure taken from Morin et al. (2005).

As very few studies have actually claimed to have observed local scale chemical ODEs (Boudries and Bottenheim, 2000; Jacobi et al., 2006), a question is then raised of where the ODE chemistry is occurring. Given that the Arctic Ocean is generally covered by frozen saline surfaces during the Arctic spring, it is reasonable to hypothesize that large amounts of halogens could be produced from its surface. Utilizing air mass trajectory



modeling methods (discussed further in Chapters 3 and 4), Simpson et al. (2007a) found that during periods of enhanced BrO, air masses often passed over Arctic Ocean sea ice before arriving at observation sites (Figure 1.13, left). Similarly, Bottenheim and Chan (2006) found that air masses with low amounts of O<sub>3</sub>

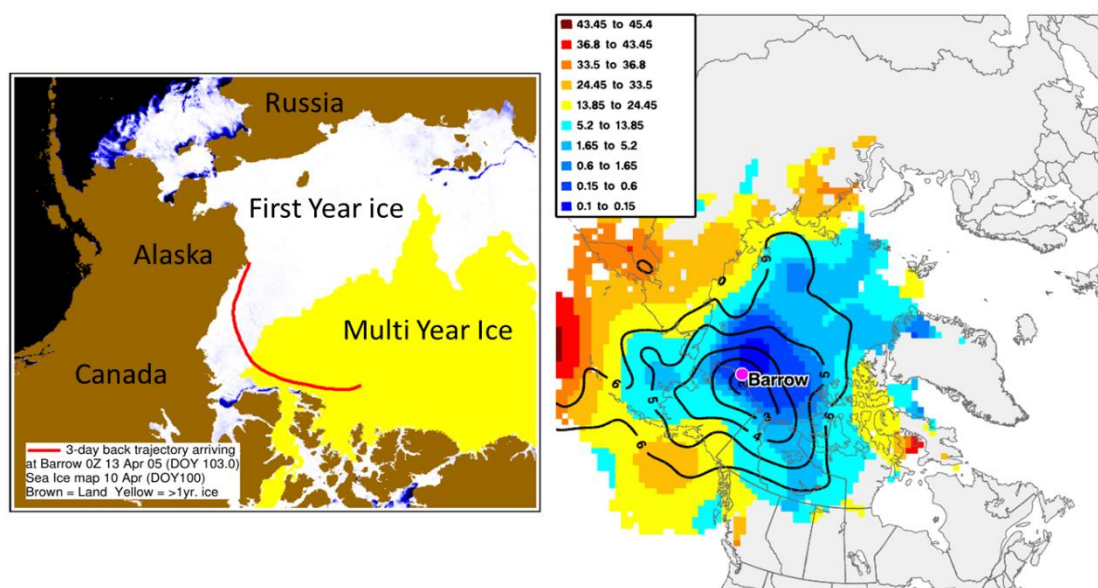


Figure 1.13 Example back trajectory during a high BrO event. Trajectory starts in Barrow, AK, and travels backward in time over first year ice, and subsequently multi-year ice. Right – Aggregation of 10 years of back trajectories from Barrow, AK, according to O<sub>3</sub> mole fractions. Cooler colors represent lower O<sub>3</sub> mole fractions. Figure adapted from Simpson et al. (2007a) and Bottenheim and Chan (2006).

originate predominantly from over the Arctic Ocean before arriving at the coastal observatories used in their study (Figure 1.13, right).

Finally, additional evidence of ODE chemistry occurring over the Arctic Ocean comes in the form of satellite-borne observations of BrO, which have been shown to be

particularly enhanced over the frozen ocean (Begoin et al., 2010; Richter et al., 1998) (Figure 1.14). However, deriving surface information concerning BrO from these total column observations is still the subject of ongoing research (Choi et al., 2012; Salawitch et al., 2010; Theys et al., 2009, 2011).

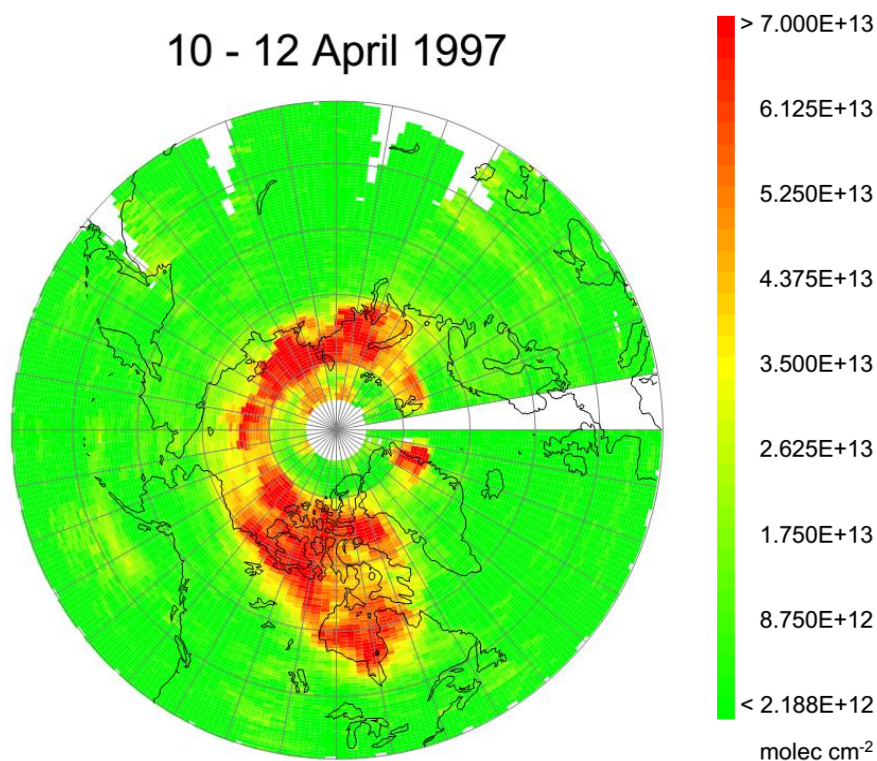


Figure 1.14 The Global Ozone Monitoring Experiment (GOME) satellite observations of BrO. As can be seen, enhanced regions of BrO include the Arctic Ocean and the Canadian archipelago. Figure adapted from Richter et al. (1998).

The majority of in situ O<sub>3</sub> and halogen observations come from coastal sites around the Arctic, such as Barrow, Alert, and Zeppelin Station (Svalbard), which all have year

round O<sub>3</sub> monitoring stations as a part of the World Meteorological Organization's Global Atmospheric Watch (GAW) program (Schultz et al., 2015). For reasons of logistics, safety and cost, long-term studies of O<sub>3</sub> over the Arctic Ocean are difficult. The only long-term study of O<sub>3</sub> above the Arctic Ocean occurred from the drifting schooner, TARA (Figure 1.15) (Bottenheim et al., 2009).

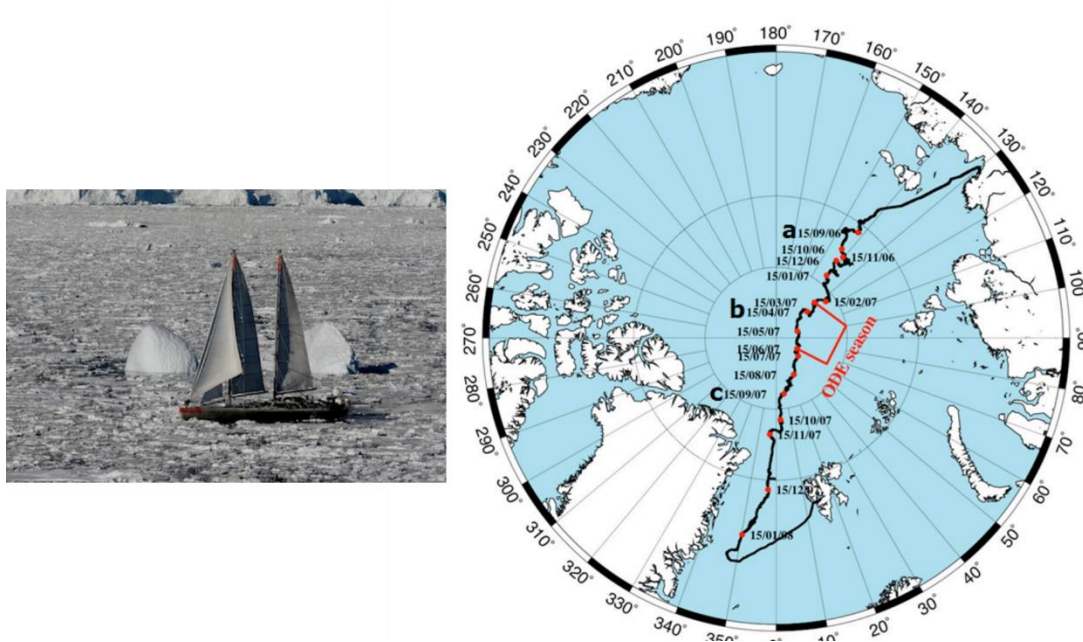


Figure 1.15 Photograph of the drifting schooner TARA (left) and its drift track (right) during its 2007 expedition. Photograph of TARA reproduced from [oceans.taraexpeditions.org/](http://oceans.taraexpeditions.org/), drift track reproduced from Bottenheim et al. (2009).

Bottenheim et al. (2009) observed essentially sustained O<sub>3</sub> depletion above 80° N during March – May 2007 (Figure 1.16), but lacked other chemical information (i.e., BrO) necessary to interpret the chemistry. Long-term studies from the Arctic Ocean surface are

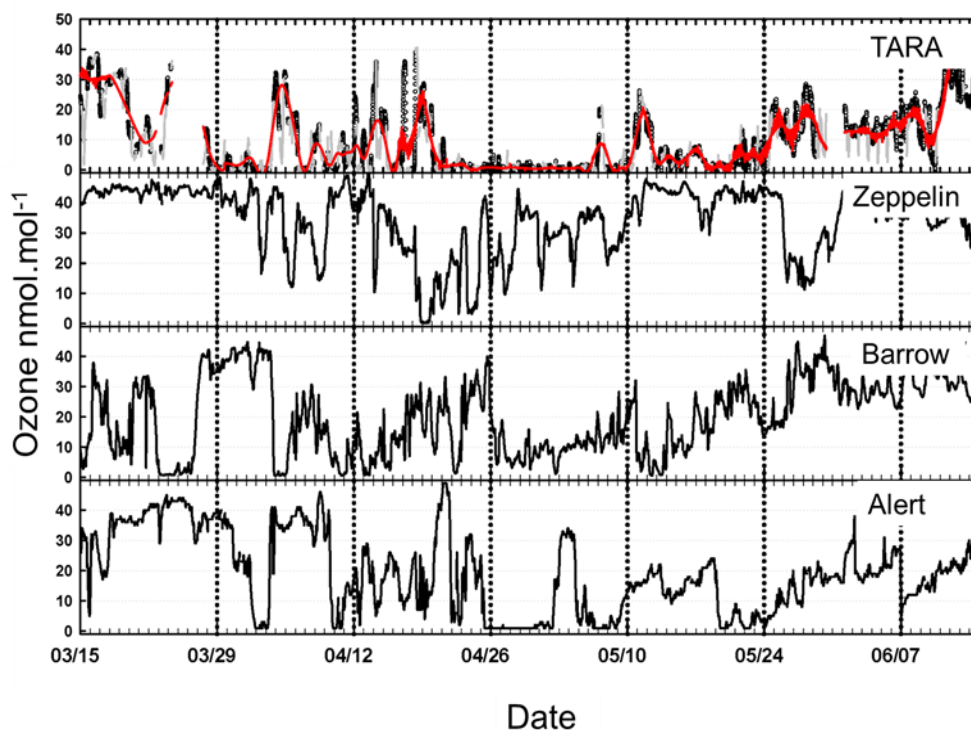


Figure 1.16 Time series measurements of  $O_3$  obtained from (top) TARA (the Arctic Ocean), Zeppelin Station, Barrow, and Alert (bottom). Relative to the coastal sites in the lower panels,  $O_3$  observed by TARA is effectively completely depleted from mid-March until late May. Figure obtained from Bottenheim et al. (2009).

necessary, though, if the community is to obtain a full understanding of  $O_3$  chemistry in the Arctic. Most recently, Knepp et al (2010) described the construction of a buoy-based observatories. These “O-Buoys” were built to observe  $O_3$ , BrO,  $CO_2$ , and a suite of meteorological variables. Since the construction of this first buoy, a total of 19 buoy deployments have occurred across the Arctic Ocean for the purpose of observing in situ  $O_3$  depletion events in order to better understand the chemistry, the corresponding kinetics, and to produce data that can be used to test our understanding of these properties using models.

There also exists the possibility that more ODEs have been observed locally at coastal sites, but the community does not fully understand the chemistry enough to explain the kinetics. As mentioned above, the majority of field and model studies to date consider Br- and Cl-containing compounds while discounting I-species due to a lack of observations above limits of detection. However, during a recent field campaign by our research group, Raso et al. (2016) detected I<sub>2</sub> within snowpack interstitial air at peak mole fractions of ~5 pmol mol<sup>-1</sup> under natural illumination. Using a peak Br<sub>2</sub> value of 250 pmol mol<sup>-1</sup>, Raso et al (2016) used a 0-D model to assess that this small amount of I<sub>2</sub> can account for almost 10% of the total simulated O<sub>3</sub> depletion, consistent with previous model studies (Calvert and Lindberg, 2004; Thompson et al., 2015). Further, Thompson et al. (2015) found in their 0-D model, constrained to real-world observations from Barrow, AK, in Spring 2009, that adding an artificial 0.2 pmol mol<sup>-1</sup> of I<sub>2</sub> could supplement Br-species to reduce O<sub>3</sub>-depletion timescales to around 8 hours. However, more field observations of I<sub>2</sub> and the full dissemination of O-Buoy observations through analysis and modelling are required to understand the role of iodine species in ODEs.

One additional outstanding question related to ODE chemistry concerns what physical environments (i.e., snowpacks, aerosols) halogen species are initially produced at polar sunrise to deplete O<sub>3</sub> via R1.15-R1.27. As seen in Figure 1.17, ODEs are typically only observed within the lowest few hundred meters of the troposphere

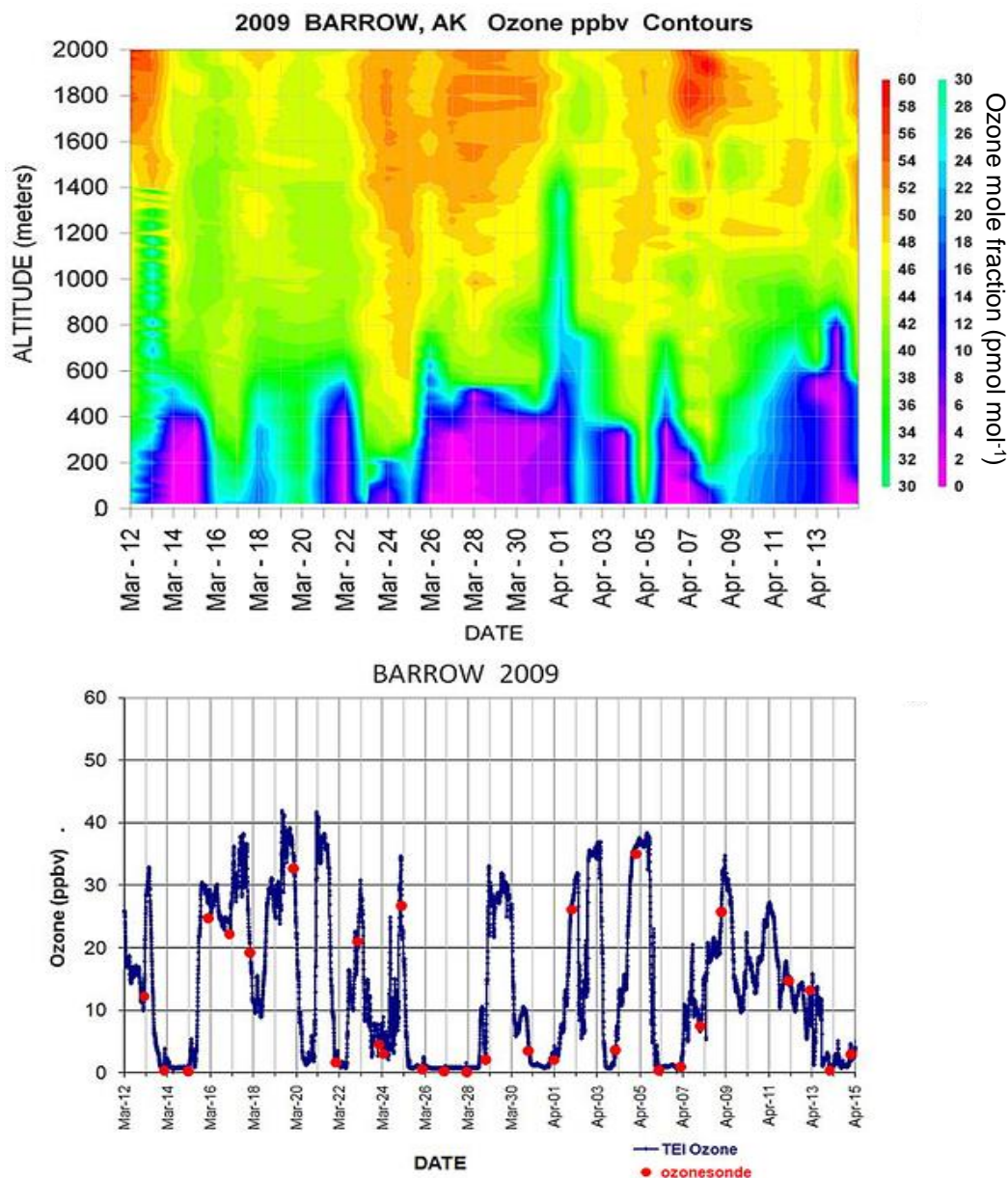


Figure 1.17 Time series of sonde-based vertical profiles of  $O_3$  in Barrow, AK, during Spring of 2009. Bottom: Surface-based time series of  $O_3$ . Figure adapted from Oltmans et al. (2012).

(Bottenheim et al., 2002b; Oltmans et al., 2012), leading researchers to believe that the corresponding halogen chemistry was similarly located. Indeed, Tackett et al. (2007) found

from balloon-based measurements of oxygenated hydrocarbons that halogen chemistry was most active within the lowest 100-200 m of the atmosphere, concluding that halogens are likely emitted from snowpacks. While Br<sub>2</sub> and BrCl had been observed within snowpacks previously (Foster et al., 2001; Spicer et al., 2002), recent field studies from our group have used chemical ionization mass spectrometry (CIMS) to detect Br<sub>2</sub> (Pratt et al., 2013), Cl<sub>2</sub> (Custard et al., 2016) and I<sub>2</sub> (Raso et al., 2016) within the interstitial air of acidic, surface snowpacks around Barrow, AK. The halogen behavior within the snowpack as observed by these CIMS-based studies is consistent: when light is introduced to acidic snowpacks, molecular halogen production is observed. Seemingly contrary to some laboratory studies (e.g., Oldridge and Abbatt, 2011; Oum et al., 1998a; Wren et al., 2013), addition of O<sub>3</sub> without light caused no significant halogen production, but enhanced halogen production when light was present. These researchers suggested a photochemical mechanism by which condensed-phase OH, photochemically formed from either nitrite or hydrogen peroxide (France et al., 2012), oxidizes halides to molecular halogens. These halogens can then exit the snowpack and enter the atmosphere through a combination of diffusion and wind-pumping, as originally proposed by a previous model study (Michalowski et al., 2000). However, these researchers could not prove that this mechanism was operative, and thus this mechanism requires explicit testing.

#### 1.4 Research Objectives

In this thesis, I will discuss my efforts to improve our understanding of fundamental Arctic O<sub>3</sub> chemistry through buoy-based (Chapters 2-4) and laboratory-based observations (Chapter 5). Specifically, the following broad scientific questions were addressed:

- 1) Do long-term, ocean based O<sub>3</sub> and BrO observations behave as would be expected from numerous attempts to model ODE chemistry (Chapter 3)?
- 2) What are the spatial extents of ODEs across the Arctic (Chapter 3)?
- 3) Can variability in O<sub>3</sub> levels be statistically explained by the types of surfaces (e.g., first year ice, multi-year ice, snow covered, open water, etc) over which an air mass traversed before arriving at the observation site (Chapter 4)?
- 4) Can condensed phase OH-radicals induce production of molecular halogens from halides present in the QBL found on frozen saline acidic surfaces (Chapter 5)?

The investigations of Questions 1-3 were only made possible by the (to-date) 19 deployments of O-Buoys, the design of which has been modified and improved since first described by Knepp et al. (2010). These changes are described in Chapter 2. Questions 1 and 2 are approached in Chapter 3 using a combination of O-Buoy observations, basic first-order kinetic relationships, and the air mass trajectory model, HYSPLIT. These results are expanded on in Chapter 4, where HYSPLIT is used to assess ODE air mass history and its trajectory over sea ice and snow before arriving at the O-Buoy. Finally, a custom-fabricated, ice-coated wall flow tube was used in tandem with CIMS to confirm whether the photochemical, OH-initiated production mechanisms for Cl<sub>2</sub>, Br<sub>2</sub>, and I<sub>2</sub>, proposed by Pratt et al. (2013), Custard et al. (2016), and Raso et al. (2016) are plausible (Chapter 5).



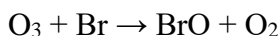
## CHAPTER 2. BUOY-BASED ARCTIC OCEAN OBSERVATIONS OF OZONE: THE O-BUOY PROJECT

### 2.1 Introduction

Since the discovery of Arctic tropospheric ozone depletion events (ODEs) in the mid-1980s, there has been great scientific effort toward fully understanding the complex chemistry and physical conditions that promote this phenomenon, discussed in more detail in Chapter 1. Crucial to this endeavor are field observations under a variety of conditions. The majority of such observations have been based at coastal sites during intensive Arctic campaigns, such as ALERT2000 (Bottenheim et al., 2002a), Ocean Air Sea Ice Snowpack Study (OASIS; <http://www.oasishome.net/>), or the BRomine, Ozone, and Mercury EXperiment (BROMEX; Nghiem et al., 2013). Though these campaigns have been able to produce the most complete set of relevant observations yet, including O<sub>3</sub>, meteorology, and a large number of the halogenated compounds relevant to ODEs, a growing body of evidence suggests that halogen activity and air masses devoid of O<sub>3</sub> originate over the Arctic Ocean (Bottenheim et al., 2009; Bottenheim and Chan, 2006; Gilman et al., 2010; Jacobi et al., 2006; Richter et al., 1998; Simpson et al., 2007a). Attempts to study O<sub>3</sub> behavior over the ocean have been conducted on ice floes (e.g., Hopper et al., 1994, 1998; Moore et al., 2014), by aircraft (e.g., Jaeschke et al., 1999; Koo et al., 2012; Leitch et al., 1994; Neuman et al., 2010; Ridley et al., 2003; Seabrook et al., 2013; Sheridan et al., 1993),

and by ship (e.g., Bottenheim et al., 2009; Gilman et al., 2010; Jacobi et al., 2006; Nghiem et al., 2012a; Pöhler et al., 2010; Seabrook et al., 2011). However, few of these Arctic Ocean studies yielded the long-term data required for seasonal analyses of O<sub>3</sub>.

Recently, a sea-ice tethered buoy-based observatory was developed to overcome the logistical obstacles required for long-term trace gas trace measurements over the Arctic Ocean (Knepp et al., 2010). These “O-Buoys” were designed for the purpose of observing ODEs from the sea ice surface by detecting O<sub>3</sub>, BrO (chemical indicative of active ODE chemistry; see R2.1, and Chapter 1), and various meteorological parameters, including temperature, wind speed, wind direction, relative humidity, and atmospheric pressure (Figure 2.1).



R2.1

The buoys then transmit this data hourly via Iridium communications to a data repository where it undergoes preliminary processing and can be viewed by the O-Buoy team scientists. Since the testing of the first O-Buoy in Elson Lagoon, Barrow, AK, in 2009, a total of 19 different deployments have occurred between 2009 and 2015 at various regions across the Arctic Ocean. The O-Buoy design is largely the same as when first described by Knepp et al. (2010) and Knepp (2010). Below, I provide a brief description of the O-Buoy instruments and components, and summarize deployment performances. Although the O-Buoy also features a carbon dioxide sensor, these data will not be discussed herein, though the interested reader is referred to Knepp (2010).

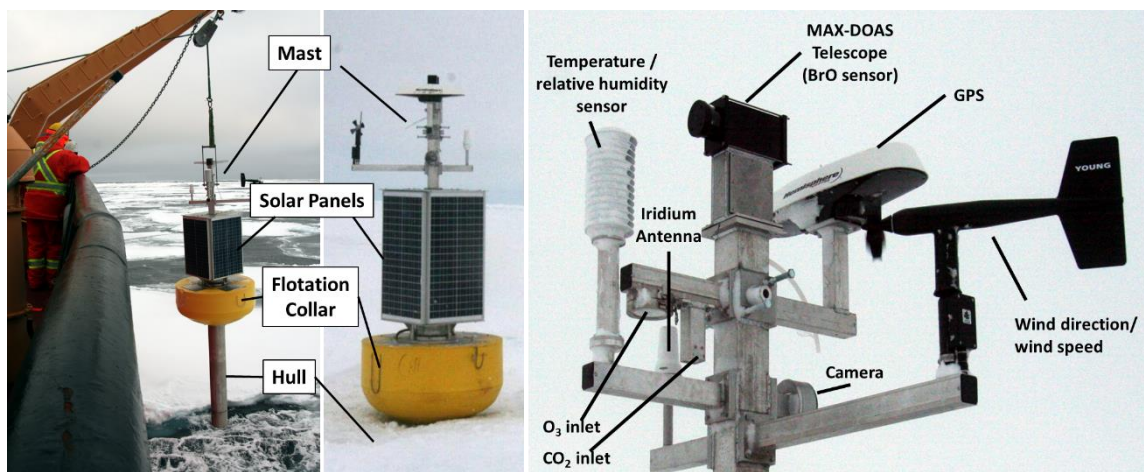


Figure 2.1 Left – photograph of lifted O-Buoy. Middle – photograph of deployed O-Buoy. Note that the hull of the buoy is installed within the sea ice in order to maintain effectively constant temperatures for the instruments. Right – close up of O-Buoy mast attachments as of 2015. All photographs are representative of the O-Buoy design as of 2015.

## 2.2 Design

Figure 2.2 shows a schematic of the O-Buoy hull, which contains critical buoy instrumentation. The hull is a water-tight, 2.4 m long, 0.3 m diameter cylinder constructed from  $\frac{1}{4}$ " aluminum by the United States Army Corps of Engineers Cold Regions Research and Engineering Laboratory (CRREL). Once deployed, the hull is surrounded by a combination of sea ice and the underlying sea water in order to provide a stable, low power-cost, temperature-controlled environment for the components within (i.e.,  $\sim -1.8$  °C, which is a typical temperature of sea water beneath sea ice). These components include three lithium battery backs, Iridium communications equipment, two carbon dioxide calibration cylinders, a data logger (Campbell Scientific Instruments CR1000), power controller, O<sub>3</sub> sensor (Sect. 2.2.1), carbon dioxide sensor (customized LI-COR 820 IR), and a Multi-AXis

Differential Optical Absorption Spectrometer (Sect. 2.2.2). Buoy operation is governed by a “Supervisory Computer” (SC; Technologic Systems TS-7260 Single Board Computer). The SC responds to user commands sent via Iridium communications or direct connections via the RS232 port on the O-Buoy mast. With minor exceptions (described in Section 2.3), the SC still operates as described by Knepp (2010).

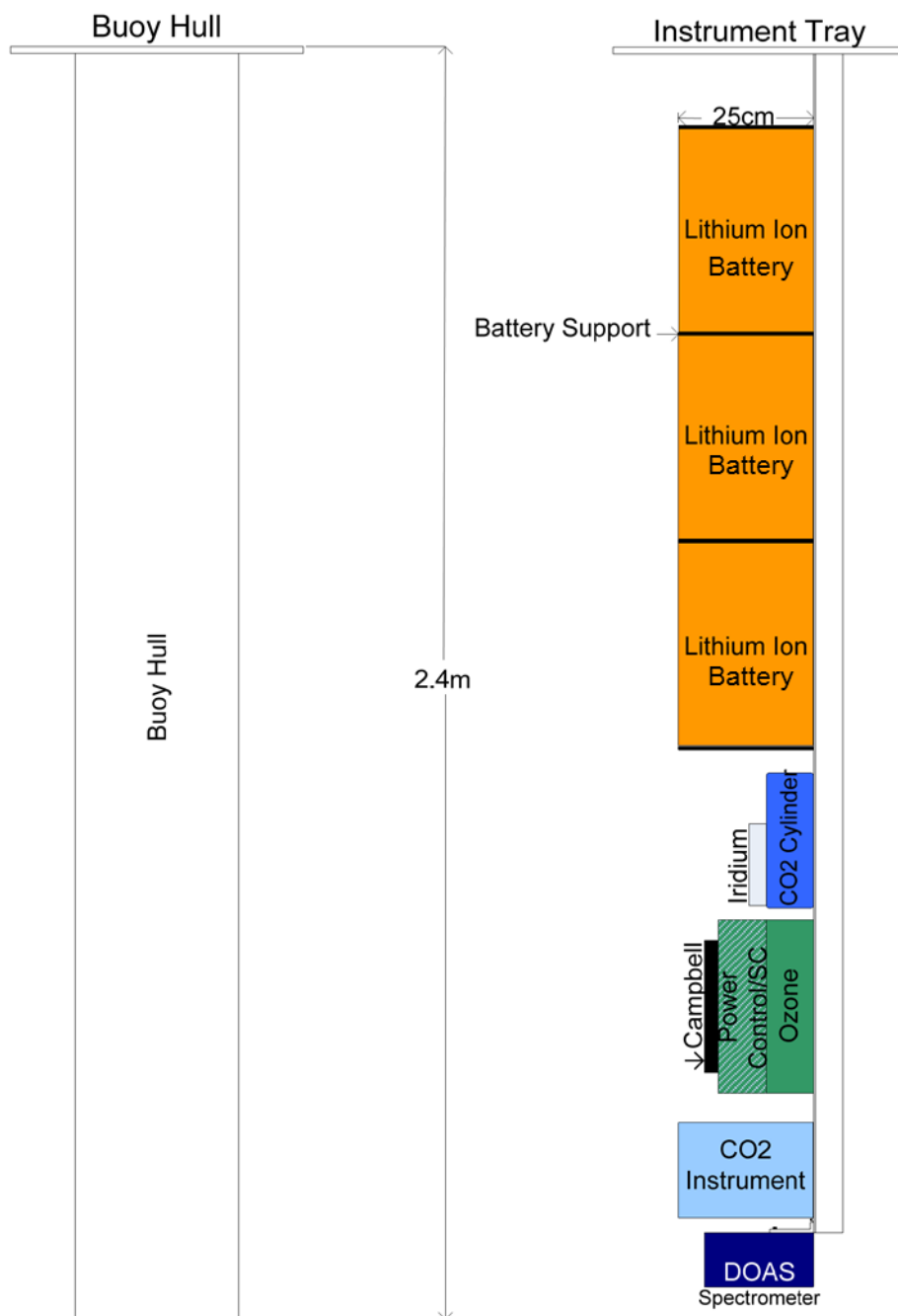


Figure 2.2 Schematic drawing of the aluminum O-Buoy hull (left) and instrument tray (right). Instrument tray reflects actual instrument placement within the hull. Figure modified from Knepp (2010).

Installed above the instrument hull is a 2 m tall mast, also machined by CRREL (photograph in Figure 2.1, schematic in Figure 2.3).

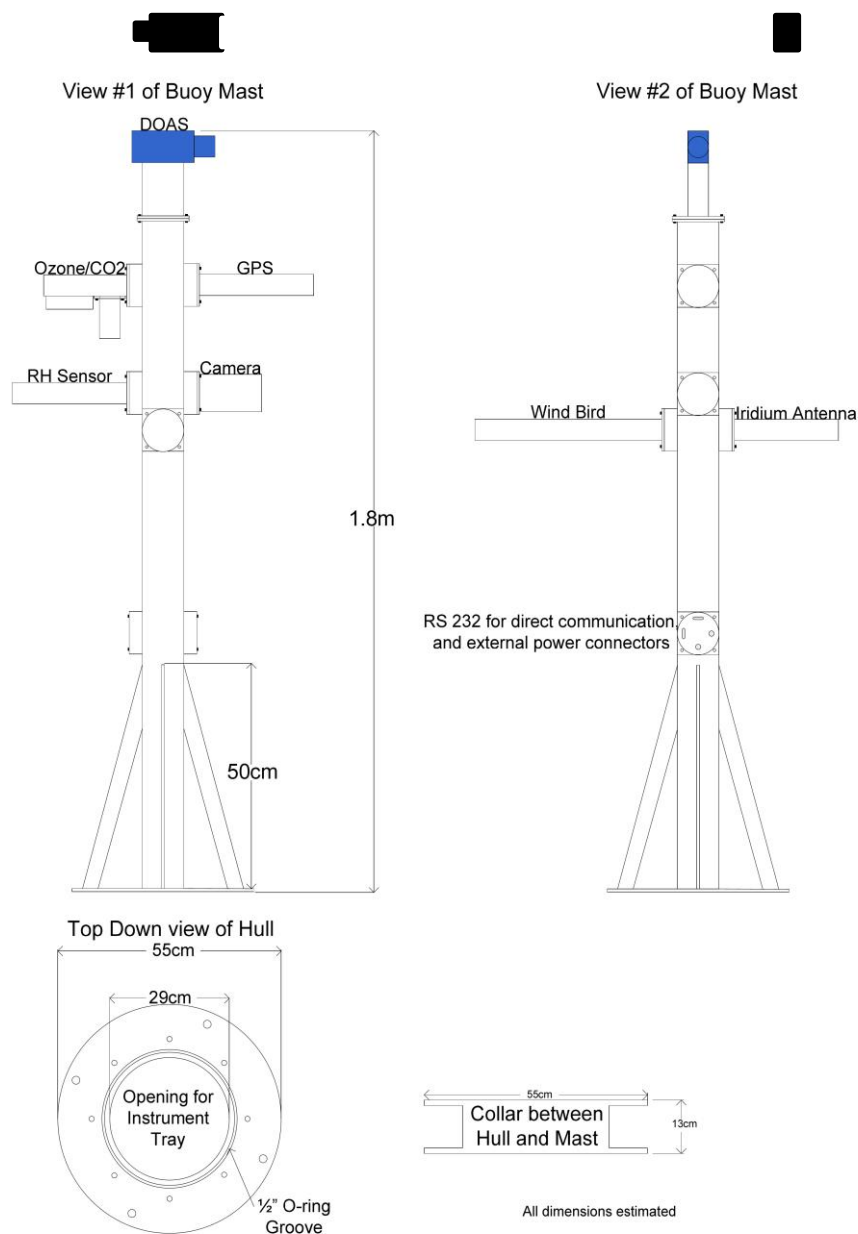


Figure 2.3 Schematic drawings of the O-Buoy mast and the collar connecting the mast with the hull. Figure adapted from Knepp (2010), reflecting the updated orientation of the MAX-DOAS scanning telescope (labeled as “DOAS” in the figure).

The mast arms hold the inlets for the O<sub>3</sub> and carbon dioxide sensors, the Iridium antenna by which communications phoned “home,” the global positioning system (GPS), and the meteorological sensors (Sect. 2.2.3). Also mounted on the mast are a camera, an RS232 connector for direct computer communications, an “on” switch, and the MAX-DOAS scanhead/telescope unit. Electrical connections between the mast attachments and the hull components were made using Amphenol Class E Environmental connectors, interfaced at the bulkhead between the mast and the hull.

In total, the dimensions of a fully assembled O-Buoy are 4.2 m tall, 1.1 m wide, and a total mass of 474 kg (O-Buoys 1-4), heavier than the 280 kg model (O-Buoy 1) first reported by Knepp et al. (2010). However, summertime camera imagery received from the first two ocean-based deployments of O-Buoys (deployed during the previous Fall) apparently showed the buoys tip over once enough ice had melted (Figure 2.4).

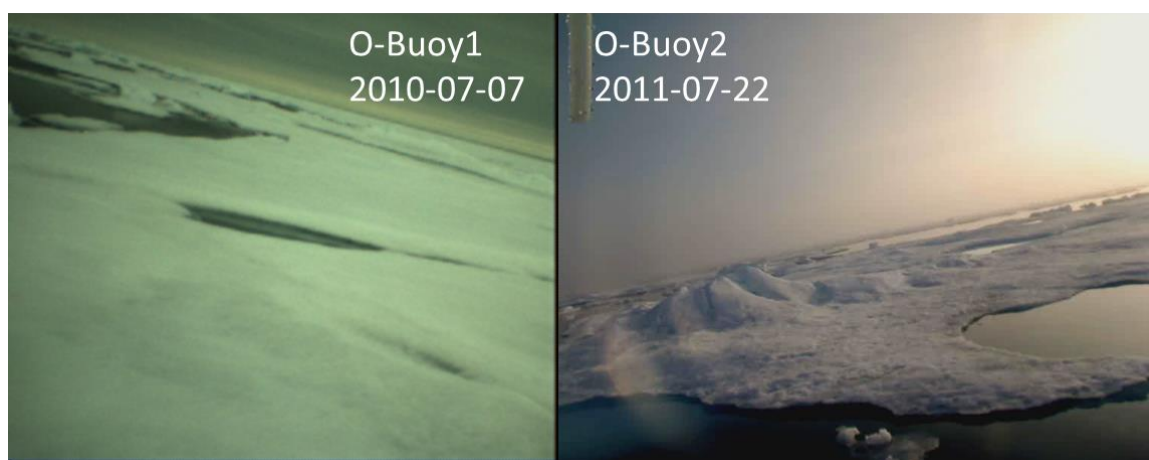


Figure 2.4 Camera images received from O-Buoy1 (left) and O-Buoy2 (right) during the summer melt. Images indicate the buoys were tipping over shortly before losing all communication.

This problem was corrected by installing a 90 kg counter-weight (Figure 2.5) to the bottom of the instrument hull immediately before deployments, increasing the total mass of the buoy to 564 kg (O-Buoy5 – O-Buoy15). This container is ~0.5 m in length, thus increasing the length of the buoy to 4.7 m.



Figure 2.5 Counter-weight is an aluminum container filled with lead shot, acting as a ballast. Left- ballast is connecting to the bottom of the O-Buoy hull with threaded rod and secured into place with the winged bar. Right – Photograph of the ballast attached to the bottom of the O-Buoy hull.

The buoy is also able to float in open water if the surrounding ice melts because of a yellow flotation collar (Gillman Corporation Type 1000) which is rated at 671 kg of buoyancy. It holds four, rechargeable lead-acid batteries (Concorde AGM) that are connected to, and subsequently charged by, four solar panels (SunWize SW-S85P) that surround the lower portion of the mast (see Figure 2.1).



### 2.2.1 Ozone Instrument

Ozone was quantified using customized 2B Technologies model 205 dual-beam O<sub>3</sub> monitors. These instruments operate on the principle of ultraviolet light absorption according to the Beer-Lambert Law (Equation 2.1).

$$A = -\ln\left(\frac{I}{I_0}\right) = \sigma * N * b \quad \text{E2.1}$$

$A$  corresponds to absorbance,  $I_0$  is the intensity of incoming light into an absorbing molecule, and  $I$  is the intensity of light transmitted through the absorber. Additionally,  $\sigma$  is the absorption cross section (effective area seen by incoming photons),  $N$  is the number density of absorbers (molecules cm<sup>-3</sup>), and  $b$  is the effective path length. In the 2B instrument, a low-pressure mercury lamp emits photons at 254 nm, corresponding to the

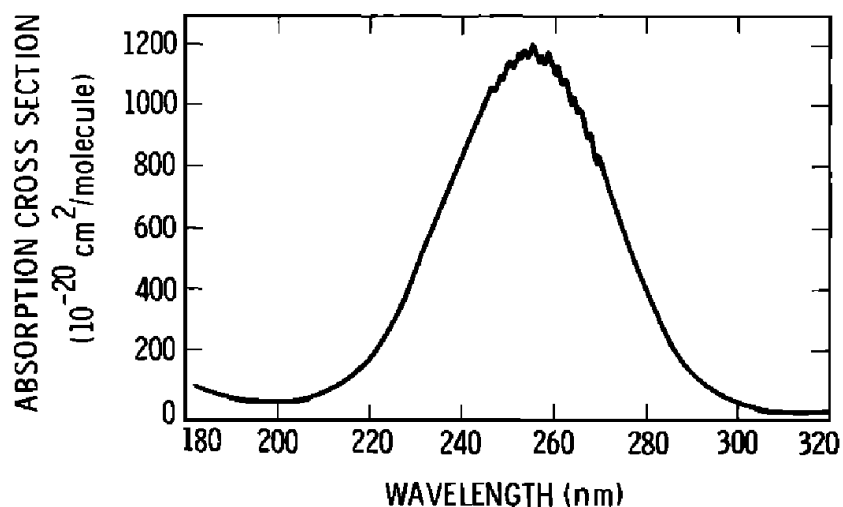


Figure 2.6 Absorption cross sections of ozone at 298K. Figure reproduced from Molina and Molina (1986).

wavelength of maximum absorption for O<sub>3</sub> (Figure 2.6). At this wavelength, O<sub>3</sub> has an absorption cross section of  $1.2 \times 10^{-17} \text{ cm}^2 \text{ molecule}^{-1}$  at 263 K (Molina and Molina, 1986).

The major sources of chemical interference from this method comes from other molecules that absorb significantly at this wavelength. This includes primarily polyaromatic hydrocarbons (PAHs) and mercury. PAHs have been found in ice core and surface snow samples on the Greenland ice cap in amounts consistent with the historical record of petroleum production (Ma et al., 2013). Indeed, ambient concentrations of PAHs are the result primarily of fossil fuel combustion and biomass burning (Jia and Batterman, 2010). The smallest and most volatile PAH (and therefore likely to be found in the Arctic atmosphere) is naphthalene (C<sub>10</sub>H<sub>8</sub>). At  $\lambda = 254 \text{ nm}$ , naphthalene has an absorption cross section of  $1.1 \times 10^{-17} \text{ cm}^2 \text{ molecule}^{-1}$  (Grosch et al., 2015), almost identical to that of O<sub>3</sub>. However, ambient concentrations of naphthalene over the Arctic Ocean are considerably lower than that of O<sub>3</sub> (average –  $3400 \text{ pg m}^{-3}$  (Ma et al., 2013), corresponding to  $0.6 \text{ pmol mol}^{-1}$ , and results in a 0.06% interference if O<sub>3</sub> was found at  $10 \text{ nmol mol}^{-1}$ ). If instead naphthalene was considered at concentrations found in urban environments (e.g.,  $11 \text{ } \mu\text{g m}^{-3}$  outside of a south China landfill (Jia and Batterman, 2010)), ambient naphthalene would then result in an interference of an additional  $2.1 \text{ nmol mol}^{-1}$  to the reported O<sub>3</sub> value (20% interference if O<sub>3</sub> were found at  $10 \text{ nmol mol}^{-1}$ ). Given that the O-Buoys are deployed in remote sites over the Arctic Ocean, it is expected this interference is negligible. Additionally, gaseous elemental mercury (GEM) has an absorption cross section 3 orders of magnitude greater than that of O<sub>3</sub> at 254 nm ( $2.4 \times 10^{-14} \text{ cm}^2 \text{ atom}^{-1}$  (Faïn et al., 2010)) and is known to undergo depletion chemistry analogously to O<sub>3</sub> in the Arctic (e.g., Steffen et al., 2008, 2014). Again, Arctic ambient levels of GEM at Barrow, AK, ( $\sim 1.8 \text{ ng m}^{-3}$ , or

about  $0.2 \text{ pmol mol}^{-1}$ ) are considerably lower than  $\text{O}_3$  (ranging from  $< 1\text{-}40 \text{ nmol mol}^{-1}$ ). If we again consider an ambient  $\text{O}_3$  level of  $10 \text{ nmol mol}^{-1}$ , the quotient of  $(\sigma_{\text{Hg}} * N_{\text{Hg}}) / (\sigma_{\text{O}_3} * N_{\text{O}_3})$  is equal to 4.4%. This indicates that GEM, under typical Arctic conditions would only significantly contribute to observed  $\text{O}_3$  levels as  $\text{O}_3$  approaches near zero levels, similarly to naphthalene.

Instrumental flow schematics can be seen in Figure 2.7 (relevant to O-Buoys 1-4), and Figure 2.8 (relevant to O-Buoys 5-15), with the only difference being the presence of a latching valve in the earlier models. Ozone is quantified based on the attenuation of light

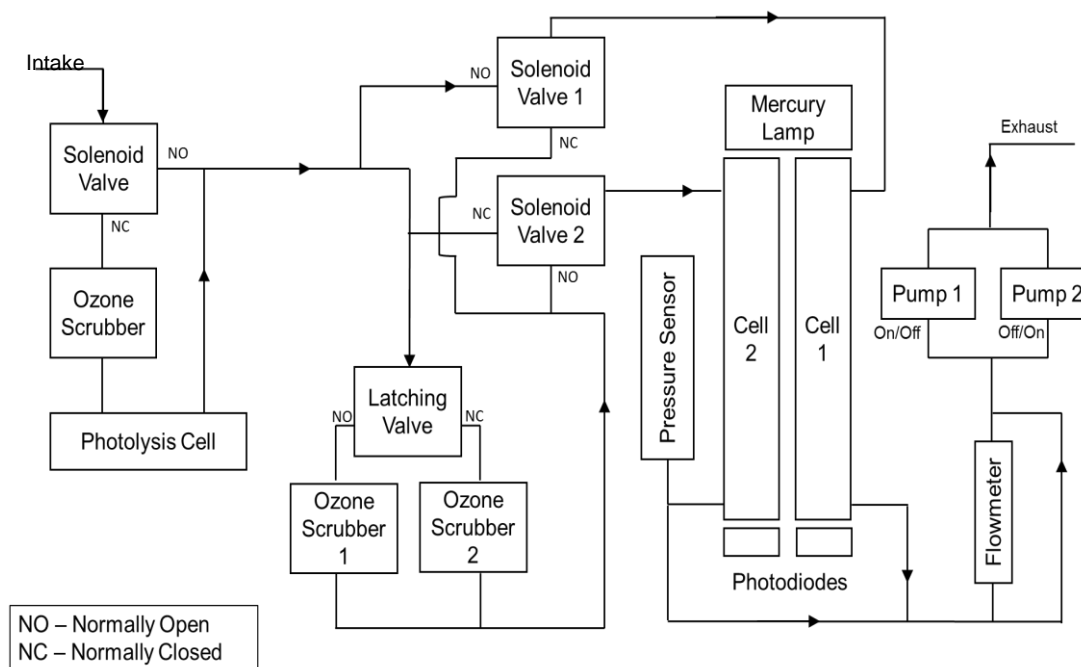


Figure 2.7 O-Buoy ozone sensor flow schematic representative of those used in O-Buoys 1-4.

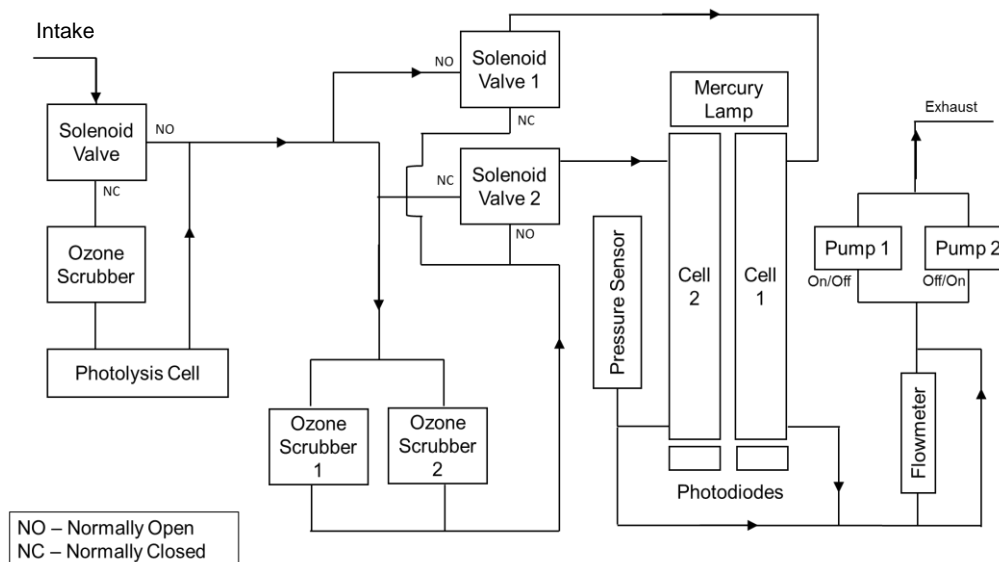


Figure 2.8 O-Buoy ozone sensor flow schematic representative of those used in O-Buoys 5-15. The primary difference between this schematic in that of Figure 2.8 is the removal of the latching valve.

$(I/I_0)$  through two 15-cm ( $b$ ) long absorption cells. Transmitted light is measured by photodiodes that have been outfitted with interference filters centered at 254 nm.

The flow rate through a new 2B 205 instrument is generally around  $2 \text{ L min}^{-1}$ , though gradually falls over the course of the pump's lifetime (ranging between 6 months to 10 months in Arctic conditions). Sample air is split such that air travels through both a pathway that scrubs the sample of  $\text{O}_3$  (thereby acting as a reference sample,  $I_0$ ) and a pathway that does not ( $I$ ). The role of the two cells, acting to measure  $I$  or  $I_0$ , is switched every two seconds by solenoid valves. In the first second after the solenoid switch, the cells are flushed with new sample air. After this, a one second measurement is made for each cell before the solenoids switch again. This method is largely flow rate independent as long as the flow rate is great enough to flush the cell before the measurement is taken

(Figure 2.9). In practice, this minimum flow rate was found to be approximately 500 mL min<sup>-1</sup>. It should be noted that while the 2B 205 instruments include their own digital flowmeters, the reported flow rates were found to differ from those measured by bubble meters or calibrated mass flow controllers. Therefore, the 2B-reported flow rates can only be used for qualitative purposes and assessing pump and instrument health.

Once  $I/I_0$  is generated by the photodiodes, the 2B microprocessor solves Equation 2.1 for number density of O<sub>3</sub> ( $N$ , molecules cm<sup>-3</sup>), and subsequently converts it into a mole fraction (nmol mol<sup>-1</sup>) using the measured cell temperature and pressure.

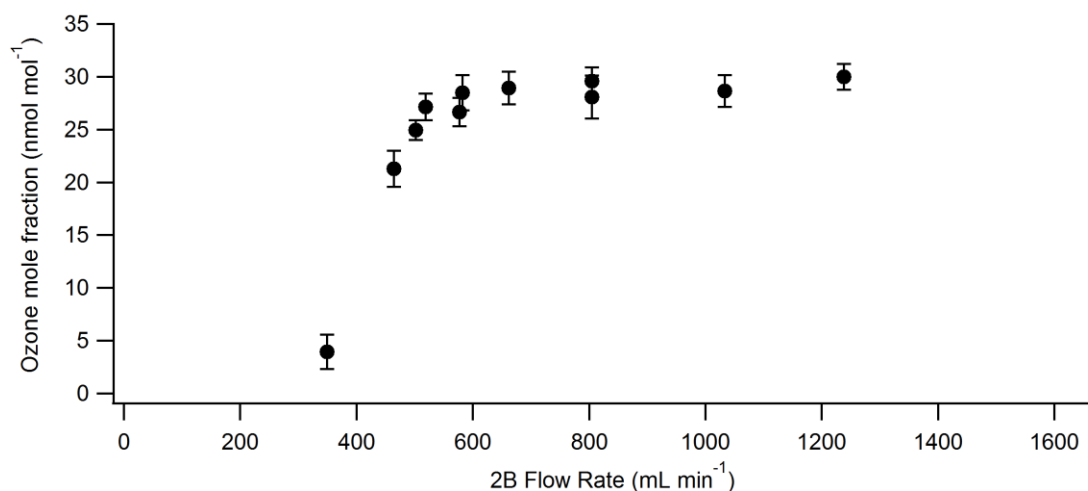


Figure 2.9 Demonstration of the effect of flow rate on 2B 205 O<sub>3</sub> data. In this test, an O-Buoy 2B 205 ozone monitor sampled from a calibrated 2B 306 ozone calibrator set to output 30 nmol mol<sup>-1</sup> of O<sub>3</sub>. Flow through the 2B 205 instrument was controlled accurately by installing a calibrated mass flow controller between the instrument pump and the detection cell (see Figures 2.8 and 2.9).

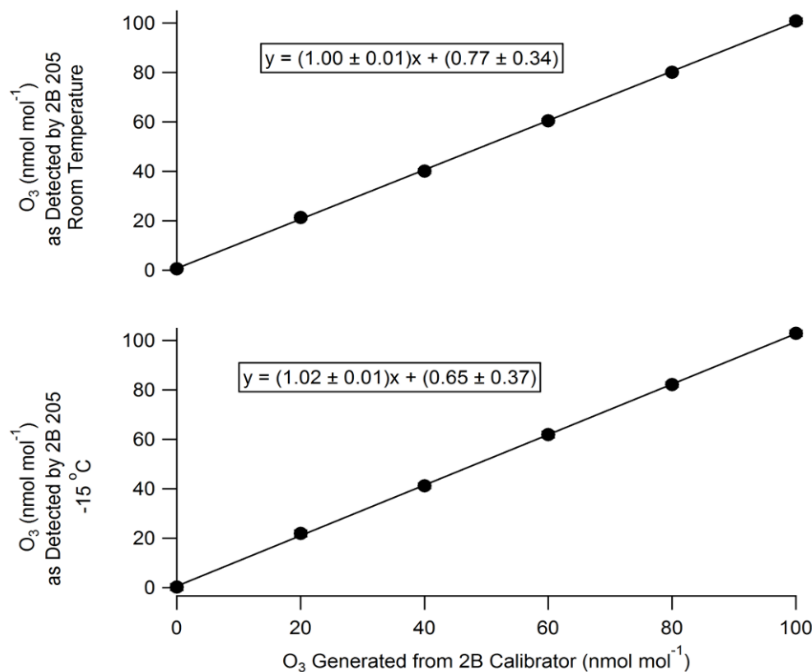


Figure 2.10 Sample laboratory calibration curves for an individual 2B held at room temperature (top) and at -15 °C. Standard deviations from calibration point averages (N=10 for each concentration) range from 0.6 – 1.3 nmol mol<sup>-1</sup>. Comparable results were obtained for the other two instruments.

Customizations from the commercially available instruments include one backup pump, an additional O<sub>3</sub> scrubber for the scrubbed path, a lamp heater, and modified firmware to control the instrument remotely. The O<sub>3</sub> instrument response did not display any statistically significant temperature-dependence during pre-deployment O<sub>3</sub> calibrations (performed using a 2B 306 Ozone Calibration Source) as long as the cell temperature of the instrument was stable (Figure 2.10), consistent with previous findings (Knepp, 2010). Cell temperature stabilization generally occurs 20-30 minutes after a cold-startup, and the first 30 minutes of O<sub>3</sub> data during these warm-up periods were excluded from data analysis.

The instrument has a manufacturer specified limit of detection of 1 nmol mol<sup>-1</sup>, and individual measurement uncertainty was calculated to range from 2.1 – 3.5 nmol mol<sup>-1</sup>. Blank measurements are performed everyday. In this mode, the first solenoid the sample contacts in the flow path is activated, sending the entirety of the sample through an ozone scrubber (Figure 2.7 and 2.8). In this way, the overall measurement variance can be estimated. This uncertainty was calculated as a sum of the averages of daily blanks from deployed instruments (average of 2.1 nmol mol<sup>-1</sup> across all deployments) and the relative standard error of the slopes,  $s_m$  (Equations 2.2-2.5) of laboratory, pre-deployment calibration curves across instruments (average slope of 1.0 ( $\pm$  1.8%) across all deployments). Therefore, the uncertainty in a given O<sub>3</sub> measurement based on the 2B itself is 1.8% \* [O<sub>3</sub>] + 2.1 nmol mol<sup>-1</sup>.

$$S_{xx} = \sum(x_i - \bar{x})^2 \quad \text{E2.2}$$

$$S_{yy} = \sum(y_i - \bar{y})^2 \quad \text{E2.3}$$

$$s_r = \sqrt{\frac{S_{yy} - m^2 S_{xx}}{N-2}} \quad \text{E2.4}$$

$$s_m = \sqrt{\frac{s_r^2}{S_{xx}}} \quad \text{E2.5}$$

$S_{xx}$  and  $S_{yy}$  are the squared sums of residuals,  $m$  represents the slope of the calibration curve, and  $N$  represents the number of points that make the calibration curve. Additional uncertainty is introduced by the O<sub>3</sub> intake filter holder installed on the O-Buoy mast, approximately 1.5 m above its base (Figure 2.11). The filter holder has been improved from the design of Knepp (2010) by maximizing the sample's contact time with Teflon and

minimizing its contact time with metal. Two stainless steel clamps hold together a Teflon cup on which a Teflon filter (90 mm, PTFE, ZITEX) rests, thereby maintaining the durability of the original design, minimizing sample air contact with metal, and maximizing contact time with Teflon (inert to O<sub>3</sub>). Using a Teflon chamber continuously filled with constant O<sub>3</sub>, it was found that air sampled through this filter holder results in an overall measurement percent error of  $-2.8 \pm 0.8\%$  when compared with air sampled directly from the chamber itself. The corrected O<sub>3</sub> values can then be calculated from Equation 2.7, and its uncertainty is propagated by Equation 2.8.

$$s_{O_3\text{measured}} = (1.8\% [O_3]_{\text{measured}}) + 2.1 \quad \text{E2.6}$$

$$([O_3]_{\text{corrected}} \pm s_{O_3\text{corrected}}) = ([O_3]_{\text{measured}} \pm s_{O_3\text{measured}}) + ((2.8 \pm 0.8)\% \times ([O_3]_{\text{measured}} \pm s_{O_3\text{measured}})) \quad \text{E2.7}$$

$$s_{O_3\text{corrected}} = \sqrt{\left(2.8\% \times [O_3]_{\text{measured}} \sqrt{\left(\frac{s_{O_3\text{measured}}}{[O_3]_{\text{measured}}}\right)^2 + \left(\frac{0.8\%}{2.8\%}\right)^2}\right)^2 + \left(\frac{s_{O_3\text{measured}}}{[O_3]_{\text{measured}}}\right)^2} \quad \text{E2.8}$$

The flow path of boundary layer air to the 2B ozone monitors is shown in Figure 2.11. The tubing diameters in this Figure are representative of the most recent configuration, and apply to O-Buoys 9-15. O-Buoys 1-4, 6-8 utilized a 0.16" – 0.32" tubing configuration, while O-Buoy 5 used a 1/8" – 1/4" configuration in order to use standard tubing sizes. Despite up to a 50% reduction in flow rate compared with using straight 1/4" tubing, these smaller tubing sizes did not significantly affect the calibration curves of the measurements.



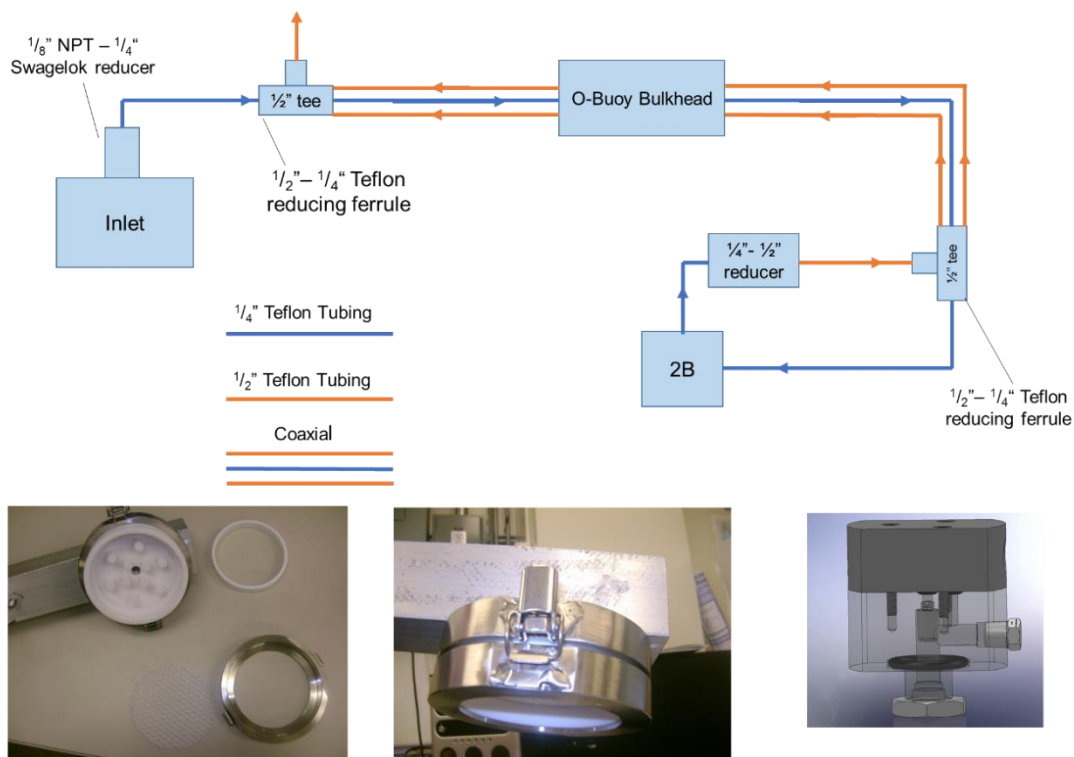


Figure 2.11 Top – flow schematic following sample air from the atmosphere through the O<sub>3</sub> filter holder to the 2B. Bottom left – Disassembled O<sub>3</sub> filter holder (labeled inlet on top portion of figure). Bottom middle – Assembled O<sub>3</sub> filter holder. Bottom right – drawing of the O<sub>3</sub> bulkhead connector.

Finally, 12V DC-DC converters were installed on the instruments to ensure that the 2Bs were consistently performing at a nominal 12V. Because the rechargeable lead acid/AGM batteries provide variable current to the sensors, it is suspected this provides added stress to the pumps and general operation of the instrument at voltages other than 12 V. This behavior is described in more detail in Section 2.3.

### 2.2.2 MAX-DOAS BrO Instrument

Multi-AXis Differential Optical Absorption Spectroscopy (MAX-DOAS) was employed by the O-Buoy as a means of detecting BrO, though it is additionally capable of detecting other trace gases (e.g., IO, O<sub>3</sub>, NO<sub>2</sub>, HONO) (Carlson et al., 2010; Hönninger et al., 2004b; Peterson, 2015). The MAX-DOAS instrument observes scattered sunlight within a spectral region where a molecule of interest absorbs (346-364 nm in this case) as a function of the elevation angle at which a telescope receives light (90, 20, 10, 5, 2, and 1°). The spectra obtained include the impacts of all of the chemical absorbers in a slanted column and are thus retrievals result in a quantity called slant column densities (SCDs; units of molecules cm<sup>-2</sup>). However, observations at all elevation angles have absorption features originating from gases in the free troposphere, and stratosphere. To remove these possible interferences, the 90° SCD, which sees minimal tropospheric / boundary layer absorption, acts as a blank that can be subtracted from SCDs at lower elevation angles. These differential slant column densities (dSCDs) have enhanced sensitivity to boundary layer gases and can be inverted to retrieve vertical profile information on molecules of interest. Separation of gases with overlapping absorption bands is achieved using software (Fayt et al., 2011) to fit a linear combination of possible absorbing spectra at each elevation angle. With the exception of the different scanning angles, this technique is similar to the commonly used Long Path DOAS (LP-DOAS), both of which are commonly used to detect average BrO activity in the Arctic over some path length with comparable precision (e.g., Frieß et al., 2011; Hausmann and Platt, 1994; Hönninger et al., 2004a, 2004b; Liao et al., 2011; Peterson et al., 2016b). Because they detect average species amounts over the spatial extent of the path length, concentrations obtained from DOAS techniques can differ from

those obtained from in situ techniques, such as chemical conversion/resonance fluorescence, though are found to be consistent when considered over similar averaging lengths (Avallone et al., 2003).

The subsequent inversion of dSCDs to obtain vertical profile information concerning BrO is a two-step procedure. The first step is to model the aerosol particle extinction vertical profile using the well-known vertical profile of the O<sub>2</sub> collision dimer, O<sub>4</sub>, which has a dSCD highly dependent on atmospheric visibility and light scattering (Greenblatt et al., 1990; Hönninger et al., 2004b). Based on the observed dSCD values of O<sub>4</sub>, a radiative transfer model (Rozanov et al., 2005) can be used to estimate particle extinction profiles based on viewing angles and aerosol light scattering properties. Once this profile is obtained, it is input into a separate Monte Carlo radiative transfer model (Deutschmann et al., 2011) that can simulate BrO dSCDs as a function of a variable BrO concentration profile (Peterson, 2015). The vertical profile of BrO is varied to give the best fit by optimal estimation.

The MAX-DOAS system is closely related to the original O-Buoy system as described by Carlson et al. (2010) and Knepp et al. (2010) (Figure 2.12). It consists of two major components: a scanhead telescope and the computer/spectrometer unit. The scanhead telescope, which takes in the scattered light, is mounted on the very top of the O-Buoy mast (Figure 2.1 and Figure 2.3), and transfers this light signal to the computer/spectrometer unit, located in the O-Buoy hull (Figure 2.2), by a fiber optic connection. The computer/spectrometer unit consists of a low-power single-board computer (Technologic Systems TS-7260), a stepper motor driver (Stepperboard BC2D20),

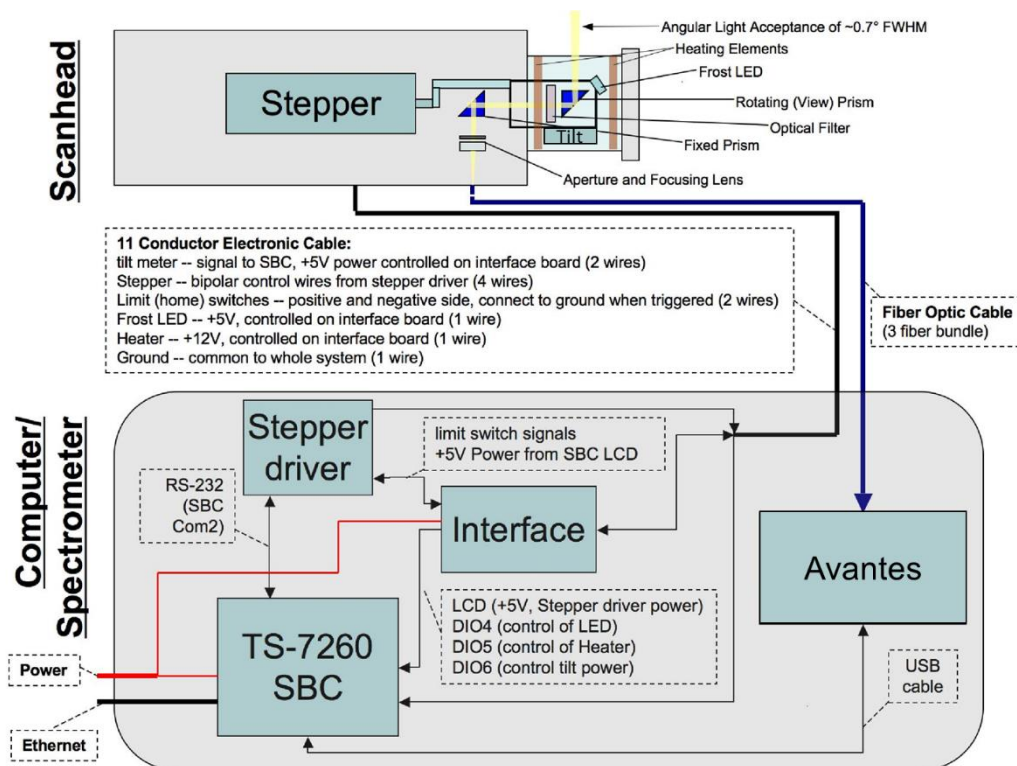


Figure 2.12 Schematic drawing of the light path for the MAX-DOAS system used in O-Buoys. Figure modified from Carlson et al. (2010) with updated spectrometer information.

interface electronics, and a miniature spectrometer (Avantes). Additionally, a tilt-sensing system was included such that the tilt of the scan head could be both measured using a digital inclinometer (Smart Tool Technologies ISU-S), and corrected (up to  $20^\circ$ ) to maintain accurate alignment of the viewing direction with the true horizon. Additionally, a tiltmeter (SignalQuest SQ-SI-360DA-3.3R-HMP-HP-IND-S) has been added directly onto the moving telescope (moved from the scanhead housing in the original design) such that direct measurement of the elevation angle is possible.

For more details on the principles of MAX-DOAS, as well as the methods used for processing the data, the reader is referred to Hönninger et al. (2004b), Carlson et al. (2010), and Peterson (2015)

### 2.2.3 Other Sensors

The O-Buoy is equipped with several, commercially available meteorological sensors. These include a wind monitor (RM Young Model 05103-45) and a temperature / relative humidity probe (Vaisala HMP155A), which are both installed on the mast (Figure 2.1), and a barometer (Vaisala PTB110), which is connected to the carbon dioxide instrument. These data are logged as five-minute averages to a Campbell data logger (CR-1000; Figure 2.3), as are instrument current draws and battery power / voltages. Additionally, the O-Buoy mast included a global positioning system (Hemisphere V100), a camera (Logitech Vision Pro), and an Iridium antenna for interaction with the science team.

## 2.3 Summary of Deployments and Observations

In total, 15 O-Buoys have been constructed for a total of 19 deployments as of the writing of this thesis.

Table 2.1 summarizes the deployment locations and dates of active operation, and the spatial data coverage is shown in Figure 2.13. In addition, a summary of the data available during deployments is presented in Figure 2.14.

Table 2.1 Summary of O-Buoy deployment locations and dates of active operation as of June 2016.

O-Buoy Number	Deployment Region	Months Active
1	Barrow, AK	Feb 2009 - May 2009
1	Beaufort Sea	Oct 2009 - Jul 2010
2	Beaufort Sea	Oct 2010 - Dec 2010, Mar 2011 - Jul 2011
3	Hudson Bay	Feb 2010 - Mar 2010
3	Hudson Bay	Feb 2011 - Apr 2011
4	Borden Island, Nunavut, Canada	Apr 2010
4	North Pole	Sept 2011 - Aug 2012
5	Beaufort Sea	Aug 2011 - Jan 2012
6	North Pole	Apr 2012 - Oct 2012
7	Beaufort Sea	Aug 2012 - Nov 2012, Jun 2013 - Aug 2013
8	Beaufort Sea	Aug 2012 - Jan 2013, Jun 2013 - Aug 2013
8	East Siberian Sea	Sept 2015 - Feb 2016
9	East Siberian Sea	Sept 2013 - Sept 2015
10	Beaufort Sea	Aug 2013 - Jan 2016, Mar 2015 - Sept 2015
11	Beaufort Sea	Oct 2014 - Sept 2015
12	Beaufort Sea	Oct 2014 - Sept 2015
13	Beaufort Sea	Sept 2015 - Apr 2016
14	Beaufort Sea	Oct 2015 - Jun 2016
15	East Siberian Sea	Sept 2015 - Feb 2016

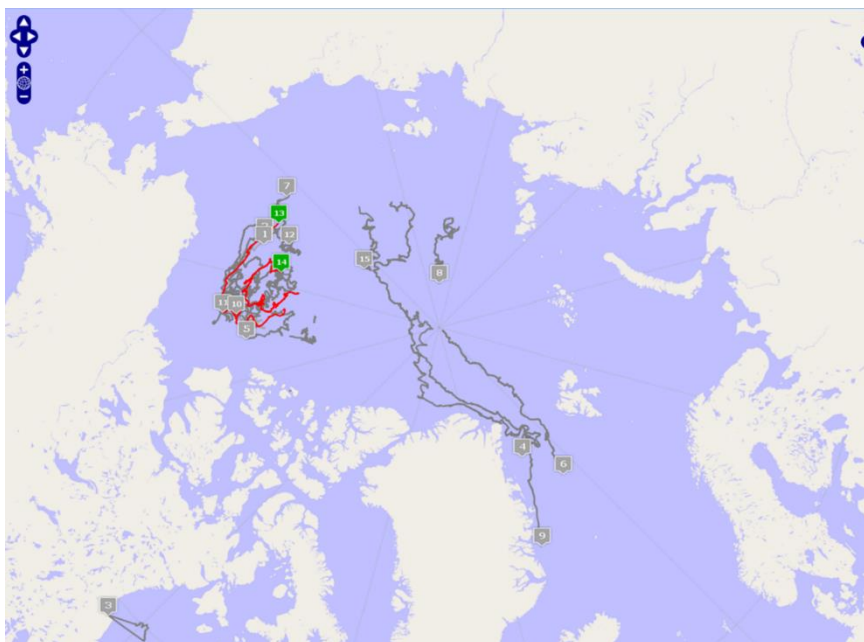


Figure 2.13 Summary of the spatial coverage of all deployments. Map is updated in real-time and can be viewed online at <http://obuoy.datatransport.org/>

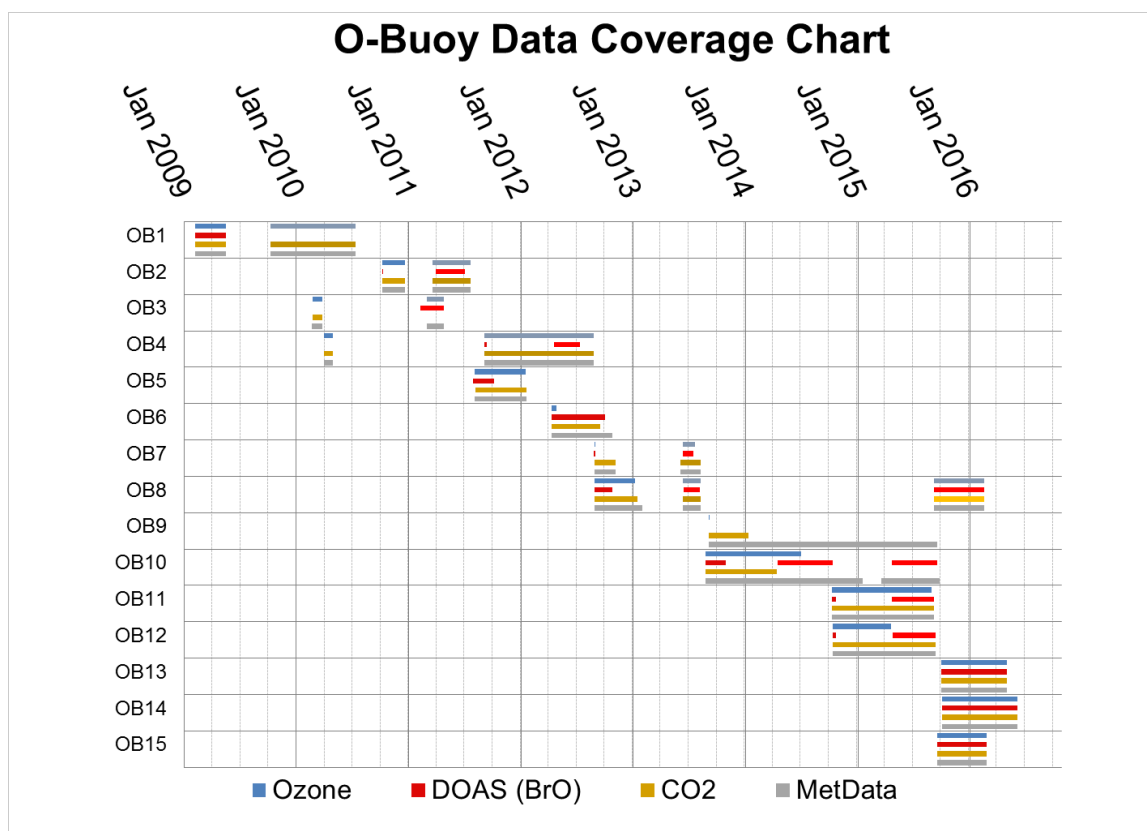


Figure 2.14 Visualization of temporal data coverage of all O-Buoy deployments. Data are current as of June 2016. Figure courtesy of William R. Simpson.

The majority of O-Buoy observations are from the Beaufort Sea, which consists of a heterogeneous mixture of seasonal and multi-year ice types. O-Buoys deployed here include OB 1, 2, 5, 7, 8, 10-14, all deployed by helicopter. Remaining deployment locations include Barrow, AK (OB1; deployed by tripod), Hudson Bay (OB3; deployed by helicopter), the North Pole (OB4, OB6; both deployed by helicopter), Borden Island (OB4; deployed by helicopter), and the East Siberian Sea (OB8, OB9, and OB15; deployed using icebreaker's crane). Sampling schedules differ for the different sensors. The

meteorological sensors are active throughout the entire deployment and updated as five minute averages. The MAX-DOAS scans through its elevation angles in a duty cycle lasting approximately 30 minutes, but is typically only active during springtime periods when the sun has risen, and the rechargeable batteries are able to maintain its power load. The 2B O<sub>3</sub> sensor operates on a reduced sampling schedule (total of 4 hours every three days) during winter while the buoy is operating from Lithium batteries, such that they are able to power the rest of the buoy throughout the winter. Toward the end of February/beginning of March, when halogen chemistry is anticipated to begin, this sampling schedule is increased to 4 hours daily. Once it is apparent depletion chemistry is occurring, and it appears either the Lithium batteries can handle the charge, or there is evidence the AGMs are beginning to charge, O<sub>3</sub> sampling is increased to 24-hours.

As can be seen in Figure 2.12 and Table 2.1, there are periods when individual instruments fail, as well as periods when the power system fails. We consider first failures of the O<sub>3</sub> and MAX-DOAS instruments. Issues with the 2B O<sub>3</sub> have most often involved the O<sub>3</sub> signal suddenly dropping to zero in concert with the flow rate (Figure 2.11; affected O-Buoys 3, 4, 6, 7, and 9). While the O-Buoy 4 O<sub>3</sub> instrument eventually recovered, no further data were received from O-Buoys 3, 6, 7, and 9 after this flow rate / O<sub>3</sub> value behavior. The actual cause for this behavior has yet to be confirmed. However, much was learned about the behavior of the 2B instruments while attempting to diagnose this issue. In the case of O-Buoy 3 and O-Buoy 4, it was noted that there was a coincident increase in current draw during the period in which the flow rate was zero. Laboratory tests indicated that complete flow restrictions through either the O<sub>3</sub> monitor inlet or exhaust lines caused an increase in current draw (~100 milliamps if flow is completely restricted). This led us



to conjecture whether a blockage had formed as a result of the expansion of humid air into the instrument, which is at lower pressure, causing water to condense. This scenario would cause this water to subsequently freeze in the sampling tubing if temperatures are low enough. Indeed, laboratory freezer tests replicating the 2B sample line (Figure 2.11) showed that it was possible for ice to form downstream of the O<sub>3</sub> filter holder when sampling humidified air. It was found that this ice formation could be significantly reduced (though not completely eliminated) by using the larger 1/4" and 1/2" tubing, utilized on O-Buoys 9-15.

In the cases of O-Buoys 6, 7, and 9, however, proper function of the O<sub>3</sub> instrument was never restored. Typically, the 2B instrument draws a current of ~500 milliamps. Interestingly in these cases, a temporary raise, or "spike" of ~100 milliamps in current above the baseline is observed alongside the falling flow rates and O<sub>3</sub> mole fractions. Following this spike, the current draw permanently drops to ~100 milliamps below baseline current (Figure 2.15), and the instrument ceases to communicate with the supervisory computer upon the next power cycle, despite still drawing current. The brief spike in

current suggests a blockage could have formed in the Teflon tubing, similarly to O-Buoy 4. The subsequent drop in current and flow rate leads us to believe that the pump likely failed. That the instrument stopped communicating with the supervisory computer is suggestive of a circuit board failure. While diagnosing this issue, it was noticed that the 2B pump's flow rate correlated with the voltage provided by the O-Buoy's power source

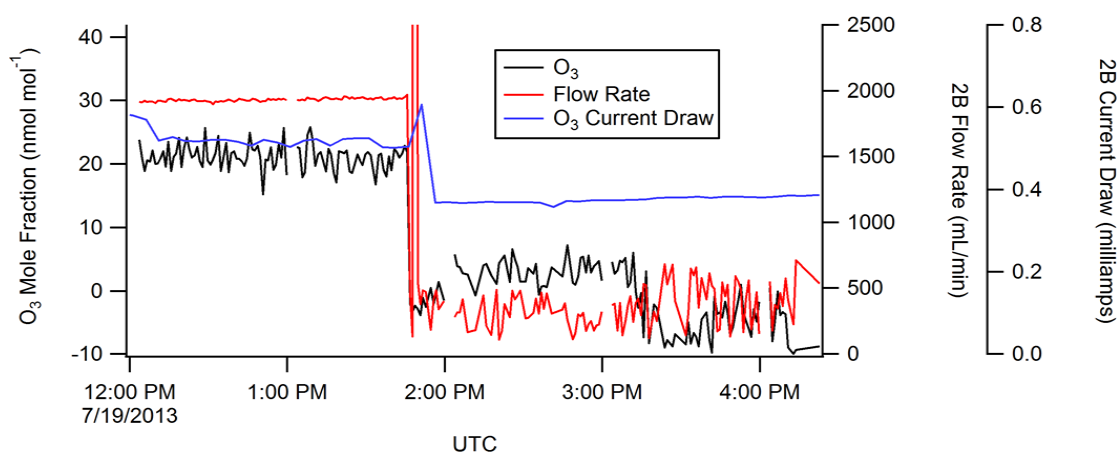


Figure 2.15 Data representative of O-Buoy O<sub>3</sub> instrument failure. These data are from O-Buoy 7, but similar behavior was also observed for O-Buoys 6, 8, and 9.

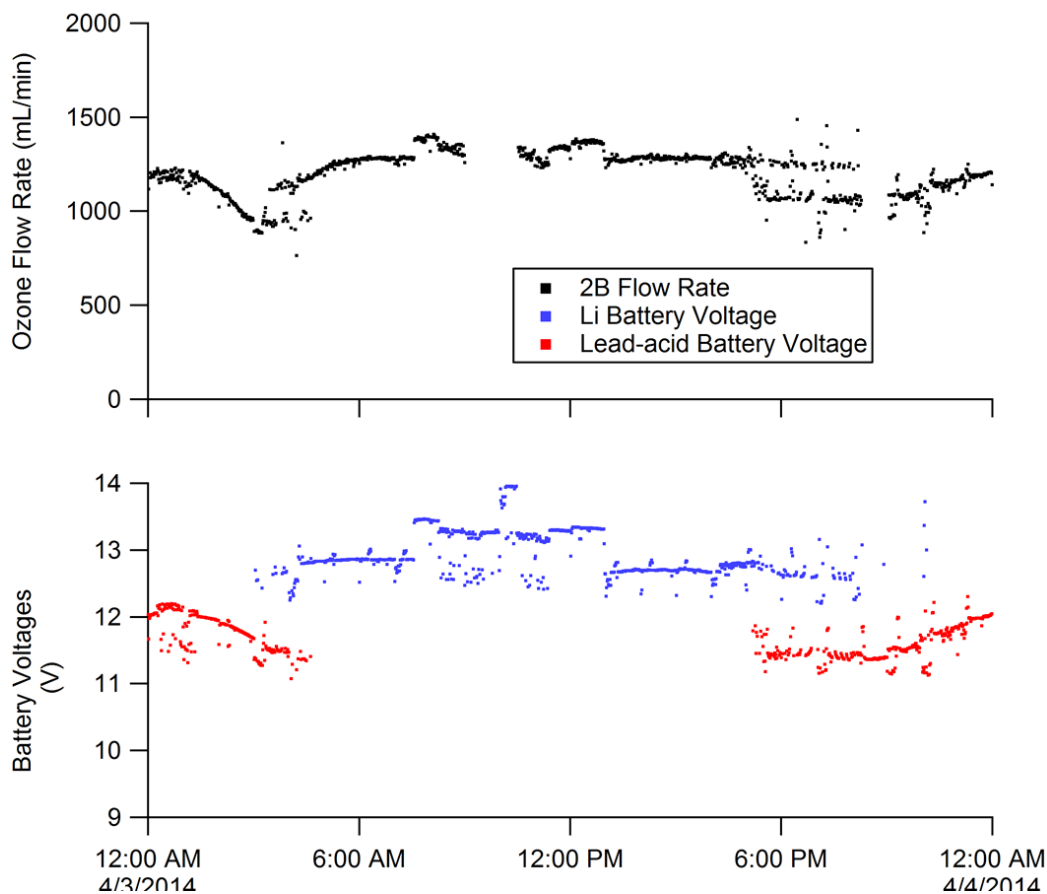


Figure 2.16 O-Buoy 10 O<sub>3</sub> instrument flow rate (top) plotted above O-Buoy 10 power source voltages.

(either Lithium batteries or AGMs; Figure 2.16). That is, a higher voltage causes the pumps installed on the 2B to perform using a higher flow rate, thereby decreasing the useful lifetime of the pump. Voltage changes are typically very gradual when the O-Buoy is utilizing a single power source. As the AGMs begin the recharge in the springtime when solar radiation increases, the O-Buoy begins to automatically switch between power sources. As can be seen in the bottom panel of Figure 2.16, this switching can be very rapid (e.g., beginning about 6:00PM) until the AGMs can produce at least 11 V consistently.

It was suspected that these rapid voltage fluctuations were stressful for the pumps and at least partially responsible for the failures. Consequently, voltage regulators were added to the design of the circuit boards such that the 2B operates under a nominal, consistent 12 V regardless of what is supplied by the O-Buoy's power source. However, unless / until one of these O<sub>3</sub> instruments that exhibited this behavior are recovered, it is only possible to speculate what actually caused these issues.

Two further apparent unique instrument failures relative to those described above were experienced by O-Buoys 10 and 12. In the case of O-Buoy10 (Figure 2.17), O<sub>3</sub> values gradually fell from levels of 30 nmol mol<sup>-1</sup> to below limits of detection in the month of July, which is a month under which ODEs are not typically observed.

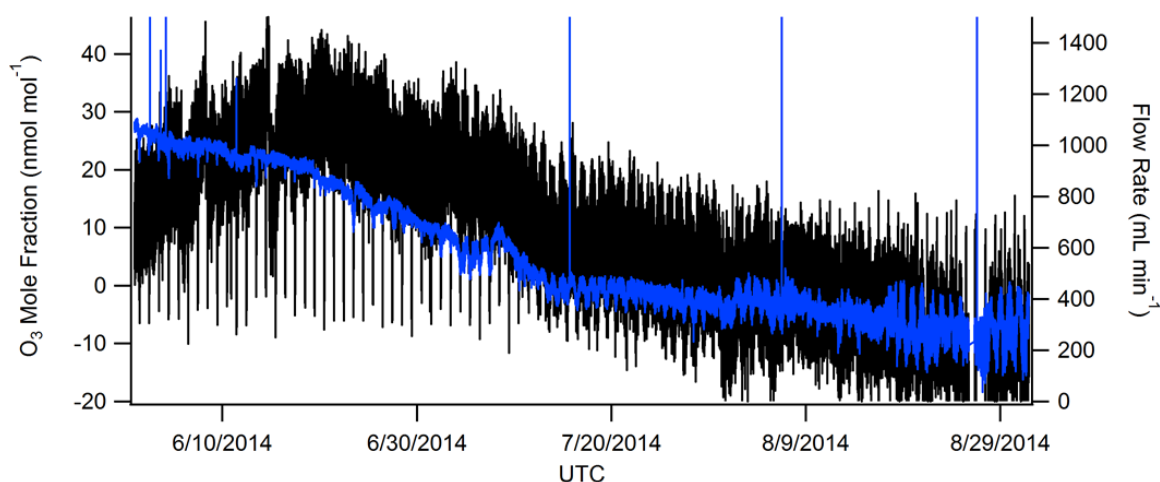


Figure 2.17 Time series of O-Buoy 10 ozone (black trace) and its reported flow rate (blue). Note that on August 24, the onboard O<sub>3</sub> generator installed on the 2B instrument was activated, which should have produced O<sub>3</sub> mole fractions approaching 1,000 nmol mol<sup>-1</sup>, though this is clearly not observed.

This was observed to occur in correlation with decreasing flow rates, though there is still indication of flow. However, we reiterate these 2B-reported flow rates are largely inaccurate. To test whether the instrument's detector was still active, we enabled the onboard O<sub>3</sub> generator but saw no response in the O<sub>3</sub> signal, suggesting the instrument had lost its ability to detect O<sub>3</sub>. In the case of O-Buoy 12, the instrument suddenly stopped communicating without any warning. In both of these cases, all instrument diagnostics (including current draws, flow rates, cell pressures) looked nominal and completely healthy. Fortunately, O-Buoy 10 was recovered in 2015, and interestingly cannot power up. We intend to work with 2B Technologies to investigate how the instrument failed in order to improve any future endeavors regarding O<sub>3</sub> observations over the Arctic Ocean.

Usable MAX-DOAS data was obtained from all deployments except for O-Buoy 1 in the Beaufort Sea (2009-2010), O-Buoy 3 in Hudson Bay (2010), and O-Buoy4 at Borden Island (2010). In these cases, the accurate azimuthal orientation of the buoy could never be established, making adequate radiative transfer modeling nearly impossible. Additionally, the Ocean Optics spectrometers used on buoys 1-6 were found to be extremely temperature sensitive, needing the optics to be aligned exactly at 0°C. The Avantes models were found to be much more stable, and yield equal-to-greater light sensitivity compared with the Ocean Optics units, and were utilized on all subsequent deployments.

Finally, we discuss cases in which the buoys stopped communicating. For O-Buoy 2, data transmission ceased approximately two months after deployment. Investigation of battery voltages showed that only one Lithium battery displayed increased load when the O<sub>3</sub> instrument was activated every three days, suggesting only one of these batteries was

working properly. However, once the sun rose, the rechargeable AGMs resumed function and the buoy was able to resume full operation.

A similar, though decidedly different, problem arose in the cases of O-Buoys 7 and 8 (2012-2013). O-Buoy 7 stopped transmitting 4 days into its deployment, while O-Buoy 8 stopped approximately four months into its deployment. For reasons that were never fully diagnosed, the Lithium battery packs drained sooner than expected. For O-Buoys deployed between 2009 and 2012 (OB1-8), the supervisory computer (SC) monitored the battery voltages and decided from which power source to draw, according to Figure 2.18. Should the AGM batteries fall below 11.5 V, the SC would switch the buoy's power source to the Lithium batteries. It was also noticed in the case of O-Buoy 8 that the AGM batteries were continuing to see a load despite the O-Buoy utilizing the Lithium batteries as its primary power source. To alleviate this behavior, the "load-disconnect" feature of the O-Buoy's power controller (MorningStar) was utilized (Figure 2.19). Before O-Buoy 9 (deployed in 2013), the AGM batteries were always exposed to the O-Buoy instrument's current load, whether or not the AGMs were being used as the primary power source, thereby gradually draining any charge they may have. This is disadvantageous, because charge is needed on the AGMs to operate the power controller, which allows the AGMs to recharge. The load-disconnect feature of the power controller disconnects the AGMs from the circuit and thus the load when battery voltage falls below 11.5 V, as before. However, in this case, the AGMs are completely shielded from the current load by the power controller. When this occurs, a new hardware circuit (called "polar bear circuit," in case a polar bear destroyed the solar panels and power controller) now automatically recognizes that the AGMs are no longer supplying power to the buoy and subsequently enables the

FET in between the Lithium batteries and the instruments. This switch then completes the circuit to the Lithium batteries, allowing the buoy to remain powered. Once the AGM voltage returns above 12.5 V, the power controller reengages the AGMs, which is recognized by the SC and disengages the Lithium current. While the issue of premature drainage of the Lithium batteries was never resolved, no such issues were observed in the deployments of O-Buoys 9-15 and the second deployment of O-Buoy 8.

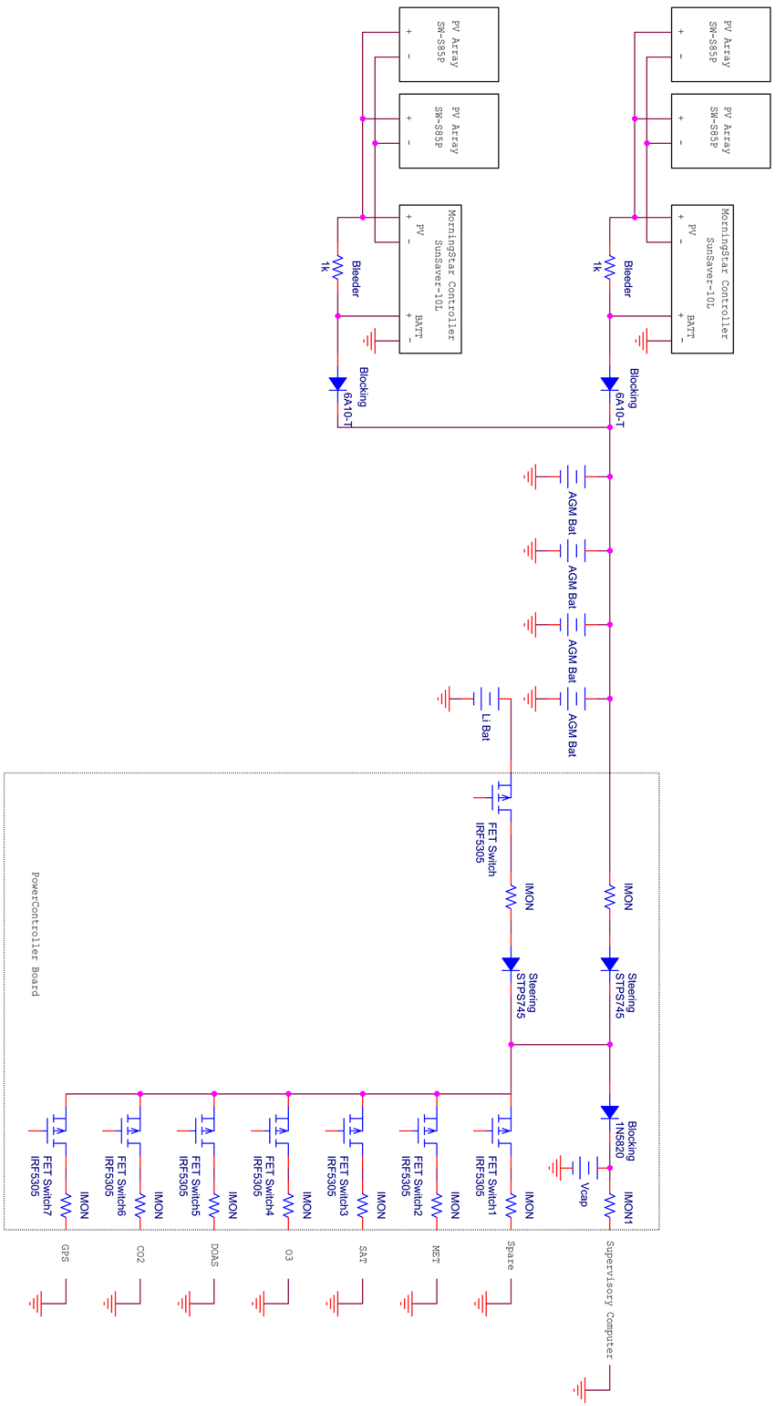


Figure 2.18 Schematic diagram of O-Buoy power going from the battery source to the relevant instrument. This schematic is relevant to O-Buoys deployed prior to 2013 (O-Buoys 1-8)



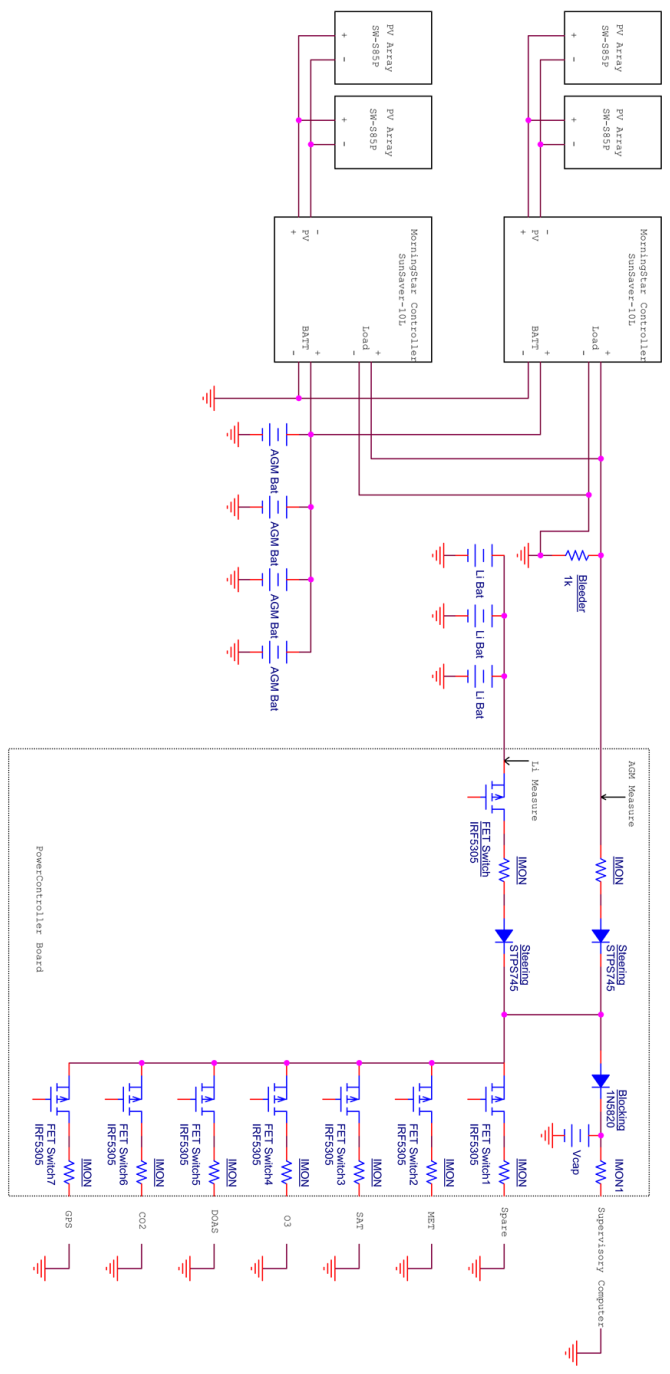


Figure 2.19 Schematic diagram of O-Buoy power going from battery source to the relevant instruments. This schematic is relevant to O-Buoys deployed beginning in 2013 (O-Buoys 9-15, and the 2<sup>nd</sup> deployment of O-Buoy 8 in 2015).

Remaining data gaps have been simpler to diagnose. In the cases of O-Buoy 5 (2011-2012), 8 and 15 (2015-2016), it is expected that storms caused the premature destruction of these buoys due to ice floe collisions and ice ridging.

## 2.4 Conclusions

Since first described by Knepp et al. (2010), the O-Buoy has undergone many more deployments and obtained much unique data that deserve analysis. Additionally, there have been many learning opportunities through instrument failures that have allowed the O-Buoy Team to improve on its design. While the issues regarding O-Buoy tilting, MAX-DOAS, and power consumption appear to have been largely resolved, it remains unclear why so many O<sub>3</sub> instruments have failed. The recovery of one of these instruments (from O-Buoy 10) will be useful in determining some possible modes of failure and possible design improvements. However, diagnosing possible modes of failure has been difficult due to the inability to retrieve these failed instruments, as well as the inability to analyze and evaluate the instruments' circuit boards as they are proprietary. The success of future buoy-based O<sub>3</sub> observations would benefit from a new O<sub>3</sub> monitor specifically designed and built to withstand operating under harsh conditions in remote environments. At Purdue, this would be most effectively done either by fully commissioning the Jonathan Amy Facility for Chemical Instrumentation (JAFCI), or through a joint effort between 2B Technologies and JAFCI. In this way, we know completely how the instrument is built, the quality/grade of the components, and are able to evaluate possible modes of failure based on field-observed symptoms.

## CHAPTER 3. THE TEMPORAL AND SPATIAL CHARACTERISTICS OF OZONE DEPLETION EVENTS FROM BUOY-BASED MEASUREMENTS IN THE ARCTIC

### 3.1 Introduction

As discussed in Chapter 1, global tropospheric oxidation is generally controlled by ozone ( $O_3$ ), which is a major greenhouse gas (Gauss et al., 2006) and the most important precursor to the primary atmospheric oxidant, hydroxyl radical (OH) (Seinfeld and Pandis, 2012; Thompson, 1992). When the sun rises in the Arctic during springtime (typically around mid-March), boundary layer  $O_3$  drops precipitously from background mole fractions of  $\sim 40 \text{ nmol mol}^{-1}$  (ppbv) to near zero levels for periods of hours, or even days, before recovering (Anlauf et al., 1994; Barrie et al., 1988; Bottenheim et al., 1986). During these ozone depletion events (ODEs), the prominent regional tropospheric oxidation pathways for hydrocarbons at the surface are driven by species other than OH radicals, notably Cl and Br atoms (Cavender et al., 2008; Jobson et al., 1994).

ODEs occur when  $O_3$  reacts with reactive halogen radicals, reactions which are traditionally thought to be very bromine-centric (Reactions R3.1-R3.2) (Simpson et al., 2007b).



O<sub>3</sub> is removed in Reaction R3.2 by Br to produce bromine monoxide (BrO). However, BrO is photolabile and can reproduce O<sub>3</sub> and Br in a null cycle. Therefore, the rate at which O<sub>3</sub> is destroyed is ultimately limited by the rate at which BrO reacts with another species to not reform O<sub>3</sub>, such as in Reactions R3.3-R3.5.



Note that R3.4 can also produce OCIO + Br, but is not listed above as OCIO primarily regenerates O<sub>3</sub> in a null cycle via photolysis.

Ozone destruction is therefore propagated by the regeneration of reactive halogen species. In the gas phase, Reactions R3.3 and R3.4 are believed to dominate at high BrO concentrations, while R3.5 is believed to play a larger role as BrO decreases (Le Bras and Platt, 1995; Piot and von Glasow, 2008). Reactions R3.3 and R3.4 directly reproduce reactive Br atoms, while the HOBr formed by Reaction R3.5 must first undergo photolysis. Additionally, Reaction R3.5 is involved in a series of heterogeneous, autocatalytic reactions referred to as the “bromine explosion”, which are believed to supply net atmospheric reactive bromine (Fan and Jacob, 1992; Tang and McConnell, 1996; Vogt et al., 1996; Wennberg, 1999b). The “bromine explosion” involves the production of HOBr as above (R3.5), or through halogen reactions with oxidized nitrogen species (Aguzzi and Rossi, 2002; Hanson and Ravishankara, 1995). Uptake of this HOBr onto acidic, bromide-

containing frozen surfaces produces  $\text{Br}_2$  (Adams et al., 2002; Huff and Abbatt, 2002), which can then undergo the  $\text{O}_3$  destroying reactions once photolyzed (R3.1). This series of reactions will exponentially increase  $\text{Br}_2$  levels until some required reagent runs out.

Hypothesized sources of reactive halogens include saline frozen surfaces found across the Arctic Ocean, such as the snowpack, blowing snow, and sea salt-derived aerosols (Abbatt et al., 2012; Fan and Jacob, 1992; Frieß et al., 2011; Jones et al., 2009; Simpson et al., 2005; Yang et al., 2008). Recent in situ experiments showed that saline, acidic surface snowpacks (above sea ice or tundra) can act as sources of  $\text{Br}_2$ ,  $\text{I}_2$ , and  $\text{Cl}_2$ , showing that a more generalized “halogen explosion” can occur within the interstitial air of the snowpack. These halogens would then release into the boundary layer via wind pumping and diffusion (Custard et al., 2016; Pratt et al., 2013; Raso et al., 2016). Conditions leading to the release of reactive halogens are explored in more detail in Chapter 5.

Despite our increasing understanding of the role of halogens in ODEs, basic ODE characteristics, such as their temporal and spatial scales, remain uncertain (Jacobi et al., 2010; Simpson et al., 2007b; Zeng et al., 2003). Current knowledge of the aforementioned  $\text{O}_3$  depletion chemical mechanisms (CM) and the corresponding kinetics estimate the timescale for  $\text{O}_3$  destruction to be on the order of days (Cao et al., 2014; Hausmann and Platt, 1994; Jobson et al., 1994; Piot and von Glasow, 2008, 2009; Tuckermann et al., 1997). However, there are few reports of Arctic ODEs that are believed to have been observed primarily as a result of local scale CM (Boudries and Bottenheim, 2000; Jacobi et al., 2006). ODEs can also be observed primarily due to air mass transport mechanisms (TM) in which air masses depleted of  $\text{O}_3$  (via CM upwind) advect over the measurement site (Morin et al., 2005; Simpson et al., 2007b) and are detected as “ozone depletion events.” Given that the

Arctic Ocean surface is sunlit, stable against vertical mixing, and ice-covered during the spring (Lehrer et al., 2004), it has been hypothesized that O<sub>3</sub>-depleted surface air could be the norm in the Arctic boundary layer during this time, and that O<sub>3</sub> is only observed at the surface due to turbulent vertical mixing in an otherwise stable boundary layer. This vertical mixing can temporarily transport free tropospheric O<sub>3</sub> from aloft to the surface, raising the surface level mole fractions to between 30 and 40 nmol mol<sup>-1</sup> (Bottenheim et al., 2009; Hopper et al., 1998; Jacobi et al., 2010; Moore et al., 2014; Peterson et al., 2016a; Strong et al., 2002; Zeng et al., 2003). Regarding the spatial scales of individual O<sub>3</sub>-depleted air masses, Ridley et al. (2003) reported Arctic ODEs extending between 600 and 900 km in length from flights during the Tropospheric Ozone Production about the Spring Equinox experiment. Recently, Jones et al. (2013) reported the observation of multiple ODEs from a network of ten O<sub>3</sub> monitors spread over the Droning Maud Land sector of Antarctica, some of which extended at least 1200 km in horizontal dimension. However, no such network of O<sub>3</sub> monitors has yet been established for the Arctic to make analogous observations.

In a study of long-term Arctic coastal measurements, Tarasick and Bottenheim (2002) observed that ODEs most often occurred at temperatures of less than 253 K, leading to the proposal that such low temperatures could be necessary for the initiation of ozone depletion. This hypothesis was strengthened by Adams et al. (2002), who reported that frozen NaCl/NaBr surfaces efficiently uptake and react with HOBr to both form and release gas phase Br<sub>2</sub> at temperatures below 253 K. This observation has been hypothesized to occur due to the precipitation of NaCl•2H<sub>2</sub>O at temperatures less than 252 K, which then requires a greater concentration of Br<sup>-</sup> to maintain the surface brine layer (Cho et al., 2002);

when  $\text{Cl}^-$  precipitates, the volume of the brine water must decrease to maintain the ionic concentration needed for the appropriate freezing point depression. Boundary layer BrO enhancements have been correlated with low temperatures (Nghiem et al., 2012a; Zeng et al., 2003), and apparently linear increases in maximum BrO concentrations have been observed with decreasing temperatures, below 258 K (Pöhler et al., 2010). Further, strong positive correlations between  $\text{O}_3$  concentration and potential temperature have been reported (Seabrook et al., 2011; Strong et al., 2002). However, Bottenheim et al. (2009) and Neuman et al. (2010) observed ODEs at temperatures as high as 267 K, emphasizing uncertainty in the temperatures required for the observation of an  $\text{O}_3$ -depleted air mass. In addition, Koo et al. (2012) report that it is perhaps the temperature variability that has a greater effect on  $\text{O}_3$  variability, an idea that is also explored in Chapter 4 of this thesis.

ODEs have often been associated with a calm, stable boundary layer. Those observed under high wind speeds (faster than  $10 \text{ m s}^{-1}$ ) are generally attributed to TM. Yang et al. (2008) hypothesized that saline snow atop sea ice could disperse during periods of high wind and become a source of both sea-salt aerosol and bromine, consequently initiating ODEs. Indeed, there have been coastal-based studies in which increased BrO and aerosol were observed during periods of elevated wind speeds ( $> 5 \text{ m s}^{-1}$ ), and  $\text{O}_3$  depletion sometimes, but not always, followed (Frieß et al., 2011; Jones et al., 2009). Alternatively, higher wind speeds could also lead to better ventilation of the snowpack in which  $\text{Br}_2$  is produced (Albert et al., 2002; Foster et al., 2001; Michalowski et al., 2000; Pratt et al., 2013; Toyota et al., 2011). Michalowski et al. (2000) discussed that the rate at which HOBr reacts with  $\text{Br}^-$  during  $\text{Br}_2$  production in the “bromine explosion” was dependent on the time scale for turbulent diffusive transport of HOBr to the snowpack

surface, which would be wind-speed dependent. However, due to few coincident observations of wind speeds, aerosol, O<sub>3</sub>, and BrO, the dependence of ODEs on wind speed remains unclear.

Arctic air masses depleted in O<sub>3</sub> typically spend a significant amount of time over the Arctic Ocean before arriving at coastal measurement sites, suggesting that the ice-covered ocean is the most probable site of ODE initiation (Bottenheim and Chan, 2006; Gilman et al., 2010; Jacobi et al., 2006; Simpson et al., 2007a). In-situ chemical and meteorological data from the Arctic Ocean are, however, sparse. Most long-term Arctic tropospheric O<sub>3</sub> measurements have been made at coastal sites, and thus most observed ODEs have been attributed to TM. Attempts to study ODEs over the Arctic Ocean have been conducted on ice floes (e.g., Hopper et al., 1994, 1998), aircraft (e.g., Jaeschke et al., 1999; Leaitch et al., 1994; Neuman et al., 2010; Ridley et al., 2003; Seabrook et al., 2013; Sheridan et al., 1993), and ships (e.g., Bottenheim et al., 2009; Gilman et al., 2010; Jacobi et al., 2006; Nghiem et al., 2012a; Pöhler et al., 2010; Seabrook et al., 2011). However, few of these studies have produced the long-term data required for in-depth studies of the temporal and spatial scales of ODEs.

Recently, a series of ice-tethered buoys were deployed to observe ODEs over the Arctic Ocean (Knepp et al., 2010). The buoys have been installed in sea ice for automated, continuous, several-month surface measurements of O<sub>3</sub>, BrO (Carlson et al., 2010), carbon dioxide, and local meteorological conditions. The data generated by the O-Buoys represent the first long-term measurements of these chemical species directly over the surface of the ice-covered Arctic Ocean. Using the initial results from this unique dataset, we estimate the timescales of O<sub>3</sub> depletion, examine the state of our understanding of the chemistry



involved, and estimate the spatial extents and meteorological conditions supporting O<sub>3</sub>-depleted air masses.

## 3.2 Methods

### 3.2.1 Instrumentation

Surface O<sub>3</sub> and meteorology measurements discussed herein were collected during five separate deployments of O-Buoys (Table 3.1), visualized in Figure 3.1.

Table 3.1 O-Buoy deployment locations and time periods of continuous measurements relevant to this study

O-Buoy Number	Latitude	Longitude	General Area	Dates of Continuous Measurements	Number of ODEs observed
1	71°N	156°W	Barrow, AK	02 Mar 2009 – 19 May 2009	13
1	77°N	135°W	Beaufort Sea	22 Mar 2010 – 14 Jul 2010	13
2	74°N	142°W	Beaufort Sea	11 Apr 2011 – 22 Jul 2011	6
3	60°N	90°W	Hudson Bay	22 Feb 2010 – 27 Mar 2010	3
4	78°N	112°W	Borden Island, Nunavut, Canada	04 Apr 2010 – 30 Apr 2010	3



Figure 3.1 Map of locations at which various O-Buoys (abbreviated OB) were deployed between 2009-2011. For the coordinates, see Table 3.1. Sea ice extent image is for the month of March 2011. Map courtesy of Google Earth, and sea ice image courtesy of the National Snow and Ice Data Center.

Details of the O-Buoy design and operation are discussed extensively by Knepp et al. (2010) and in this thesis (Chapter 2), but a brief description of details relevant to this study are provided here. At the time of data analysis, BrO data were available from both O-Buoy1 during its 2009 Barrow, AK, deployment, and O-Buoy 2 from the Beaufort Sea to compare with O<sub>3</sub> depletion timescales. The full spring O-Buoy 2 time series, including O<sub>3</sub>, BrO, and temperature, is presented in Figure 3.2.

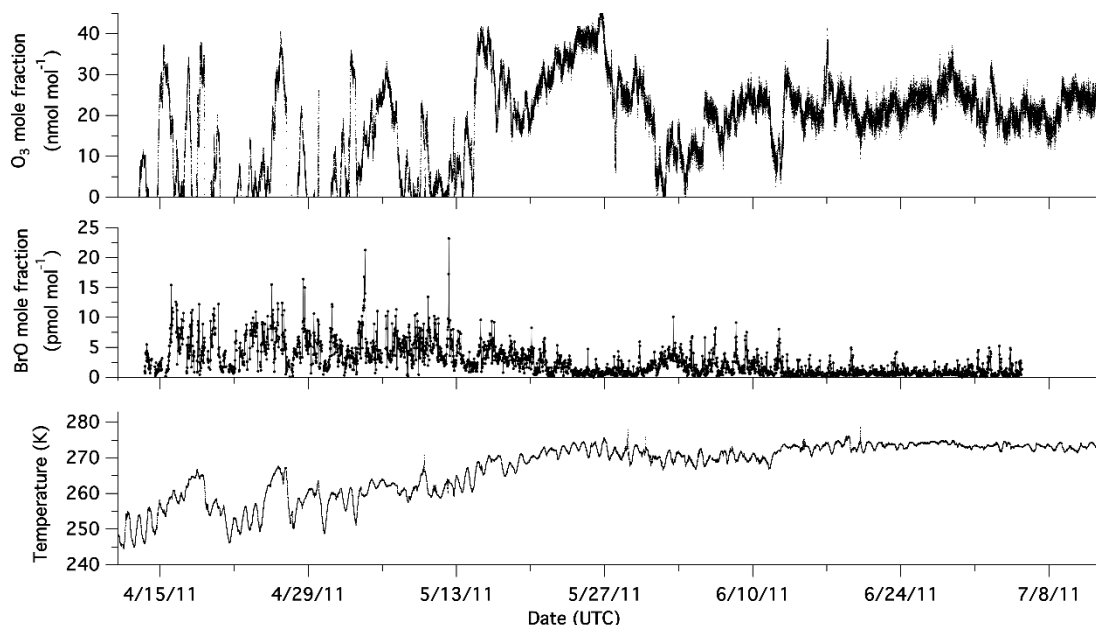


Figure 3.2 Example time series of  $O_3$ , BrO, and temperature from O-Buoy2 during its deployment in the Beaufort Sea.

The O-Buoys begin 24 hour sampling every day close to, or shortly after the time of polar sunrise, typically near the end of February or early March. Though the O-Buoys are also active during fall, winter, and late summer months, we focus mostly on springtime and early summer data herein (dates presented in Table 3.1).

Temperature was measured using a Vaisala model HMP45C temperature and relative humidity probe. Wind speed was measured using a RM Young Model 05103 anemometer. The range of wind speeds observed across the four O-Buoys deployed was  $0\text{--}15\text{ m s}^{-1}$ . It was observed in the 2009 Barrow, AK, O-Buoy1 deployment, however, that the anemometer was susceptible to icing, which would impede its ability to spin freely and provide accurate measurements. This effect was most prominent during the same

deployment, in which wind speed fell from a mean of about  $2 \text{ m s}^{-1}$  to  $0 \text{ m s}^{-1}$  for a period of four days. To mitigate the impact of this effect on the interpretation of the results, wind data were not utilized in our analysis when wind speed was measured as  $0 \text{ m s}^{-1}$ . While there is reason to believe that wind speeds are indeed low during these periods, the actual wind speed is unknown. Thus, if the average wind speed calculated during an ODE contained  $> 50\%$  of such values, the wind data for that event were not included in the data analysis. We also acknowledge that an icing effect could create a measurement bias toward lower values. However, as discussed in the text (Section 3.3.3), on average this appears to be a minor issue in terms of our use of the anemometer data (e.g. to calculate ODE spatial scales) as we find effectively equivalent results using our anemometer wind speeds and those estimated using the HYSPLIT backwards trajectory model (Sect. 3.2.3).

Ozone was measured using custom-built 2B Technologies model 205 dual-beam  $\text{O}_3$  monitors. Customizations include one backup pump, one backup  $\text{O}_3$  scrubber, a lamp heater, and modified firmware to control the instrument remotely. The instrument inlet, which contained a 90 mm quartz fiber filter (Pall Life Sciences) to prevent intake of large particles, is located on the mast of the buoy  $\sim 2 \text{ m}$  above the sea ice, while the instrument itself is located inside the hull of the buoy beneath the sea ice such that it operates under a near constant temperature ( $\sim -1.5 \text{ }^\circ\text{C}$ ). Sample averaging by the ozone monitors differed between buoy deployments: O-Buoy 1 used 10 second averages, O-Buoy 3 used two second averages, and both O-Buoy 2 and O-Buoy 4 used one minute averages. For analysis, all data were smoothed to 5 minute moving averages.

BrO was detected using a multi-axis differential optical absorption spectroscopy (MAX-DOAS) instrument. The scan head telescope, located at the top of the buoy mast,

collects scattered radiation and sends it through a fiber optic cable to the computer/spectrometer module, which consists of a single board computer (Technologic Systems TS-7260), a stepper motor driver (Stepperboard BC2D15), interface electronics, and a miniature spectrometer (Ocean Optics HR2000, 318-455 nm). The scan elevation angle is controlled by the O-Buoy's supervisory computer and observes light at angles of 90 (zenith), 20, 10, 5, 2, and 1 degree(s) over a period of 30 minutes (Carlson et al., 2010). The zenith spectrum from a 30-minute data measurement period was used as the reference spectrum for the lower elevation angle spectra, which minimizes the differential absorption by stratospheric species. To obtain differential slant column densities (dSCD), the QDOAS software was used (Fayt et al., 2011) to fit both the logarithm of the ratio of each low elevation spectra and zenith spectra in the wavelength region 346-364 nm (convolved absorber cross sections detailed in Table 3.2), as well as a 3<sup>rd</sup> order polynomial to account for broadband features and a spectral offset to account for stray light.

Table 3.2 Cross sections used in spectral analysis. Each cross section is convolved using an instrument function determined by the 334 nm Hg peak.

Species	Cross Section Reference
BrO (228 K)	Wilmouth et al. (1999)
O <sub>3</sub> (243 K)	Malicet et al. (1995)
NO <sub>2</sub> (220 K)	Vandaele et al. (1998)
O <sub>4</sub>	Hermans et al. (2001)
Ring	Determined from zenith spectra using Chance and Spurr (1997)

Fit residuals for both O-Buoy1 and O-Buoy2 were less than  $1 \times 10^{-3}$  resulting in BrO dSCD errors less than  $4 \times 10^{13}$  molecules  $\text{cm}^{-2}$  and  $\text{O}_4$  dSCD errors of less than  $1 \times 10^{42}$  molecules<sup>2</sup>  $\text{cm}^{-5}$ . Retrieval of BrO mole fractions from dSCD data is a two-step inverse problem. First, the aerosol profile is determined from  $\text{O}_4$  dSCDs using both the SCIATRAN radiative transfer model as a forward model, and the estimation techniques detailed in Frieß et al. (2006). Then, a vertical profile of BrO mole fractions from the ground to 2 km (100 m intervals) was obtained using both the radiative transfer model McArtim (Deutschmann et al., 2011) as a forward model, and similar optimal estimation techniques detailed in Frieß et al. (2011). Because we are only considering surface  $\text{O}_3$  measurements, only the average BrO mole fractions in the lowest 100 m were used in subsequent portions of this study.

The BrO detection limit is a function of the geometry of the observation and the state of the atmosphere at the time of the measurement. We estimated a range for the detection limit ( $2\sigma$ ) of  $3.7 \times 10^{12}$  (clear sky) to  $1.5 \times 10^{13}$  mol  $\text{cm}^{-2}$  (impaired visibility) for the total integrated column BrO through 2km ( $\text{VCD}_{2\text{km}}$ ) by looking at the distribution of  $\text{VCD}_{2\text{km}}$  values over a month in late summer where no BrO was observed. To evaluate the error associated with the retrieved surface mole fractions, it is necessary to consider both dSCD measurement error and smoothing error (Rodgers, 2000). Smoothing error calculations quantify the error resulting from the inability of the instrument to observe fine structure in the vertical profile. The smoothing error was estimated through considering the mean of an ensemble of profiles retrieved in late summer ( $\bar{x}$ ) when the dSCD measurements indicated no measurable BrO. This allowed us to assume the actual profile ( $x_a$ ) is given by 0 pmol  $\text{mol}^{-1}$  (pptv) BrO through 2 km. The average surface mole fraction

smoothing errors ( $\epsilon_s$ ) for the entire O-Buoy2 campaign were estimated using Equation 3.1, where  $A$  represents the averaging kernel matrix and  $I$  is the identity matrix (Rodgers, 2000).

$$\epsilon_s = (A - I)(\bar{x} - x_a) \quad \text{E3.1}$$

Individual surface mole fraction errors due to smoothing error averaged 0.3 pmol mol<sup>-1</sup> for the O-Buoy2 campaign. Including individual mole fraction errors due to propagated dSCD measurement error, total surface mole fraction errors range from 0.7 to 6.9 pmol mol<sup>-1</sup>, with average and median errors corresponding to ~3.0 and 3.3 pmol mol<sup>-1</sup> respectively. Due to the timing of the O-Buoy1 deployment, we were unable to estimate smoothing error in the manner described above. Therefore, only errors due to propagated dSCD measurement error were considered. For O-Buoy1, total surface mole fraction errors range from 0.7 to 4.5 pmol mol<sup>-1</sup>, with average and median errors corresponding to ~2.5 and 2.6 pmol mol<sup>-1</sup> respectively.

### 3.2.2 ODE Definition

Several definitions of ODE conditions can be found throughout the literature. For example, some studies define an ODE, partial or severe, as when O<sub>3</sub> mixing ratios are below 20 nmol mol<sup>-1</sup> (Ridley et al., 2003), 10 nmol mol<sup>-1</sup> (Tarasick and Bottenheim, 2002), 5 nmol mol<sup>-1</sup> (Bottenheim et al., 2009; Frieß et al., 2011; Jacobi et al., 2010), or 4 nmol mol<sup>-1</sup> (Piot and von Glasow, 2008, 2009; Ridley et al., 2003). For this study, a specific set of ODE criteria, defined below, were developed to examine ODEs identified using the O-Buoy data set. We define and distinguish periods of “major” ozone depletion events

(MODEs; defined differently here than originally defined by Ridley et al. (2003) (see below)) from a less severe ODE term to enable us to compare and contrast the temporal and spatial differences between them. Note that as defined below, any ODE can include the shorter periods of MODEs, but the MODE criteria are not necessary for an event to be defined as an ODE. These criteria are visually illustrated in Figure 3.3 using sample O-Buoy data.

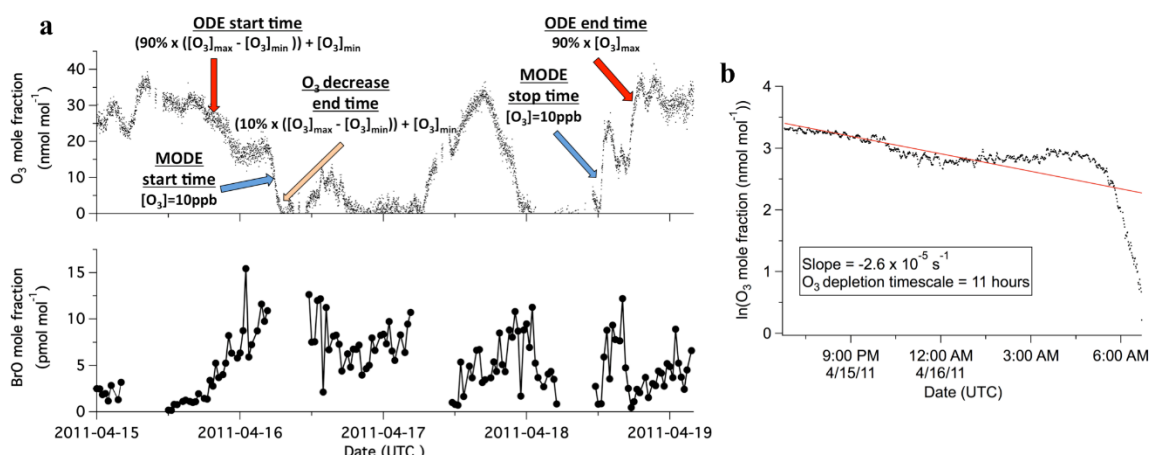


Figure 3.3 a) Example ODE from O-Buoy2 deployment in the Beaufort Sea with ODE definitions illustrated. The brief resurgence of  $O_3$  on 17 April does not rise above  $25 \text{ nmol mol}^{-1}$  for longer than 12 hours and is thus not considered as separating two ODEs. Error bars are not displayed to more clearly show the time series. As discussed in Sect. 3.2.1, individual measurement errors for  $O_3$  ranged from 2.1 to  $3.5 \text{ nmol mol}^{-1}$ , and BrO measurement errors ranged from 0.7 to  $6.9 \text{ pmol mol}^{-1}$  (median and average error  $\sim 3 \text{ pmol mol}^{-1}$ ). b) Example of  $O_3$  depletion timescale calculation based on the depletion range (ODE start time –  $O_3$  decrease end time) from a). The natural logarithm of the  $O_3$  values is plotted against time, and the inverse slope of this plot represents the  $O_3$  depletion timescale.



Background O<sub>3</sub> conditions were established if O<sub>3</sub> mole fractions stayed above 25 nmol mol<sup>-1</sup> for longer than 12 hours. If O<sub>3</sub> dropped below 15 nmol mol<sup>-1</sup> for longer than one hour, the event was considered to be an ODE. The ODE start time is defined as the time at which O<sub>3</sub> drops below 90% of its local maximum concentration prior to depletion. If O<sub>3</sub> subsequently rose above 25 nmol mol<sup>-1</sup> for longer than 12 hours, the ODE was considered terminated; the ODE end time was defined as the time when O<sub>3</sub> reached 90% of the local maximum O<sub>3</sub> mole fraction after rising above 25 nmol mol<sup>-1</sup> for more than 12 hours. It should be noted that the increase in O<sub>3</sub> mole fraction on 17 April 2011 seen in Figure 3.3 does not recover above 25 nmol mol<sup>-1</sup> for longer than 12 hours, and its subsequent decrease does not represent a new ODE. For the calculation of the O<sub>3</sub> depletion timescale, an O<sub>3</sub> decrease stop time was defined as the time at which O<sub>3</sub> first reached 10% of the difference of the preceding maximum and ultimate minimum O<sub>3</sub> mole fractions during the ODE.

MODEs are cases for which O<sub>3</sub> dropped below 10 nmol mol<sup>-1</sup> for longer than one hour, with the start time defined as the time at which O<sub>3</sub> fell below 10 nmol mol<sup>-1</sup>. If O<sub>3</sub> then increased above 10 nmol mol<sup>-1</sup> for longer than 12 hours, the MODE is considered terminated, with the MODE stop time defined as the time at which O<sub>3</sub> recovered above 10 nmol mol<sup>-1</sup>.

### 3.2.3 Air Mass Trajectory Analysis

The NOAA HYSPLIT air mass trajectory model (Draxler et al., 2012; Draxler and Hess, 1998; Draxler and Rolph, 2003) was utilized to examine backward trajectories during O<sub>3</sub>-depleted conditions, as defined in Sect. 3.2.2. Backward air mass trajectories were

calculated starting from a height of 10 m above ground level using the ODE stop time as the start time of the model (note that three events, one from each O-Buoy 2, 3, and 4, did not have well defined ODE stop times, and thus were not analyzed here). Isobaric trajectories were chosen because the stable surface air in which the ODEs occur is typically well isolated from the air aloft (Oltmans et al., 2012; Seabrook et al., 2013); as long as O<sub>3</sub> is in ODE conditions, the air is likely to be surface layer air. The trajectory run lengths were defined by the ODE durations (ODE stop time – ODE start time; see Figure 3.4 for the distribution of ODE time lengths), such that the final point of the backward trajectories corresponded to the defined ODE start times.

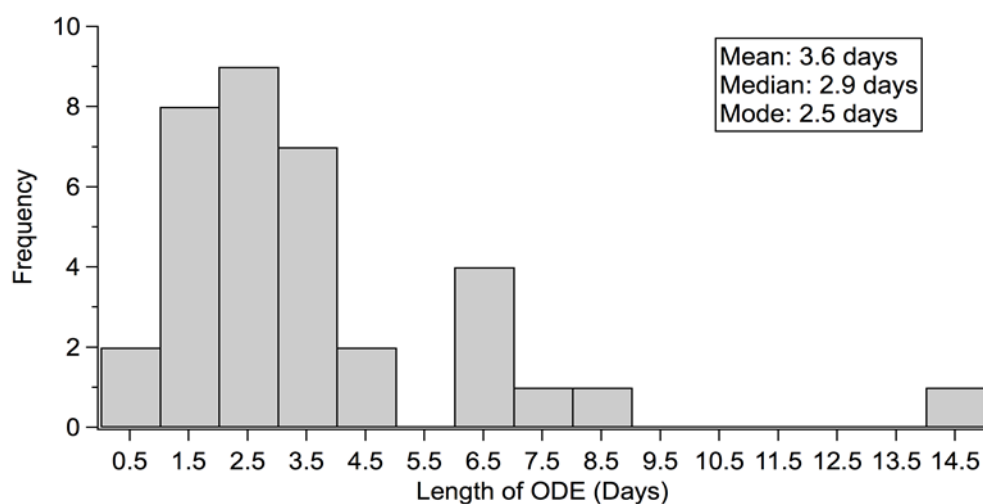


Figure 3.4 Time lengths of ODEs as defined by the ODE start time and the O<sub>3</sub> decrease stop time.

ODE spatial scales were defined as the maximum distance between any two points of the backward air mass trajectory, as this would represent an upper limit to an event's spatial size (illustrated visually in Figure 3.5). This analysis was performed for both the broader ODE definition and MODEs.

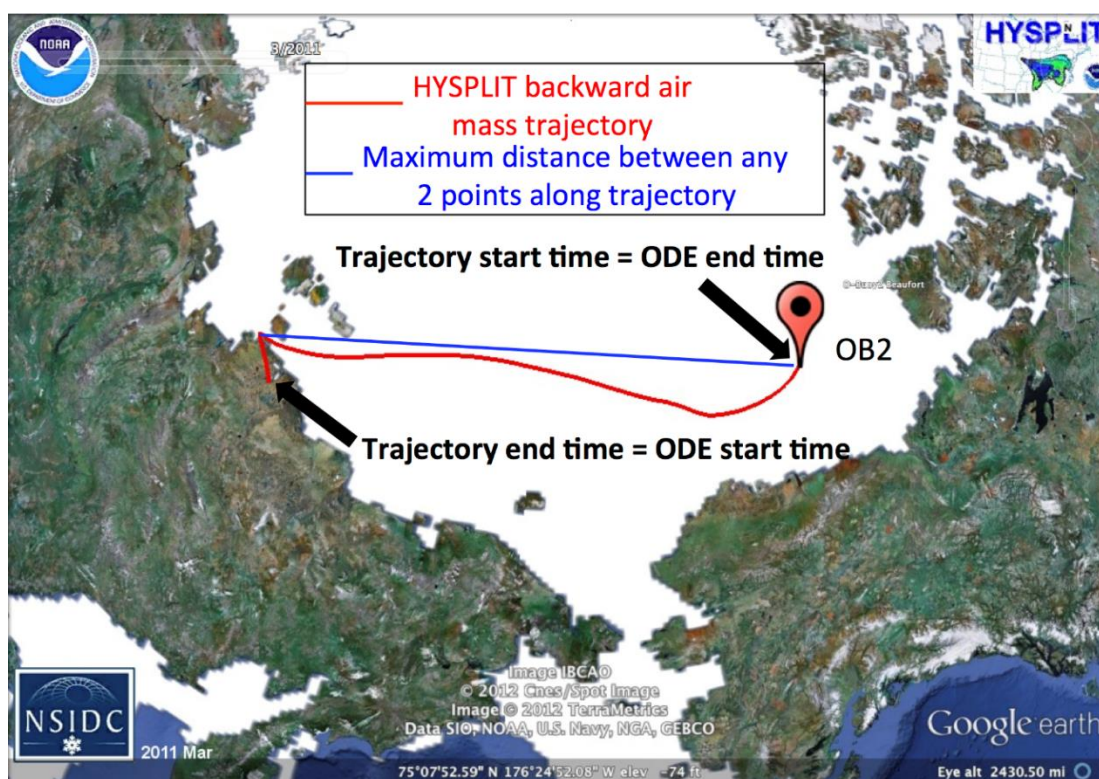


Figure 3.5 Example HYSPLIT backward air mass trajectory. The HYSPLIT model was run backward starting from the ODE end time until the ODE start time. ODE spatial dimensions were determined by calculating the maximum Great Circle distance between any two points along the trajectory.

Of the ODE air masses modeled isobarically, all but one remained near the surface (below 200 m above ground level) throughout the course of the trajectory. The outlier ODE air mass, occurring during O-Buoy1 2009 at Barrow, AK, rose above 800 m and likely did not represent surface layer air; this event was therefore excluded from HYSPLIT analyses. For comparison, we also estimated the ODE spatial scales by the same method using isentropic back trajectories (starting height of 10 m above ground level); by determining the distance between the start and end points for each isobaric trajectory; and by using Equation 3.2:

$$D_{\text{ODE}} = v_{\text{wind}} \times t_{\text{ODE}} \quad \text{E3.2}$$

where  $D_{\text{ODE}}$  is the ODE diameter,  $v_{\text{wind}}$  is the average local wind speed from the anemometer, and  $t_{\text{ODE}}$  is the duration of the ODE.

The HYSPLIT model was also used to estimate some meteorological parameters at each position along the isobaric backward trajectories. For this analysis, the average and minimum air temperatures along each trajectory were compared with the temperatures recorded by the O-Buoy during each ODE. The path lengths and time lengths of individual trajectories were used to estimate the average wind speeds of the air masses, which were compared with the wind speeds obtained from the O-Buoy anemometer. Wind rose plots were created based on the quadrant in which the air mass trajectory spent the most time during a given ODE (north (315°-45°), south (135°-225°), east (45°-135°), and west (225°-315°)). Only four quadrants were used in the wind rose plots because there is a large level of uncertainty associated with using a back trajectory model for this purpose (Kahl, 1993).

The angles used were obtained by calculating the bearing between the O-Buoy and each point along each back trajectory for each ODE.

#### 3.2.4 Monte Carlo Experiment

A Monte Carlo experiment was performed to determine whether it was a statistical possibility that the observed ODEs resulted primarily from TM, given the estimated size distribution. In the limit of an ODE as large as the Arctic Ocean, the ODE would be observed at the O-Buoy primarily due to local CM. Thus, for some ODE size limit, it is not feasible for all ODE observations to result from TM. For this simulation experiment, we estimated the probability that assumed circular depletion regions overlap with a point of interest (an O-Buoy) when randomly placed about a defined area represented by the ice-covered Arctic Ocean. The diameters of the circles were defined by the ODE size distribution estimated from Beaufort Sea (O-Buoy1 and O-Buoy2) observations (Section 3.2.3); these particular ODEs were chosen for this exercise because of the similar locations and drift trajectories of the buoys, providing the needed statistics for the analysis. Nineteen ODEs were observed between the two deployments (in 2010 and 2011), with ODE sizes ranging from 210 - 3532 km (see Sect 3.3.2). The circles, with sizes taken from the observed size distribution (Section 3.2.3), were simultaneously and randomly placed in an area defined by the average sea ice extent of the Arctic Ocean between March 2010 and 2011 (

Figure 3.6), as reported by the National Snow & Ice Data Center (<http://www.nsidc.org/>).

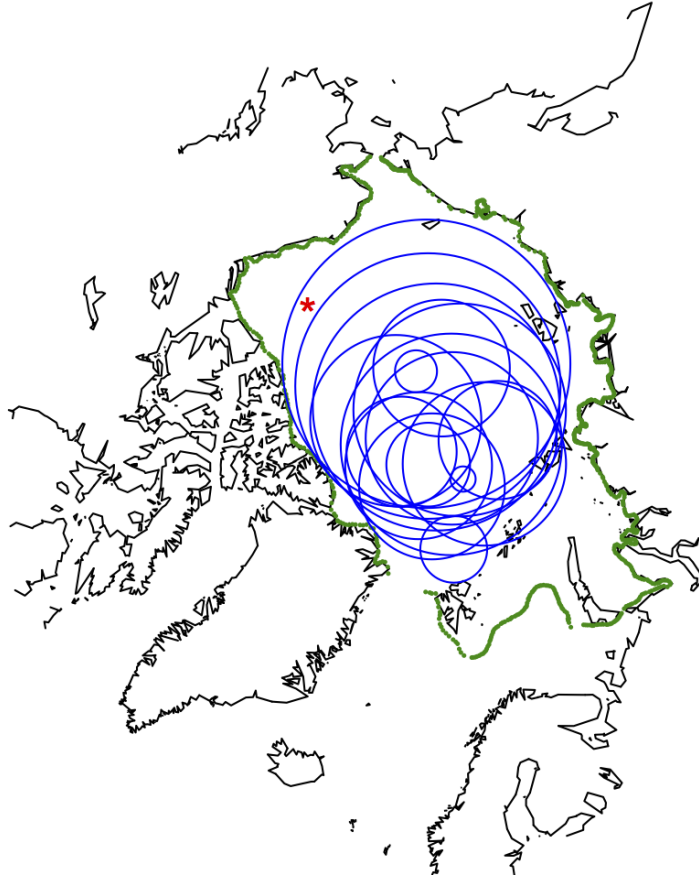


Figure 3.6 Visualization of one iteration out of 2000 of the Monte Carlo experiments. The area of interest within the Arctic is defined by the green outline. Blue circles represent ODE air masses. The red star represents the average location of the O-Buoy between O-Buoys1 and 2. Seventeen different sized air masses were randomly placed simultaneously within the area of interest.

We note, however, two O-Buoy2 events were excluded from this analysis. The first was removed due to an undefined ODE spatial scale (discussed in Sect. 3.2.3). The other ODE size excluded (diameter of 3532 km) was estimated to be larger than the defined area. Thus, a total of 17 circles were used in these simulations. The number of circles that overlapped with the location of the buoy (assumed to be  $74.75^\circ$  N,  $142^\circ$  W, an

approximate location of both O-Buoys 1 and 2) was determined for multiple iterations of the experiments.

Figure 3.6 represents one iteration of the experiment, which was repeated 2000 times in order to obtain a statistical distribution of the number of overlaps. Additionally, a sequence of similar Monte Carlo experiments was repeated for individual ODE sizes 1000 times to obtain the probability that each circle size overlaps with the location of the buoy. This simulation experiment was conducted to examine the relationship between ODE size and the probability that the ODE would only be observed due to TM.

### 3.3 Results and Discussion

#### 3.3.1 Ozone Depletion Timescale

For O-Buoys 1–4, a total of 38 ODEs were observed between the months of February and June (see Table 3.1 for breakdown of each O-Buoy). On the assumption that  $O_3$  decrease is an exponential decay process, and to express the observed depletion time scales in an objective manner, the apparent  $O_3$  depletion timescale ( $\tau_{O_3}$ ) at the beginning of an ODE was estimated as the reciprocal of the slope of  $\ln[O_3]$  versus time (during the period ODE start time -  $O_3$  decrease stop time, as discussed in Sect. 3.2.2; Figure 3.3b). This timescale is observed due to a combination of both CM and TM, though the extent to which each factor affects  $\tau_{O_3}$  is unknown. Because we are analyzing the slopes, this analysis is mostly insensitive to the ODE start / depletion stop times as long as the depletion range of the plot constitutes the majority of the defined timeframe. As seen in Figure 3.7a,

$\tau_{\text{O}_3}$  ranged from 30 minutes to longer than 50 hours (maximum of 14 days), with the majority (76%) shorter than 24 hours (median  $\tau_{\text{O}_3}$  of 11 hours).

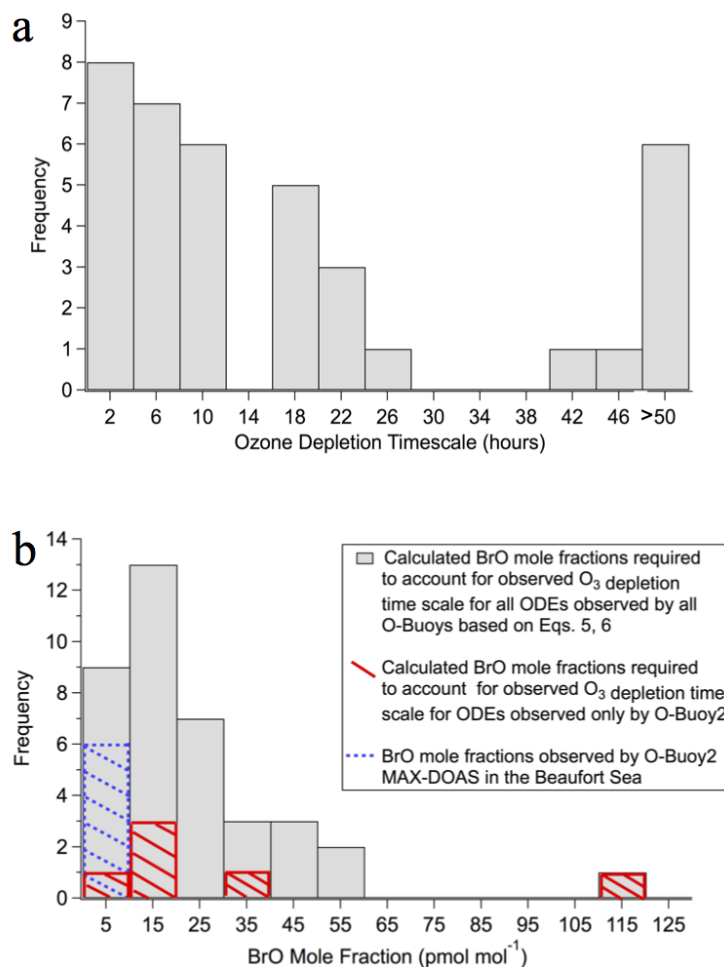


Figure 3.7 a) Histogram of the distribution of calculated  $\text{O}_3$  depletion timescales during ODEs. To more clearly show the majority of events, the six events with  $\tau_{\text{O}_3}$  greater than 50 hours are grouped together on the histogram. b) Calculated BrO concentrations are shown for the observed ODEs, assuming local chemistry, considering BrO and an assumed ClO mole fraction of  $6 \text{ pmol mol}^{-1}$ , and other  $\text{O}_3$  destruction pathways, using Equation 3.6 as discussed in Sect. 3.3.1. The mode calculated BrO mole fraction is  $15 \text{ pmol mol}^{-1}$ . Measured BrO for O-Buoy2 is shown as the blue hatched bar, and the corresponding BrO required to account for the observed ozone depletion rates for O-Buoy2 events are shown as solid red diagonal bars.



These timescales correspond to O<sub>3</sub> decrease rates ( $-\frac{d[O_3]}{dt}$ ) that range between 0.02 and 30 nmol mol<sup>-1</sup> hr<sup>-1</sup> (average and standard deviation:  $3.5 \pm 5.4$  nmol mol<sup>-1</sup> hr<sup>-1</sup>). By comparison, Tuckermann et al. (1997) reported O<sub>3</sub> decrease rates ranging from 0.24 to 7 nmol mol<sup>-1</sup> hr<sup>-1</sup> from their measurements in Ny-Ålesund, Spitsbergen. Removing coastal site data (O-Buoy1 2009, deployed in Barrow, AK) from the histogram did not significantly alter the  $\tau_{O_3}$  distribution. For the six ODEs with  $\tau_{O_3}$  equal to 50 hours or longer, two cases occurred in June after changes in O<sub>3</sub> levels had become much more gradual, relative to the sporadic and episodic nature of the preceding months (Feb. through May). Apart from these two events, which occurred at higher temperatures, there was no clear difference in the local average wind speeds or temperatures that was unique to the remaining four of these six events. However, a likely cause for these extended events is poor vertical mixing in the absence of frontal passages. Recent work by Moore et al. (2014) and Peterson et al. (2016) provides evidence of coastal O<sub>3</sub> recovery to background levels when air passes over open leads. This recovery is hypothesized to occur due to increased convective mixing and downward transport of ozone from aloft. Thus, a longer depletion timescale may also imply a large-scale ice-covered surface.

If the observed ODEs were indeed dominated by the CM at the location of the O-Buoys (i.e. TM is minimized in the apparent  $\tau_{O_3}$ ), it is surprising that the majority of cases featured such short apparent timescales of O<sub>3</sub>-depletion ( $\tau_{O_3} < 12$  h). As discussed in Section 3.3.1, previous model estimates of O<sub>3</sub>-depletion timescales due to chemistry are typically on the order of days (Hausmann and Platt, 1994; Jobson et al., 1994; Piot and von

Glasow, 2008, 2009; Tuckermann et al., 1997). Generally, fast  $\tau_{\text{O}_3}$  observed at coastal sites have been attributed to TM. In these cases,  $\text{O}_3$  is hypothesized to be chemically destroyed upwind (i.e. over the Arctic Ocean), and the apparent  $\tau_{\text{O}_3}$  is a function of both the rate at which the  $\text{O}_3$ -depleted air mass travels across the measurement site, and the horizontal concentration gradient at the edges of those air masses. For example, Morin et al. (2005) observed  $\text{O}_3$  levels to fall from mole fractions of  $\sim 30 \text{ nmol mol}^{-1}$  to less than  $5 \text{ nmol mol}^{-1}$  in around 3 minutes from over the Arctic Ocean, 6 km off the coast of Alert, Canada. However, fast  $\text{O}_3$  depletion attributed to local chemistry has been previously reported: using measurements from aboard the icebreaker RV *Polarstern* in the Arctic Ocean, Jacobi et al. (2006) observed a decrease in  $\text{O}_3$  from  $40 \text{ nmol mol}^{-1}$  to  $< 1 \text{ nmol mol}^{-1}$  in less than 7 hours.

To interpret the results from the O-Buoys, we first explore the extent to which known chemical mechanisms could account for the observed  $\tau_{\text{O}_3}$  values (i.e. the CM dominates while the TM is minimal). Rates of  $\text{O}_3$  loss during ODEs have been previously thought to be limited by Reactions R3.3-R3.4 at high BrO levels, estimated by Equation 3.3 below (Le Bras and Platt, 1995; Platt and Janssen, 1995).

$$\left(-\frac{d[\text{O}_3]}{dt}\right) = 2k_{\text{BrO}+\text{BrO}}[\text{BrO}]^2 + 2k_{\text{BrO}+\text{ClO}}[\text{BrO}][\text{ClO}] \quad \text{E3.3}$$

Recently, Liao et al. (2012a) and Liao et al. (2014) report that R3.3 and R3.4 only account for around 40% of the total  $\text{O}_3$ -depletion chemistry observed during the 2009 OASIS field campaign. Thompson et al. (2016), using a 0-D model constrained by chemical data

collected during the same campaign, found that Br-atom destruction of O<sub>3</sub> has a low homogeneous gas phase radical propagation chain length (close to 1). Because of this small chain length, the dominant source of Br atoms that destroy O<sub>3</sub> appears to be the photolysis of Br<sub>2</sub> and BrCl emitted from the surface or aerosols, and thus most of the BrO that is produced terminates via reaction with HO<sub>2</sub> (R3.5) (or NO<sub>2</sub> for more polluted areas, such as Barrow, AK). Indeed, estimating the rate using Equation 3.3 assumes that all Br atoms are produced from Reactions R3.3 and R3.4, which is inconsistent with the observed, often large concentrations of Br<sub>2</sub> (Liao et al., 2012a). The BrO termination pathways would result in more heterogeneous recycling of Br atoms. They then compared  $\frac{d[O_3]}{dt}$  as calculated by both Equation 3.3 and by the net chemical O<sub>3</sub>-destruction rate (Equation 3.4).

$$\begin{aligned} \left(-\frac{d[O_3]}{dt}\right) = & k[Br][O_3] + k[Cl][O_3] + k[O(^1D)][H_2O] \\ & + k[OH][O_3] + k[HO_2][O_3] - k[BrO][NO] \\ & -J[BrO] - k[ClO][NO] - J[ClO] \end{aligned} \quad E3.4$$

In calculating  $\frac{d[O_3]}{dt}$ , a regression between the rates showed that using only Equation 3.3 underestimates the net  $\frac{d[O_3]}{dt}$  (from Equation 3.4) by a factor of 4.1 on average by neglecting other chemical pathways (Thompson et al., 2015). Therefore, we estimate the BrO mole fractions required to cause the observed  $\tau_{O_3}$  according to Eqs. 3.5 and 3.6 below. These equations include the factor of 4.1 that accounts for the production of bromine atoms via Br<sub>2</sub> and BrCl photolysis, two molecular halogens derived from heterogeneous recycling of species such as HOBr and BrONO<sub>2</sub> on halide-containing aerosols or the saline snowpack

(Abbatt et al., 2012; Simpson et al., 2007b). A constant ClO concentration of  $1.7 \times 10^8$  molecules  $\text{cm}^{-3}$  ( $6 \text{ pmol mol}^{-1}$  at 248 K and atmospheric pressure) was assumed based on average concentrations measured during the 2009 OASIS campaign (Stephens, 2012).

$$\left(-\frac{d[\text{O}_3]}{dt}\right) = 4.1 \times (2k_{\text{BrO}+\text{BrO}}[\text{BrO}]^2 + 2k_{\text{BrO}+\text{ClO}}[\text{BrO}][\text{ClO}]) \quad \text{E3.5}$$

$$\tau_{\text{O}_3} = \frac{[\text{O}_3]_{\text{avg}}}{4.1 \times (2k_{\text{BrO}+\text{BrO}}[\text{BrO}]^2 + 2k_{\text{BrO}+\text{ClO}}[\text{BrO}][\text{ClO}])} \quad \text{E3.6}$$

Because Thompson et al. (2015, 2016) utilized a temperature of 248 K in their model, consistent with average local temperatures at Arctic coastal sites in the springtime, we also use this temperature for our BrO mole fraction estimations. The rate constants  $k_{\text{BrO}+\text{BrO}} = 3.8 \times 10^{-12} \text{ cm}^3 \text{ molecules}^{-1} \text{ s}^{-1}$  and  $k_{\text{BrO}+\text{ClO}} = 8.2 \times 10^{-12} \text{ cm}^3 \text{ molecules}^{-1} \text{ s}^{-1}$  were calculated based on Sander et al. (2011) and Atkinson et al. (2007), respectively. However, it should be noted that the rate constants change by only  $< 8\%$  when calculated at 273K ( $k_{\text{BrO}+\text{BrO}} = 3.5 \times 10^{-12} \text{ cm}^3 \text{ molecules}^{-1} \text{ s}^{-1}$  and  $k_{\text{BrO}+\text{ClO}} = 7.6 \times 10^{-12} \text{ cm}^3 \text{ molecules}^{-1} \text{ s}^{-1}$ ). We note that  $k_{\text{BrO}+\text{ClO}}$  includes both R3.4a and R3.4b. The calculated BrO mole fractions corresponding to the estimated  $\tau_{\text{O}_3}$  range from  $\sim 1 \text{ pmol mol}^{-1}$  ( $\tau_{\text{O}_3} = 356 \text{ hours}$ ) to  $115 \text{ pmol mol}^{-1}$  ( $\tau_{\text{O}_3} = 28 \text{ minutes}$ ), with a median of  $16 \text{ pmol mol}^{-1}$  (Figure 3.7b). The majority of the calculated distribution of BrO required is fairly comparable to previously reported enhanced surface BrO mole fraction ranges, which often peak around  $20\text{-}40 \text{ pmol mol}^{-1}$  (Hausmann and Platt, 1994; Hönninger et al., 2004b; Pöhler et al., 2010; Tuckermann et al., 1997). Indeed, 32 out of 38 events were calculated to require less than  $40 \text{ pmol mol}^{-1}$  of BrO for  $\text{O}_3$  depletion. If, however, expected BrO were calculated based on Equation 3.6

without the factor of 4.1 (i.e. expected BrO based R3.3 and R3.4), this number decreases to 20 out of 38 events. For the O-Buoy1 (Barrow, AK) and O-Buoy2 deployments, MAX-DOAS BrO data are available for comparison with the calculated BrO estimations (Figure 3.7b; Table 3.3).

Table 3.3 Average BrO mole fractions during periods of O<sub>3</sub> decrease from O-Buoy2 MAX-DOAS, the corresponding propagated errors, and the estimated BrO required for the observed O<sub>3</sub> depletion timescales based on Equation 3.6 (Sect. 3.3.1).

ODE start time (UTC)	O <sub>3</sub> decrease stop time (UTC)	Observed $\tau_{\text{O}_3}$ (hours)	Average observed BrO (pmol mol <sup>-1</sup> )	Measurement uncertainty (pmol mol <sup>-1</sup> )	Estimated BrO required from observed $\tau_{\text{O}_3}$ (pmol mol <sup>-1</sup> )
15 Apr 2011 18:47	16 Apr 2011 06:41	10.5	7.2	3.5	17.5
19 Apr 2011 04:15	19 Apr 2011 04:53	0.5	5.4	3.5	114.7
26 Apr 2011 14:46	26 Apr 2011 22:29	16.2	5.2	3.2	14.8
03 May 2011 11:37	03 May 2011 14:50	1.6	2.6	2.3	33.5
06 May 2011 12:58	07 May 2011 21:32	11.8	5	3.5	15.1
26 May 2011 21:22	28 May 2011 00:59	40.6	0.9	3.2	9.7

Though these observed BrO mole fractions exhibit maxima higher than 20 pmol mol<sup>-1</sup> (ex. Figure 3.2), the average BrO mole fractions during periods of O<sub>3</sub> decrease (ODE start time – O<sub>3</sub> decrease stop time; Sect. 3.2.2) were found to be much less than 20 pmol mol<sup>-1</sup> (Table 3.3).

The amount of MAX-DOAS data available during the 2009 deployment of O-Buoy1 in Barrow was limited by the amount of solar radiation present. The solar elevation angle remained low enough such that there can exist substantial gaps between subsequent periods of BrO measurements. In spite of these gaps, the average BrO mole fractions during three ODEs were comparable to the calculated BrO required for the observed ozone depletion timescale (Table 3.4).

Table 3.4 Average BrO mole fractions during periods of O<sub>3</sub> decrease from O-Buoy1 at Barrow, AK, MAX-DOAS, the corresponding propagated errors, and the estimated BrO required for the observed O<sub>3</sub> depletion timescales based on Equation 3.5.

ODE start time (UTC)	O <sub>3</sub> decrease stop time (UTC)	Observed $\tau_{\text{O}_3}$ (hours)	Average observed BrO (pmol mol <sup>-1</sup> )	Measurement uncertainty (pmol mol <sup>-1</sup> )	Estimated BrO required from observed $\tau_{\text{O}_3}$ (pmol mol <sup>-1</sup> )
30 Mar 2009 20:06	31 Mar 2009 19:20	24.3	8.5	3.2	9.0
12 Apr 2009 06:18	14 Apr 2009 11:22	71.7	13.0	3.2	4.0
02 May 2009 05:51	02 May 2009 23:00	18.7	13.1	3.0	15.2

In the events starting 30 Mar 2009 (Figure 3.8a) and 12 Apr 2009 (Figure 3.8b), O<sub>3</sub> levels can be seen to decrease as BrO begins to rise before the several hour BrO data gaps. As

can be seen from Table 3.4, the average BrO observed during this period was 8.5 pmol mol<sup>-1</sup> and 13.0 pmol mol<sup>-1</sup> for 30 Mar and 12 Apr, respectively, while the observed rate of O<sub>3</sub> depletion was calculated to require 9.0 pmol mol<sup>-1</sup> and 4.0 pmol mol<sup>-1</sup>, respectively. The 30 Mar event occurred with relatively steady winds (between 6 and 8 m s<sup>-1</sup>), while the 12 Apr event wind speeds gradually fell from 10 m s<sup>-1</sup>. Both events occurred under fairly steady temperatures. The third event (02 May 2009) required 15.2 pmol mol<sup>-1</sup> BrO, while the observed BrO was 13.1 pmol mol<sup>-1</sup>. This event also occurred under steadily decreasing temperatures and calm winds ( $\leq 5$  m s<sup>-1</sup>; Figure 3.8c). While there are no BrO data at the onset of O<sub>3</sub> depletion, there was a noticeable increase in BrO levels in the mid-afternoon. Forty-eight hour HYSPLIT backward trajectories (Draxler, 1999) were computed every 2 hours during the period of O<sub>3</sub> decrease, starting from the O<sub>3</sub> decrease stop time (Figure 3.8d,e, f). For the 30 Mar and 12 Apr events, the trajectories agreed that the air masses

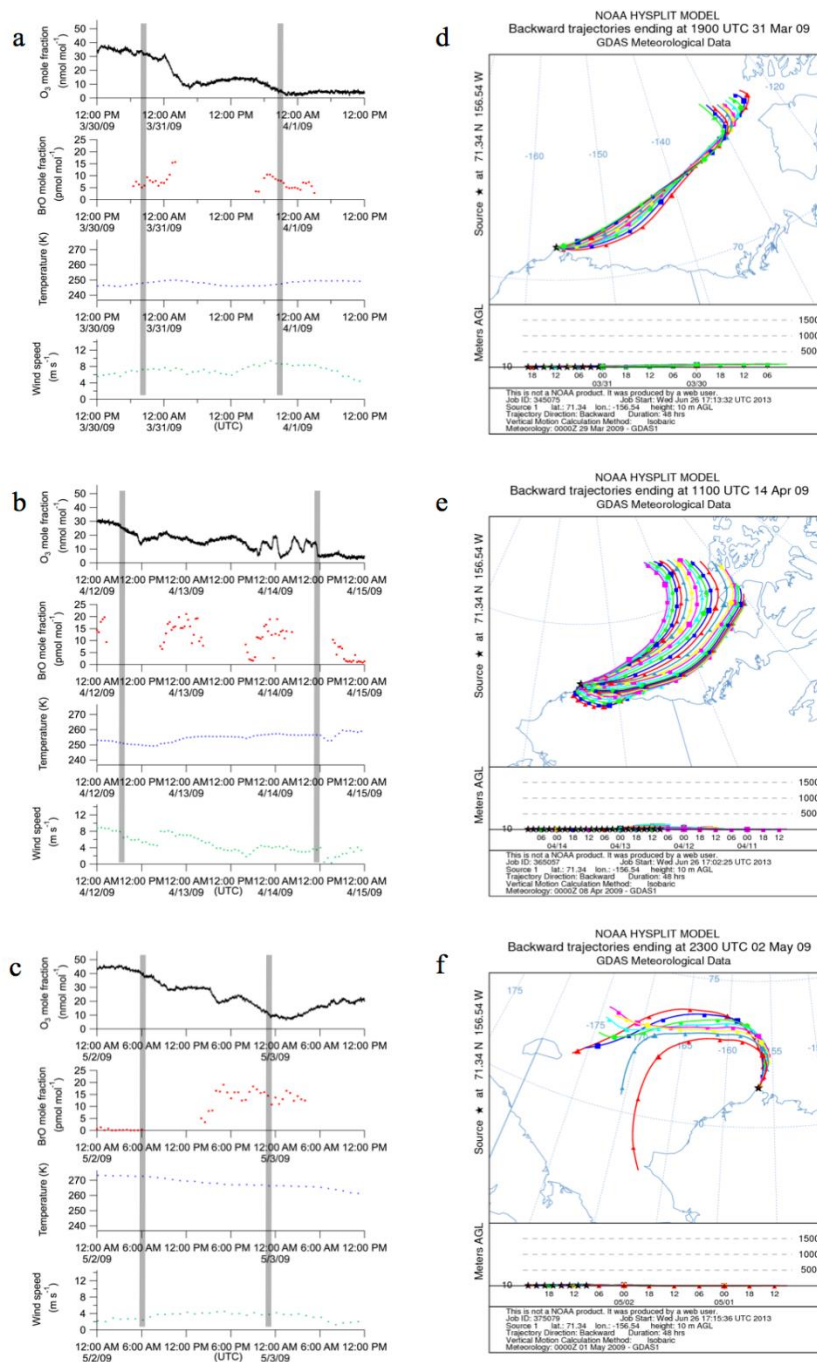


Figure 3.8 Periods of O<sub>3</sub> decrease from O-Buoy1 at Barrow and corresponding 48 hour HYSPLIT backward trajectories (computed every two hours during these time periods). Decrease starts at a, b) 20:06 30 Mar 2009; c, d) 06:18 12 Apr 2009; and e, f) 05:51 02 May 2009. Transparent black bars represent the ODE start time and O<sub>3</sub> decrease stop time as defined in Sect. 3.2.2.



travel near the coast of the Canadian archipelago, an area for which satellites have observed enhanced BrO (Choi et al., 2012; Koo et al., 2012; Richter et al., 1998; Salawitch et al., 2010). The trajectories during the 02 May O<sub>3</sub> decrease showed that air had traveled from across the sea ice in the Beaufort and Chuckchi Seas.

It would be expected that Barrow, a coastal location, would observe ODEs primarily due to the advection of O<sub>3</sub> depleted air, given the evolution of the solar elevation angle during polar spring and findings from previous studies (Bottenheim and Chan, 2006; Koo et al., 2012; Oltmans et al., 2012). The observations here are not inconsistent with these ODEs initiating locally relative to the O-Buoy given the presence of BrO; in the absence of O<sub>3</sub>, the lifetime of BrO is controlled by its photolysis, which is about 100 seconds (Lehrer et al., 2004; Simpson et al., 2007), and thus observations of local BrO in the boundary layer should be indicative of active O<sub>3</sub> destruction chemistry. However, the gaps in the BrO data prevent us from making any further conclusions.

For the cases in which there were enough BrO data to make comparisons, observed BrO levels were found to be lower than the calculated BrO required by Eqs. 3.5 and 3.6, even when considering the propagated measurement error (Table 3.3; described in Section 3.2.1). Indeed, in two of the O-Buoy2 cases, the observed BrO levels are less than a tenth of that required. This result is surprising since the Arctic Ocean is the assumed originating site for ODEs. At least for O-Buoy2, the observed BrO, assumed 6 pmol mol<sup>-1</sup> ClO, and factor of 4.1 cannot account for the apparent  $\tau_{O_3}$ .

Possible reasons for the observed small  $\tau_{O_3}$  values can be summarized by the following two hypotheses:

- 1) There are chemical mechanisms for O<sub>3</sub> destruction that are currently not being considered, or other radical levels (e.g. IO, ClO, HO<sub>2</sub>) are higher than assumed here.
- 2) Most ODEs chemically initiate upwind of the O-Buoys such that the observed  $\tau_{\text{O}_3}$  largely result from TM, as discussed above.

Concerning the first hypothesis, the presence of I<sub>2</sub> has been directly observed only recently at the coastal site of Barrow, AK (Raso et al., 2016). Models have shown that iodine chemistry has the potential to have a significant impact on O<sub>3</sub> destruction chemistry due to the very fast rate constant for IO reaction with BrO (~32 times faster than Reaction R3.3) (Atkinson et al., 2007; Calvert and Lindberg, 2004). In a photochemical box model, Saiz-Lopez et al. (2007) found the ozone loss rate increased by a factor of 4 when iodine was included with bromine chemistry to destroy ozone (via IO + BrO,  $k_{\text{IO} + \text{BrO}} = 1.2 \times 10^{-10} \text{ cm}^3 \text{ molecule}^{-1} \text{ s}^{-1}$  at 248 K). Additionally, the enhanced salinity of first year ice could be a reason for enhanced chlorine radical production as compared to coastal (e.g. Barrow) observations, or snowpack sources of HO<sub>x</sub> (HONO (Zhou et al., 2001), HCHO (Sumner et al., 2002; Sumner and Shepson, 1999), or H<sub>2</sub>O<sub>2</sub> (Hutterli et al., 2001; Jacobi et al., 2002)) could enhance HO<sub>2</sub> levels and thus reactivity.

We can potentially test for O<sub>3</sub>-depletion chemistry missing from Equations 3.4-3.6 by examining the distribution of the ozone tendency,  $(\frac{d[\text{O}_3]}{dt})$ , with and without the calculated component from the chemistry included in Equation 3.5. First, the observed short-term ozone tendency was calculated for values of dt between consecutive BrO measurements (currently O-Buoy1 at Barrow, and O-Buoy2 in the Beaufort Sea) and

plotted in Figure 3.9. Both distributions are zero centered (average Barrow: 0.15 nmol mol<sup>-1</sup> hr<sup>-1</sup>; average Beaufort: 0.01 nmol mol<sup>-1</sup> hr<sup>-1</sup>) with heavy tails on each side.

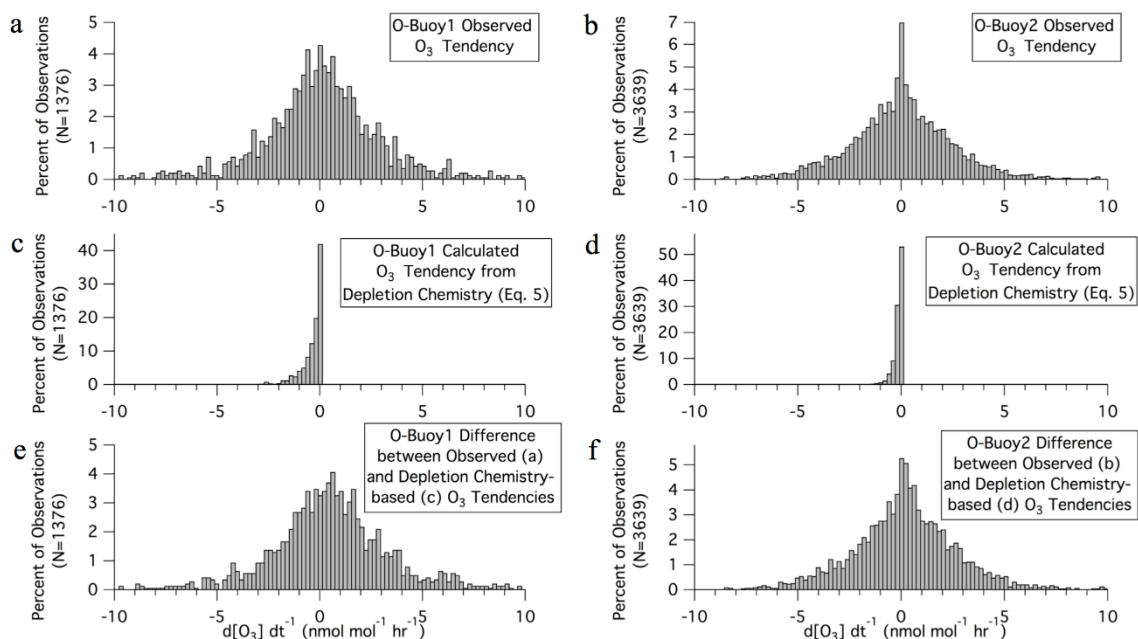


Figure 3.9 Histogram of the O<sub>3</sub> tendency for observations from O-Buoy1 at Barrow, AK (a,c,e), and O-Buoy2 in the Beaufort Sea (b,d,f). Top plots (a, b) show the distributions of observed O<sub>3</sub> tendencies between consecutive BrO measurement points. Middle plots (c, d) represent the O<sub>3</sub> tendency distribution based on the depletion chemistry accounted for by Equation 3.5. Bottom plots (e, f) result from the difference of the observed O<sub>3</sub> tendency (a, b) and the contributions of the chemistry accounted for by Equation 3.5 (c, d).

Then,  $\frac{d[\text{O}_3]}{dt}$  was calculated using Equation 3.5, as above (Figure 3.9c, d); this represents the component of the observed  $\frac{d[\text{O}_3]}{dt}$  resulting from O<sub>3</sub> depletion chemistry. By subtracting these two results, we obtain the distribution of ozone tendencies not accounted for by the considered chemical mechanisms (Figure 3.9e, f). These two distributions (representing

all observations, and those with known chemistry removed) do differ significantly after this subtraction at the 95% confidence level according to the Kolmogorov-Smirnov test (p-value =  $4.9 \times 10^{-4}$  and  $1.4 \times 10^{-6}$  for the O-Buoy1 and 2 results, respectively). Both distribution averages become more shifted from zero, with an average  $\frac{d[O_3]}{dt}$  of  $-0.43 \text{ nmol mol}^{-1} \text{ hr}^{-1}$  for O-Buoy1, and  $-0.18 \text{ nmol mol}^{-1} \text{ hr}^{-1}$  for O-Buoy2. However, it can be shown that the overall symmetry does slightly improve after subtraction by calculating skewness (Equation 3.7),

$$\text{skewness} = \frac{\sum_{i=1}^N (x_i - \bar{x})^3}{(N-1)s^3} \quad \text{E3.7}$$

where  $N$  represents the number of measurements and  $s$  represents the standard deviation of a sample. Skewness decreases in magnitude from  $-0.38$  to  $-0.25$  for the O-Buoy1 at Barrow case, and from  $-0.82$  to  $-0.80$  in the O-Buoy2 in the Beaufort Sea case. Springtime chemical  $O_3$  production in the Arctic boundary layer has been found to be essentially negligible (Helmig et al., 2009, 2012), and so it is likely the positive portions of these distributions result from air mass transport and vertical mixing. This analysis then produces a result not inconsistent with the idea that the remainder of the negative  $\frac{d[O_3]}{dt}$  represents air mass transport.

Hypothesis two, in which the TM dominates the observed  $\tau_{O_3}$ , is in line with those of many previous studies (e.g., Bottenheim et al., 2009; Hausmann and Platt, 1994; Jacobi et al., 2010; Morin et al., 2005). As discussed in these studies, fast  $O_3$  depletion can often be attributed to changes in air mass flow, and surface  $O_3$  mole fractions can return to

background levels upon the passage of low-pressure systems, with associated enhanced vertical mixing. The idea that most of the negative side of the ozone tendency distribution results from transport and not local chemistry is statistically possible only if the average spatial scale of an ODE region is below some critical size (discussed below in Sect. 3.3.2).

### 3.3.2 ODE Spatial Scales

To estimate the spatial scales of ODEs, we combined O-Buoy observations with backward air mass trajectory analysis (Sect. 3.2.3). This analysis assumes  $O_3$  depletes within an air mass upwind via CM, and this air mass subsequently roams across the measurement site; the size of this  $O_3$ -depleted air mass can be estimated from the length of time  $O_3$  is depleted and the wind speed (i.e., TM dominates the CM at the observation site). We emphasize, however, that the observations likely involve some combination of both TM and in situ CM, given O-Buoy detection of BrO, which is indicative of active  $O_3$  depletion chemistry. It is of course conceptually possible that other transport scenarios exist; for instance, conditions could exist in some region upwind that result in the continuous depletion of  $O_3$ -containing air masses that pass over this region. This depleted air may then pass over the buoy. If the depleted air remains intact, however, the spatial scale calculations would still apply.

As shown in Figure 3.10, the median of the one-dimensional length for the ODEs was 877 km. While the estimated size distribution of the MODEs ( $O_3 < 10 \text{ nmol mol}^{-1}$ ) showed no clear mode, it is clear that the distribution contains mostly (relatively) smaller events, with a median size of 282 km.

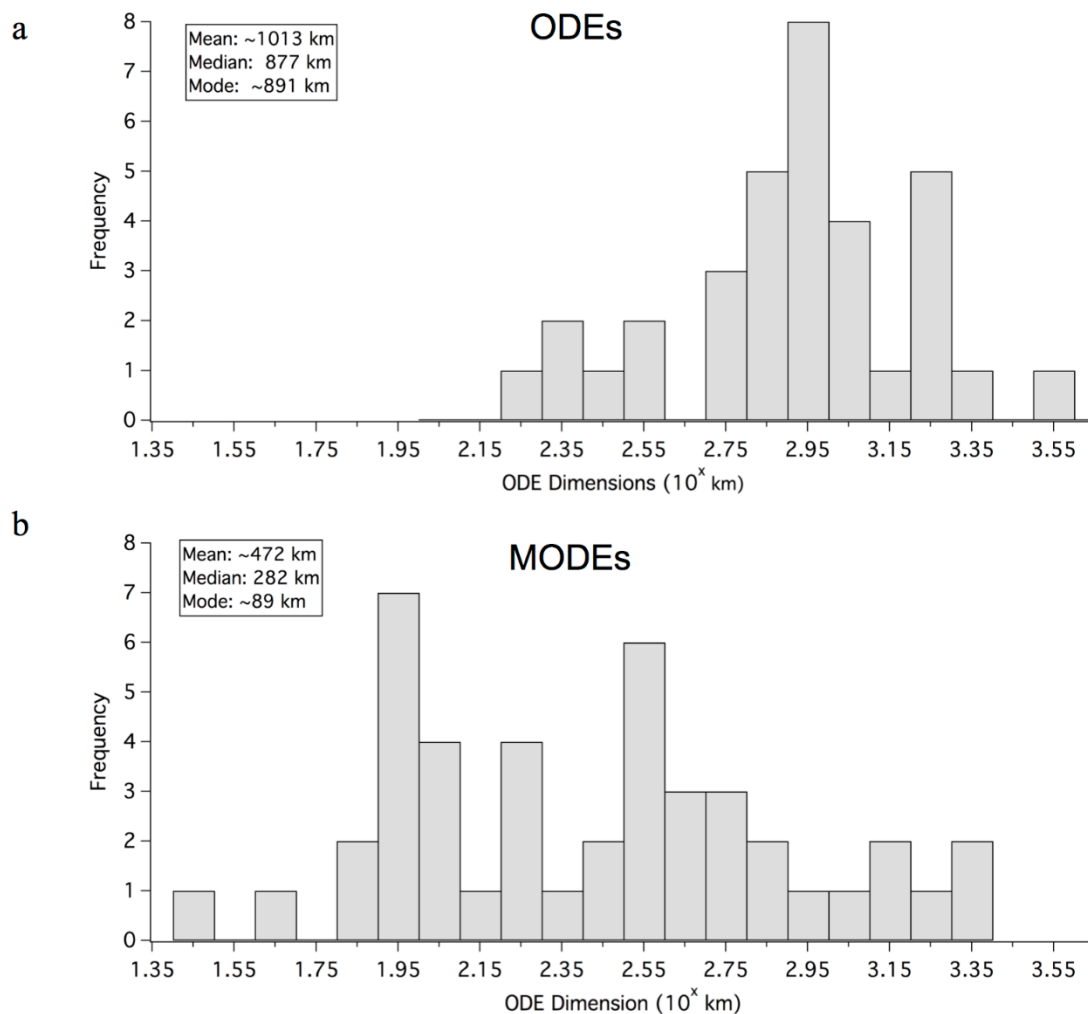


Figure 3.10 a) Histogram of ODE dimensions for all ODEs. The median of the distribution is 877 km. b) Histogram of dimensions of MODEs. The median of the distribution is 282 km.

The distribution of results is also consistent with observations by Jones et al. (2013) and Ridley et al. (2003), who both reported ODEs of spatial dimensions of at least 1200 km and between 600 and 900 km, respectively. The results presented here strongly suggest that large areas of the Arctic are at least partially depleted during Arctic springtime with local embedded areas that are more depleted. While these isobaric trajectories likely

represent the near-surface transport path of depleted air (Seabrook et al., 2013), we also estimated the ODE spatial scales using isentropic back trajectories (starting at 10 m above ground level) and the local wind speeds using the O-Buoy anemometer (Equation 3.2). The means for the isobaric- ( $1013 \pm 379$  km), isentropic- ( $1260 \pm 279$  km), and local wind speed-based ( $1154 \pm 341$  km) spatial scale distributions were statistically similar at the 95% confidence level (confidence intervals reported here). Additionally, spatial scale estimation using the distance between the isobaric trajectory start and end points yielded comparable results (mean  $947 \pm 238$  km).

As discussed in Sect. 3.3.1, known chemical mechanisms could not account for the observed  $\tau_{\text{O}_3}$  values, suggesting these fast  $\tau_{\text{O}_3}$  values were due in large part to TM. A Monte Carlo simulation experiment was conducted with the aim of examining the statistical possibility that all observed ODEs, based on the general ODE definition ( $\text{O}_3 \leq 15 \text{ nmol mol}^{-1}$ ), could have occurred upwind of the buoy and were observed because of TM. As described in Sect. 3.2.4, the simulations were conducted by randomly placing circles (hypothetical ODEs/source regions) across an area the size of the Arctic Ocean sea ice. These circles were defined using the distribution of ODE spatial scales determined from the 17 events observed by the O-Buoy1 and O-Buoy2 deployments (Figure 3.11).

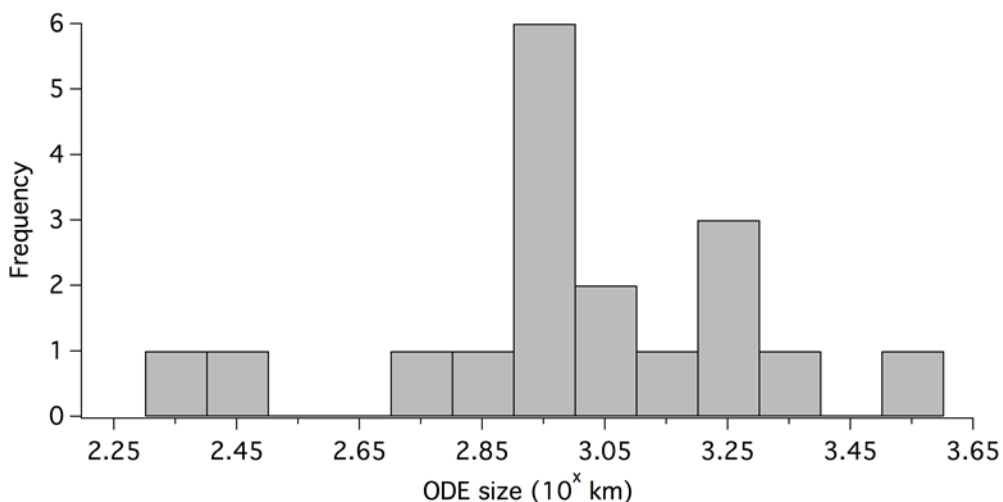


Figure 3.11 Distribution of ODE sizes utilized in the Monte Carlo experiments (subset of those estimates in Figure 3.10). These 18 sizes come from O<sub>3</sub> data observed from O-Buoy1 in 2010 and O-Buoy2 in 2011, both deployed in the Beaufort Sea. Note that this distribution includes the largest ODE size that was excluded from the Monte Carlo simulations.

We note that assuming circular regions for ODEs could underestimate the ODE size since it assumes the center of the event passes over the buoy, when in fact a secant is more likely. Additionally, the area could be overestimated if the true ODE shapes are actually elliptical or irregular in shape. For this statistical exercise, we made the assumptions that the circles could appear (initiate) anywhere across the Arctic Ocean, and that the circles could also represent possible sizes of ODE source regions. While there is evidence to suggest the existence of specific source regions favorable to ODE formation (Bottenheim et al., 2009; Bottenheim and Chan, 2006; Koo et al., 2012; Simpson et al., 2007a; Theys et al., 2011), no definitive conclusions have yet been made from in-situ observations regarding either the locations or the sizes of such regions. We also assume



that that the circle must be contained wholly within the bounds shown in Figure 3.6 in order to equally represent all sizes from the distribution. We acknowledge that this assumption could overestimate the frequency with which ODEs overlap with the buoy, as ODEs have been observed in sub-Arctic regions, such as Kangerlussuaq, Greenland (67°N, 51°W) (Miller et al., 1997), and Hudson Bay (55°N, 75°W; Hönninger et al., 2004a). However, this approach could also underestimate the frequency of overlap, as ODEs that initiate remotely from the buoy would be less likely to be part of the observed distribution of events; in other words, it is also possible that the study region for the Monte Carlo simulation could be too large. It is also assumed that the circles represent fully formed O<sub>3</sub>-depleted air masses or source regions, and that a circle overlapping with the buoy represents “local” ODE initiation relative to the O-Buoy.

The Monte Carlo simulations show that the randomly placed circles most often do not overlap with the measurement site (Figure 3.12a). In fact, only very large sizes (larger than ~1750 km) were likely to intercept the O-Buoy location with a significant probability (> 10%), as shown in Figure 3.12b. Specifically, none of the 17 circles overlapped with the O-Buoy site in 58% of the 2000 simulation iterations, and only one circle (in 17) overlapped with the O-Buoy site in 33% of iterations. For the median ODE size, the probability of any individual event overlapping the Buoy was less than 1%, as shown in

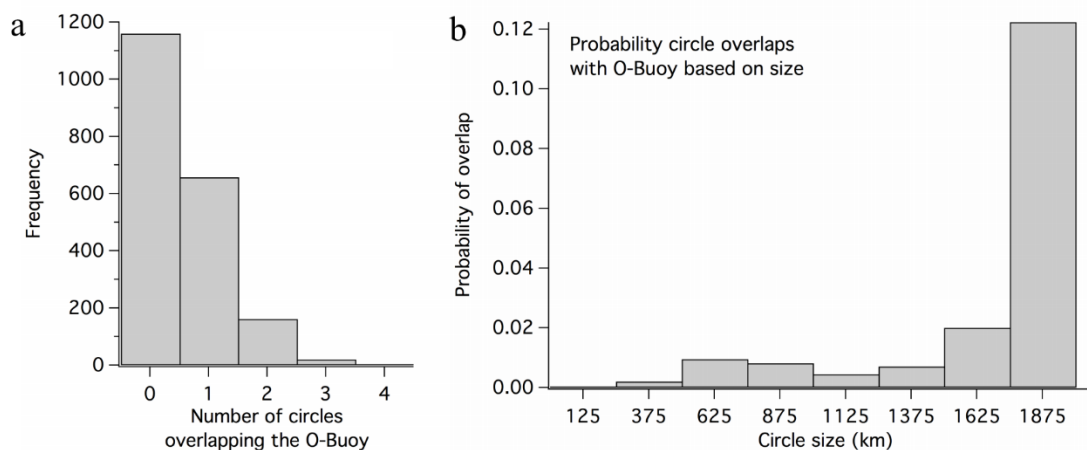


Figure 3.12 Results from Monte Carlo simulation experiment. a) Based on the size distribution as defined by the ODE definition ( $O_3 \leq 15 \text{ pmol mol}^{-1}$ ), circular areas were shown to not overlap with the site of the O-Buoy 58% of the time (mode = 0), followed by an overlap of one circle 33% of the time. b) Plot of the probability that an individual circle overlaps with the measurement site vs the size of the circle.

Figure 3.12b. Therefore, the spatial statistics exercise supports the possibility that the overwhelming majority of ODEs observed by the O-Buoys in the Beaufort Sea could have been observed primarily due to TM, and ODEs initiated upwind. We emphasize that this Monte Carlo exercise does not prove that this is the case, only that this hypothesis is not inconsistent with the observed ODE spatial scales. The practical question is then raised as to how many buoys (observation sites) must be present to increase the probability of observing an ODE primarily due to local chemistry (with the assumption of equal probability of initiation across the Arctic Ocean and that ODE sizes represent source regions, as assumed for the Monte Carlo experiment). If, for example, two additional O-Buoys were deployed near North Pole ( $86^\circ \text{ N}$ ,  $54^\circ \text{ W}$ ) and in the East Siberian Sea ( $75^\circ \text{ N}$ ,  $170^\circ \text{ E}$ ), both potential sites of future O-Buoy deployments, repeating the simulations

showed that five out of 17 circles overlapped with at least one measurement site, with no simulation iterations resulting in zero circle overlaps (Figure 3.13).

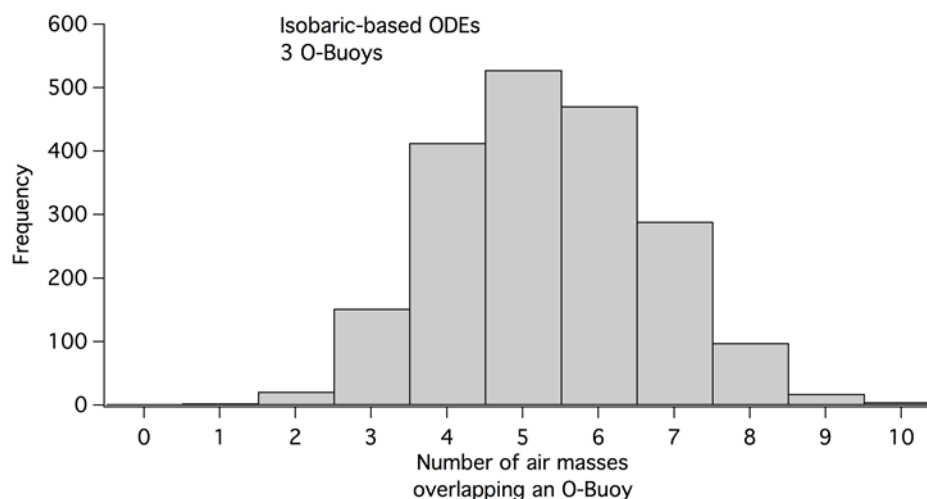


Figure 3.13 Results from Monte Carlo simulation experiment with three observation sites. Histogram shows the number of times a circular air mass overlapped with at least one observation site out of 2000 iterations.

This result emphasizes the need for multiple, simultaneous deployments of O-Buoys across different geographical regions to ensure that local scale chemistry is observed within one deployment season.

To examine if there is a consistent upwind region from which ODEs travel, wind rose plots were constructed for the ODEs observed by O-Buoy1 and O-Buoy2 in the Beaufort Sea, as shown in Figure 3.14.

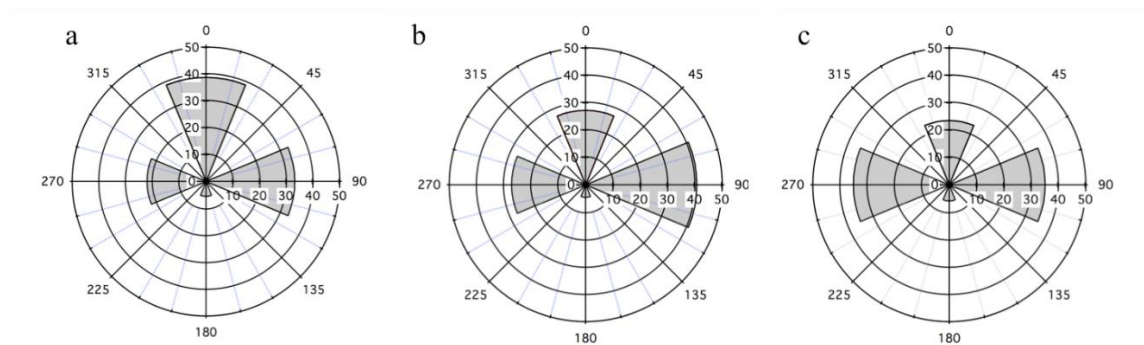


Figure 3.14 Wind rose plots based on the HYSPLIT backward air mass trajectories showing measured wind direction (degrees) and frequency (%), for a) ODEs, b) MODEs, and c) non-ODEs observed during the two O-Buoy Beaufort Sea deployments (see Figure 3.1 and Table 3.1).

As above, the O-Buoys deployed in the Beaufort Sea were chosen because of their similar locations and drift trajectories, providing the needed statistics for the analysis. During ODEs (Figure 3.14a), air masses most commonly traveled from the north (~39% of cases), followed by the east (~33% of cases) and the west (~22% of cases). For the MODE air masses, the trajectories most often originated from the eastern sector (~41% of cases; Figure 3.14b), and the northern and western sectors accounted for ~27% of cases each. Finally, for cases in which  $O_3$  was not depleted (non-ODE cases; Figure 3.14c), the eastern and western sectors each accounted for 35% of cases, and the north accounted for 24%. Only one event in each case showed an air mass originating from the south, toward the Alaskan and Canadian coasts. The results presented are consistent with a hypothesis that all regions that are sea-ice covered can support ODE chemistry. Notably, the region to the east of the buoys (i.e. from the Canadian archipelago and eastern Beaufort Sea) features sea ice that historically contains a high fraction of multi-year ice (Kwok et al., 2009), and GOME satellite imagery has previously shown large amounts of BrO to be

present in this region (Choi et al., 2012; Koo et al., 2012; Richter et al., 1998; Salawitch et al., 2010). Using backward air mass trajectories originating from the coastal sites of Alert, Canada, and Zeppelinfjellet, Svalbard, Bottenheim and Chan (2006) suggested that ODE air mass source regions could be in the East Siberian Sea, an area to the northwest of the O-Buoys that features first year ice that breaks up in spring. It should be noted, however, that Bottenheim and Chan (2006) only reported trends during the month of April, as opposed to this study that examined ODEs from as early as February to as late as June (Table 3.1 and Figure 3.2). Unfortunately, there were not enough events per month here to observe any clear monthly source region trends. Additionally, while the ODE and MODE cases show slight preferences for northern or eastern winds, respectively, the non-ODE cases do not appear to differ significantly from the ODE and MODE cases. As recently presented by Moore et al. (2014), it is also possible that O<sub>3</sub> recovers when air passes over open sea ice leads due to convective mixing, and air that passed over unbroken ice was more often O<sub>3</sub>-depleted, and thus local sea ice conditions and the overlying snowpack could have a more direct impact on O<sub>3</sub> levels than the wind direction.

### 3.3.3 Temperature and Wind Speed during ODEs

Figure 3.15 shows the distribution of average temperatures that applied during the ODEs in this study.

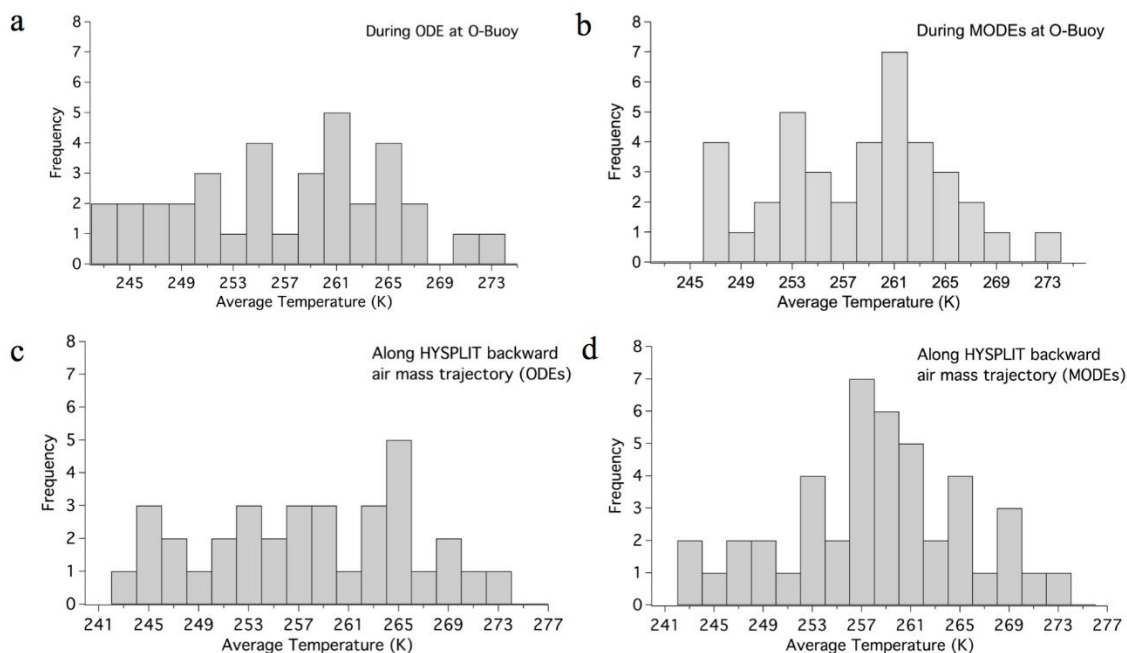


Figure 3.15 Histograms of the average ambient temperature measured by the O-Buoys during a) ODEs and b) MODEs. Histograms of the average temperature along the HYSPLIT backward air mass trajectories for c) ODEs and d) MODEs.

Local average temperatures during ODEs ranged between 243 K and 273 K (Figure 3.15a; median 257 K). The apparent mode of the distribution (261 K) is 8 K warmer than the hypothesized required upper limit temperature for rapid ozone depletion (253 K). Indeed, ~66% of the ODEs occurred at average temperatures greater than 253 K. An illustrative event is shown in Figure 3.2; the O-Buoy2 ODE occurring in early June shows a noticeable increase in BrO while temperatures average around 270 K. The temperatures for MODEs resulted in a similar distribution (Figure 3.15b). If, however, ODEs most often originate upwind from the site of O-Buoys, the local temperatures could be irrelevant, as the actual depletion chemistry may have taken place at a location where the temperature was much lower. To examine this, the isobaric HYSPLIT backward air mass trajectories were utilized

to estimate the average temperatures experienced by the observed air mass upwind. In Figure 3.15c and Figure 3.15d, we present histograms of the average temperatures from each air mass trajectory for both ODEs and MODEs, which were observed to be very similar (medians: ~258 K and 257 K for ODE and MODE, respectively) and not significantly different from those measured at the O-Buoys. As with the local observations, ~2/3 of the trajectory temperature averages were above 253 K, though we acknowledge that there is a high level of uncertainty associated with using an air mass back trajectory model for such a purpose in a data sparse region (Kahl, 1993). Additionally, we analyzed the minimum temperatures observed by the O-Buoy and from HYSPLIT trajectories during the same depletion periods. The median minimum temperatures observed at the O-Buoy are 251 K and 253 K for the ODE and MODE cases, respectively. Similarly, the median minimum temperatures obtained from HYSPLIT trajectories are 250 K and 254 K for the ODE and MODE cases, respectively. In both cases, it is interesting that only about half of the events were observed with minimum temperatures less than the eutectic temperature of NaCl (252 K), consistent with the results above. This analysis reveals no apparent temperature threshold for O<sub>3</sub> depletion, and shows that temperatures below 253 K were not necessary to observe ozone-depleted air masses, corroborating the conclusions of Bottenheim et al. (2009) and Jacobi et al. (2010).

Recent reports discuss the possibility that ODEs can be initiated after blowing snow events (Frieß et al., 2011; Jones et al., 2009; Yang et al., 2008, 2010), which presumably produce the availability of new saline surfaces, whether in suspended aerosol form, or through redeposition of sea salt aerosol to the physical surface. Blowing snow events occur during periods of higher wind speeds ( $> 8 \text{ m s}^{-1}$ ) (Frieß et al., 2011), implying that there

might be a relationship between wind speed and ODEs. We thus performed an analysis for wind speeds analogous to the temperatures using both local O-Buoy data and HYSPLIT backward trajectories. Figure 3.16 shows that ODEs observed at the O-Buoy were characterized by low measured wind speeds (median of  $3.6 \text{ m s}^{-1}$  and a mode of  $3.5 \text{ m s}^{-1}$ ), relative to what is needed for blowing snow.

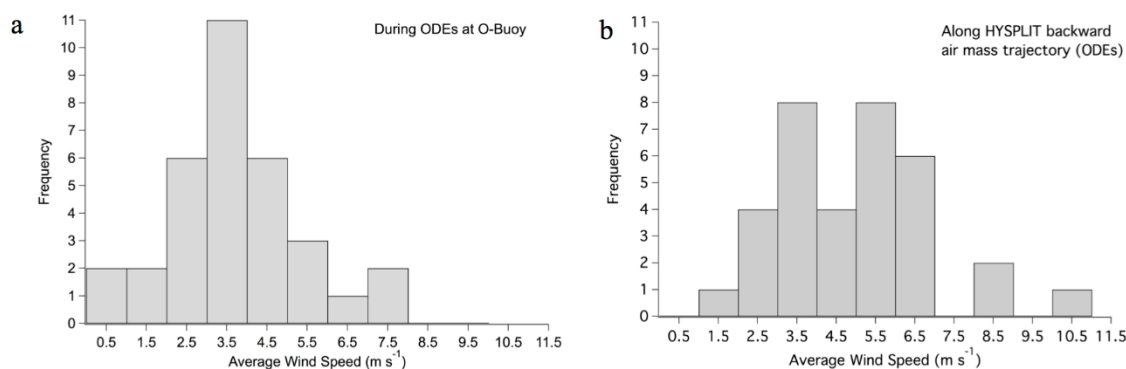


Figure 3.16 a) Histogram of the average wind speed measured by the O-Buoys during ODEs. b) Histogram of average wind speeds from  $\text{O}_3$ -depleted air masses, as determined from the HYSPLIT backward air mass trajectories.

However, there is also a difficulty in this analysis in that, under these circumstances, when the air is most of the time at least partly depleted, such a histogram may reflect, at least in part, the normal distribution of wind speeds found in the Arctic troposphere. Therefore, for comparison, periods when  $\text{O}_3$  was not depleted (non-ODEs) were examined. As shown in Figure 3.17, there was no apparent difference in the modes for non-ODEs relative to the depleted cases.



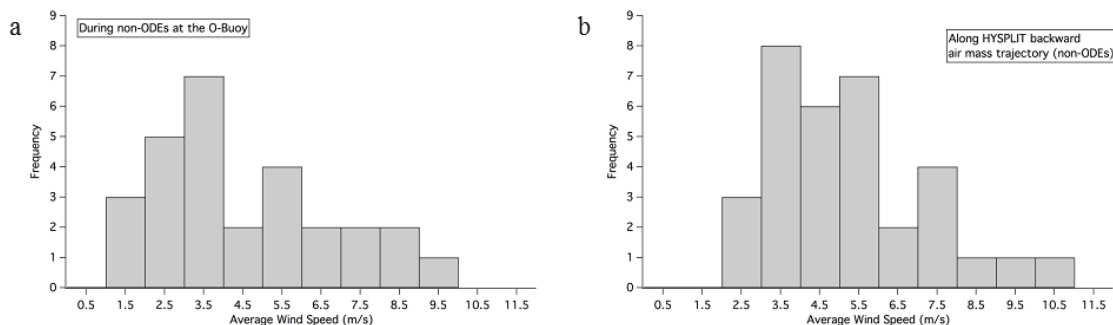


Figure 3.17 a) Histogram of the average wind speed measured by the O-Buoys during non-ODEs. b) Histogram of average wind speeds from non-ODEs, as determined from the HYSPLIT backward air mass trajectory.

We reiterate that the O-Buoy wind speed measurements reported here could be biased low (see Sect. 3.2.1); thus, we compare this distribution to one determined by the HYSPLIT method below.

The distribution of average wind speeds along the HYSPLIT trajectories (Figure 3.16b) reveals a faster median wind speed of  $4.9 \text{ m s}^{-1}$ , potentially consistent with ODEs occurring at somewhat higher wind speeds. However, the distribution showed no clear preference for higher wind speeds for ODEs. During non-ODE periods (Figure 3.17), we found the majority of wind speeds to be between  $3$  and  $6 \text{ m s}^{-1}$ , similar to that for the ODE cases, showing that the wind speeds characterizing the upwind air masses observed for ODEs are not different from those for non-depleted conditions. From this analysis, we found that elevated wind speed appeared to be neither a prerequisite, nor a defining characteristic for ODEs, as also found by Helmig et al. (2012) and Solberg et al. (1996).

### 3.4 Conclusions

The O-Buoy was developed in part to enable the observation of ODEs at the hypothesized location of their initiation, the frozen Arctic Ocean surface. Surface measurements of ambient O<sub>3</sub>, BrO, temperature, and wind speed from five separate O-Buoy deployments were utilized to gain insights into the characteristics of ODEs observed over the Arctic Ocean.

The apparent timescales of O<sub>3</sub> depletion during ODEs, based on both CM and TM, were calculated to be shorter (median of 11 hours) than previous modeled chemical estimates (e.g., Hausmann and Platt, 1994) by a factor of two or more. This observation suggests the O<sub>3</sub> depletion timescales are dominated by TM, accelerated chemical mechanisms involving higher radical levels, or novel chemical mechanisms. Given recent observations of up to 5 pmol mol<sup>-1</sup> of I<sub>2</sub> within coastal Arctic snowpacks, chemical modeling of O-Buoy data will be able to more thoroughly interrogate whether chemistry can account for the ODE kinetics.

If TM are assumed to dominate local observations, spatially, the majority of the Arctic Ocean marine boundary layer is likely at least partially depleted in O<sub>3</sub> during spring, suggesting that O<sub>3</sub>-depleted air masses remain intact for long periods of time after halogen chemistry has subsided. Regions of MODEs (O<sub>3</sub> < 10 nmol mol<sup>-1</sup>) were, on average, smaller, with a median of 282 km, compared to a median of 877 km for ODEs (O<sub>3</sub> ≤ 15 nmol mol<sup>-1</sup>). An expanded network of O<sub>3</sub> monitors across the Arctic Ocean is required to effectively capture the spatial extent of the small, actively O<sub>3</sub>-depleting air masses, as well as that of the larger, depleted air masses. Monte Carlo simulations supported the possibility that these spatial ODE sizes are consistent with depletion upwind of the O-Buoy, followed

by air mass transport to the buoy. However, the degree to which process dominates local observations of ODEs (TM vs. CM) is unknown, as O-Buoy observations of BrO indicate that there is generally always some degree of chemistry involved. Thus, to further address the question of the O<sub>3</sub> depletion timescales, more long-term O<sub>3</sub> and halogen measurements over the Arctic Ocean sea ice are necessary, particularly in locations such as the East Siberian and Chukchi Seas.

There was no apparent temperature dependence observed for the presence of an ODE, and low temperatures (i.e. less than 253 K) were not required for the observation of an ODE. The distribution of wind speeds local to the O-Buoy was moderately low during ODEs (mode of  $\sim 3.5 \text{ m s}^{-1}$ ), showing that ODEs were primarily observed under relatively calm conditions. While higher average wind speeds (median  $\sim 5 \text{ m s}^{-1}$ ) were estimated for the course of the backward air mass trajectory, we did not observe a clear preference for ODEs occurring during higher wind speeds. Concurrent measurements of blowing snow, sea salt aerosol, ozone, and halogens, in addition to wind speed, are required to better understand the relationship between wind speed and ODEs.

CHAPTER 4. AIR MASS HISTORIES AND METEOROLOGY DURING PERIODS  
OF OZONE DEPLETION EVENTS FROM ARCTIC OCEAN-BASED  
MEASUREMENTS

4.1 Introduction

The rise of the springtime sun in polar regions causes the rapid and episodic depletion of boundary layer O<sub>3</sub> concentrations (Anlauf et al., 1994; Barrie et al., 1988; Bottenheim et al., 1986). These so-called ozone depletion events (ODEs) cause shifts in regional tropospheric oxidation pathways for pollutants, such as hydrocarbons, that must be driven by species other than OH radicals, particularly Cl and Br atoms (Cavender et al., 2008; Jobson et al., 1994). The chemistry underlying this phenomenon is believed to be driven by halogen radicals (i.e., X = Br, I, and Cl), as shown below (R4.1-2).

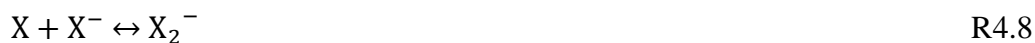


Molecular halogens (X<sub>2</sub>) are believed to enter the Arctic atmosphere through the oxidation of halide ions within acidic brines or brine-like layers (quasi brine layer, QBL) that exists on the surfaces of surface-level snowpacks and aerosol

(Barrie et al., 1994a; Custard et al., 2016; Fan and Jacob, 1992; Michalowski et al., 2000; Pratt et al., 2013; Raso et al., 2016; Roberts et al., 2008; Tang and McConnell, 1996; Vogt et al., 1996, 1999). This chemistry is detailed more thoroughly in Chapter 5, though the relevant reactions are presented below. It is hypothesized that during polar sunrise, the flux of photons into the snowpack photolyzes hydrogen peroxide and nitrite within snow grains to produce hydroxyl radicals, as in Reactions 4.3-4.5 (Chu and Anastasio, 2003, 2005; France et al., 2012).



The OH radicals formed from these reactions react with halides, which ultimately form molecular halogens (R.4.6-4.10; Raso et al., 2016).



In addition, heterogeneous processes can allow for the exponential buildup of halogens in the atmosphere through a series of reactions known as the “halogen explosion.”



In this series of reactions one gas phase X atom (in the form of HOX) enters the QBL / brine, while two are ejected back into the atmosphere.

ODEs have been believed to require a source of bromine atoms, sunlight (R4.1), surfaces (e.g., frozen saline surfaces like snow or ice, or sea salt aerosol) that promote halogen recycling (i.e., the halogen explosion), low temperatures (e.g.,  $< -20^\circ\text{C}$ ) (Tarasick and Bottenheim, 2002), and a stably stratified boundary layer (Anderson and Neff, 2008; Anlauf et al., 1994; Bottenheim et al., 2002b; Jacobi et al., 2010; Lehrer et al., 2004). While bromine atoms are critical to  $\text{O}_3$  depletion, recent modeling and field results indicate that low levels of iodine could possibly be contributing significantly to this ODE chemistry (Calvert and Lindberg, 2004; Raso et al., 2016; Saiz-Lopez et al., 2007; Thompson et al., 2015; Vogt et al., 1999). With regard to low temperatures, multiple laboratory studies have found efficient production of  $\text{Br}_2$  when frozen halide surfaces are exposed to HOBr at temperatures below  $-20^\circ\text{C}$  via R-4.12 - 4.14 (Adams et al., 2002; Huff and Abbatt, 2002). Because the eutectic point of  $\text{NaCl}\cdot 2\text{H}_2\text{O}$  is  $-21^\circ\text{C}$ , it is expected that the  $\text{Cl}^-$  reservoir from

the quasi-brine layer (QBL) that exists on frozen surfaces is depleted by precipitation. To maintain the presence of a QBL, freezing point depression dictates that the liquid volume of the QBL must decrease, thereby increasing the concentration of the remaining ions in solution (i.e., enhancing available surface  $\text{Br}^-$ ) (Koop et al., 2000) and enhancing atmospheric interactions. Recent studies, however, note that low temperatures are not required for the observation of  $\text{O}_3$ -depleted air (e.g., Bottenheim et al., 2009; Halfacre et al., 2014; Koo et al., 2012). It has recently been proposed that it is not the actual temperature that affects  $\text{O}_3$  as much as the variation in temperature (Koo et al., 2012). This would be consistent with studies observe recoveries in  $\text{O}_3$  associated with rising temperatures (e.g., Bottenheim et al., 2009) and depletions in  $\text{O}_3$  associated with decreasing temperatures (e.g., Zeng et al., 2003). However, this, in combination with changes in pressure, suggest changes in air mass flow and possibly indicate  $\text{O}_3$  changes are the results of air masses with differing  $\text{O}_3$  mole fractions and temperatures (Jacobi et al., 2010). Finally, stable boundary layers are characterized by temperature inversions, which can be characterized when temperature increases with height in the boundary layer (Stull, 1988) (Figure 4.1). In these cases, cooler, denser air is found closer to the surface and vertical transportation of air is inhibited, thereby limiting  $\text{O}_3$  depleted air masses to the surface.

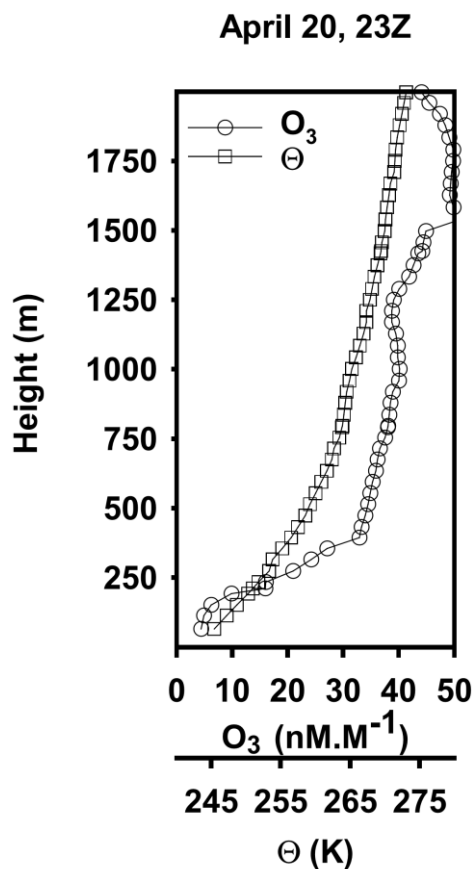


Figure 4.1 Example of low ozone mole fraction during a temperature inversion (noted by increasing potential temperature with height) at Alert, NU (Figure 4.2). Figure reproduced from Bottenheim et al. (2002).

There exists a large body of evidence to suggest ODE chemistry occurs predominantly over the frozen Arctic Ocean (and coastal Antarctic Southern Ocean). The earliest extensive field studies of this chemistry, occurring at the coast of Alert, NU, Canada (see Figure 4.2), found correlations between low O<sub>3</sub> concentrations and wind directions arriving from the north and northeast (Anlauf et al., 1994; Barrie et al., 1988; Bottenheim et al., 1990).



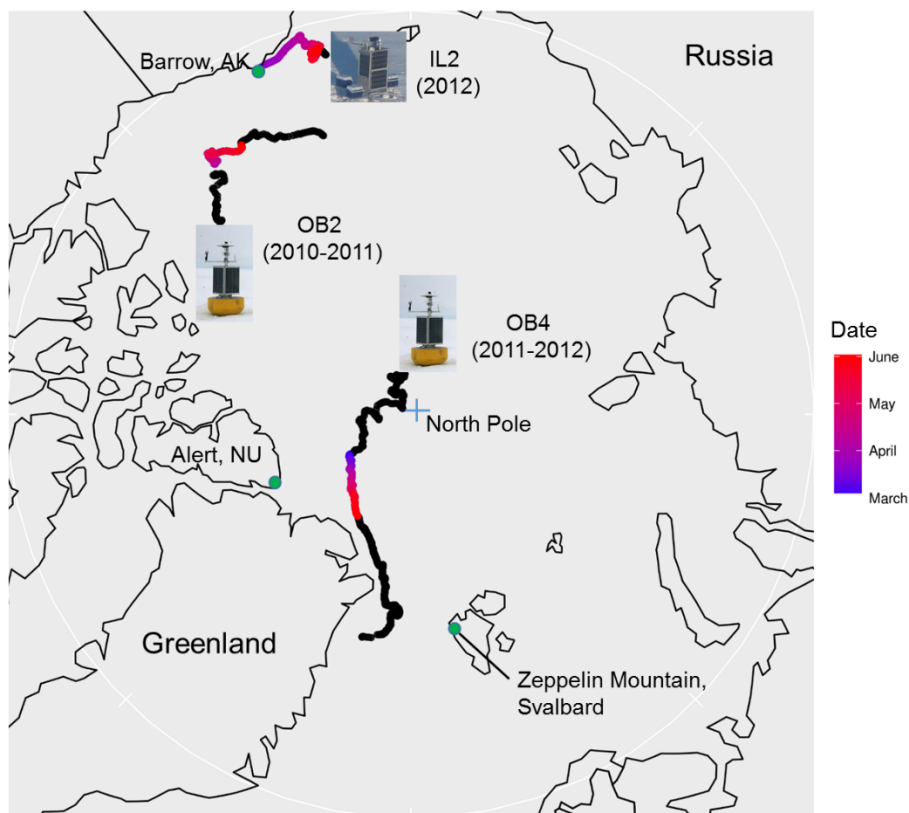


Figure 4.2 Map of O-Buoy drift tracks relevant to this study. O-Buoy 2 (OB2) was deployed in and drifted around the Beaufort Sea. O-Buoy 4 (OB4) was deployed near the North Pole, and drifted south through the Fram Strait. Icelander 2 (IL2) was installed on an ice floe to the west of Barrow, AK.

These are directions associated with the Arctic Ocean. In addition, an 18-day study on an ice floe 160 km northwest of Alert found no clear trends in wind direction and ODEs, but found that  $O_3$  depletion remained below limits of detection for longer periods of time than concurrent measurements at Alert (Hopper et al., 1994). Early reports from Barrow, AK, did not show such a clear relationship; while higher  $O_3$  values at Alert were associated with free troposphere air mixed down to the surface by winds blowing over the nearby surrounding rough and elevated terrain, the area surrounding Barrow is relatively flat.

Oltmans et al. (1989) found that while ODEs were not associated with southerly winds at Barrow (i.e., winds traveling over land), southerly winds are generally infrequent during the Arctic spring along Alaska's north slope region. Since these initial reports, a number of studies have utilized backward air mass trajectory modeling to further investigate the relationship between ODEs and their potential origin over the Arctic Ocean. Concerning coastal sites, Solberg et al. (1996) found that ODEs at Zeppelin Mountain were most frequent when air traveled over the Arctic Ocean before arriving at the observation site. Simpson et al. (2007a) and Peterson et al. (2016b) both found that air masses with enhanced BrO concentrations arriving at Barrow exhibited some previous correlation with sea ice contact ( $R = 0.74$  and  $0.39$ , respectively). In the most extensive ODE backward trajectory study to date, Bottenheim and Chan (2006) modeled air masses based on nine years of April coastal  $O_3$  data from Alert, NU, Canada; Zeppelin Mountain, Svalbard; and Barrow, AK (Figure 4.3).

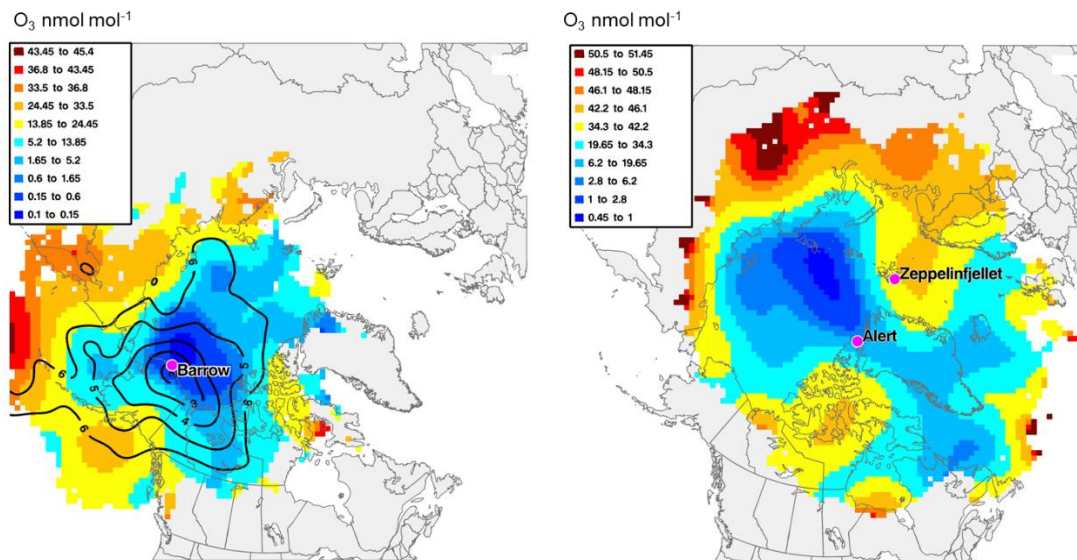


Figure 4.3 Results from the backward air mass analysis by Bottenheim and Chan (2006). Cool colors represent lower O<sub>3</sub> concentrations, while hotter colors represent higher O<sub>3</sub> concentrations. Figure reproduced from Bottenheim and Chan (2006).

It is clearly seen in each case that the lowest O<sub>3</sub> values originate from air masses that spent time over the Arctic Ocean. Low O<sub>3</sub>-containing air masses arriving at the Barrow site most often arrived within 1 day's travel upwind, while similarly depleted air arriving at Mount Zeppelin and Alert were from several days upwind, with the most depleted air traveling over the East Siberian Sea. In addition, several backward trajectory analyses have been conducted for ship-based observations, but no common ODE "source" region has been identified beyond those areas covered by sea ice (Bottenheim et al., 2009; Gilman et al., 2010; Jacobi et al., 2006). In addition, high levels of BrO have been observed over the Arctic Ocean by satellite observations (Richter et al., 1998; Theys et al., 2009, 2011).

There exist several different surface types in the Arctic region. First year ice (FYI) is newly formed ice over the Arctic winter. Because it is formed directly from ocean water,

FYI is characterized as being highly saline and is thought to act as a large reservoir of halogens to the atmosphere. Multi-year ice (MYI) is ice that has existed for more than one year and survived the summer melt season. Because it has already interacted with the atmosphere, MYI is typically not as saline as FYI. However, areas predominantly covered by MYI have been associated with sustained ODEs (Bottenheim et al., 2009; Jacobi et al., 2010), while ODEs over or near regions dominated by FYI or mixed ice types (including coastal sites) appear to be more intermittent (e.g., Halfacre et al., 2014). Open water is believed to be a source of sea salt aerosols, which are thought to contribute to ODEs by supplying additional sources of halides and reactive surfaces to the Arctic atmosphere (Michalowski et al., 2000; Simpson et al., 2005). Alternatively, cracks in the sea ice, called leads (Figure 4.4), have been recently linked with the recovery of O<sub>3</sub> levels by inducing turbulent vertical mixing (Moore et al., 2014). This mixing occurs because of the large temperature gradient that exists between open water (typically around -1.8°C) and the overlying atmosphere (temperatures ranging from -40°C to -10°C until late May, when ODEs begin to cease). Finally, ODEs have also been observed over land (e.g., Peterson et al., 2016a), and halogen explosions have been observed within snowpacks atop the frozen tundra (e.g., Pratt et al., 2013). However, inland sites are not generally considered to be associated with ODE conditions, as they are less influenced by air of marine origin, and can be more influenced by O<sub>3</sub> rich air masses from southern latitudes, partially as a result of increased mechanical turbulence (Helmig et al., 2012).



Figure 4.4 Example of an open lead. Leads are cracks in sea ice that form as stress relief. Photo courtesy Alek Petty (NASA Goddard Space Flight Center / University of Maryland)..

In this study, we utilize the unique, long-term Arctic Ocean dataset provided by O-Buoys (see Chapters 2, 3; Halfacre et al., 2014; Knepp et al., 2010) to expand on the above work to further clarify a) what external variables (i.e., air mass history, local meteorological parameters, underlying surface type) contribute to ozone variability, and b) whether a specific source region conducive to ODE chemistry region can be located from “in situ” Arctic Ocean observations.

## 4.2 Methods

### 4.2.1 Instrumentation

In situ surface O<sub>3</sub> and meteorology measurements were obtained by O-Buoys. For a detailed description, see Chapter 2, 3, and Knepp et al. (2010). Briefly, O<sub>3</sub> was detected using a custom 2B Technologies 205 dual beam O<sub>3</sub> monitor. This instrument operates on the principal of ultraviolet light absorption at 254 nm, based on the wavelength of maximum absorption of O<sub>3</sub> (Molina and Molina, 1986). Meteorological sensors include a wind monitor for wind speed and direction, (RM Young Model 05103-45) a temperature/relative humidity probe (Vaisala HMP155A), and a barometer (Vaisala PTB110). We note that the wind monitor propeller was susceptible to icing, calling into question its accuracy at low wind speeds (Halfacre et al., 2014; Knepp et al., 2010). All wind data with recorded values of 0 m/s were removed from analysis. Radiation data (relative to the maximum value observed within a buoy's deployment) used herein originate from inverted O-Buoy MAX-DOAS observations of radiative intensity at 360 nm (see Chapter 3 for a description of the inversion procedure). In addition, data will be used from an O-Buoy derivative, called "Icelanders," that were active during the 2012 BRomine, Ozone and Mercury EXperiment at Barrow, AK (Nghiem et al., 2013). Icelanders utilize the same instrumentation as O-Buoys, but were designed to lay atop sea ice (opposed to being installed within the ice itself).

O-Buoys utilized in this analysis include O-Buoys 2 and 4. O-Buoy 2 was deployed in multi-year ice in the Beaufort Sea (77°N, 135°W) on 8 October 2010, and drifted around the Beaufort Gyre (circular, wind-driven ocean current in the Beaufort Sea) until it ceased

transmission on 22 July 2011. O-Buoy 4 was deployed near the North Pole (88°N, 157°W) and drifted south until its ultimate recovery on 25 August 2012 (drift tracks in Figure 4.2). Icelander 2 was installed atop sea ice west of Barrow, AK (71°N, 156°W), and drifted westward until it ceased transmission on 12 June 2012.

#### 4.2.2 Air Mass Trajectory Analysis

The NOAA HYSPLIT air mass trajectory model (Draxler et al., 2012; Draxler and Hess, 1998; Draxler and Rolph, 2003) was utilized to examine backward trajectories throughout each of these measurement campaigns. Starting from the time the Arctic Ocean O<sub>3</sub> sampling frequency was switched to 24-hours, 24-hour backward trajectories were calculated for each hour until June 1. In each trajectory, 10,000 hypothetical particles were released and tracked backward in time for 24 hours according to 1° resolution meteorological fields derived from the National Centers for Environmental Prediction Global Data Assimilation System modeling. The average spatial particle concentrations during these times were obtained for 0.25° (i.e.~30km) x 0.25° x 50 m (height) box sizes. A height of 50 m was chosen as the top of the model to represent air that interacts with the surface. Additionally, the particle concentrations were converted to number of particles by multiplying by volume (0.25° x 0.25° x 50 m) for statistical analyses (Section 4.3.2).

#### 4.2.3 Satellite Surface Type Observations

Two different satellite surface products were used herein. Daily sea ice coverage and type were assessed using the scatterometer installed on the Oceansat-2 satellite (Nghiem et al., 2012b). Its principal of operation is scatterometry, in which the

scatterometer transmits electromagnetic radiation (frequency of 13.4 GHz) to the surface, and measures the radiation scattered back from the snow and ice below (backscatter). The energy of these waves are functions of the electrical properties and roughness of the surface from which the scattering took place, and can be directly related to the type of surface on which the scattering occurred based on the polarization of the beam and the incidence angle (Ezraty and Cavanié, 1999). In the case of Oceansat-2, these surfaces include land, open water, first year ice (FYI), multi-year ice (MYI), and mixed ice types at a 2-dimensional resolution of  $0.25^\circ \times 0.25^\circ$ .

Arctic Ocean snow depth and coverage was also assessed daily using a data product based on observation from the passive microwave sensors: Scanning Multichannel Microwave Radiometer (SMMR) and Special Sensor Microwave/Imager (SSM/I). In contrast to the active scatterometry instruments used with Oceansat-2, the SMMR and SSM/I instruments detect microwave radiation directly emitted from snow and ice and operate over several frequencies. Snow and sea ice are distinguished on the basis of snow emissivity. In fact, snow depth can only be estimated over FYI because the microwave signature between snow and MYI is too similar for unambiguous separation (Comiso et al., 2003). The available surface characteristics include snow depth (0-100 cm), land, open water, multi-year ice, and grids where some summer snow melt is observed. Given the coarseness of the data and the heterogeneity of snow depth (e.g., Webster et al., 2014), the snow depths were divided into three classes for this analysis: shallow snow depth (1-9 cm), moderate snow depth (10-17 cm), and deep snow depth (18 – 100 cm). Data were obtained from the NASA Goddard Cryospheric Sciences website in 25 km polar stereographic grids (<http://neptune.gsfc.nasa.gov/csb/index.php?section=53>).



The HYSPLIT results were spatially and temporally matched with the satellite retrievals. Temporally, this was done by matching the date of the trajectory start time with the date of the satellite retrieval. The Oceansat-2 grids, obtained at  $0.25^\circ$  resolution, were matched directly with the HYSPLIT output. Conversely, the snow depth data were re-gridded to  $0.25^\circ \times 0.25^\circ$  grids by matching a snow depth datum to the nearest corresponding location on this new grid. If, however, a grid cell was greater than 30 km from the nearest snow depth known location, the grid was considered to have missing data.

To relate the satellite observations with the HYSPLIT results, the number of particles over each type of surface were summed for each individual trajectory. In this way, a time series of the surface composition seen by an air mass before arriving at the observation site can be assessed statistically. This can be seen in Figure 4.5 - Figure 4.7 based on the satellite sea ice retrievals.

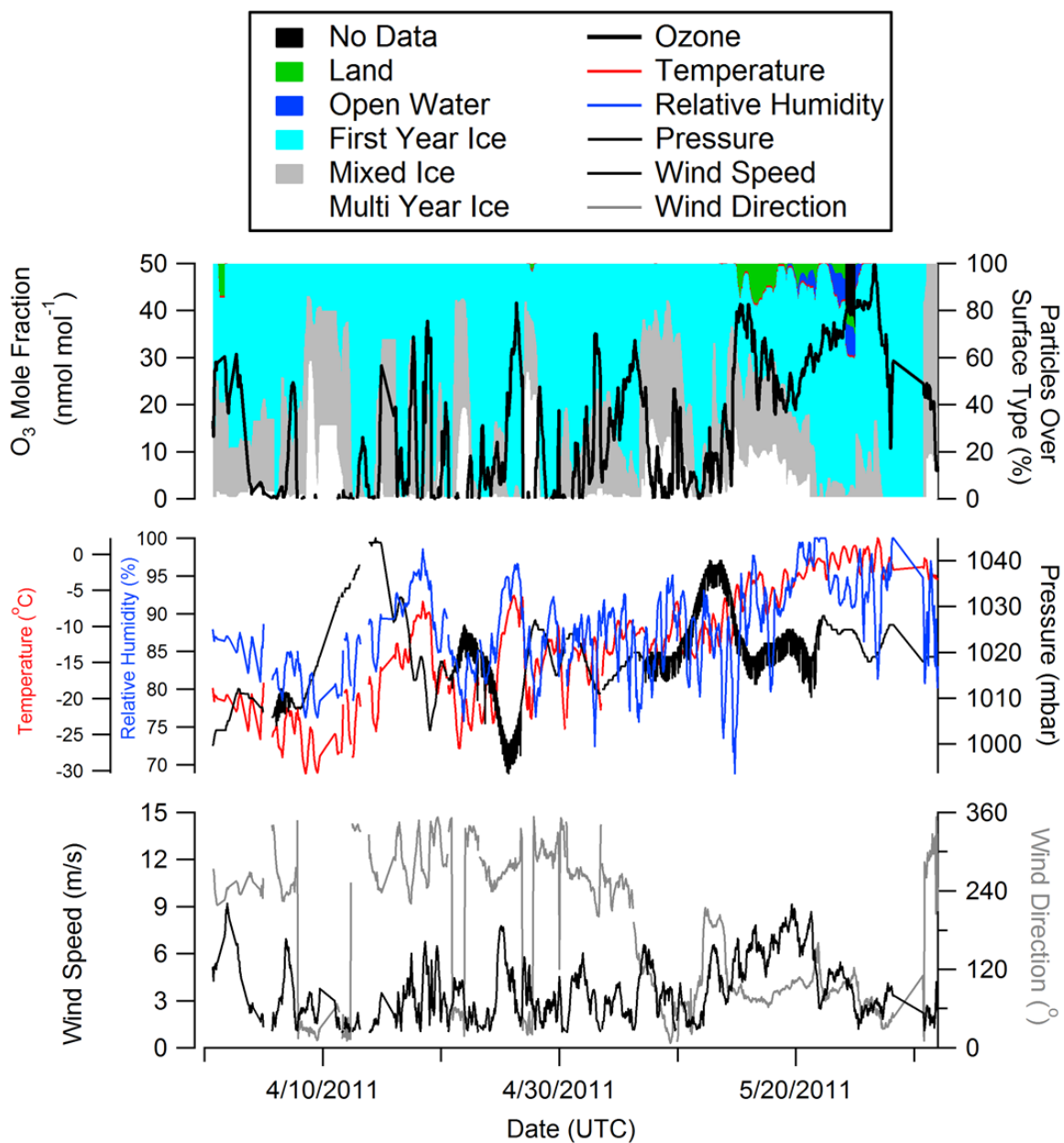


Figure 4.5 Time series of O-Buoy2 observations and HYSPLIT results. Top –  $O_3$  mole fractions plotted over the particle distribution as determined by HYSPLIT and Oceansat-2 satellite imagery. Middle – Temperature (red trace), relative humidity (blue trace), and atmospheric pressure as observed by O-Buoy 2. Bottom – Wind speed (black trace) and wind direction (gray trace) as observed by O-Buoy 2.

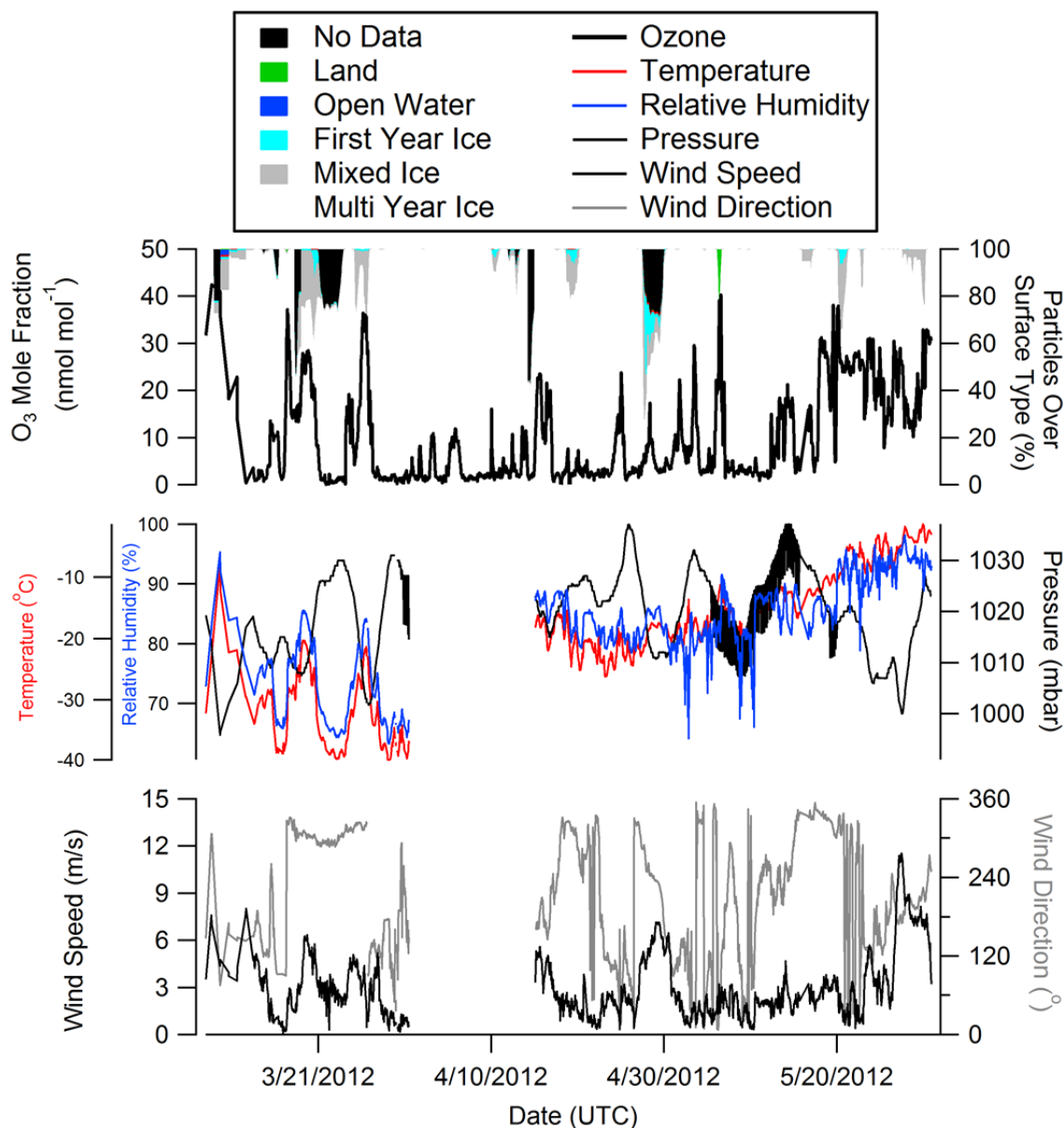


Figure 4.6 Time series of O-Buoy4 observations and HYSPLIT results. Top –  $O_3$  mole fractions plotted over the particle distribution as determined by HYSPLIT and Oceansat-2 satellite imagery. Middle – Temperature (red trace), relative humidity (blue trace), and atmospheric pressure as observed by O-Buoy 4. Bottom – Wind speed (black trace) and wind direction (gray trace) as observed by O-Buoy 4.

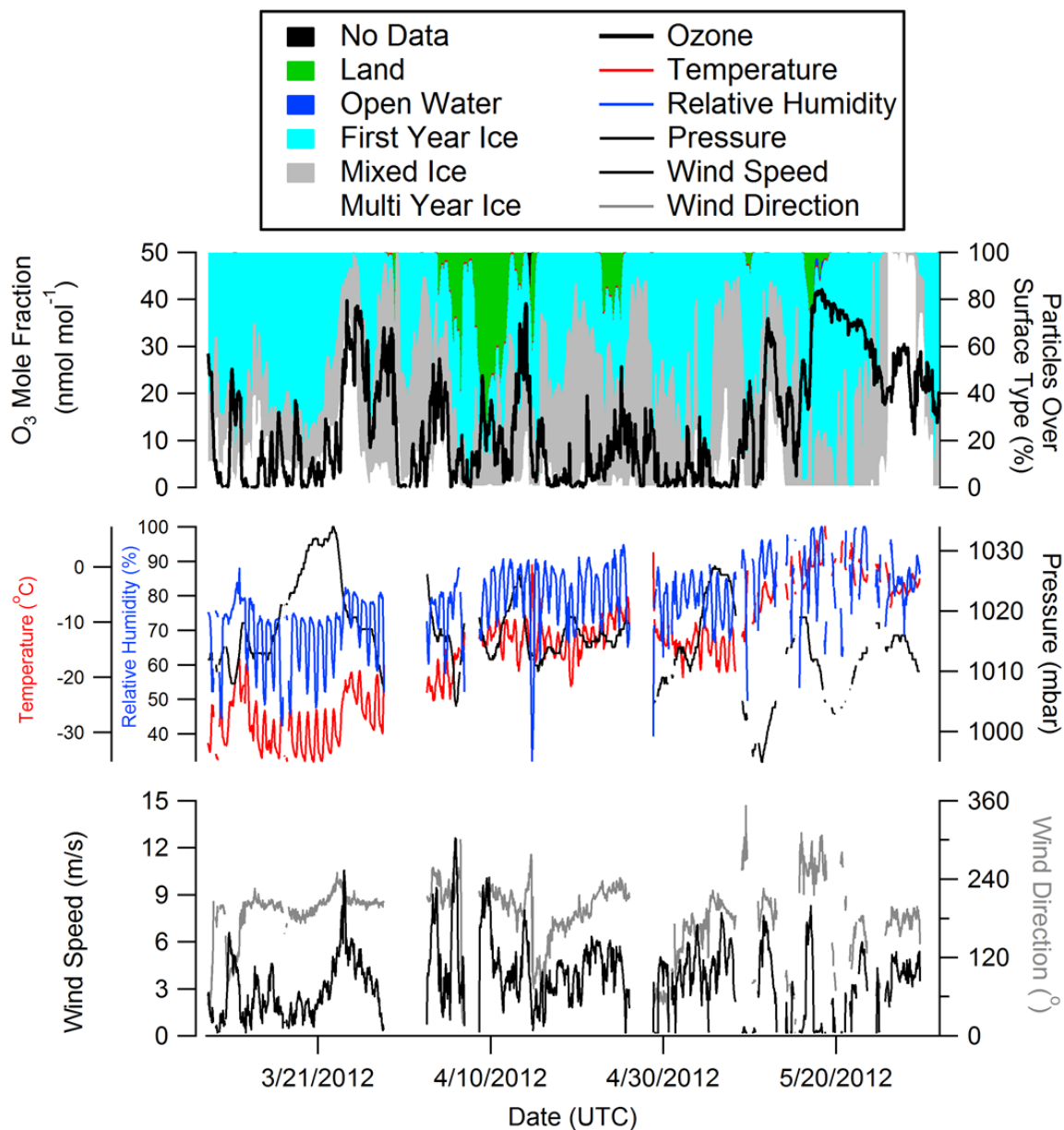


Figure 4.7 Time series of Icelander 2 observations and HYSPLIT results. Top – O<sub>3</sub> mole fractions plotted over the particle distribution as determined by HYSPLIT and Oceansat-2 satellite imagery. Middle – Temperature (red trace), relative humidity (blue trace), and atmospheric pressure as observed by Icelander 2. Bottom – Wind speed (black trace) and wind direction (gray trace) as observed by Icelander 2.

### 4.3 Results

#### 4.3.1 Air Mass History and Surface Composition

Figure 4.5-Figure 4.7 present time series observations of  $O_3$  and the types of surfaces (as observed by Oceansat-2) in contact with air masses 24 hours before arriving at the observation sites. Starting first with O-Buoy 2 results (Figure 4.5), it is clear that air travels across a heterogeneous mixture of FYI and MYI, though some amount of FYI exposure is present across all measurements. This is not unexpected, as the Beaufort Sea is known for having a large amount of seasonal ice (Melling et al., 2005) with decreasing amounts of MYI (Krishfield et al., 2014). Interestingly, there appears to exist some amount of general anti-correlation between  $O_3$  concentrations (black trace) and multi-year ice exposure (white) prior to 15 April. For instance, before 10 April, the initial  $O_3$  decrease is met with increasing exposure to MYI and mixed ice, while the brief rise in  $O_3$  concentrations on 7 April can be characterized by a decrease in relative mixed ice / MYI exposure. Later in the season, beginning on 15 May, there is substantial  $O_3$  recovery that occurs in concert with an increasing fraction of air exposure to land, and later water (20 May). This would seem to be consistent with previous observations of convective mixing events that inject  $O_3$ -rich free tropospheric air into the boundary layer. Such events have been observed over open leads (Moore et al., 2014; Peterson et al., 2016b) and land (Strong et al., 2002). However, this relationship is not consistent throughout the time series. For instance, sudden  $O_3$  recoveries occur during 14 April, 17 April, and 18 April, at times when exposure to mixed ice types is increasing. In addition, the increase in land and water exposure in May seems to be associated with increasing  $O_3$  despite the majority of particles

originating over sea ice. It is possible these “recovery events” are also associated with downward mixing that injects greater concentrations of O<sub>3</sub> from the free troposphere into the boundary layer. If this is indeed the case, it is clear that O<sub>3</sub> levels cannot be explained by air mass history alone and will require additional consideration of the local meteorology observed by O-Buoys, discussed below.

At O-Buoy4, air travels over predominantly MYI before arriving at the O-Buoy, and some of the O<sub>3</sub> variability is temporally coincident with more heterogeneity in the surface composition (Figure 4.4). If air mass exposure to MYI is more indicative of O<sub>3</sub>-depletion chemistry than other surface types, one might expect O<sub>3</sub> levels to be generally lower for O-Buoy 4 than O-Buoy 2. Indeed, 86% of the O-Buoy 4 O<sub>3</sub> observations in April were less than 10 nmol mol<sup>-1</sup>, opposed to 70% of observations from O-Buoy 2 (Figure 4.8).

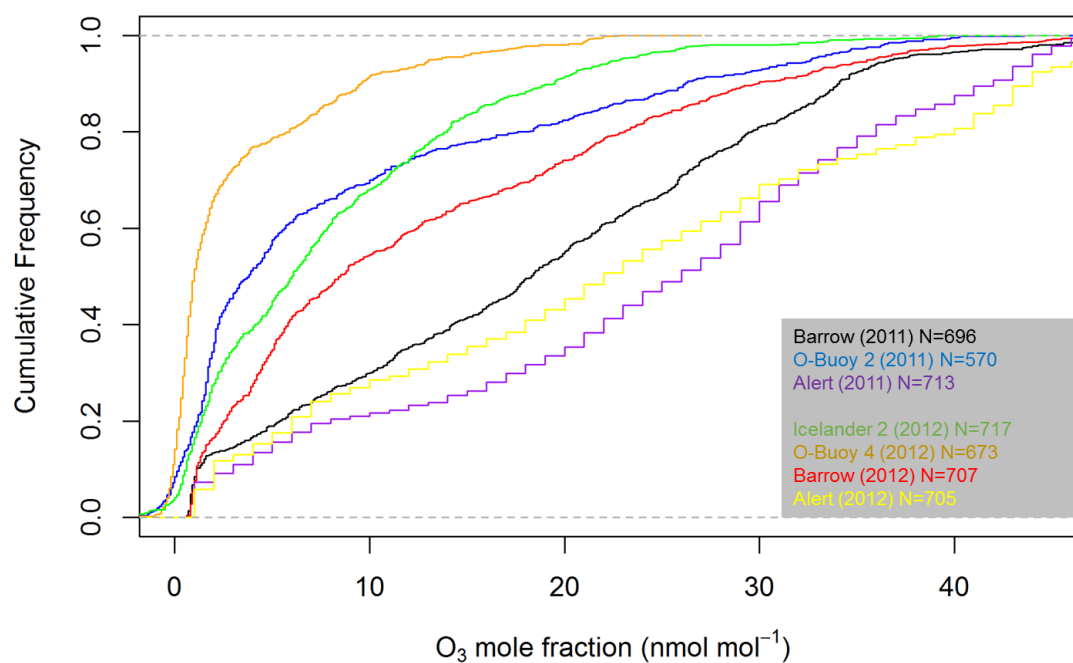


Figure 4.8 Cumulative frequencies of ozone concentrations from both coastal sites (Alert and Barrow) and Arctic Ocean sites (O-Buoy 2 and 4, Iceland 2) during April. Data from Alert courtesy Jan Bottenheim, data from Barrow, AK, courtesy Sam Oltmans (NOAA).

Plots of exposure to different ice types against O<sub>3</sub> mole fractions reveal that this relationship is not straightforward (Figure 4.9), as both low and high ozone values are observed for varying amounts of exposure to each ice type. If, however, ODEs can be observed over any ice surface (presumably because of saline snow coverage), and because these observation sites are obviously surrounded by ice, ice coverage could be negligible as an ODE predictor at observation sites over the Arctic Ocean.

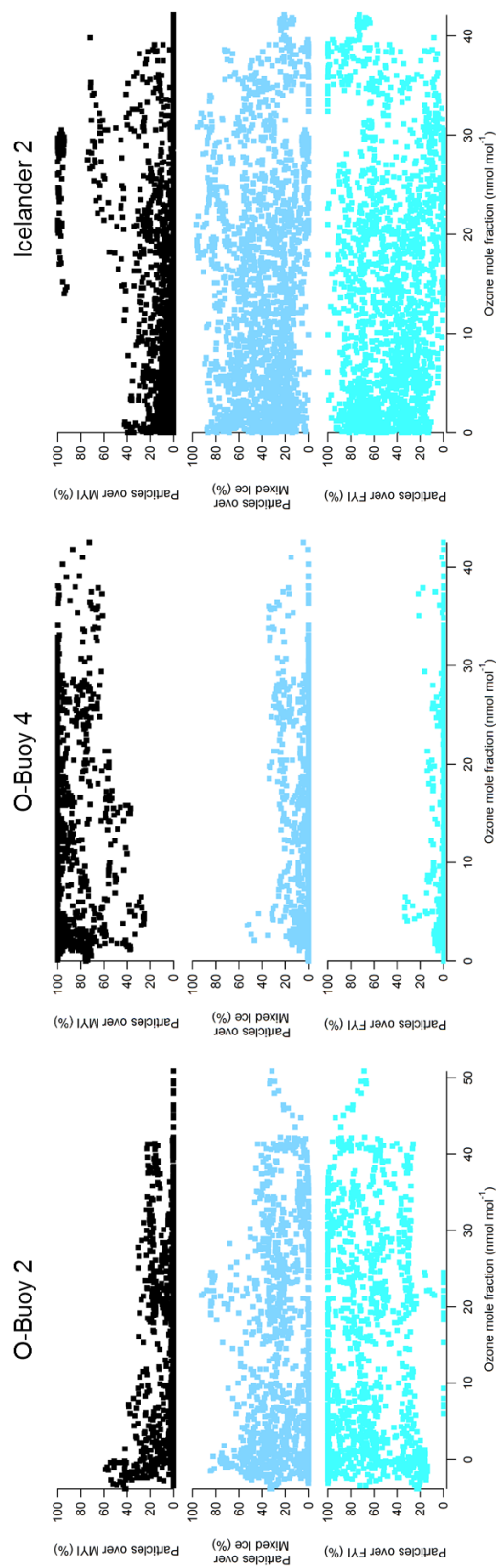


Figure 4.9 Scatter plots of particles over a surface type (y-axes) against  $O_3$  levels for O-Buoy 2 (left; 1 April – 1 June 2011), O-Buoy 4 (middle; 4 March – 1 June, 2012), and Iceland 2 (right; 8 March – 1 June, 2012).



The results from the Icelander appear to be more complicated than the O-Buoys (Figure 4.7). In this case, increasing FYI exposure would appear to yield lower O<sub>3</sub>, while MYI and mixed ice types appear to correspond to greater amounts of O<sub>3</sub>. In addition, exposure to land masses appeared to greatly affect O<sub>3</sub> variability observed by O-Buoys, while increases in O<sub>3</sub> at the Icelander would appear to be influenced less by land. However, O<sub>3</sub> is found below 10 nmol mol<sup>-1</sup> for only 68% of observations during April (Figure 4.8). Analyzing the sea ice type against O<sub>3</sub> mole fractions (Figure 4.9) displays no obvious trends.

#### 4.3.2 Explaining O<sub>3</sub> Variability

A series of basic statistical methods were employed to investigate what variables affect O<sub>3</sub> variability at Arctic Ocean observation sites. First, Pearson correlation coefficients ( $r$ ) were calculated for individual variables as they relate to O<sub>3</sub> observations across all platforms according to Equation 4.1.

$$r_{O_3,Y} = \frac{s_{O_3,Y}}{s_{O_3}s_Y} \quad \text{E4.1}$$

Here  $r$  represents the correlation coefficient,  $s_{O_3,Y}$  is the covariance between O<sub>3</sub> and the explanatory variable, and  $s_{O_3}$  and  $s_Y$  represent the standard deviations for O<sub>3</sub> and the explanatory variable, respectively. The results are summarized in Figure 4.10.

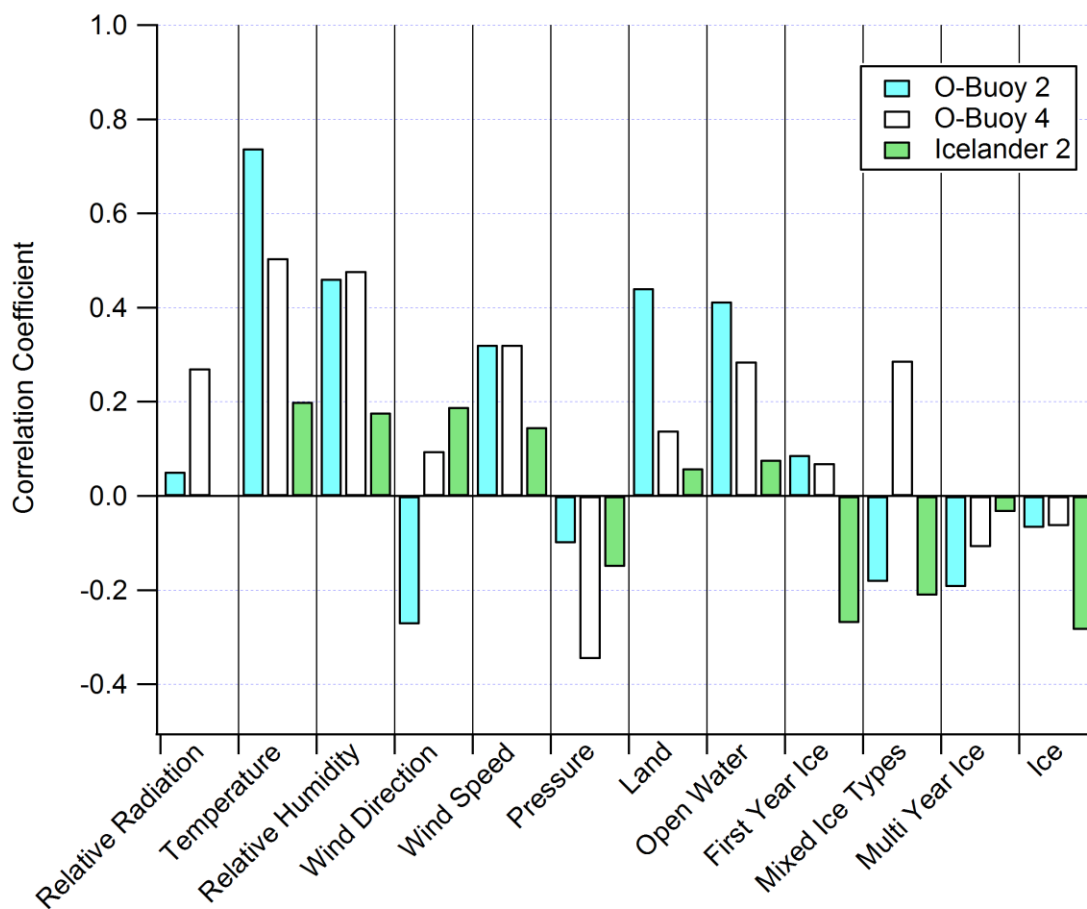


Figure 4.10 Correlation coefficients calculated between O<sub>3</sub> mole fractions and other explanatory variables. “Ice” represents the sum of all ice types.

From these calculations, it is seen that O<sub>3</sub> has positive correlation with temperature, relative humidity, wind speed, and periods when air has at least some contact with land and open water. These variables can all be associated with turbulence. For instance, simultaneous increases in temperature, relative humidity, and wind speeds could be indicative of air passing over open leads. Due to the large temperature gradient that exists between open

water and the overlying atmosphere, increases in sensible and latent heat fluxes induce convective mixing that could increase O<sub>3</sub> levels by mixing down O<sub>3</sub>-rich free tropospheric air (Moore et al., 2014). Additionally, air masses traveling over land can be subjected to turbulence induced by mechanical shearing of wind across irregular surfaces (Stull, 1988). Across datasets, temperature has the most positive correlation with O<sub>3</sub> among variables ( $r = 0.74, 0.51, 0.20$  for O-Buoy 2, O-Buoy 4, and Icelander 2, respectively). Relative radiation data is not available from Icelander 2, but O-Buoys 2 and 4 both show that O<sub>3</sub> is positively correlated with radiation, which can also be a driver of turbulent mixing. Conversely, O<sub>3</sub> is shown to be negatively correlated with atmospheric pressure, and exposure to ice. Low pressure systems can be related to high ozone either by the presence of storms, or by the transport of high ozone air from southerly latitudes (Jacobi et al., 2010). Inconsistent observations are seen in the cases of wind direction and air that has passed over FYI and Mixed Ice types.

To probe how well variables could explain variance in O<sub>3</sub>, linear models were first developed for each independent variable using O<sub>3</sub> mole fractions as the dependent variable, followed by multivariate linear models evaluating O<sub>3</sub> against combinations of independent variables. The power of these models is evaluated using the adjusted R<sup>2</sup> (Equation 4.2), where  $n$  is the number of observations and  $p$  is the total number of explanatory variables in the model.

$$\bar{R}^2 = 1 - (1 - R^2) \frac{n-1}{n-p} \quad \text{E4.2}$$

Considering first the series of individual linear regressions, all explanatory variables were statistically significant ( $p < 0.05$ ) with the exceptions of O-Buoy 2 relative radiation and MYI exposure for Icelander 2. Adjusted  $R^2$  values are presented in Figure 4.11. Exposure to various ice types appears to be only weakly related to  $O_3$  levels at all sites, explaining at most 4% of the total variation in  $O_3$  at O-Buoy 2 (due to MYI exposure), 8% at O-Buoy 4 (due to exposure to mixed ice types), and 9% at Icelander 2 (due to exposure to any ice at all). In the case of the O-Buoys, temperature and relative humidity are the most powerful predictors, explaining 54% and 21% of  $O_3$  variability, respectively, at O-Buoy 2, and 25% and 22% of variability, respectively, at O-Buoy 4. Remaining relatively strong predictors include air mass exposure to land and open water at O-Buoy 2 ( $R^2 = 0.19, 0.17$ , respectively), atmospheric pressure at O-Buoy 4 ( $R^2 = 0.12$ ), and wind speed at O-Buoys 2 and 4 ( $R^2 = 0.10$  in both cases). All other variables have  $R^2$  values that explain less than 10% of the variance individually.

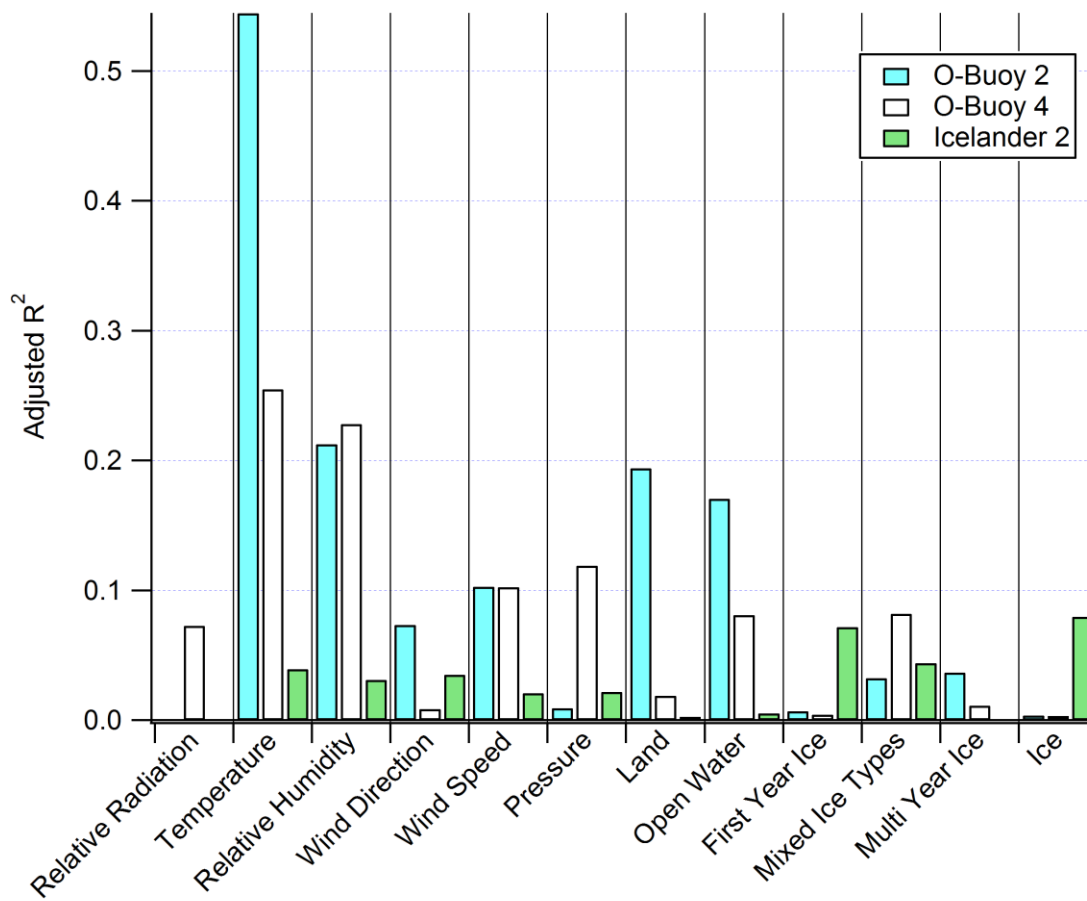


Figure 4.11 Adjusted  $R^2$  values for linear models relating  $O_3$  to individual explanatory variables (x-axis). All bars represent cases in which the corresponding variable was found to be significant ( $p < 0.05$ ).

Multivariate linear regressions were also performed to discover how well these explanatory variables together can account for  $O_3$  variance (Multiple  $R^2$  displayed in Figure 4.12). A set of three different linear models were created that attempt to model  $O_3$  as a function of the following variables:

- 1) local meteorology (relative radiation, temperature, relative humidity, atmospheric pressure, wind speed, and wind direction)
- 2) surface types over which air traveled (land, open water, FYI, mixed ice types, and MYI)
- 3) combined model (both local meteorology and surface types)

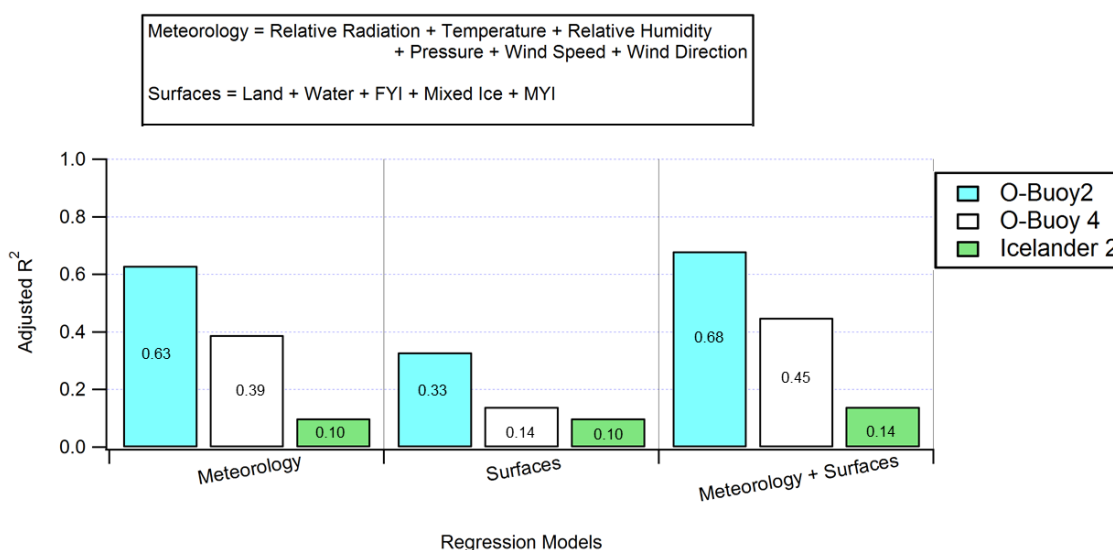


Figure 4.12 Adjusted  $R^2$  values from the models represented by Equations 4.3-4.6. Values are listed within each bar.

It is clear from Figure 4.12 that the meteorological parameters are more powerful explanatory variables than is the exposure to various surface types at the O-Buoy sites, while they are nearly equivalent at the site of the Iceland. Additionally, using both meteorological and surface type variables only increases the  $R^2$  of the models by 0.03-0.05 over using only meteorology. For O-Buoy 2, temperature was the most powerful variable in predicting  $O_3$  variability, as shown in Figure 4.10Figure 4.11. In these multivariate

models, wind speed and wind direction were found to not be significant predictors in each model in which they were included, likely due to both having moderate correlations with temperature ( $r_{\text{temp,wind speed}} = 0.37$ ,  $r_{\text{temp,wind direction}} = -0.30$ ), meaning they only add marginal additional explanatory power if temperature is included in the model. Additionally, when only the satellite surface types are considered together, mixed ice types are not found to be significant because of its correlation with FYI ( $r_{\text{FYI,Mixed Ice}} = -0.48$ ). When the model is expanded to include meteorology, mixed ice is once again found to be significant.

In the case of O-Buoy 4, wind direction is not found to be significant in any model, while land and FYI exposure are found to be insignificant predictors in the combined model (3), perhaps because the overwhelming majority of observations do not feature these surface types. In terms of meteorology, both these surface types have the strongest correlation with wind direction ( $r_{\text{land,wind direction}} = -0.12$ ,  $r_{\text{FYI,wind direction}} = -0.20$ ), suggesting that they provide even less predictive power than wind direction. Given the significance of meteorology in tandem with the low amounts of  $\text{O}_3$  at Arctic Ocean observatories (Figure 4.8), there is thus evidence to suggest that  $\text{O}_3$ -depleted air is the norm during the Arctic spring time over sea ice covered areas in the Arctic Ocean, absent significant influence of land.

For Icelander 2, wind speed and exposure to open water were not significant predictors in any of the models. It should be noted, of course, that the air approaching Icelander 2 had little exposure to open water (Figure 4.7). In addition, relative humidity was not significant in the combined model when FYI was included as a predictor ( $r_{\text{FYI,relative humidity}} = -0.38$ ). Land exposure, while deemed not significant under Model 1, was found to be significant in the combined model. However, this area is traditionally covered by

both thin, FYI and an abundance of open leads (Röhrs and Kaleschke, 2012) that do not often appear in the coarse satellite imagery used in this study.

#### 4.4 Discussion

Numerous studies have performed backward air mass trajectory analysis to find strong correlations between low O<sub>3</sub> values and air that has passed over areas of sea ice before arriving at coastal observation sites (e.g., Bottenheim and Chan, 2006; Gilman et al., 2010). In this study, utilizing observations obtained in areas surrounded predominately by sea ice, only very weak relationships were found between air mass history and ambient O<sub>3</sub> mole fractions ( $|r| \leq 0.3$ ). In addition, averaging the particle concentrations by their spatial locations when O<sub>3</sub> < 10 nmol mol<sup>-1</sup> for each observation site shows no particular trends or source region beyond the majority of particles traveling over ice covered regions before arriving at the site of the O-Buoy (Figures 4.10-12).



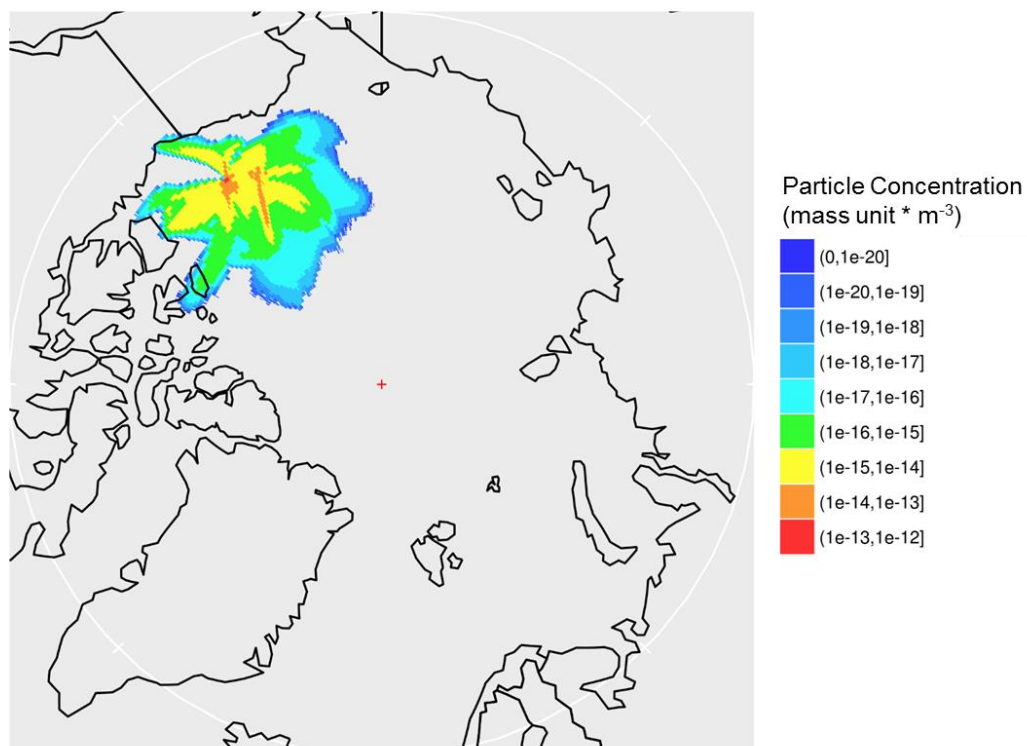


Figure 4.13 For O-Buoy 2, average particle concentrations during periods when O<sub>3</sub> levels fall below 10 nmol mol<sup>-1</sup>.

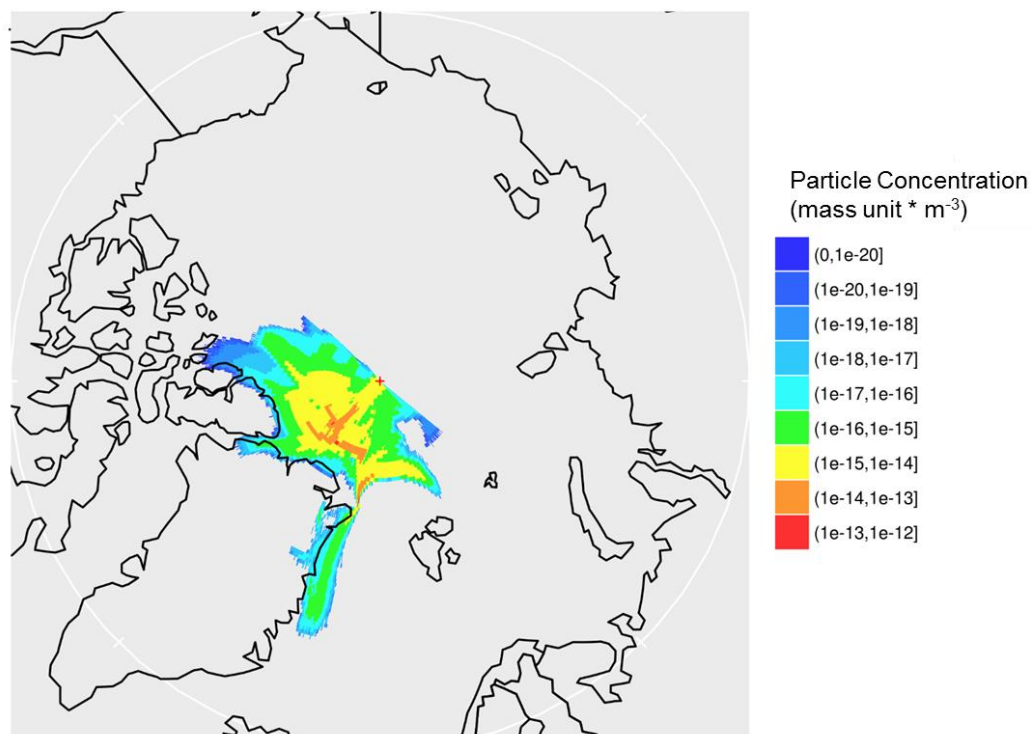


Figure 4.14 For O-Buoy 4, average particle concentrations and positions during periods when  $\text{O}_3$  levels fall below  $10 \text{ nmol mol}^{-1}$ .

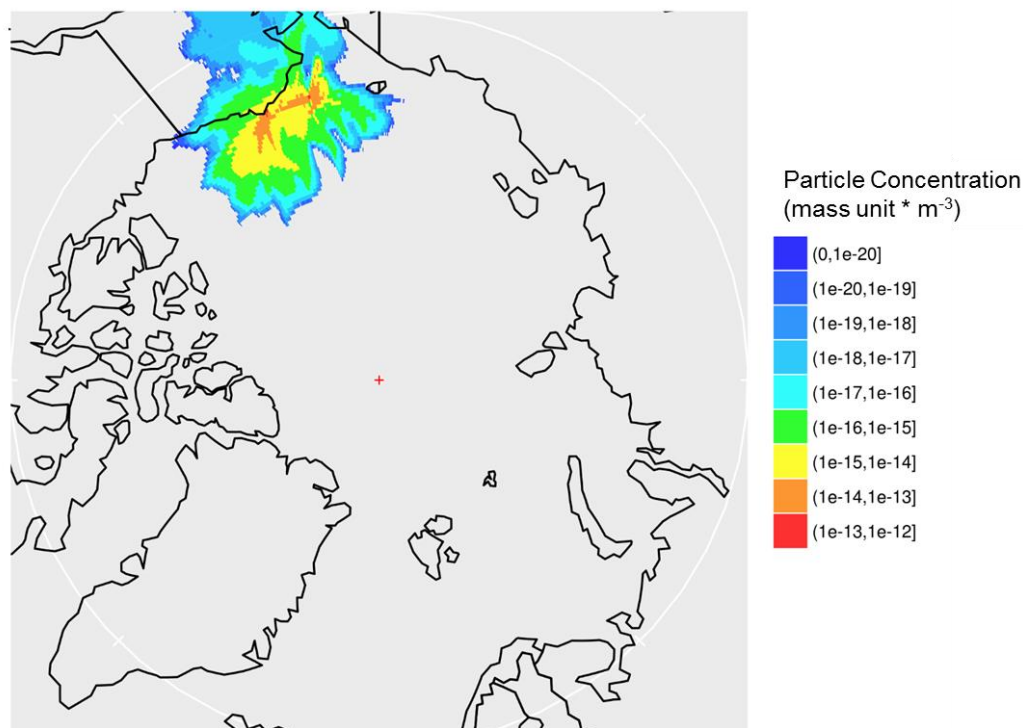


Figure 4.15 For Icelander 2, average particle concentrations during periods when  $O_3$  levels fall below  $10 \text{ nmol mol}^{-1}$ .

Because these instrument platforms are surrounded by ice, it stands to reason that the power of ice as a predictor is lessened if ODEs do in fact initiate over any ice-covered region. However, ice during the Arctic springtime is largely covered by snow (Webster et al., 2014), which has previously been shown to be an efficient producer of molecular halogens when exposed to sunlight under acidic conditions via R4.3-R4.10, and even more effective than sea ice (Custard et al., 2016; Foster et al., 2001; Pratt et al., 2013; Raso et al., 2016). A parameter possibly more powerful than ice coverage in predicting  $O_3$  variability is snow coverage and/or snow depth because the pH of snow is expected to be lower with greater physical separation from the buffered sea-ice brine (pH~8.2). Comiso et al. (2003) report

satellite retrievals of average snow depth (0-100 cm) at a resolution of 12.5 km (available at <http://neptune.gsfc.nasa.gov/csb/index.php?section=53>), though such products have not yet been used to compare with ODEs. If the snowpack depth is a powerful predictor of ODE-favorable conditions, it would be expected that ODEs would initiate over snowpack at some minimum depth. This is because brine on sea ice, which is alkaline, can migrate upward at least 8 – 18 cm into the snow (Dominé et al., 2004), thereby reducing its potential for halogen production (Pratt et al., 2013). In addition, the snowpacks MYI are regarded as having deeper snowpack depths than for seasonal ice (Webster et al., 2014), and therefore may be regions more conducive to halogen production chemistry. However, this analysis assumes broadly that surface snowpacks across the Arctic are largely acidified (by deposition of acidic sulfate aerosol, or of acidic gases such as HCl, HBr, and HNO<sub>3</sub> (Barrie et al., 1994a, 1994b; Li et al., 1994)), which may not be true. Regardless, it is clear that snowpack depth is important information to include as a potentially important variable.

Based on Figure 4.8, our results are consistent with an Arctic Ocean that is largely O<sub>3</sub> depleted. It is clearly seen that the ice-based observatories (O-Buoy 2 (2011), O-Buoy 4 (2012), and Icelander 2 (2012)) have substantially higher numbers of observations below 10 nmol mol<sup>-1</sup> (86, 70, and 68%, respectively) than do coastal-based observatories for the same periods of time (30 and 54% at Barrow during 2011 and 2012, and 22% and 28% at Alert during 2011 and 2012). As local-scale meteorological variables appear to account for much more O<sub>3</sub> variability than air mass history, we hypothesize that increases in O<sub>3</sub> above the Arctic Ocean in spring reflects transport of high O<sub>3</sub> from aloft to the surface (point of measurement) as a result of turbulent events. For O-Buoys 2 and 4, the most powerful explanatory variable with regard to O<sub>3</sub> was temperature. Positive correlations

between  $O_3$  and temperature related to ODEs has been an ongoing area of discussion. It had been previously thought that low temperatures (i.e.,  $< -20^\circ\text{C}$ ) could be required to initiate ODEs (Seabrook et al., 2011; Tarasick and Bottenheim, 2002). This is due to freezing dynamics associated with saltwater. As seawater freezes, it excludes impurities to a brine layer on its exterior surfaces (Bartels-Rausch et al., 2014). As temperatures continue to decrease, the volume of the quasi-brine layer (QBL) decreases (Figure 4.16), to maintain a concentration of ions in the QBL consistent with that needed for that amount of freezing point depression. This behavior can be represented quantitatively by Equation E4.3 (Kuo et al., 2011).

$$x_s = 1 - (1 - x_{s,0}) \exp \left[ \frac{-\Delta H_w^{fus}}{R} \left( \frac{1}{T} - \frac{1}{T_m} \right) \right] \quad \text{E4.3}$$

In Equation 4.3,  $x_s$  is the mole fraction of solute in the QBL,  $x_{s,0}$  is the solute mole fraction in the melted solution,  $R$  is the gas constant,  $\Delta H_w^{fus}$  is the enthalpy of fusion of water,  $T$  is the temperature of the system, and  $T_m$  is the bulk melting temperature of ice. Below the  $\text{NaCl} \cdot 2\text{H}_2\text{O}$  eutectic point, however,  $\text{NaCl} \cdot 2\text{H}_2\text{O}(\text{s})$  precipitates out of the QBL (Figure 4.17).

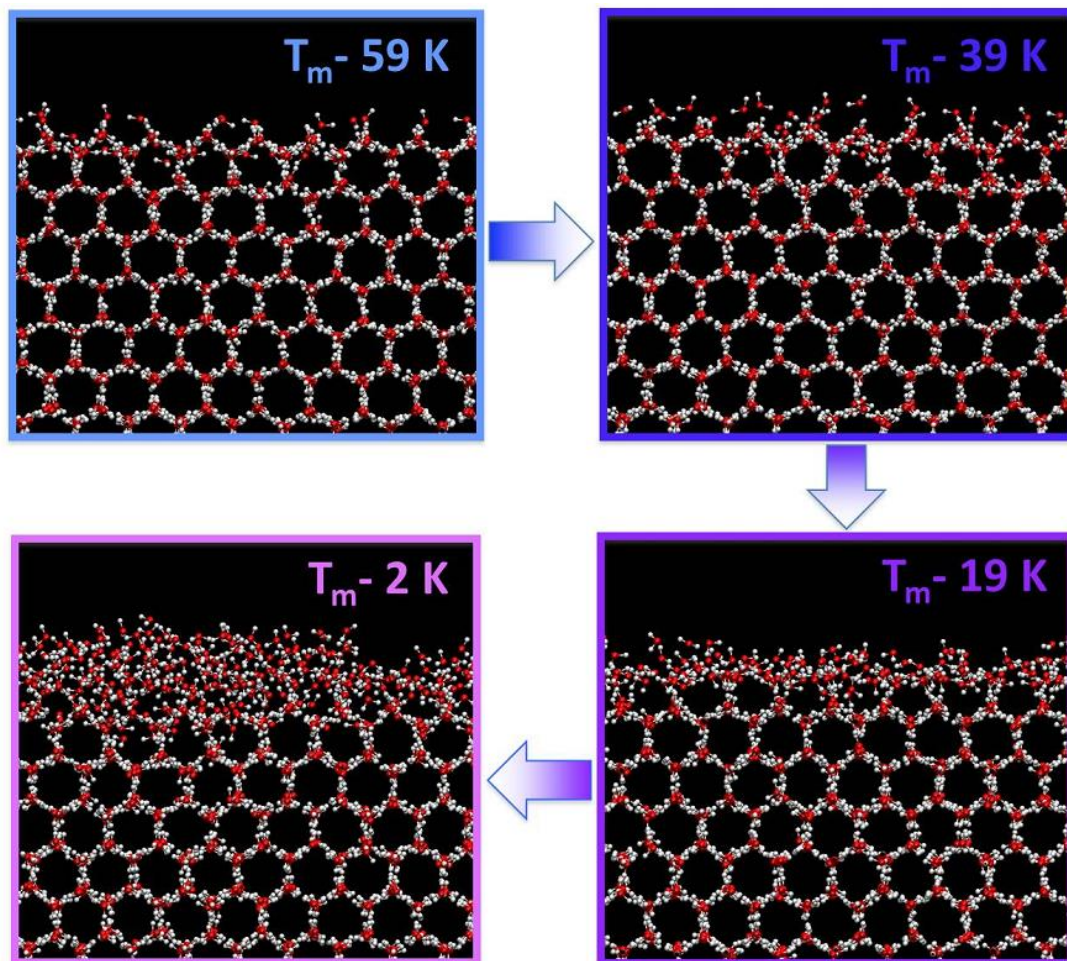


Figure 4.16 Molecular dynamics simulation demonstrating the thickness of the disordered surface on frozen water based on temperature.  $T_m$  represents the melting temperature of the simulated ice. Figure reproduced from Bartels-Rausch et al. (2014).

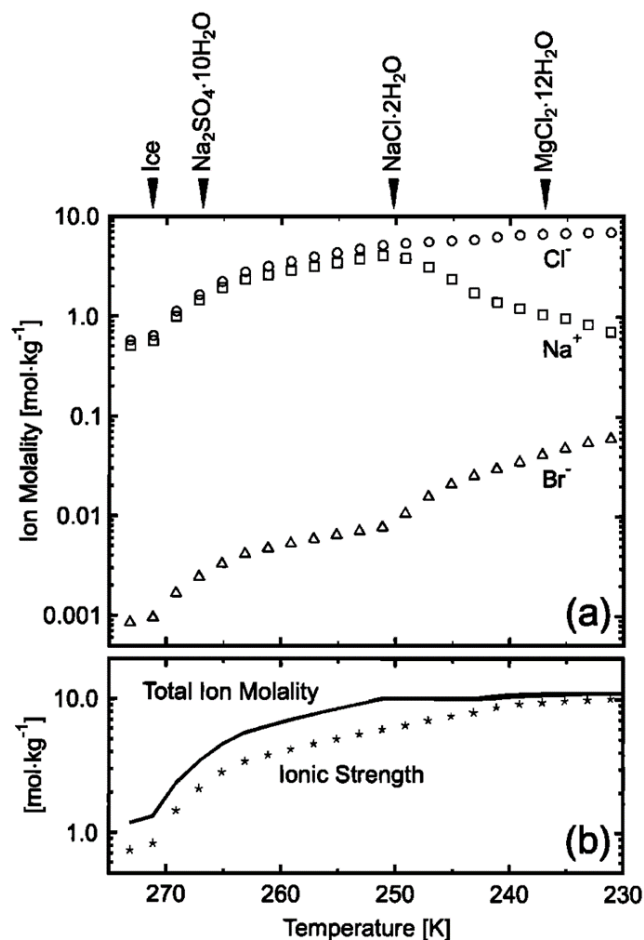


Figure 4.17 Effects of temperature on the concentration and ionic strength in the QBL. Eutectic points of different species are listed on the top axis. a) individual ion molality changes as a function of temperature for sea salt. b) Effects of temperature on the total solution molality and ionic strength. Figure reproduced from Koop et al. (2000).

As can be seen in Figure 4.17a, lower temperatures correspond to increasing concentrations of halides in the QBL. At the NaCl·2H<sub>2</sub>O eutectic point, the increasing anion concentration with decreasing temperature must then derive from Br<sup>-</sup> ions (Koop et al., 2000). As discussed in Chapter 5, this behavior increases the relative surface enhancement of Br<sup>-</sup> ions

(relative to  $\text{Cl}^-$ ) and their potential for atmospheric interactions and ODE chemistry. Thus, it has been hypothesized that ODEs will be more prevalent below 251K (e.g., Tarasick and Bottenheim, 2002)

It is also now accepted that ODEs can actually occur under a wide range of temperatures, including up to  $0^\circ\text{C}$  (Bottenheim et al., 2009; Halfacre et al., 2014; Jacobi et al., 2010; Neuman et al., 2010). A similar relationship has also been noted between BrO and temperature by Pöhler et al. (2010). They postulated that it is the temperature gradient that controls BrO release, as cold air moving over relatively warm open leads causes turbulent mixing. This enables the release of more reactive bromine from snow and allegedly sea ice into the atmosphere that undergoes R4.1-R4.2 to produce BrO and enable ODEs. However, Moore et al. (2014) proposed that these same dynamics were often associated with the downward mixing of  $\text{O}_3$ -rich free tropospheric air from aloft, resulting in the recovery of ambient  $\text{O}_3$  levels. Of course, these chemical concentration increases are not mutually exclusive, as increasing ambient concentrations of both  $\text{O}_3$  and Br is certain to produce more BrO without necessarily causing an ODE until the boundary layer stabilizes again. It would thus appear that higher temperatures appear important as they relate to turbulent mixing, discussed below.

The relationship with the remaining significant variables (i.e., positive correlation with wind speed, negative correlation with pressure) are possibly indicative of turbulent or stable conditions. Atmospheric stability is typically determined by vertically profiling the temperature gradient in the atmosphere. Under dry conditions, the “dry adiabatic lapse rate” is typically  $-9.8^\circ\text{C km}^{-1}$  (Stull, 1988) (i.e., temperature decreases with altitude). When the actual lapse rate is less than this, or when temperatures increase with height, the



atmosphere is considered stable. These conditions can be generally associated with calm winds, high pressure, and low surface temperature (if the temperature of the surface cools faster than the air slightly aloft, a temperature inversion will develop) (Boylan et al., 2014; Jacobi et al., 2010). Air above snow and ice is often stable, because snow and ice are near-perfect black body radiators in the IR. These conditions are not conducive to the vertical transport of air, and it would be expected that surface-based halogen chemistry could cause rapid O<sub>3</sub> depletion in this regime, in the presence of sunlight. Conversely, when pressure is low, wind speeds are high, and/or surface temperatures are warm (relative to the surrounding air), these are conditions that are indicative of atmospheric instability (Boylan et al., 2014), and conducive to the downward mixing of O<sub>3</sub>-rich air from aloft (above the depleted region) due to low Arctic boundary layers (typically ranging between 200-500 m above ground level) (Bottenheim et al., 2002b; Boylan et al., 2014; Hopper and Hart, 1994; Oltmans et al., 2012). Unfortunately, without vertical temperature information we cannot definitively confirm the state of the boundary layer during these time periods.

Alternatively, Jacobi et al. (2010) used mappings of geopotential height and sea level pressure to interpret a similar set of Arctic Ocean data. They determined that increases in O<sub>3</sub> levels could be associated with the passing of warm fronts originating from lower latitudes, often accompanied with warmer temperatures and lower local atmospheric pressure. Because of this they ascertained that these warm fronts were associated with the advection of O<sub>3</sub> rich air from southerly latitudes. While these relationships are consistent with a largely O<sub>3</sub> depleted Arctic Ocean, interrupted by intermittent turbulent mixing from

aloft or advection, additional vertical profile information, as well as synoptic scale meteorological data are needed for further interpretation.

#### 4.5 Conclusions

Observations of O<sub>3</sub>, meteorology, and surfaces were used in this study to both assess under what conditions O<sub>3</sub> depleted air masses arrived at measurement sites. 68%, 70%, and 86% of the ozone observations during April were less than 10 nmol mol<sup>-1</sup> for Icelander 2, O-Buoy2, and O-Buoy 4, respectively. ODEs observed at both O-Buoy 2 and Icelander 2 mostly traveled over FYI, while the air arriving at O-Buoy 4 had been exposed to mostly MYI. However, interactions with surfaces only accounted for up to 33% of O<sub>3</sub> variability (O-Buoy 2), and as little as 10% at Icelander 2. In the cases of O-Buoy 2 and 4, local meteorology was much more powerful for this purpose, with particular regard to temperature.

The results presented here are consistent with an Arctic Ocean that is largely O<sub>3</sub> depleted during the springtime, interrupted by the occasional downward mixing of free tropospheric O<sub>3</sub>, or the advection of O<sub>3</sub> rich air from southern latitudes. However, this work is yet incomplete, and there is more information to be derived. The statistical analysis was performed on observation periods as a whole, though it may be more appropriate to perform it solely on periods of O<sub>3</sub> variation above some minimum standard deviation. As different mechanisms can control the rise of O<sub>3</sub> levels (e.g., wind speed, turbulent mixing), higher amounts of correlation and R<sup>2</sup> could be obtained if periods of O<sub>3</sub> variation are analyzed individually. In addition, it should be investigated whether a statistically significant relationship exists between air mass exposure to snow covered surfaces and O<sub>3</sub>

levels, given the observation of halogen explosions occurring in acidic snowpack interstitial air, and the amount of Arctic Ocean that is potentially covered by snow-covered ice (i.e.,  $\sim 1.4 \times 10^6$  km; <https://nsidc.org/>).

## CHAPTER 5. LABORATORY STUDIES OF OXIDATIVE RELEASE OF MOLECULAR CHLORINE, BROMINE, AND IODINE FROM FROZEN SURFACES

### 5.1 Introduction

It is now well-established that gas-phase halogen species influence the oxidation capacity of the atmosphere (Barrie and Platt, 1997; Carpenter et al., 2013; Platt and Hönninger, 2003; Saiz-Lopez and von Glasow, 2012; Simpson et al., 2007b, 2015; and references therein). In polar regions during springtime, the photolysis of molecular halogens causes dramatic depletion of surface-level O<sub>3</sub> (Reactions R5.1-R5.2, where X represents Cl, Br, or I), and simultaneously converts Hg<sup>0</sup> to low volatility oxidation products that deposit to the surface (Steffen et al., 2008, 2014).



XO produced in Reaction R5.2 rapidly photolyzes to regenerate O<sub>3</sub> and X<sub>2</sub> in a null cycle, or react with another halogen oxide to irreversibly remove ambient O<sub>3</sub>. Alternatively, XO can react with HO<sub>2</sub> to form HOX (Reaction R5.3), which can react heterogeneously with salt-laden surfaces, including sea-salt aerosol particles (McConnell et al., 1992) and the “disordered interface” (also referred to as a quasi-liquid or quasi-brine layer) that exists on

frozen saline surfaces (Bartels-Rausch et al., 2014; Cho et al., 2002) to exponentially increase atmospheric concentrations of  $X_2$  (Reaction R5.4) (Garland and Curtis, 1981; Tang and McConnell, 1996; Vogt et al., 1996; Wennberg, 1999a).



This exponential increase in halogen concentrations is generally referred to as the “halogen explosion,” and is hypothesized to be the major mechanism by which halogen concentrations increase in the atmosphere. While Br, I, and Cl atoms can theoretically all participate in  $O_3$  destruction (Simpson et al., 2015; Thompson et al., 2015), this “explosion” has traditionally been considered in terms of a “bromine explosion,” as bromine has been assessed to be the primary agent for the rapid destruction of  $O_3$  and Hg (Simpson et al., 2007b; Stephens et al., 2012). Additionally, this mechanism is believed to be enhanced under acidic conditions, consistent with laboratory studies of condensed (Fickert et al., 1999) and frozen surfaces (e.g., Wren et al., 2013).

Iodine has the potential to increase the rate of  $O_3$  destruction (Thompson et al., 2015). However, at estimated levels in the atmosphere, it is suggested to only slightly enhance Br-induced depletions (Raso et al., 2016). Finally, Cl reacts faster with hydrocarbons than does  $O_3$ , and therefore, it dominates the oxidation of volatile organic compounds in the polar boundary layer (Atkinson et al., 2006; Jobson et al., 1994).

While much is known about the possible atmospheric chemistry of halogens/halogenated radicals in relation to O<sub>3</sub> destruction, the chemical mechanisms by which molecular halogens are produced on snow surfaces are not clearly understood (Liao et al., 2014; Pratt et al., 2013). However, there have been recent reports of in situ, light-induced production of Cl<sub>2</sub> (Custard et al., 2016), Br<sub>2</sub> (Pratt et al., 2013; Raso et al., 2016), and I<sub>2</sub> (Raso et al., 2016) within snowpack interstitial air, and this production is enhanced following the addition of O<sub>3</sub>. The Br<sub>2</sub>-producing snowpacks studied by Pratt et al. (2013) were characterized as having larger surface area, lower pH ( $\leq 6.3$ ), greater [Br<sup>-</sup>]/[Cl<sup>-</sup>] molar ratios ( $\geq 1/148$ ), and lower salinity relative to the other frozen samples collected near Barrow, Alaska. The proposed mechanism for this chemistry is based on laboratory studies of condensed-phase hydroxyl radical-mediated halogen oxidation (Reactions R5.5-R5.12), followed by partitioning of the molecular halogen to the gas phase (Abbatt et al., 2010; Knipping et al., 2000; Oum et al., 1998b).



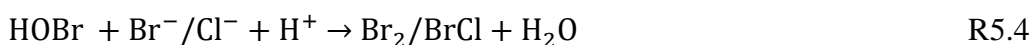


Direct, light-induced halogen production from frozen surfaces in the presence of OH has been previously demonstrated in the laboratory for Br<sub>2</sub> and possibly for I<sub>2</sub> (Abbatt et al., 2010), but analogous chemistry for Cl<sub>2</sub> has yet to be observed. Additionally, photochemical production of I<sub>2</sub> has been directly observed in the absence of hydroxyl radicals (Kim et al., 2016). Employing cavity ring-down spectroscopy, Kim et al. (2016) reported photochemical production of I<sub>2</sub> from a frozen solution independent of OH, a process that was enhanced by known aqueous-phase chemistry (R5.13-5.14, R5.10-R5.12). This proposed photochemical mechanism involves an (I<sup>-</sup>-O<sub>2</sub>) charge-transfer complex (Levanon and Navon, 1969).



A question is thus raised regarding the necessity of or impact of OH for I<sub>2</sub> production under environmentally-relevant conditions.

Similarly, the role of O<sub>3</sub> in halogen production is unclear. Previous laboratory studies have demonstrated that halide-doped frozen surfaces exposed to O<sub>3</sub> can directly lead to Br<sub>2</sub> production (independently of radiation, R15-R16) (Oldridge and Abbatt, 2011; Oum et al., 1998a; Wren et al., 2013).



Wren et al. (2013) found that Cl<sub>2</sub> production in their experiment was produced primarily via heterogeneous recycling of HOCl, resulting from BrCl photolysis. However, the observation that O<sub>3</sub> induces halogen production is somewhat in contrast to the above field observations of snowpacks, in which O<sub>3</sub> was not shown to produce halogens on its own (i.e., in the dark). Rather, the presence of O<sub>3</sub> was shown to provide additional production only in the presence of light (Custard et al., 2016; Pratt et al., 2013; Raso et al., 2016), raising a question of whether O<sub>3</sub> is more important for initial halogen release, or in a gas phase propagation/recycling capacity (i.e., per the halogen explosion).

In this study, we utilize a custom coated-wall flow reactor in tandem with chemical ionization mass spectrometry (CIMS) to increase our understanding of Br<sub>2</sub>, Cl<sub>2</sub>, and I<sub>2</sub> production from ice surfaces that mimic sea ice. The effects of photochemically produced OH radical, O<sub>3</sub> addition, and pH are tested as they related to the yields of these halogens.



## 5.2 Methods

### 5.2.1 Materials

Sample solutions were composed to mimic the halide composition of seawater, either through dissolved Instant Ocean (Spectrum Brands) or commercially available halide salts at a composition that mimics Instant Ocean (for consistency) in solutions referred to hereafter as “saltwater.” Except for Instant Ocean, all chemicals were purchased from Sigma Aldrich. Halide salts include solid NaCl (puriss. p.a. grade,  $\geq 99.5\%$  purity), NaBr (puriss. grade,  $>99\%$  purity), KI (puriss. p.a. grade,  $\geq 99.5\%$  purity). The halide concentrations in these solutions are  $0.56\text{M Cl}^-$ ,  $7.2 \times 10^{-4}\text{M Br}^-$ , and  $1.9 \times 10^{-6}\text{M I}^-$ . We note that such an iodide concentration can be 1-2 orders of magnitude greater than those found in actual seawater (Herring and Liss, 1974; Tsunogai and Sase, 1969), which contains  $\text{Cl}^-$ ,  $\text{Br}^-$ , and  $\text{I}^-$  at ratios of  $1:1/660:1/200,000$ . Solutes were dissolved in nano-grade “Ultrapure” water (Weaver, 2015). This water is characterized as having less than 225 parts per trillion of total organic carbon, and less than  $15\text{ pmol mol}^{-1}$  of boron, the most likely ionic contaminant (typically present as  $\text{B}(\text{OH})_4^-$ ) (Hilal et al., 2011).

While previous investigators have adjusted the pH of their samples, it is very difficult to know the pH in the disordered interface (Bartels-Rausch et al., 2014; Wren and Donaldson, 2012) of frozen samples, since ions are excluded into it. To obviate this problem, the aqueous solutions were buffered so that upon freezing, the same pH will exist in the QBL. All solutions were buffered by either 20 mM acetic acid (ACS reagent grade,  $\geq 99.7\%$  purity)/acetate (puriss. p.a. grade) buffer ( $\text{pH} \approx 4.5\text{-}4.7$ ), or 20 mM bisulfate (ReagentPlus grade, 99% purity)/sulfate (ReagentPlus grade,  $\geq 99.0\%$  purity) buffer ( $\text{pH}$

$\approx 1.7 - 2.0$ ). pH values of sample solutions were determined before and after experiments, with no significant changes observed. 100  $\mu\text{M}$  of either hydrogen peroxide (trace analysis grade,  $\geq 30\%$  purity) or sodium nitrite (ReagentPlus grade,  $\geq 99.0\%$  purity) were included as photolytic hydroxyl radical precursors, via reactions R5, and R6-7.

### 5.2.2 Flow tube

Experiments were carried out in a 150 cm long, 2.5 cm ID frozen-walled Pyrex flow tube contained within a temperature-controlled cooling jacket. In each experiment, 80.0 mL of sample solution was poured into the tube, which was subsequently sealed. The flow tube was then rotated on motorized rollers within a 170 cm x 50 cm x 50 cm, insulated wooden cooling chamber. Crushed dry ice was placed along the bottom of the chamber, and fans were used to circulate the air such that the flow tube was evenly cooled. After  $\sim 30$  minutes, the sample was evenly frozen (ice thickness of 0.9 mm). The flow tube was subsequently transferred to a 156 cm x 50 cm x 50 cm wooden, Mylar-lined experiment chamber, and connected to a chiller set to 258 K (i.e., above the  $\text{NaCl}\cdot 2\text{H}_2\text{O}$  eutectic point). The cooling liquid used for the chiller was a mixture of 60% ethylene glycol and 40% distilled water. Six UVA-340 solar simulator lamps (Q-Labs) were installed in the experiment box (two on each side except bottom), and each side was lined with reflective Mylar material to ensure the flow tube was evenly irradiated on all sides when the lamps were illuminated. A flow schematic representing typical experiments is shown in Figure 5.1.

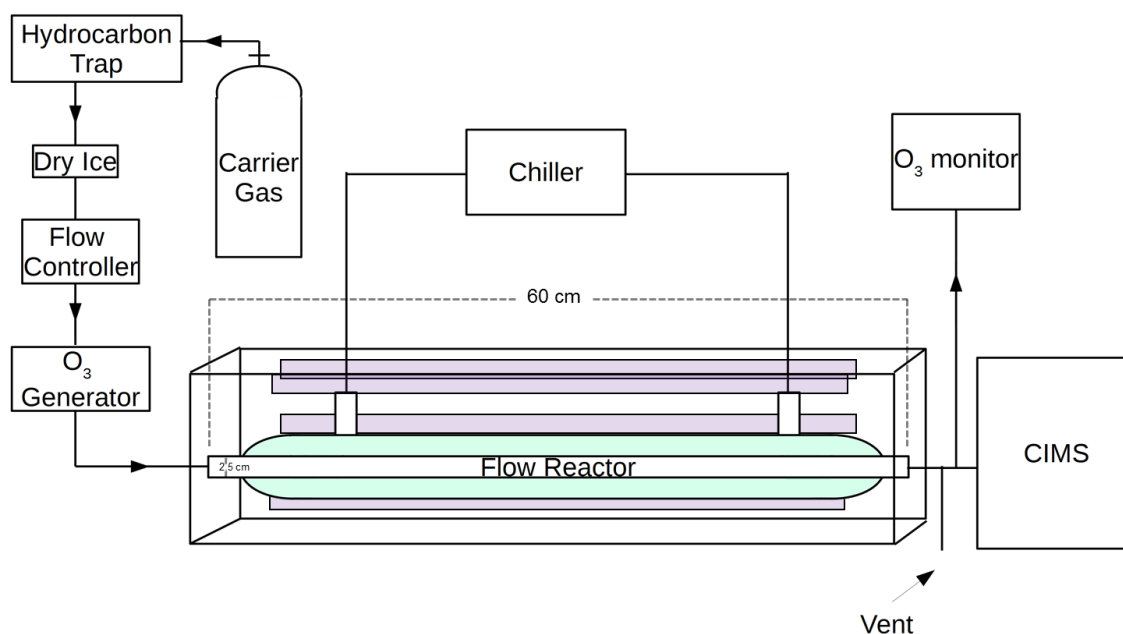


Figure 5.1 Experimental schematic representing the majority of experiments. Purple bars represent powered solar simulator bulbs. The green shading around the flow tube or flow reactor represents cooling liquid (60% ethylene glycol, 40% water) circulated through the chiller. The flow reactor region itself has an inner diameter of 2.5 cm.

The carrier gas (Air, Ultra Zero grade, Praxair) was scrubbed of hydrocarbons (using activated charcoal) and water by travelling through coiled stainless steel tubing surrounded by crushed dry ice (replaced throughout the course of an experiment). Before entering the experiment coated-wall flow tube, the carrier gas travels through a commercial O<sub>3</sub> generator (2B Technologies model 306). Carrier gas air entered the tube near room temperature (20°C). At the start of experiments, the O<sub>3</sub> generator was set to 0 nmol mol<sup>-1</sup>. Carrier gas then enters the flow tube in the dark experiment chamber. In most experiments, the carrier gas was regulated to a volumetric flow rate of 4.0 L/min, which yields a flush time in the flowtube of ~12 seconds. On exiting the flow tube, sample air was characterized

using a Thermo Environmental 49i O<sub>3</sub> monitor (flow rate of ~1.5 L/min) and a chemical ionization mass spectrometer (CIMS, sampling flow rate of ~1.7 L/min, described below in Sect. 2.3). Excess flow air was vented away. At various times in the experiment, the solar simulator bulbs are activated, and O<sub>3</sub> was added to the system by powering the O<sub>3</sub> generator.

### 5.2.3 CIMS

Halogen species were detected using a chemical ionization mass spectrometer (CIMS), described previously by Liao et al. (2011) and Pratt et al. (2013). Chemical ionization is achieved by ion-molecule reactions that occur between iodide-water clusters (I(H<sub>2</sub>O)<sub>n</sub>)<sup>-</sup> and the sample gas. The iodide-water clusters are formed when iodide ions, generated by flowing 5 ppm methyl iodide through a <sup>210</sup>Po ionizer (NRD) combine with water in the humidified flow tube region of the CIMS (note: this flow tube region is specific to the CIMS and is different from the experimental flow tube described in Sect 5.2.2).

A typical CIMS sampling cycle consisted of an 8.35 second duty cycle. Dwell times for all monitored species were 250 milliseconds with the exception of the iodide water cluster (which is used as an internal standard, detected as m/z 147, I(H<sub>2</sub><sup>18</sup>O)<sup>-</sup>), which was set to a dwell time of 100 milliseconds. Thirty-three species in total were scanned during this duty cycle (full list can be found in Table 1), but the majority of our results concern masses related to Br<sub>2</sub> (m/z 285 and 287: I<sup>79</sup>Br<sup>79</sup>Br<sup>-</sup> and I<sup>81</sup>Br<sup>79</sup>Br<sup>-</sup>, respectively), Cl<sub>2</sub> (m/z 197 and 199: I<sup>35</sup>Cl<sup>35</sup>Cl<sup>-</sup> and I<sup>37</sup>Cl<sup>35</sup>Cl<sup>-</sup>), and I<sub>2</sub> (m/z 381: I<sub>3</sub><sup>-</sup>).

Table 5.1 Table 1: List of species monitored by chemical ionization mass spectrometry (I(H<sub>2</sub>O)<sub>n</sub><sup>-</sup> as reagent ion) with corresponding *m/z* values.

Species	<i>m/z</i>
IH <sub>2</sub> <sup>18</sup> O <sup>-</sup>	147
I <sup>79</sup> Br <sup>-</sup>	206
I <sup>81</sup> Br <sup>-</sup>	208
I <sup>79</sup> Br <sup>79</sup> Br <sup>-</sup>	285
I <sup>79</sup> Br <sup>81</sup> Br <sup>-</sup>	287
I <sup>35</sup> Cl <sup>-</sup>	162
I <sup>37</sup> Cl <sup>-</sup>	164
I <sup>35</sup> Cl <sup>35</sup> Cl <sup>-</sup>	197
I <sup>35</sup> Cl <sup>37</sup> Cl <sup>-</sup>	199
I <sup>79</sup> Br <sup>35</sup> Cl <sup>-</sup>	241
I <sup>81</sup> Br <sup>35</sup> Cl <sup>-</sup> / I <sup>79</sup> Br <sup>37</sup> Cl <sup>-</sup>	243
I <sub>3</sub> <sup>-</sup>	381
I <sup>79</sup> BrO <sup>-</sup>	222
I <sup>81</sup> BrO <sup>-</sup>	224
I <sup>35</sup> ClO <sup>-</sup>	178
I <sup>37</sup> ClO <sup>-</sup>	180
IO <sup>-</sup>	270
IHO <sup>79</sup> Br	223
IHO <sup>81</sup> Br	225
IHO <sup>35</sup> Cl <sup>-</sup>	179
IHO <sup>37</sup> Cl <sup>-</sup>	181
IHOI <sup>-</sup>	271
I <sup>35</sup> ClNO <sub>2</sub> <sup>-</sup>	208
I <sup>37</sup> ClNO <sub>2</sub> <sup>-</sup>	210

The presence of Br<sub>2</sub> and Cl<sub>2</sub> was confirmed by measuring the ratios between the two isotope signals for each mass, compared to the natural abundances (i.e., 1.95 for *m/z* 287:285, and 1.54 for *m/z* 197:199). Background-subtracted signals not within ±25% of these naturally occurring isotopic ratios were deemed invalid and removed from analysis.

As the introduction of O<sub>3</sub> to the experimental system significantly increases the background signal for the primary Cl<sub>2</sub> isotope (m/z 197, I<sup>35</sup>Cl<sup>35</sup>Cl<sup>-</sup>), much of the Cl<sub>2</sub> data in these O<sub>3</sub> regions was similarly deemed invalid. Additionally, full mass scans (ranging from m/z 10 to m/z 400) were performed one time per hour throughout the majority of experiments, to look for all major products.

CIMS calibrations were performed using I<sub>2</sub>, Br<sub>2</sub>, and Cl<sub>2</sub> permeation devices (VICI) at the start and conclusion of each experiment. Br<sub>2</sub> and Cl<sub>2</sub> permeation outputs were quantified using the spectrophotometric method described in Liao et al. (2012b). The I<sub>2</sub> permeation output was quantified according to Raso et al. (2016). The output gas of the I<sub>2</sub> permeation device was flowed through an impinger with a NaHCO<sub>3</sub> (30mM)/NaHSO<sub>3</sub> (5mM) reducing solution. This solution quantitatively reduces I<sub>2</sub> to I<sup>-</sup>, which was then determined using a Dionex DX500 ion chromatography system. Permeation rates were calculated for each experiment and found to be  $(1.9 \pm 0.1) \times 10^{-11}$ ,  $(5.5 \pm 0.1) \times 10^{-10}$ , and  $(8.6 \pm 0.1) \times 10^{-10}$  moles per minute of I<sub>2</sub>, Br<sub>2</sub>, and Cl<sub>2</sub>, respectively (uncertainties representing standard error of the mean). Sensitivities were then determined by dividing the CIMS response signal by the permeation source concentration outputs. However, sensitivities for each species were found to statistically vary between experiments, and so overall sensitivities were calculated for individual experiments based on the average of the sensitivities calculated at the start and completion of each experiment. Corresponding uncertainties for these calibration factors thus represent the 1σ standard deviation of the mean sensitivity. In addition, the sensitivity for HOBr<sup>-</sup> species was estimated based on the Br<sub>2</sub> sensitivity, using a factor of  $0.5 \pm 25\%$  that of the sensitivity for m/z 287 (Liao et al., 2012b). Background measurements were also performed before and after the experiment

by passing the carrier gas through the experimental flow tube (without O<sub>3</sub>, in the dark) through a glass wool scrubber, previously shown by Raso et al. (2016) to effectively eliminate halogenated compounds. The average background values were subtracted from the raw signals. Average limits of detection (3σ) across all experiments for the halogens are  $1.8 \pm 0.4$ ,  $1.2 \pm 0.3$ , and  $9.0 \pm 2.0$  pmol mol<sup>-1</sup> for Br<sub>2</sub>, Cl<sub>2</sub>, and I<sub>2</sub> respectively (uncertainties representing standard error of the mean).

### 5.3 Results

In the discussion of the experiments that follow, we address whether OH can produce I<sub>2</sub>, Br<sub>2</sub>, and Cl<sub>2</sub> from frozen saline surfaces, as hypothesized from recent field experiments (Pratt et al., 2013; Raso et al., 2016), as well as the role of pH. In addition, we test whether O<sub>3</sub> can enhance this production. Typical experimental timeseries can be seen in Figure 5.2.

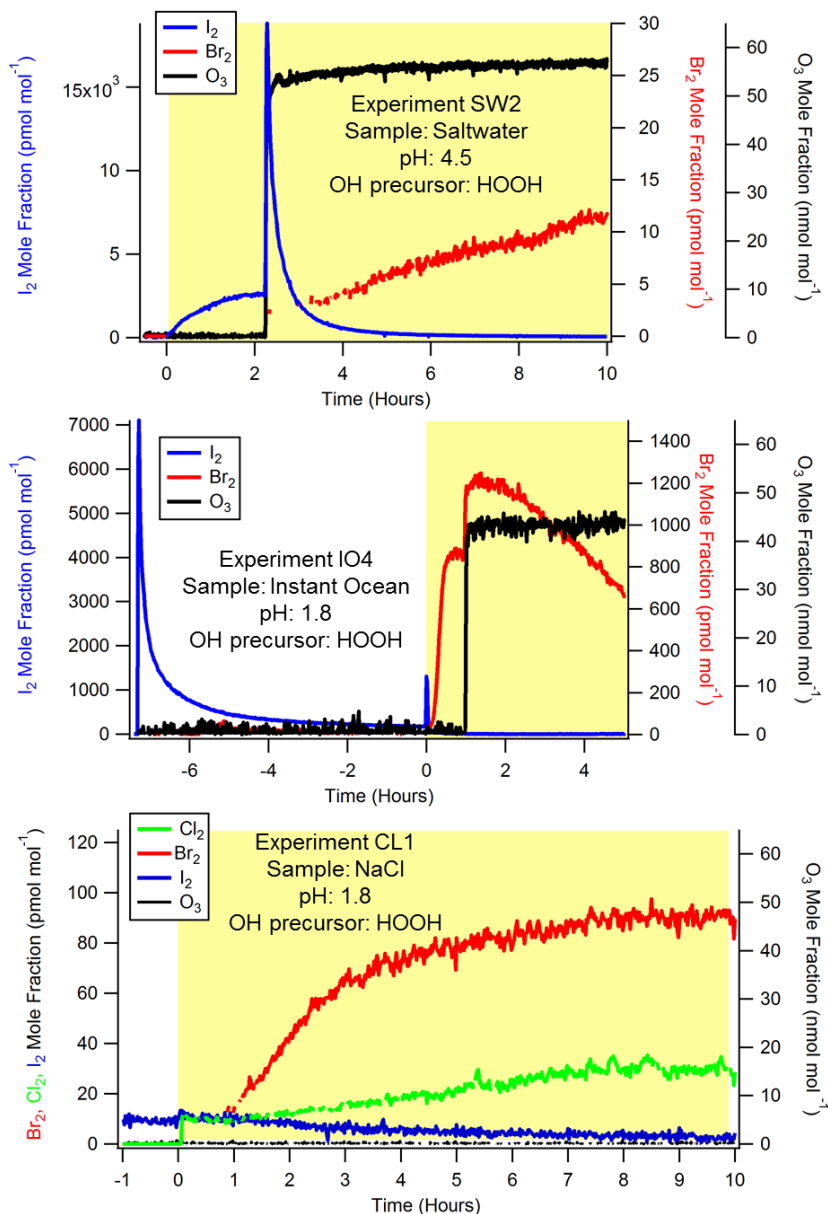


Figure 5.2 Representative experiments. Top: Saltwater experiment (SW2) at pH=4.5. Middle: Instant Ocean experiment (IO4) at pH = 1.8. Bottom: NaCl experiment (CL1) at pH = 1.8. Timescale represents hours from the activation of the lights, and the yellow shading represents presence of radiation from solar simulator bulbs. Gaps in data represent periods when the isotopic ratios in a species were deemed invalid (outside of  $\pm 25\%$  of naturally occurring abundances). Note:  $Cl_2$  signal before time =0 was artificially added.



The flow tube was connected to the CIMS under dark conditions and without O<sub>3</sub>. Once signals stabilized, lights were activated (defining t=0 in plots) for 1-2 hours, after which, ~50 nmol mol<sup>-1</sup> of O<sub>3</sub> was added to the system. Results from all experiments can be found in Table 5.2-Table 5.5, and major results are discussed below. Individual experiments are identified by IO#, SW#, or CL#, where IO refers to dissolved Instant Ocean based samples, SW refers to samples composed of dissolved reagent-grade salts, and CL refers to the sample composed of dissolved NaCl. Unless otherwise specified, integrated halogen yields represent the yields over the course of 1 hour. In the case of Sect 5.3.1, this hour occurs from t=0 (i.e., lights on) until t=1, whereas in Sect 5.3.2, the starting integration time indicates the time at which O<sub>3</sub> was activated. Additionally, reported uncertainties are calculated as the integrated sum multiplied by the relative uncertainty in the sensitivity.

### 5.3.1 Effects of the Hydroxyl Radical

Photochemical halogen production was observed for I<sub>2</sub>, Br<sub>2</sub>, and Cl<sub>2</sub> as seen in Figure 5.2. Relative to Br<sub>2</sub> and Cl<sub>2</sub>, I<sub>2</sub> was observed most readily when [I<sup>-</sup>]/[Br<sup>-</sup>] was close to the initial ratio in the dark of  $2.6 \times 10^{-3}$ , per the halide concentrations found in Instant Ocean (Sect. 5.2.1). In the presence of HOOH we find that I<sub>2</sub> mole fractions increase rapidly once the lights are activated (e.g., Figure 5.2 top). Of the four experiments performed at pH ≈4.7 (IO1, IO2, SW1, SW2) with HOOH, three produced statistically similar I<sub>2</sub> yields after the lights had been activated for one hour ( $7.7 \pm 1.6$  nmol, experiments IO1, SW1, SW2).

Table 5.2 List of experiments performed using an explicit OH source (i.e., HOOH or NO<sub>2</sub><sup>-</sup>). Yields represent the integrated total moles of gas-phase molecular halogens produced up to 1 hour after turning on the solar simulator lamps. s<sub>x</sub> represent the propagated uncertainty from these integrations, resulting primarily as a function of the uncertainty in the sensitivity (Sect. 5.2.3).

Experiment	Oxidant	pH	I <sub>2</sub> yield (nmol)	s <sub>I<sub>2</sub></sub> (nmol)	Br <sub>2</sub> yield (nmol)	s <sub>Br<sub>2</sub></sub> (nmol)	Cl <sub>2</sub> yield (nmol)	s <sub>Cl<sub>2</sub></sub> (nmol)
IO1	HOOH	4.7	9.1	3.1	0.0021	0.0002		
IO2	HOOH	4.7	0.65	0.01	0.034	0.002		
IO3	NO <sub>2</sub> <sup>-</sup>	2.0	6.7	0.2	0.081	0.002		
IO4	HOOH	1.7	0.82	0.22	5.5	0.1		
IO5	HOOH	1.7	0.33	0.04	3.5	0.8		
SW1	HOOH	4.7	5.9	1.1	0.021	0.001		
SW2	HOOH	4.5	8.1	3.9	0.018	0.003		
SW3	NO <sub>2</sub> <sup>-</sup>	1.8	4.0	0.1	0.013	0.001		
SW4	NO <sub>2</sub> <sup>-</sup>	2.2	0.16	0.07	5.4	0.9		
SW5	HOOH	1.8	0.75	0.13	6.0	1.2		
CL1	HOOH	1.8	0.10	0.01	0.10	0.01	0.093	0.003

It appears that a factor of 10 less I<sub>2</sub> was produced by IO2 based on the times chosen for integration. On connecting the flow tube to the CIMS in this experiment, there appeared to be already I<sub>2</sub> within the tube, possibly induced by room light during the transfer of the flow tube from the cooling box to the experimental light box. However, this production is believed to be minimal relative to the production from the solar simulator bulbs in the photolysis box. This is based on the relative absorption spectrum for hydrogen peroxide, which ceases significant absorption above 400 nm (Phibbs and Giguère, 1951), and emission spectrum of typical fluorescent lights, which begin significant emission above 400 nm (Figure 5.3).

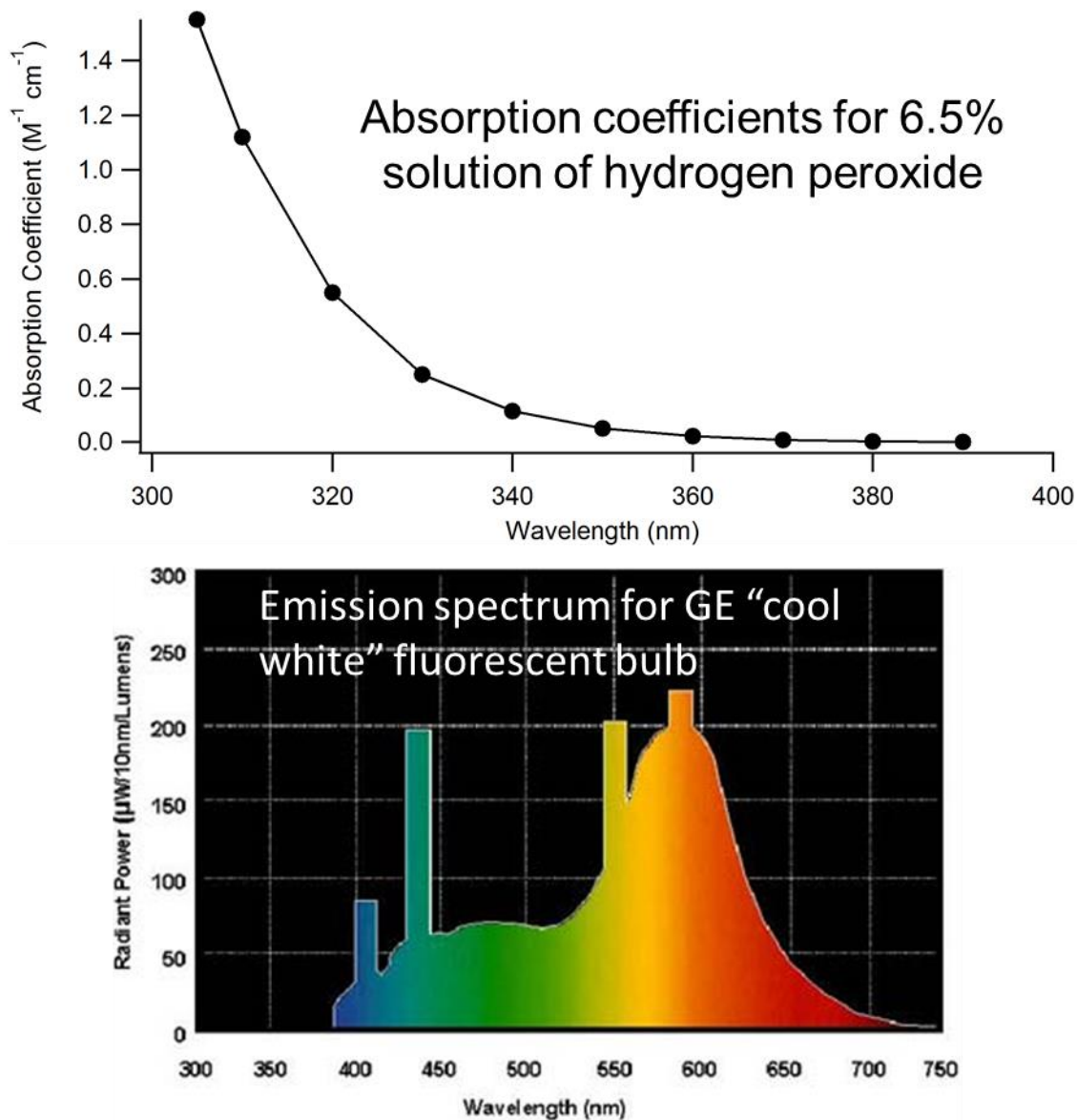


Figure 5.3 Absorption coefficients hydrogen peroxide and emission spectrum for General Electric "Cool White" fluorescent bulb. Top plot was reproduced from data provided from Phibbs and Giguère (1951), and bottom plot was taken from the website of General Electric (<http://www.gelighting.com/LightingWeb/na/resources/tools/lamp-and-ballast/spectral-power-distribution-curves.jsp>)

When the solar simulator bulbs were activated, this  $I_2$  signal quickly returned to the baseline, before rising and exhibiting the same qualitative features as Figure 5.2 (top panel). If instead the limits of integration are chosen starting when the  $I_2$  signal begins rising (i.e., during a period that resembles the other experiments), the integrated  $I_2$  yield ( $1.1 \pm 0.6$  nmol) more closely resemble the aforementioned experiments. Conversely, in the absence of OH (Table 5.3), integrated  $I_2$  yields over the course of one hour are significantly lower. At pH=4.7, IO7 (dissolved Instant Ocean) produced  $0.11 \pm 0.06$  nmol of  $I_2$ , while our two saltwater experiments (SW6, SW7) produced an average of  $0.028 \pm 0.011$  nmol of  $I_2$  without the presence of HOOH or  $NO_2^-$ . Neither  $Br_2$  nor  $Cl_2$  were produced above limits of detection.

Table 5.3 List of experiments performed using an explicit OH source (i.e., HOOH or  $NO_2^-$ ). Yields represent the integrated totals of halogens 1 hour after turning on the  $O_3$  generator.  $s_x$  represent the propagated uncertainty from these integrations, resulting primarily as a function of the uncertainty in the sensitivity (Sect. 5.2.3).

Experiment	Oxidant	pH	$I_2$ yield (nmol)	$s_{I_2}$ (nmol)	$Br_2$ yield (nmol)	$s_{Br_2}$ (nmol)
IO6	NA	4.7	0	0	0	0
IO7	NA	4.7	0.11	0.06	0	0
IO8	NA	2.0	14	3	0	0
SW6	NA	4.7	0.020	0.006	0	0
SW7	NA	4.5	0.036	0.001	0	0
SW8	NA	1.8	6.0	0.2	0	0

After initiating the lights, we note that  $I_2$  does begin increasing after the course of ~30 minutes, but it is at a much lower rate than when HOOH is present in solution. This production likely stems from the mechanisms outlined by Kim et al. (2016) (R5.13-14,

R5.10-12), which require only light, oxygen, and acidic conditions. In fact, we find that further increasing the acidity of solution appears to greatly enhance this production (discussed below). At least in the case of the Instant Ocean solutions, is also possible that an  $\text{NO}_3^-$  contaminant exists in the salt, which could act as an OH source analogously to  $\text{NO}_2^-$  (R5.6-5.7). While the manufacturer reported concentration is 0 ppm, we could not quantitatively confirm this using ion chromatography due to the high ionic strength of our solutions.

At lower pH (<2), large amounts of  $\text{I}_2$  were found to exit the tube upon connection to the CIMS (i.e., in the absence of light and  $\text{O}_3$ ). There are two possible sources of this production. As indicated above, transferring the flow tube from the cooling box could have generated OH radicals that subsequently produced  $\text{I}_2$ . Alternatively, a dark reaction mechanism between  $\text{HOOH}$  and  $\text{I}^-$  could have occurred:



This reaction sequence is often considered when discussing marine biota biochemistry (Küpper et al., 1998), but is not often referenced when considering Arctic chemistry which can have acidic surfaces with  $\text{HOOH}$  present (e.g., Anastasio et al., 2007). Integrating the  $\text{I}_2$  mole fractions from the moment the tube is connected to the CIMS until the lights are activated, an average of  $59 \pm 41$  nmols of  $\text{I}_2$  were released in the dark during experiments IO4, IO5, and SW5, corresponding to 39% of the initial 150 nmol of  $\text{I}^-$  in solution. After

this time, we saw little, if any, photochemical production of  $I_2$ , perhaps due to the depletion of available  $I^-$  at the ice surface. For comparison with the experiments involving HOOH, we employed  $NO_2^-$  as an alternative source of OH (R5.6-7). We note that  $NO_2^-$ , along with hydrogen peroxide, has been assessed to account for 96% of photochemical OH formation at Barrow, AK (France et al., 2012). Though  $NO_2^-$  has been shown to produce aqueous  $H_2ONO^+$  that produces trihalide species (which exist in equilibrium with  $X_2$  as in R5.12) under acidic conditions in the dark (O'Driscoll et al., 2006, 2008; O'Sullivan and Sodeau, 2010), and some dark  $I_2$  production was observed here, we were still able to observe photochemical  $I_2$  production in these cases. Integrated Instant Ocean and saltwater  $I_2$  yields in these cases were comparable after exposure to light ( $6.7 \pm 0.2$  and  $4.0 \pm 0.1$  nmol  $I_2$  for IO3 and SW3, respectively). Interestingly in cases without OH precursors, photochemical  $I_2$  production yields ( $14 \pm 3$  nmol for IO8, and  $6.0 \pm 0.2$  nmol for SW8) were within a factor of 2 of the  $I_2$  produced by  $NO_2^-$  photolysis. As referred to above, this production likely stems from the mechanisms outlined by Kim et al. (2016) (R5.13-14, R5.10-R12). While the Kim et al. (2016) mechanism would appear to occur at a slower rate than OH-mediated production at  $pH \approx 4.7$ , it is possible at low pH that significant dark oxidation of  $I^-$  still occurs with  $H_2ONO^+$  as described above, thereby reducing available  $I^-$  for reaction and retarding the rate of OH-mediated production. Conversely, without OH precursors,  $I^-$  would not deplete in the dark, which enables the Kim et al. (2016) mechanism to proceed at an apparently comparable rate in these experiments.

When  $[I^-]/[Br^-]$  resembles the initial conditions of Instant Ocean (i.e., IO1-IO3, SW1-SW3),  $Br_2$  is not observed as readily as  $I_2$ . At  $pH \approx 4.7$ ,  $Br_2$  remains below limits of detection (average  $1.8 \pm 0.4$  pmol mol<sup>-1</sup> across experiments) in just the presence of light

and HOOH. As discussed above, especially at  $\text{pH} < 2$ , substantial amounts of  $\text{I}_2$  are produced in the dark in reactions with hydrogen peroxide, thus decreasing the  $[\text{I}^-]/[\text{Br}^-]$ . In these low pH cases,  $\text{Br}_2$  is the dominant photochemical product, yielding an average of  $4.5 \pm 0.5$  nmol from IO4 and IO5, and  $6.0 \pm 1.2$  nmol from SW5, which used HOOH as an OH precursor, and  $5.4 \pm 0.9$  nmol from SW4, which used  $\text{NO}_2^-$  as an OH precursor. While we cannot provide an accurate estimate of the  $[\text{I}^-]/[\text{Br}^-]$  at  $\text{pH} < 2$ , we can roughly estimate how much  $\text{I}_2$  evolved before turning on the lights to assess the remaining moles of I in the quasi-brine layer, and essentially provide upper limits toward what  $[\text{I}^-]/[\text{Br}^-]$  was during  $\text{Br}_2$  release. Though highly uncertain, we estimate  $[\text{I}^-]/[\text{Br}^-]$  at low pH in solutions with hydrogen peroxide the moment before the lights turn on to have an average value of  $(1.6 \pm 0.7) \times 10^{-4}$ , which leads to photochemical production of  $\text{Br}_2$ . This is about an order of magnitude less than the starting  $[\text{I}^-]/[\text{Br}^-]$  of  $2.6 \times 10^{-3}$ .

Photochemical chlorine production was only observed from a frozen solution of NaCl (CL1) and hydrogen peroxide at low pH (1.8), as shown in Figure 5.2c. After one hour,  $0.93 \pm 0.03$  pmol of  $\text{Cl}_2$  was detected by CIMS, as was  $100 \pm 10$  pmol of  $\text{Br}_2$ . However, as shown in Fig 2c, significant changes are not apparent until hour 1. Note that the sudden rise at  $t=0$  is an artifact, as before this point the isotopic ratios were not consistent with  $\text{Cl}_2$ . Integrating instead from  $t=0$  until  $t=2$  hours, the  $\text{Cl}_2$  yield is equal to  $190 \pm 10$  pmol, while the  $\text{Br}_2$  yield increases to  $310 \pm 20$  pmol. The  $\text{Br}^-$  impurity of this NaCl salt solution, quantified by ion chromatography, was determined to be  $(4.5 \pm 0.3) \times 10^{-6}$  M, meaning  $\text{Cl}_2$  production was observed at  $[\text{Br}^-]/[\text{Cl}^-]$  of  $8.1 \times 10^{-6}$  ( $1/124,000$ ). As a point of reference, this ratio is possibly similar to the one used by Wren et al. (2013), who observed  $\text{O}_3$  and photochemical-induced  $\text{Cl}_2$  production using NaCl salt with 0.001%  $\text{Br}^-$

impurity ( $[\text{Br}^-]/[\text{Cl}^-] \leq 1/134,000$ ). A key difference between this work and Wren et al. (2013) is that the  $\text{Cl}_2$  produced here occurred in the absence of both  $\text{O}_3$  and associated gas phase recycling chemistry, but with a condensed phase OH source. These results are possibly (though not necessarily) more representative of what was observed in situ within the snowpack by Custard et al. (2016), where  $\text{O}_3$  levels tend to be lower than the overlying air (Albert et al., 2002; Helmig et al., 2012). However, Liao et al. (2014) reported that ambient  $\text{Cl}_2$  concentrations correlate with both light and  $\text{O}_3$ . The roles of both OH-mediated and  $\text{O}_3$ -mediated  $\text{X}_2$  production are further explored in Sect. 5.4.

Thus, we see a similar result for  $\text{Br}_2$  production in the presence of  $\text{I}^-$ , and  $\text{Cl}_2$  production in the presence of  $\text{Br}^-$ . Specifically,  $\text{Br}_2$  is not observed until  $\text{I}_2$  production decreases the  $\text{I}^-/\text{Br}^-$  ratio, and  $\text{Cl}_2$  is not observed until/unless the  $\text{Br}^-/\text{Cl}^-$  ratio is sufficiently low. It is worth noting that as discussed by Gladich et al. (2011) larger more polarized halide ions tend to be enriched at the ice-air interface .

Given that OH has been demonstrated to dominate the photochemical production of these halogens, at least at moderate pH, effective relative rate constants ( $k_{\text{X}}/k_{\text{Y}}$ ) for production under these experimental conditions can be calculated from experiments in which simultaneous halogen production is observed, assuming that the flux out of the ice is proportional to the production rate:

$$\frac{\text{Flux}_{\text{X}_2}}{\text{Flux}_{\text{Y}_2}} = \frac{k_{\text{X}}[\text{X}^-][\text{OH}][\text{H}^+]}{k_{\text{Y}}[\text{Y}^-][\text{OH}][\text{H}^+]} \quad \text{E5.1}$$



Flux is calculated as the integrated sum of  $X_2$  divided by integration time ( $t=0-3$  minutes, starting from the moment the lights turn on) and the surface area of the ice coverage in the flow tube. While we do not know the actual concentration of OH, it is identical within individual experiments and thus cancels here, as does surface area. The remaining variables are the halide ion concentrations, defined in Section 5.2, thus allowing us to solve for the effective relative rate constant,  $k_X/k_Y$ . At  $\text{pH} = 1.8$ , we estimate  $k_{\text{Br}^-}/k_{\text{Cl}^-} = (2.4 \pm 0.2) \times 10^5$  from experiment CL1, or, in other words, production of  $\text{Br}_2$  is 240,000 times more efficient from OH radical reaction than is production of  $\text{Cl}_2$  via  $\text{OH} + \text{Cl}^-$ . Across the six experiments performed at low pH using Instant Ocean (IO3, IO4, IO5) and salt water (SW3, SW4, SW5), we calculate an average  $k_{\text{I}^-}/k_{\text{Br}^-}$  of  $(8.9 \pm 4.0) \times 10^3$  (reported uncertainty is the standard error of the mean) at an average pH of 1.85. Thus, we can speculate that for these experiments, the dominant sink for OH is reactions with halide ions. This is supported by the fact that  $\text{I}_2$  and  $\text{Br}_2$  production are not significantly different between Instant Ocean and saltwater solutions (i.e., the organic matter in Instant Ocean does not appear to be the dominant OH sink). Therefore, OH radicals are readily consumed by  $\text{I}^-$ , and thus  $[\text{OH}]$  is too low for significant oxidation reaction with  $\text{Br}^-$ . As  $\text{I}^-$  is consumed,  $\text{HOOH}$  continues to photolyze, thereby increasing  $[\text{OH}]$  such that  $\text{Br}_2$  production becomes apparent. Similarly,  $[\text{OH}]$  is too low for significant  $\text{Cl}_2$  production, until/unless  $[\text{Br}^-] / [\text{Cl}^-]$  is very low.

5.3.2 Effects of O<sub>3</sub>

The addition of O<sub>3</sub> to the irradiated sample in the flow tube causes additional production of I<sub>2</sub> and Br<sub>2</sub>, as seen in Figure 5.2 (top) and Figure 5.2 (middle) under both pH conditions (Table 5.4 Table 5.5).

Table 5.4 List of experiments performed without using an explicit OH source (i.e., without HOOH or NO<sub>2</sub><sup>-</sup>). Yields represent the integrated totals of halogens 1 hour after turning on the solar simulator lamps (t = 0 through t=1hr). s<sub>x</sub> represent the propagated uncertainty from these integrations, resulting primarily as a function of the uncertainty in the sensitivity (Sect. 5.2.3).

Experiment	Oxidant	pH	I <sub>2</sub> yield (nmol)	s <sub>I<sub>2</sub></sub> (nmol)	Br <sub>2</sub> yield (nmol)	s <sub>Br<sub>2</sub></sub> (nmol)
IO1	HOOH	4.7	6.9	2.4	0.014	0.001
IO2	HOOH	4.7	21	1.0	0.038	0.002
IO4	HOOH	1.7	0.042	0.012	12	1
IO5	HOOH	1.7	0.11	0.01	9.2	2.0
SW1	HOOH	4.7	51	9.0	0.024	0.002
SW2	HOOH	4.5	51	25	0.027	0.004
SW3	NO <sub>2</sub> <sup>-</sup>	1.8	1.1	0.1	0.46	0.01
SW4	NO <sub>2</sub> <sup>-</sup>	2.2	0	0	13	2
SW5	HOOH	1.8	0.018	0.003	15	3

Table 5.5 List of experiments performed without using an explicit OH source (i.e., without HOOH or NO<sub>2</sub><sup>-</sup>). Yields represent the integrated totals of halogens 1 hour after turning on the O<sub>3</sub> generator. s<sub>x</sub> represent the propagated uncertainty from these integrations, resulting primarily as a function of the uncertainty in the sensitivity (Sect. 5.2.3).

Experiment	Oxidant	pH	I <sub>2</sub> yield (nmol)	s <sub>I<sub>2</sub></sub> (nmol)	Br <sub>2</sub> yield (nmol)	s <sub>Br<sub>2</sub></sub> (nmol)
IO6	NA	4.7	26	9	0.015	0.001
IO7	NA	4.7	47	29	0.0063	0.0006
IO8	NA	2.0	2.6	0.5	0.14	0.03
SW6	NA	4.7	55	18	0.0021	0.0003
SW7	NA	4.5	48	2	0.0042	0.0001
SW8	NA	1.8	38	1	0.93	0.02

In experiments with higher pH (where  $[\text{Br}^-]/[\text{I}^-]$  remains low), exposure to  $\text{O}_3$  causes a sharp increase in  $\text{I}_2$  (as in Figure 5.2a). As the  $\text{I}_2$  signal decays, the corresponding  $\text{Br}_2$  signals gradually increase, consistent with the interpretation above. In the presence of OH precursors, after one hour of  $\text{O}_3$  exposure in the flow tube,  $\text{I}_2$  yields are comparable for Instant Ocean (IO1, IO2) and saltwater (SW1, SW2), with an average of  $14 \pm 10$  nmol and  $51 \pm 1$  nmol, respectively, as were the yields of  $\text{Br}_2$  ( $0.026 \pm 0.017$  and  $0.026 \pm 0.002$  nmol). When  $\text{pH} < 2$ , the effects of  $\text{O}_3$  vary according to the remaining availability of  $\text{I}^-$ . In cases where the  $\text{I}^-$  reservoir has been reduced from dark reactions with  $\text{HOOH}$  (R19), exposure to  $\text{O}_3$  causes a much smaller, or non-detectable, increase in the  $\text{I}_2$  signal (ranging from below limits of detection, (average of  $9.0 \pm 2.0$  pmol mol<sup>-1</sup> across all experiments), to  $0.11 \pm 0.06$  nmol in IO5), which is at least an order of magnitude less than what was observed at the higher pH. However,  $\text{O}_3$  did cause additional  $\text{Br}_2$  production after one hour (average of  $11 \pm 2$  nmol for IO4 and IO5, and  $14 \pm 2$  nmol for SW4 and SW5). In contrast, for SW3 (using  $\text{NO}_2^-$  as an OH source), there is relatively little initial consumption of  $\text{I}^-$  by dark reaction. When  $\text{O}_3$  was added in this case, an  $\text{I}_2$  yield of  $1.1 \pm 0.1$  nmol was observed, comparable to what was observed at the higher pH.  $\text{Br}_2$  ( $0.46 \pm 0.01$  nmol) was also significantly less than observed when  $\text{I}^-$  was initially depleted. Unfortunately, the addition of  $\text{O}_3$  introduced a strong interference for the signal observed at  $m/z$  197 ( $^{35}\text{Cl}^{35}\text{Cl}^-$ ) rendering  $\text{Cl}_2$  isotopic ratios invalid during these times, and hence no information regarding the relationship between chlorine and  $\text{O}_3$  could be ascertained in this work.

In experiments without an OH source,  $\text{I}_2$  yields are greatest when  $\text{O}_3$  is introduced to the illuminated tube in both pH regimes (Table 5.5). This likely originates from a combination of the mechanism proposed by Kim et al. (2016), heterogeneous recycling,

and the favorable aqueous reaction between  $O_3$  and  $I^-$  ( $k = 2.0 \times 10^{-12} \text{ cm}^3 \text{ molecules}^{-1} \text{ s}^{-1}$  (Liu et al., 2001)) discussed further below.

#### 5.4 Discussion

The ability of the hydroxyl radical to convert  $I^-$ ,  $Br^-$ , and  $Cl^-$  to  $I_2$ ,  $Br_2$ , and  $Cl_2$ , respectively, from frozen saline surfaces was demonstrated above. Under the halide compositions of Instant Ocean,  $I_2$  production was observed under all experimental conditions in the presence of light and  $O_3$  (with the exception of the experiments using only NaCl salt (negligible  $I^-$  impurity)). Bromine production was observed at moderately acidic pH ( $\sim 4.7$ ) in low amounts only after  $O_3$  was introduced in the presence of light. This  $O_3$ -induced production was seemingly not affected by the presence or absence of an explicit OH source. At lower pH (when  $I^-$  had depleted from dark reactions)  $Br_2$  production was readily observed in the presence of lights, and enhanced when the samples were exposed to  $O_3$ . However, if  $I^-$  was not substantially depleted before exposing the samples to radiation,  $I_2$  remained the dominant product. Finally,  $Cl_2$  was only observed photochemically (in the absence of  $O_3$ ) at low pH using high-grade NaCl salt ( $[Br^-]/[Cl^-] = 8.1 \times 10^{-6}$ ) in the presence of HOOH, i.e. largely in the absence of both  $I^-$  and  $Br^-$ . We again note that our observations do not mean  $O_3$  cannot produce  $Cl_2$ , only that it introduced an interfering signal at  $m/z$  197, rendering us unable to obtain such information.

These results appear to be consistent with an acid-enhanced production mechanism in which the dominant products are largely dependent on relative halide ratios. It is expected that  $I_2$  is produced most readily in frozen solutions given the high polarizability and surface affinity of  $I^-$  in aqueous solutions (Gladich et al., 2011). That is, surface

concentrations will be relatively enhanced with larger, more polarizable anions, which favors production of I<sub>2</sub> over Br<sub>2</sub>, and Br<sub>2</sub> over Cl<sub>2</sub>, until the larger ions are depleted through oxidation, and then the next largest ion becomes more readily oxidized. More importantly, in terms of relative reaction rates, the oxidation potentials for I<sup>-</sup>, Br<sup>-</sup>, and Cl<sup>-</sup> are significantly different (e.g., it is a much lower energy process to oxidize I<sup>-</sup> relative to the other halogens). The standard reduction potentials for Cl<sub>2</sub>, Br<sub>2</sub>, and I<sub>2</sub> are 1.360, 1.098, and 0.620V for Cl<sub>2</sub>, Br<sub>2</sub>, and I<sub>2</sub>, respectively (Chemical Rubber Company and Lide, 2005). This is reflected in the estimated relative  $k_{\text{I}^-}/k_{\text{Br}^-}$  of  $(8.9 \pm 4.0) \times 10^3$  (calculated for pH=1.9), and that for  $k_{\text{Br}^-}/k_{\text{Cl}^-} = (2.4 \pm 0.2) \times 10^5$  (calculated for pH=1.8).

Though in situ frozen surfaces largely vary with regard to composition due to atmospheric processing and variable uptake (Krnavek et al., 2012), molecular halogen levels have been previously observed at concentrations within the snowpack gas phase within a factor of 2-10 of each other. For instance, Br<sub>2</sub> has been observed at peak levels of 35 pmol mol<sup>-1</sup> (Custard et al., 2016), I<sub>2</sub> up to 5 pmol mol<sup>-1</sup> (Raso et al., 2016), and Cl<sub>2</sub> levels ranging from 0-20 pmol mol<sup>-1</sup> (Custard et al., 2016). Despite substantially lower natural abundances of I<sup>-</sup>, especially if sea salt aerosol is presumed to be the dominant source of I<sup>-</sup> to these surfaces in the Arctic (Simpson et al., 2005), I<sub>2</sub> is still observed at levels approaching those typical of Cl<sub>2</sub> and Br<sub>2</sub>. The relative rate constants (ease of X<sup>-</sup> oxidation by OH radicals) we calculate would then appear to explain that the reactivity of the larger ions compensate for the low abundances, leading to comparable production rates in our laboratory experiments, and comparable snowpack gas phase concentrations. Using a modified version of Eq. 5.1, we can estimate relative in situ OH-mediated halogen

production rates using published halide ratios from melted in situ snow samples from Barrow, AK (Eq. 5.2).

$$\frac{\frac{d[X_2]}{dt}}{\frac{d[Y_2]}{dt}} = \frac{k_{X^-}[X^-][OH][H^+]}{k_{Y^-}[Y^-][OH][H^+]} \quad \text{E5.2}$$

Using the maximum and minimum reported  $[Br^-]/[Cl^-]$  values of  $0.026 \pm 0.20$  and  $0.0068$

$\pm 0.04$  from Pratt et al. (2013), we find a corresponding range for  $\frac{\frac{d[Br_2]}{dt}}{\frac{d[Cl_2]}{dt}}$  of  $(6.3 \pm 48) \times 10^3$

to  $(1.6 \pm 10) \times 10^3$ . Similarly for Raso et al. (2016), who reported  $[Br^-]/[Cl^-]$  values ranging

from  $0.014 \pm 0.003$  and  $0.077 \pm 0.130$ ,  $\frac{\frac{d[Br_2]}{dt}}{\frac{d[Cl_2]}{dt}}$  is found to range  $(3.4 \pm 0.8) \times 10^3$  to  $(1.8 \pm$

$3.1) \times 10^4$ .  $\frac{\frac{d[I_2]}{dt}}{\frac{d[Br_2]}{dt}}$  can additionally be estimated from Raso et al. (2016). In this case, where

$0.020 \pm 0.004 \leq [I^-]/[Br^-] \leq 0.090 \pm 0.081$ ,  $\frac{\frac{d[I_2]}{dt}}{\frac{d[Br_2]}{dt}}$  values are found to range from  $1.8 \pm 1.0$

$\times 10^2$  to  $8.0 \pm 7.5 \times 10^2$ . Finally,  $[I^-]/[Cl^-]$  ranging from  $(5.1 \pm 0.7) \times 10^{-4}$  to  $(5.1 \pm 0.7) \times$

$10^{-3}$ , we obtain  $\frac{\frac{d[I_2]}{dt}}{\frac{d[Cl_2]}{dt}}$  values of  $(1.1 \pm 0.5) \times 10^6$  to  $(8.1 \pm 3.7) \times 10^6$ . Note that even though

simultaneous production of  $I_2$  and  $Cl_2$  was not observed herein,  $k_{I^-}/k_{Cl^-}$  was calculated by

multiplying  $k_{I^-}/k_{Br^-}$  by  $k_{Br^-}/k_{Cl^-}$ . The results of these calculations indicate that the observed

relative rates of production more than compensate for the relative halide abundances.

However, they are inconsistent with the observed relative snowpack interstitial air

abundances from field observations, which show similar (within a factor 10) abundances

in irradiated snowpack interstitial air. We thus draw the following conclusions:

1. There exist important competing loss processes of Br<sub>2</sub> and I<sub>2</sub> after initial production.

2. Other Cl<sub>2</sub> production pathways account for the majority of ambient concentrations.

Concerning hypothesis 1, one likely loss process includes aqueous inter-halogen partitioning, as in R5.18 (where X = I or Br, and Y = I, Br, or Cl):



Photolysis of X<sub>2</sub> is faster for the larger molecular halogens. For example, Thompson et al., (2015) report  $J_{X_2} = 0.15, 4.4 \times 10^{-2},$  and  $2.1 \times 10^{-3} \text{ s}^{-1}$  for I<sub>2</sub>, Br<sub>2</sub>, and Cl<sub>2</sub>, respectively during solar noon in March at Barrow, AK, or photolytic lifetimes of 7s, 23s, and 476s, respectively. Thus faster photolysis of the larger halogens in the snowpack air will contribute to leveling the production rate differences, given penetration of actinic radiation into the snowpack (King and Simpson, 2001).

There also exists much evidence to support hypothesis 2. Most recently, Wren et al. (2013) observed substantial Cl<sub>2</sub> production from their artificial snow samples in the presence of both O<sub>3</sub> and light, invoking the “halogen explosion” mechanism described in Sect. 1. In this scenario, HOI or HOBr can liberate Cl from the QBL to produce ICl or BrCl, which can undergo R5.1-4 to produce HOCl that ultimately produces Cl<sub>2</sub> (i.e., via R5.4).



Liao et al. (2014) observed results consistent with this mechanism above the snowpack in Barrow, AK, reporting a strong correlation between  $\text{Cl}_2$  levels,  $\text{O}_3$  levels, and solar radiation. This pathway is certainly viable for producing  $\text{Cl}_2$  in our experiments, given the flow tube was flushed with a residence time of 12 seconds. While our experimental conditions focus on the processes that initiate production of  $\text{Br}_2$  and  $\text{I}_2$ , rather than the recycling chemistry (R5.1-4), heterogeneous recycling can help explain the observed enhancements in  $\text{Br}_2$  and  $\text{I}_2$  in the presence of radiation and  $\text{O}_3$ .

While  $\text{O}_3$ -mediated halogen production has been observed directly from frozen surfaces in previous laboratory studies of frozen surfaces (Oldridge and Abbatt, 2011; Oum et al., 1998a; Wren et al., 2013), experiments on samples in the Arctic have not exhibited similar behavior without light, which raises a question of the role of  $\text{O}_3$  in initial halogen release in the Arctic spring. Ozone was found to stimulate additional and substantial  $\text{I}_2$  and  $\text{Br}_2$  production in the experiments herein, as shown in Sect 5.3.2. This additional production could possibly result from the combination of several mechanisms. First, as discussed above,  $\text{O}_3$  can react with halides on frozen saline surfaces to produce molecular bromine or iodine per reactions R5.13-14, R5.4 (Carpenter et al., 2013; Gladich et al., 2015; Hayase et al., 2010; Oum et al., 1998a; Shaw and Carpenter, 2013; Wren et al., 2013). Evidence supporting this mechanism is represented by CIMS signals corresponding to HOX (formed by R16) and IHOX<sup>-</sup> (Figure 5.4-Figure 5.5).



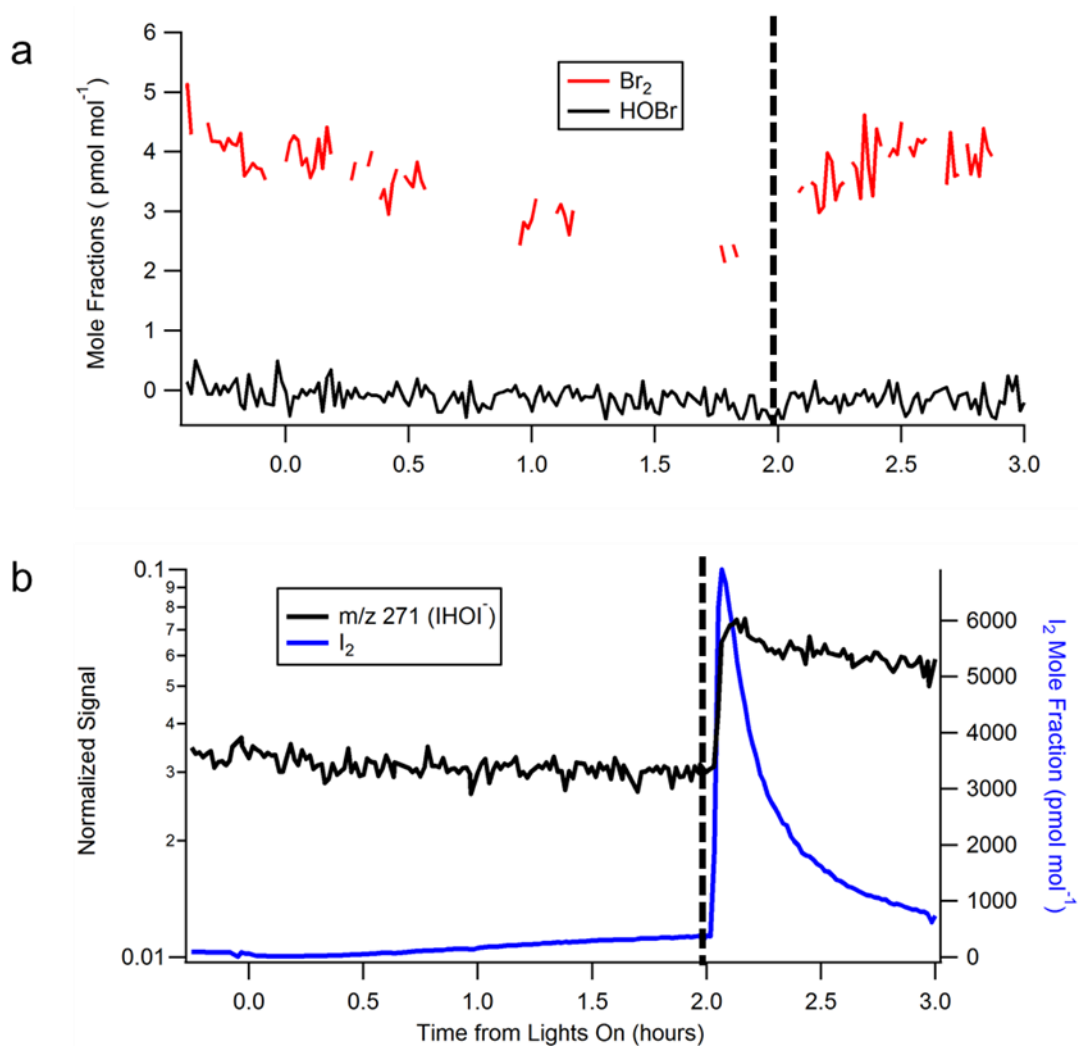


Figure 5.4 HOX signals from experiment IO2. Vertical lines represent time when O<sub>3</sub> is introduced to the system. a) red traces correspond to Br<sub>2</sub> mole fractions (calibrated signal at  $m/z$  287,  $I^{79}\text{Br}^{81}\text{Br}^-$ ), and black trace to HOBr (calibrated signal at  $m/z$  225:  $\text{IHO}^{81}\text{Br}^-$ ). Note that the HOBr signal, while calibrated, should be used only for qualitative purposes as its identity could not be confirmed using isotopic ratios with  $m/z$  223 due to relatively large background. b) blue trace corresponds to I<sub>2</sub> (calibrated signal at  $m/z$  381), and black corresponds to HOI ( $m/z$  271:  $\text{IHOI}^-$ ).

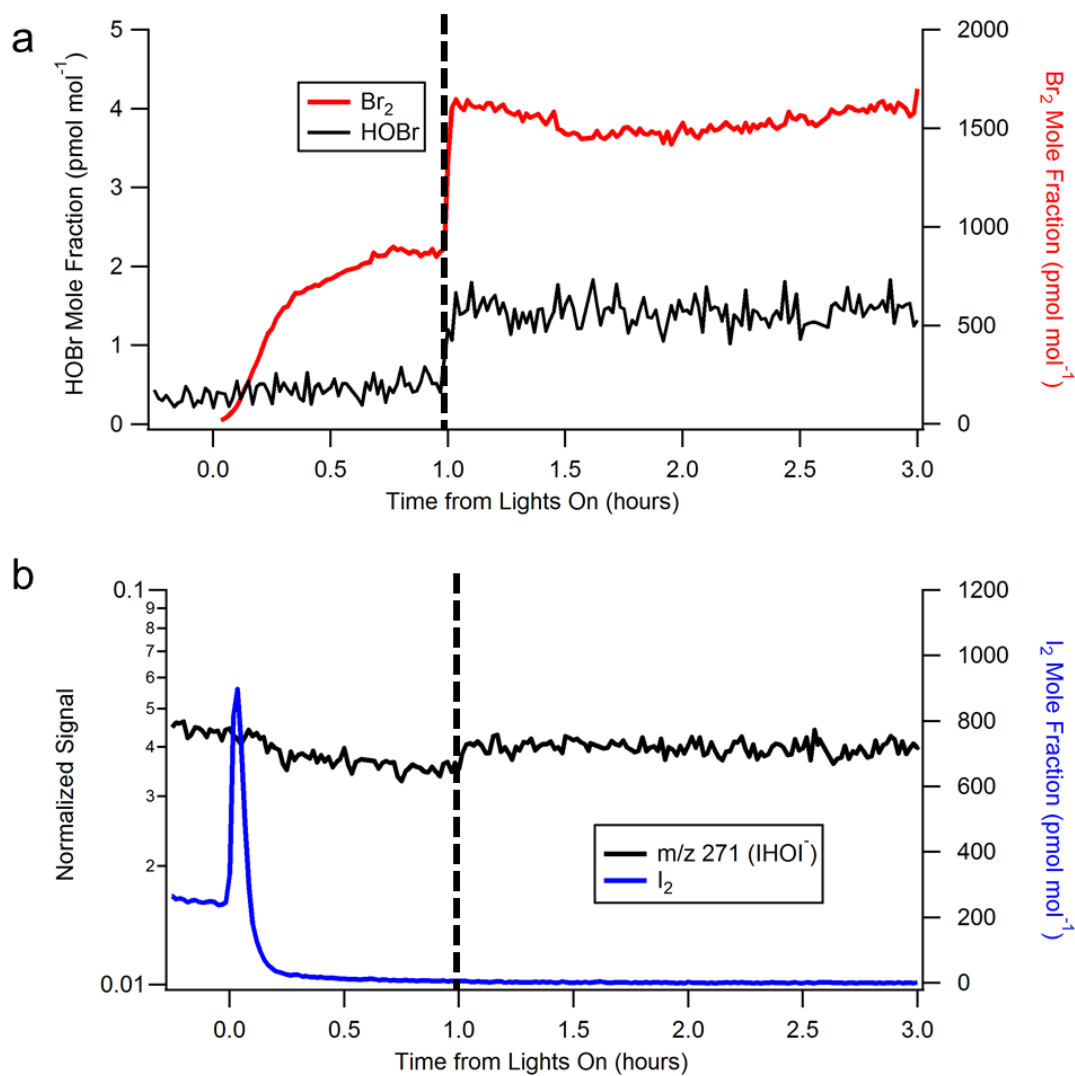


Figure 5.5 HOX signals from experiment SW5. a) red traces correspond to Br<sub>2</sub> mole fractions, and greyscale signals to HOBr m/z 225 - IHO<sup>81</sup>Br<sup>-</sup>). Note that the HOBr signal, while calibrated, should be used only for qualitatively purposes as its identity could not be confirmed using isotopic ratios with m/z 223. b) blue trace corresponds to I<sub>2</sub> mole fractions, and black corresponds to HOI (m/z 271 - IHOI<sup>-</sup>).

Figure 5.4 shows the pH=4.7 experiment using saltwater (Figure 5.2a). In the top portion, it can be seen that the addition of O<sub>3</sub> at hour 2 corresponds to the sudden increase of Br<sub>2</sub>. However, corresponding HOBr production is not observed in this case, perhaps either due to limits of detection, or the relatively low abundance of Br<sub>2</sub>, limiting production of HOBr. In the bottom portion, large increases in I<sub>2</sub> and HOI are readily observed. Conversely, in the low pH cases (corresponding to the experiment in the middle panel of Figure 5.2) when substantial portions of I<sup>-</sup> had already reacted prior to activating the lights, the addition of O<sub>3</sub> at hour 1 produces negligible I<sub>2</sub> or HOI (Figure 5.5, bottom). However, HOBr (m/z 225) is apparently produced following the addition of O<sub>3</sub>, together with rising Br<sub>2</sub> concentrations. We note in this case that m/z 223, representative of <sup>79</sup>HOBr, does not appear to show an enhancement when O<sub>3</sub> is added to the system, but it is noted to have a much higher background signal than m/z 225, possibly as the result of an interference. However, it is more likely that HOX is formed in the gas phase from reactions R5.1-R5.3. Commercial-grade sea-salts contain organic material, the photolysis of which can produce HO<sub>x</sub> precursors such as HCHO, which after production could volatilize from the ice, and then photolyze (Dominé and Shepson, 2002; Sumner and Shepson, 1999). Given a flow tube flush time of 12 seconds, gas phase production of HOX is possible, and could potentially enhance X<sub>2</sub> production, given a timescale for molecular diffusion of 6.5 seconds for HOBr from the center of the tube to the ice surface. At this flow rate, there is enough time for 1-2 heterogeneous reaction cycles.

Since it has been shown that halogen activation is pH-dependent, this raises the question of the pH of relevant Arctic surfaces. Sulfate aerosol pH in the Arctic is estimated to be about 0 (Fan and Jacob, 1992), while in the continental United States, it is typically

0.5-3 (e.g., Guo et al., 2015). Pratt et al. (2013) indicate that for Arctic surface production of Br<sub>2</sub>, the snow pH must be acidic, and that no production is observed from well-buffered ice brine or other highly saline surfaces. However, the actual snowpack surface pH is unknown, as the freeze-concentration effect tends to concentrate ions at the surface in the QBL. Thus, given the prevalence of HOOH on surfaces (deposited from gas-phase production, R5.19), and with low pH, reactions R5.17 and R5.4 could subsequently lead to I<sub>2</sub> production in the dark, which could then be present during polar sunrise.



This is consistent with a peak in I<sup>-</sup> levels from aerosol measurements that occurs in Spring and Fall (Barrie and Hoff, 1985). Sturges and Barrie (1988) report that I<sup>-</sup> in Arctic aerosols is enriched relative to sea salt by a factor of 10<sup>3</sup> – 10<sup>4</sup>. There must then be active in situ photochemistry and recycling on surfaces. It is likely that both Br<sub>2</sub> and Cl<sub>2</sub> are produced via OH radical initiation, but that bromine explosion chemistry (and similar chemistry for chlorine) dominates after this initial production, and is more important to producing Cl<sub>2</sub> (via HOCl). The work of Pratt et al. (2013) proposes the role of O<sub>3</sub> in accelerating Br<sub>2</sub> production in the snowpack interstitial air via HOBr production and subsequent deposition on surfaces, and that also likely occurs for chlorine (Liao et al., 2014; Wren et al., 2013).

## 5.5 Summary and Conclusions

It has been shown herein that the hydroxyl radical can act as an effective halide ion oxidant for I<sub>2</sub>, Br<sub>2</sub>, and Cl<sub>2</sub> under acidic conditions. Rates of release appear to be

influenced by both pH and relative halide amounts, in which the observed product is highly influenced by which ions are enhanced at the ice surface. An opportunity exists to further explore this chemistry via surface interrogation methods, for which recent developments have been shown to effectively characterize the surface composition of frozen solutions of sodium chloride under near atmospherically relevant conditions (Orlando et al., 2016). While OH can produce Br<sub>2</sub> and I<sub>2</sub> most rapidly, it appears that heterogeneous recycling of HOCl could be a more dominant mechanism behind production of gas phase Cl<sub>2</sub>. We find the addition of O<sub>3</sub> provides additional production of at least Br<sub>2</sub> and I<sub>2</sub>, probably through gas-phase production of HOX. These results lend support for the mechanisms proposed by the recent in situ snowpack experiments near Barrow, AK (Custard et al., 2016; Pratt et al., 2013; Raso et al., 2016). Additionally, they indicate the need to canvas snow pH to ascertain how widespread the potential is for halogen chemistry around the Arctic.

## CHAPTER 6. CONCLUSIONS

The work presented in this thesis contributes to our understanding of the behavior of surface-level ozone in the Arctic during springtime. Ozone depletion events (ODEs) have been long believed to initiate over the Arctic Ocean since their discovery in the late 1980s (Oltmans and Komhyr, 1986), though very few long-term field observations are available to study ODEs “in situ.” Here, the first analyses of long-term Arctic Ocean-based  $O_3$  measurements from buoy-based observatories have been used to ascertain “in situ” timescales of  $O_3$  decay (median 11 hours), the spatial extents of ODEs (median diameter of ~900 km), as well as the temperatures (range of 243 – 273 K) and wind speeds (<1 – 7.5 m/s) under which ODEs are observed (Chapter 3). Even though a major finding of Chapter 3 was that the ODEs could still be observed due primarily because of air mass transport, as is often claimed at coastal sites (e.g., Bottenheim et al., 1986, 2002b; Hausmann and Platt, 1994; Tuckermann et al., 1997) it was found in Chapter 4 that sea ice surface types had only minor influence on  $O_3$  variability over local meteorology. Paired with the observation that the majority of Arctic Ocean based measurements are below  $10 \text{ nmol mol}^{-1}$ , this suggests that the Arctic is largely  $O_3$  depleted during springtime, and possibly only interrupted during periods of turbulent activity. While these results improve our

knowledge of ODEs as they occur over the Arctic Ocean, they more importantly illuminate the need for future work to fully understand their underlying mechanisms. As discussed in Chapter 3, a recent modelling study by Thompson et al. (2015) finds that the inclusion of very small amounts of iodine ( $0.025 - 0.5 \text{ pmol mol}^{-1}$ ) to a 0-D chemical model constrained to actual observations of  $\text{O}_3$ , chlorine, and bromine species at Barrow, AK, can deplete  $\text{O}_3$  from  $35 \text{ nmol mol}^{-1}$  to  $5 \text{ nmol mol}^{-1}$  at timescales resembling those in Chapter 3. A similar modeling study constrained to O-Buoy observations can be undertaken to determine what concentrations of reactive halogens are required to mimic those results. Further, as has been discussed throughout this thesis, advances in mass spectrometry have enabled quantitative measurements of low levels of molecular halogens. While this technique has been employed at Barrow, AK, (Custard et al., 2016; Liao et al., 2011, 2012a, 2014; Pratt et al., 2013; Raso et al., 2016), and in aircraft studies off the Alaskan coast (Neuman et al., 2010), there is a need to expand CIMS observations to the Arctic Ocean, possibly at ice camps, to confirm the presence of  $\text{I}_2$  activity and thus its role in ODEs.

In addition, there is some difficulty in interpreting the effects of O-Buoy meteorology as it relates to  $\text{O}_3$  variability. Are sudden changes in temperature and pressure a localized event, possibly related to the opening of a nearby lead, while  $\text{O}_3$  levels in the Arctic at large remain depleted? Could they instead be more indicative of a synoptic scale event or storm, and ODE chemistry must once again occur before on a large scale before low  $\text{O}_3$  is observed again? While the O-Buoy project has so far seen 19 buoy deployments as of this writing, concurrent deployments without catastrophic failures of at least the  $\text{O}_3$  instrument are limited to OB11-12 (deployed in Fall 2014), and OB13-14 (deployed in Fall 2015), both sets of which were deployed in the Beaufort Sea. In addition, we have the

coincident observations of OB4 and Icelander 2 in 2012, though they were separated by more than 2000 km. Further effort should be placed into concurrent buoy deployments at multiple sites around the Arctic Ocean, though securing spots on multiple icebreakers and securing capital for ship time is certainly a non-trivial task.

The mechanism and conditions by which molecular halogens are introduced into the boundary layer remains a subject of debate, though a hydroxyl radical based chemical mechanism has been recently proposed from field observations of snowpack interstitial air (Pratt et al., 2013; Raso et al., 2016). The photolysis of hydroxyl radical precursors was demonstrated to produce molecular chlorine, bromine, and iodine from frozen acidic surfaces in Chapter 5. Similar to the field based results, bromine and iodine production were further enhanced in the presence of  $O_3$ , though we cannot comment on  $O_3$ 's influence on chlorine production. Not only have we improved our understanding of fundamental halogen chemistry, the relative rates of halogen production quantified in this work are likely to benefit chemical models that attempt to simulate the onset of ODEs during polar spring.

In closing, there still exists much work to be done before our understanding of ODE chemistry can be considered “full.” While the Arctic is far removed from the majority of human life, it is highly likely the chemistry discussed herein also occurs in snow-covered mid-latitude regions during wintertime, which has yet to be seriously considered in its effects on the mid-latitude  $O_3$  budget. Though the Arctic is undergoing rapid change that will likely soon cause an end to Arctic ODE chemistry entirely, it remains our best laboratory for investigating this phenomenon given its pristine condition, and evaluating how these chemical pathways may ultimately affect human life and the rest of the planet.



## LIST OF REFERENCES

## LIST OF REFERENCES

Abbatt, J., Oldridge, N., Symington, A., Chukalovskiy, V., McWhinney, R. D., Sjostedt, S. and Cox, R. A.: Release of Gas-Phase Halogens by Photolytic Generation of OH in Frozen Halide–Nitrate Solutions: An Active Halogen Formation Mechanism?, *J. Phys. Chem. A*, 114(23), 6527–6533, doi:10.1021/jp102072t, 2010.

Abbatt, J. P. D., Thomas, J. L., Abrahamsson, K., Boxe, C., Granfors, A., Jones, A. E., King, M. D., Saiz-Lopez, A., Shepson, P. B., Sodeau, J., Toohey, D. W., Toubin, C., von Glasow, R., Wren, S. N. and Yang, X.: Halogen activation via interactions with environmental ice and snow in the polar lower troposphere and other regions, *Atmos Chem Phys*, 12(14), 6237–6271, doi:10.5194/acp-12-6237-2012, 2012.

Adams, J. W., Holmes, N. S. and Crowley, J. N.: Uptake and reaction of HOBr on frozen and dry NaCl/NaBr surfaces between 253 and 233 K, *Atmospheric Chem. Phys.*, 2(1), 79–91, doi:10.5194/acp-2-79-2002, 2002.

Aguzzi, A. and Rossi, M. J.: Heterogeneous Hydrolysis and Reaction of BrONO<sub>2</sub> and Br<sub>2</sub>O on Pure Ice and Ice Doped with HBr, *J. Phys. Chem. A*, 106(24), 5891–5901, doi:10.1021/jp014383e, 2002.

Albert, M. R., Grannas, A. M., Bottenheim, J., Shepson, P. B. and Perron, F. E.: Processes and properties of snow–air transfer in the high Arctic with application to interstitial ozone at Alert, Canada, *Atmos. Environ.*, 36(15–16), 2779–2787, doi:10.1016/S1352-2310(02)00118-8, 2002.

Anastasio, C., Galbavy, E. S., Hutterli, M. A., Burkhart, J. F. and Friel, D. K.: Photoformation of hydroxyl radical on snow grains at Summit, Greenland, *Atmos. Environ.*, 41(24), 5110–5121, doi:10.1016/j.atmosenv.2006.12.011, 2007.

Anderson, P. S. and Neff, W. D.: Boundary layer physics over snow and ice, *Atmos Chem Phys*, 8(13), 3563–3582, doi:10.5194/acp-8-3563-2008, 2008.

Anlauf, K. G., Mickle, R. E. and Trivett, N. B. A.: Measurement of ozone during Polar Sunrise Experiment 1992, *J. Geophys. Res.*, 99(D12), 25345, doi:10.1029/94JD01312, 1994.

- Atkinson, R., Baulch, D. L., Cox, R. A., Crowley, J. N., Hampson, R. F., Hynes, R. G., Jenkin, M. E., Rossi, M. J., Troe, J. and IUPAC Subcommittee: Evaluated kinetic and photochemical data for atmospheric chemistry: Volume II - gas phase reactions of organic species, *Atmospheric Chem. Phys.*, 6(11), 3625–4055, doi:10.5194/acp-6-3625-2006, 2006.
- Atkinson, R., Baulch, D. L., Cox, R. A., Crowley, J. N., Hampson, R. F., Hynes, R. G., Jenkin, M. E., Rossi, M. J. and Troe, J.: Evaluated kinetic and photochemical data for atmospheric chemistry: Volume III - gas phase reactions of inorganic halogens, *Atmospheric Chem. Phys.*, 7(4), 981–1191, doi:10.5194/acp-7-981-2007, 2007.
- Avallone, L. M., Toohey, D. W., Fortin, T. J., McKinney, K. A. and Fuentes, J. D.: In situ measurements of bromine oxide at two high-latitude boundary layer sites: Implications of variability, *J. Geophys. Res. Atmospheres*, 108(D3), 4089, doi:10.1029/2002JD002843, 2003.
- Barrie, L. and Platt, U.: Arctic tropospheric chemistry: an overview, *Tellus B*, 49(5), 450–454, doi:10.1034/j.1600-0889.49.issue5.2.x, 1997.
- Barrie, L. A. and Hoff, R. M.: Five years of air chemistry observations in the Canadian Arctic, *Atmospheric Environ.* 1967, 19(12), 1995–2010, doi:10.1016/0004-6981(85)90108-8, 1985.
- Barrie, L. A., Hoff, R. M. and Daggupaty, S. M.: The influence of mid-latitude pollution sources on haze in the Canadian arctic, *Atmospheric Environ.* 1967, 15(8), 1407–1419, doi:10.1016/0004-6981(81)90347-4, 1981.
- Barrie, L. A., Bottenheim, J. W., Schnell, R. C., Crutzen, P. J. and Rasmussen, R. A.: Ozone destruction and photochemical reactions at polar sunrise in the lower Arctic atmosphere, *Nature*, 334(6178), 138–141, doi:10.1038/334138a0, 1988.
- Barrie, L. A., Olson, M. P. and Oikawa, K. K.: Arctic Air Chemistry The flux of anthropogenic sulphur into the arctic from mid-latitudes in 1979/80, *Atmospheric Environ.* 1967, 23(11), 2505–2512, doi:10.1016/0004-6981(89)90262-X, 1989.
- Barrie, L. A., Staebler, R., Toom, D., Georgi, B., den Hartog, G., Landsberger, S. and Wu, D.: Arctic aerosol size-segregated chemical observations in relation to ozone depletion during Polar Sunrise Experiment 1992, *J. Geophys. Res.*, 99(D12), 25439, doi:10.1029/94JD01514, 1994a.
- Barrie, L. A., Li, S.-M., Toom, D. L., Landsberger, S. and Sturges, W.: Lower tropospheric measurements of halogens, nitrates, and sulphur oxides during Polar Sunrise Experiment 1992, *J. Geophys. Res. Atmospheres*, 99(D12), 25453–25467, doi:10.1029/94JD01533, 1994b.

- Barrie, L. A., Bottenheim, J. W. and Hart, W. R.: Polar Sunrise Experiment 1992 (PSE 1992): Preface, *J. Geophys. Res. Atmospheres*, 99(D12), 25313–25314, doi:10.1029/94JD01929, 1994c.
- Bartels-Rausch, T., Jacobi, H.-W., Kahan, T. F., Thomas, J. L., Thomson, E. S., Abbatt, J. P. D., Ammann, M., Blackford, J. R., Bluhm, H., Boxe, C., Domine, F., Frey, M. M., Gladich, I., Guzmán, M. I., Heger, D., Huthwelker, T., Klán, P., Kuhs, W. F., Kuo, M. H., Maus, S., Moussa, S. G., McNeill, V. F., Newberg, J. T., Pettersson, J. B. C., Roeselová, M. and Sodeau, J. R.: A review of air–ice chemical and physical interactions (AICI): liquids, quasi-liquids, and solids in snow, *Atmos Chem Phys*, 14(3), 1587–1633, doi:10.5194/acp-14-1587-2014, 2014.
- Begoin, M., Richter, A., Weber, M., Kaleschke, L., Tian-Kunze, X., Stohl, A., Theys, N. and Burrows, J. P.: Satellite observations of long range transport of a large BrO plume in the Arctic, *Atmos Chem Phys*, 10(14), 6515–6526, doi:10.5194/acp-10-6515-2010, 2010.
- Beine, H. J., Honrath, R. E., Dominé, F., Simpson, W. R. and Fuentes, J. D.: NO<sub>x</sub> during background and ozone depletion periods at Alert: Fluxes above the snow surface, *J. Geophys. Res. Atmospheres*, 107(D21), 4584, doi:10.1029/2002JD002082, 2002.
- Blacet, F. E.: Photochemistry in the Lower Atmosphere, *Ind. Eng. Chem.*, 44(6), 1339–1342, doi:10.1021/ie50510a044, 1952.
- Bottenheim, J. W. and Chan, E.: A trajectory study into the origin of spring time Arctic boundary layer ozone depletion, *J. Geophys. Res. Atmospheres*, 111(D19), D19301, doi:10.1029/2006JD007055, 2006.
- Bottenheim, J. W., Gallant, A. G. and Brice, K. A.: Measurements of NO<sub>y</sub> species and O<sub>3</sub> at 82° N latitude, *Geophys. Res. Lett.*, 13(2), 113–116, doi:10.1029/GL013i002p00113, 1986.
- Bottenheim, J. W., Barrie, L. A., Atlas, E., Heidt, L. E., Niki, H., Rasmussen, R. A. and Shepson, P. B.: Depletion of lower tropospheric ozone during Arctic spring: The Polar Sunrise Experiment 1988, *J. Geophys. Res. Atmospheres*, 95(D11), 18555–18568, doi:10.1029/JD095iD11p18555, 1990.
- Bottenheim, J. W., Dibb, J. E., Honrath, R. E. and Shepson, P. B.: An introduction to the ALERT 2000 and SUMMIT 2000 Arctic research studies, *Atmos. Environ.*, 36(15–16), 2467–2469, doi:10.1016/S1352-2310(02)00135-8, 2002a.
- Bottenheim, J. W., Fuentes, J. D., Tarasick, D. W. and Anlauf, K. G.: Ozone in the Arctic lower troposphere during winter and spring 2000 (ALERT2000), *Atmos. Environ.*, 36(15–16), 2535–2544, doi:10.1016/S1352-2310(02)00121-8, 2002b.

- Bottenheim, J. W., Natcheva, S., Morin, S. and Nghiem, S. V.: Ozone in the boundary layer air over the Arctic Ocean: measurements during the TARA transpolar drift 2006–2008, *Atmos Chem Phys*, 9(14), 4545–4557, doi:10.5194/acp-9-4545-2009, 2009.
- Boudries, H. and Bottenheim, J. W.: Cl and Br atom concentrations during a surface boundary layer ozone depletion event in the Canadian High Arctic, *Geophys. Res. Lett.*, 27(4), 517–520, doi:10.1029/1999GL011025, 2000.
- Boylan, P., Helmig, D., Staebler, R., Turnipseed, A., Fairall, C. and Neff, W.: Boundary layer dynamics during the Ocean-Atmosphere-Sea-Ice-Snow (OASIS) 2009 experiment at Barrow, AK, *J. Geophys. Res. Atmospheres*, 119(5), 2261–2278, doi:10.1002/2013JD020299, 2014.
- Brown, D., Cabbage, M. and McCarthy, L.: NASA, NOAA Analyses Reveal Record-Shattering Global Temperatures, NASA [online] Available from: <http://www.nasa.gov/press-release/nasa-noaa-analyses-reveal-record-shattering-global-warm-temperatures-in-2015> (Accessed 5 June 2016), 2016.
- Calvert, J. G. and Lindberg, S. E.: Potential influence of iodine-containing compounds on the chemistry of the troposphere in the polar spring. I. Ozone depletion, *Atmos. Environ.*, 38(30), 5087–5104, doi:10.1016/j.atmosenv.2004.05.049, 2004.
- Cao, L., Sihler, H., Platt, U. and Gutheil, E.: Numerical analysis of the chemical kinetic mechanisms of ozone depletion and halogen release in the polar troposphere, *Atmos Chem Phys*, 14(7), 3771–3787, doi:10.5194/acp-14-3771-2014, 2014.
- Carlson, D., Donohoue, D., Platt, U. and Simpson, W. R.: A low power automated MAX-DOAS instrument for the Arctic and other remote unmanned locations, *Atmos Meas Tech*, 3(2), 429–439, doi:10.5194/amt-3-429-2010, 2010.
- Carpenter, L. J., MacDonald, S. M., Shaw, M. D., Kumar, R., Saunders, R. W., Parthipan, R., Wilson, J. and Plane, J. M. C.: Atmospheric iodine levels influenced by sea surface emissions of inorganic iodine, *Nat. Geosci.*, 6(2), 108–111, doi:10.1038/ngeo1687, 2013.
- Cavender, A. E., Biesenthal, T. A., Bottenheim, J. W. and Shepson, P. B.: Volatile organic compound ratios as probes of halogen atom chemistry in the Arctic, *Atmospheric Chem. Phys.*, 8(6), 1737–1750, doi:10.5194/acp-8-1737-2008, 2008.
- Chameides, W. L., Fehsenfeld, F., Rodgers, M. O., Cardelino, C., Martinez, J., Parrish, D., Lonneman, W., Lawson, D. R., Rasmussen, R. A., Zimmerman, P., Greenberg, J., Middleton, P. and Wang, T.: Ozone precursor relationships in the ambient atmosphere, *J. Geophys. Res. Atmospheres*, 97(D5), 6037–6055, doi:10.1029/91JD03014, 1992.
- Chance, K. V. and Spurr, R. J. D.: Ring effect studies: Rayleigh scattering, including molecular parameters for rotational Raman scattering, and the Fraunhofer spectrum, *Appl. Opt.*, 36(21), 5224, doi:10.1364/AO.36.005224, 1997.

Chapman, S.: XXXV. On ozone and atomic oxygen in the upper atmosphere, Lond. Edinb. Dublin Philos. Mag. J. Sci., 10(64), 369–383, doi:10.1080/14786443009461588, 1930.

Chemical Rubber Company and Lide, D. R., Eds.: CRC handbook of chemistry and physics: a ready-reference book of chemical and physical data, 86. ed., CRC Press, Boca Raton., 2005.

Cho, H., Shepson, P. B., Barrie, L. A., Cowin, J. P. and Zaveri, R.: NMR Investigation of the Quasi-Brine Layer in Ice/Brine Mixtures, *J. Phys. Chem. B*, 106(43), 11226–11232, doi:10.1021/jp020449+, 2002.

Choi, S., Wang, Y., Salawitch, R. J., Canty, T., Joiner, J., Zeng, T., Kurosu, T. P., Chance, K., Richter, A., Huey, L. G., Liao, J., Neuman, J. A., Nowak, J. B., Dibb, J. E., Weinheimer, A. J., Diskin, G., Ryerson, T. B., da Silva, A., Curry, J., Kinnison, D., Tilmes, S. and Levelt, P. F.: Analysis of satellite-derived Arctic tropospheric BrO columns in conjunction with aircraft measurements during ARCTAS and ARCPAC, *Atmos Chem Phys*, 12(3), 1255–1285, doi:10.5194/acp-12-1255-2012, 2012.

Chu, L. and Anastasio, C.: Quantum Yields of Hydroxyl Radical and Nitrogen Dioxide from the Photolysis of Nitrate on Ice, *J. Phys. Chem. A*, 107(45), 9594–9602, doi:10.1021/jp0349132, 2003.

Chu, L. and Anastasio, C.: Formation of Hydroxyl Radical from the Photolysis of Frozen Hydrogen Peroxide, *J. Phys. Chem. A*, 109(28), 6264–6271, doi:10.1021/jp051415f, 2005.

Comiso, J. C., Cavalieri, D. J. and Markus, T.: Sea ice concentration, ice temperature, and snow depth using AMSR-E data, *IEEE Trans. Geosci. Remote Sens.*, 41(2), 243–252, doi:10.1109/TGRS.2002.808317, 2003.

Cooper, O. R., Parrish, D. D., Ziemke, J., Balashov, N. V., Cupeiro, M., Galbally, I. E., Gilge, S., Horowitz, L., Jensen, N. R., Lamarque, J.-F., Naik, V., Oltmans, S. J., Schwab, J., Shindell, D. T., Thompson, A. M., Thouret, V., Wang, Y. and Zbinden, R. M.: Global distribution and trends of tropospheric ozone: An observation-based review, *Elem. Sci. Anthr.*, 2, 29, doi:10.12952/journal.elementa.000029, 2014.

Custard, K. D., Raso, A., Shepson, P. B., Staebler, R. M. and Pratt, K. A.: Production and release of molecular bromine and chlorine from the Arctic coastal snowpack, *J. Geophys. Res.*, (in preparation), 2016.

Deutschmann, T., Beirle, S., Frieß, U., Grzegorski, M., Kern, C., Kritten, L., Platt, U., Prados-Román, C., Puķi-te, J., Wagner, T., Werner, B. and Pfeilsticker, K.: The Monte Carlo atmospheric radiative transfer model McArtim: Introduction and validation of Jacobians and 3D features, *J. Quant. Spectrosc. Radiat. Transf.*, 112(6), 1119–1137, doi:10.1016/j.jqsrt.2010.12.009, 2011.

- Dominé, F. and Shepson, P. B.: Air-Snow Interactions and Atmospheric Chemistry, *Science*, 297(5586), 1506–1510, doi:10.1126/science.1074610, 2002.
- Dominé, F., Sparapani, R., Ianniello, A. and Beine, H. J.: The origin of sea salt in snow on Arctic sea ice and in coastal regions, *Atmos Chem Phys*, 4(9/10), 2259–2271, doi:10.5194/acp-4-2259-2004, 2004.
- Draxler, R. and Rolph, G.: HYSPLIT (HYbrid Single-Particle Lagrangian Integrated Trajectory) NOAA Air Resources Laboratory, Silver Spring MD, 2003.
- Draxler, R., Stunder, B., Rolph, G., Stein, A. and Taylor, A.: HYSPLIT 4 User Guide Overview., 2012.
- Draxler, R. R. and Hess, G.: An overview of the HYSPLIT\_4 modelling system for trajectories, *Aust. Meteorol. Mag.*, 47(4), 295–308, 1998.
- Evans, M. J., Jacob, D. J., Atlas, E., Cantrell, C. A., Eisele, F., Flocke, F., Fried, A., Mauldin, R. L., Ridley, B. A., Wert, B., Talbot, R., Blake, D., Heikes, B., Snow, J., Walega, J., Weinheimer, A. J. and Dibb, J.: Coupled evolution of BrO<sub>x</sub>-ClO<sub>x</sub>-HO<sub>x</sub>-NO<sub>x</sub> chemistry during bromine-catalyzed ozone depletion events in the arctic boundary layer, *J. Geophys. Res. Atmospheres*, 108(D4), 8368, doi:10.1029/2002JD002732, 2003.
- Ezraty, R. and Cavanié, A.: Intercomparison of backscatter maps over Arctic sea ice from NSCAT and the ERS scatterometer, *J. Geophys. Res. Oceans*, 104(C5), 11471–11483, doi:10.1029/1998JC900086, 1999.
- Faïn, X., Moosmüller, H. and Obrist, D.: Toward real-time measurement of atmospheric mercury concentrations using cavity ring-down spectroscopy, *Atmos Chem Phys*, 10(6), 2879–2892, doi:10.5194/acp-10-2879-2010, 2010.
- Fan, S.-M. and Jacob, D. J.: Surface ozone depletion in Arctic spring sustained by bromine reactions on aerosols, *Nature*, 359(6395), 522–524, doi:10.1038/359522a0, 1992.
- Farman, J. C., Gardiner, B. G. and Shanklin, J. D.: Large losses of total ozone in Antarctica reveal seasonal ClO<sub>x</sub>/NO<sub>x</sub> interaction, *Nature*, 315(6016), 207–210, doi:10.1038/315207a0, 1985.
- Fayt, C., De Smedt, I., Letocart, V., Merlaud, A., Pinardi, G., Van Roozendael, M. and Roozendael, M.: QDOAS Software user manual, Belg. Inst. Space Aeron. Bruss. Belg., 2011.
- Fickert, S., Adams, J. W. and Crowley, J. N.: Activation of Br<sub>2</sub> and BrCl via uptake of HOBr onto aqueous salt solutions, *J. Geophys. Res. Atmospheres*, 104(D19), 23719–23727, doi:10.1029/1999JD900359, 1999.

Finlayson-Pitts, B. J. and Pitts, J. N.: Chemistry of the upper and lower atmosphere: theory, experiments, and applications, Academic Press, San Diego., 2000.

Foster, K. L., Plastridge, R. A., Bottenheim, J. W., Shepson, P. B., Finlayson-Pitts, B. J. and Spicer, C. W.: The Role of Br<sub>2</sub> and BrCl in Surface Ozone Destruction at Polar Sunrise, *Science*, 291(5503), 471–474, doi:10.1126/science.291.5503.471, 2001.

France, J. L., Reay, H. J., King, M. D., Voisin, D., Jacobi, H. W., Domine, F., Beine, H., Anastasio, C., MacArthur, A. and Lee-Taylor, J.: Hydroxyl radical and NO<sub>x</sub> production rates, black carbon concentrations and light-absorbing impurities in snow from field measurements of light penetration and nadir reflectivity of onshore and offshore coastal Alaskan snow, *J. Geophys. Res.*, 117, doi:10.1029/2011JD016639, 2012.

Frieß, U., Monks, P. S., Remedios, J. J., Rozanov, A., Sinreich, R., Wagner, T. and Platt, U.: MAX-DOAS O<sub>4</sub> measurements: A new technique to derive information on atmospheric aerosols: 2. Modeling studies, *J. Geophys. Res.*, 111(D14), doi:10.1029/2005JD006618, 2006.

Frieß, U., Sihler, H., Sander, R., Pöhler, D., Yilmaz, S. and Platt, U.: The vertical distribution of BrO and aerosols in the Arctic: Measurements by active and passive differential optical absorption spectroscopy, *J. Geophys. Res.*, 116, doi:10.1029/2011JD015938, 2011.

Garland, J. A. and Curtis, H.: Emission of iodine from the sea surface in the presence of ozone, *J. Geophys. Res.*, 86(C4), 3183, doi:10.1029/JC086iC04p03183, 1981.

Gauss, M., Myhre, G., Isaksen, I. S. A., Grewe, V., Pitari, G., Wild, O., Collins, W. J., Dentener, F. J., Ellingsen, K., Gohar, L. K., Hauglustaine, D. A., Iachetti, D., Lamarque, F., Mancini, E., Mickley, L. J., Prather, M. J., Pyle, J. A., Sanderson, M. G., Shine, K. P., Stevenson, D. S., Sudo, K., Szopa, S. and Zeng, G.: Radiative forcing since preindustrial times due to ozone change in the troposphere and the lower stratosphere, *Atmos Chem Phys*, 6(3), 575–599, doi:10.5194/acp-6-575-2006, 2006.

Gilman, J. B., Burkhart, J. F., Lerner, B. M., Williams, E. J., Kuster, W. C., Goldan, P. D., Murphy, P. C., Warneke, C., Fowler, C., Montzka, S. A., Miller, B. R., Miller, L., Oltmans, S. J., Ryerson, T. B., Cooper, O. R., Stohl, A. and de Gouw, J. A.: Ozone variability and halogen oxidation within the Arctic and sub-Arctic springtime boundary layer, *Atmos Chem Phys*, 10(21), 10223–10236, doi:10.5194/acp-10-10223-2010, 2010.

Gladich, I., Shepson, P. B., Carignano, M. A. and Szleifer, I.: Halide Affinity for the Water–Air Interface in Aqueous Solutions of Mixtures of Sodium Salts, *J. Phys. Chem. A*, 115(23), 5895–5899, doi:10.1021/jp110208a, 2011.

Gladich, I., Francisco, J. S., Buszek, R. J., Vazdar, M., Carignano, M. A. and Shepson, P. B.: Ab Initio Study of the Reaction of Ozone with Bromide Ion, *J. Phys. Chem. A*, 119(19), 4482–4488, doi:10.1021/jp5101279, 2015.



Greenblatt, G. D., Orlando, J. J., Burkholder, J. B. and Ravishankara, A. R.: Absorption measurements of oxygen between 330 and 1140 nm, *J. Geophys. Res. Atmospheres*, 95(D11), 18577–18582, doi:10.1029/JD095iD11p18577, 1990.

Grosch, H., Sárossy, Z., Egsgaard, H. and Fateev, A.: UV absorption cross-sections of phenol and naphthalene at temperatures up to 500 °C, *J. Quant. Spectrosc. Radiat. Transf.*, 156, 17–23, doi:10.1016/j.jqsrt.2015.01.021, 2015.

Guo, H., Xu, L., Bougiatioti, A., Cerully, K. M., Capps, S. L., Hite Jr., J. R., Carlton, A. G., Lee, S.-H., Bergin, M. H., Ng, N. L., Nenes, A. and Weber, R. J.: Fine-particle water and pH in the southeastern United States, *Atmos Chem Phys*, 15(9), 5211–5228, doi:10.5194/acp-15-5211-2015, 2015.

Halfacre, J. W., Knepp, T. N., Shepson, P. B., Thompson, C. R., Pratt, K. A., Li, B., Peterson, P. K., Walsh, S. J., Simpson, W. R., Matrai, P. A., Bottenheim, J. W., Netcheva, S., Perovich, D. K. and Richter, A.: Temporal and spatial characteristics of ozone depletion events from measurements in the Arctic, *Atmos Chem Phys*, 14(10), 4875–4894, doi:10.5194/acp-14-4875-2014, 2014.

Hanson, D. R. and Ravishankara, A. R.: Heterogeneous chemistry of bromine species in sulfuric acid under stratospheric conditions, *Geophys. Res. Lett.*, 22(4), 385–388, doi:10.1029/94GL03379, 1995.

Hausmann, M. and Platt, U.: Spectroscopic measurement of bromine oxide and ozone in the high Arctic during Polar Sunrise Experiment 1992, *J. Geophys. Res. Atmospheres*, 99(D12), 25399–25413, doi:10.1029/94JD01314, 1994.

Hayase, S., Yabushita, A., Kawasaki, M., Enami, S., Hoffmann, M. R. and Colussi, A. J.: Heterogeneous Reaction of Gaseous Ozone with Aqueous Iodide in the Presence of Aqueous Organic Species, *J. Phys. Chem. A*, 114(19), 6016–6021, doi:10.1021/jp101985f, 2010.

Helmig, D., Cohen, L. D., Bocquet, F., Oltmans, S., Grachev, A. and Neff, W.: Spring and summertime diurnal surface ozone fluxes over the polar snow at Summit, Greenland, *Geophys. Res. Lett.*, 36(8), doi:10.1029/2008GL036549, 2009.

Helmig, D., Boylan, P., Johnson, B., Oltmans, S., Fairall, C., Staebler, R., Weinheimer, A., Orlando, J., Knapp, D. J., Montzka, D. D., Flocke, F., Frieß, U., Sihler, H. and Shepson, P. B.: Ozone dynamics and snow-atmosphere exchanges during ozone depletion events at Barrow, Alaska, *J. Geophys. Res. Atmospheres*, 117(D20), D20303, doi:10.1029/2012JD017531, 2012.

Hermans, C., Vandaele, A. C., Coquart, B., Jenouvrier, A., Merienne, M. F., Fally, S., Carleer, M. and Colin, R.: Absorption bands of O<sub>2</sub> and its collision-induced bands in the 30 000–7500 cm<sup>-1</sup> wavenumber region, Deepak, Hampton, VA., 2001.

- Herring, J. R. and Liss, P. S.: A new method for the determination of iodine species in seawater, *Deep Sea Res. Oceanogr. Abstr.*, 21(9), 777–783, doi:10.1016/0011-7471(74)90085-0, 1974.
- Hewitt, C. N., Kok, G. L. and Fall, R.: Hydroperoxides in plants exposed to ozone mediate air pollution damage to alkene emitters, *Publ. Online* 01 March 1990  
Doi101038344056a0, 344(6261), 56–58, doi:10.1038/344056a0, 1990.
- Hilal, N., Kim, G. J. and Somerfield, C.: Boron removal from saline water: A comprehensive review, *Desalination*, 273(1), 23–35, doi:10.1016/j.desal.2010.05.012, 2011.
- Hönninger, G., Leser, H., Sebastián, O. and Platt, U.: Ground-based measurements of halogen oxides at the Hudson Bay by active longpath DOAS and passive MAX-DOAS, *Geophys. Res. Lett.*, 31(4), L04111, doi:10.1029/2003GL018982, 2004a.
- Hönninger, G., von Friedeburg, C. and Platt, U.: Multi axis differential optical absorption spectroscopy (MAX-DOAS), *Atmos Chem Phys*, 4(1), 231–254, doi:10.5194/acp-4-231-2004, 2004b.
- Honrath, R. E., Peterson, M. C., Guo, S., Dibb, J. E., Shepson, P. B. and Campbell, B.: Evidence of NO<sub>x</sub> production within or upon ice particles in the Greenland snowpack, *Geophys. Res. Lett.*, 26(6), 695–698, doi:10.1029/1999GL900077, 1999.
- Honrath, R. E., Lu, Y., Peterson, M. C., Dibb, J. E., Arsenault, M. A., Cullen, N. J. and Steffen, K.: Vertical fluxes of NO<sub>x</sub>, HONO, and HNO<sub>3</sub> above the snowpack at Summit, Greenland, *Atmos. Environ.*, 36(15–16), 2629–2640, doi:10.1016/S1352-2310(02)00132-2, 2002.
- Hopper, J. F. and Hart, W.: Meteorological aspects of the 1992 Polar Sunrise Experiment, *J. Geophys. Res. Atmospheres*, 99(D12), 25315–25328, doi:10.1029/94JD02400, 1994.
- Hopper, J. F., Peters, B., Yokouchi, Y., Niki, H., Jobson, B. T., Shepson, P. B. and Muthuramu, K.: Chemical and meteorological observations at ice camp SWAN during Polar Sunrise Experiment 1992, *J. Geophys. Res. Atmospheres*, 99(D12), 25489–25498, doi:10.1029/94JD02303, 1994.
- Hopper, J. F., Barrie, L. A., Silis, A., Hart, W., Gallant, A. J. and Dryfhout, H.: Ozone and meteorology during the 1994 Polar Sunrise Experiment, *J. Geophys. Res. Atmospheres*, 103(D1), 1481–1492, doi:10.1029/97JD02888, 1998.
- Horowitz, L. W., Walters, S., Mauzerall, D. L., Emmons, L. K., Rasch, P. J., Granier, C., Tie, X., Lamarque, J.-F., Schultz, M. G., Tyndall, G. S., Orlando, J. J. and Brasseur, G. P.: A global simulation of tropospheric ozone and related tracers: Description and evaluation of MOZART, version 2: MOZART-2 DESCRIPTION AND EVALUATION, *J. Geophys. Res. Atmospheres*, 108(D24), n/a-n/a, doi:10.1029/2002JD002853, 2003.

- Hubbell, B. J., Hallberg, A., McCubbin, D. R. and Post, E.: Health-Related Benefits of Attaining the 8-Hr Ozone Standard, *Environ. Health Perspect.*, 113(1), 73–82, 2005.
- Huff, A. K. and Abbatt, J. P. D.: Kinetics and Product Yields in the Heterogeneous Reactions of HOBr with Ice Surfaces Containing NaBr and NaCl, *J. Phys. Chem. A*, 106(21), 5279–5287, doi:10.1021/jp014296m, 2002.
- Hutterli, M. A., McConnell, J. R., Stewart, R. W., Jacobi, H.-W. and Bales, R. C.: Impact of temperature-driven cycling of hydrogen peroxide ( $H_2O_2$ ) between air and snow on the planetary boundary layer, *J. Geophys. Res. Atmospheres*, 106(D14), 15395–15404, doi:10.1029/2001JD900102, 2001.
- Jacobi, H.-W., Frey, M. M., Hutterli, M. A., Bales, R. C., Schrems, O., Cullen, N. J., Steffen, K. and Koehler, C.: Measurements of hydrogen peroxide and formaldehyde exchange between the atmosphere and surface snow at Summit, Greenland, *Atmos. Environ.*, 36(15–16), 2619–2628, doi:10.1016/S1352-2310(02)00106-1, 2002.
- Jacobi, H.-W., Kaleschke, L., Richter, A., Rozanov, A. and Burrows, J. P.: Observation of a fast ozone loss in the marginal ice zone of the Arctic Ocean, *J. Geophys. Res. Atmospheres*, 111(D15), D15309, doi:10.1029/2005JD006715, 2006.
- Jacobi, H.-W., Morin, S. and Bottenheim, J. W.: Observation of widespread depletion of ozone in the springtime boundary layer of the central Arctic linked to mesoscale synoptic conditions, *J. Geophys. Res.*, 115(D17), doi:10.1029/2010JD013940, 2010.
- Jaeschke, W., Salkowski, T., Dierssen, J. P., Trümbach, J. T., Krischke, U. and Günther, A.: Measurements of Trace Substances in the Arctic Troposphere as Potential Precursors and Constituents of Arctic Haze, *J. Atmospheric Chem.*, 34(3), 291–319, doi:10.1023/A:1006277230042, 1999.
- Jia, C. and Batterman, S.: A Critical Review of Naphthalene Sources and Exposures Relevant to Indoor and Outdoor Air, *Int. J. Environ. Res. Public Health*, 7(7), 2903–2939, doi:10.3390/ijerph7072903, 2010.
- Jobson, B. T., Niki, H., Yokouchi, Y., Bottenheim, J., Hopper, F. and Leitch, R.: Measurements of  $C_2$ - $C_6$  hydrocarbons during the Polar Sunrise 1992 Experiment: Evidence for Cl atom and Br atom chemistry, *J. Geophys. Res.*, 99(D12), 25355, doi:10.1029/94JD01243, 1994.
- Jones, A. E., Anderson, P. S., Begoin, M., Brough, N., Hutterli, M. A., Marshall, G. J., Richter, A., Roscoe, H. K. and Wolff, E. W.: BrO, blizzards, and drivers of polar tropospheric ozone depletion events, *Atmospheric Chem. Phys.*, 9(14), 4639–4652, doi:10.5194/acp-9-4639-2009, 2009.

- Jones, A. E., Wolff, E. W., Brough, N., Bauguitte, S. J.-B., Weller, R., Yela, M., Navarro-Comas, M., Ochoa, H. A. and Theys, N.: The spatial scale of ozone depletion events derived from an autonomous surface ozone network in coastal Antarctica, *Atmospheric Chem. Phys.*, 13(3), 1457–1467, doi:10.5194/acp-13-1457-2013, 2013.
- Kahl, J. D.: Arctic air, snow and ice chemistry A cautionary note on the use of air trajectories in interpreting atmospheric chemistry measurements, *Atmospheric Environ. Part Gen. Top.*, 27(17), 3037–3038, doi:10.1016/0960-1686(93)90336-W, 1993.
- Keil, A. D. and Shepson, P. B.: Chlorine and bromine atom ratios in the springtime Arctic troposphere as determined from measurements of halogenated volatile organic compounds, *J. Geophys. Res. Atmospheres*, 111(D17), D17303, doi:10.1029/2006JD007119, 2006.
- Kim, K., Yabushita, A., Okumura, M., Saiz-Lopez, A., Cuevas, C. A., Blaszczyk-Boxe, C. S., Min, D. W., Yoon, H.-I. and Choi, W.: Production of Molecular Iodine and Triiodide in the Frozen Solution of Iodide: Implication for Polar Atmosphere, *Environ. Sci. Technol.*, 50(3), 1280–1287, doi:10.1021/acs.est.5b05148, 2016.
- Knepp, T. N.: A multi-scale approach to elucidating the role of ice surfaces and synoptic meteorology in spring-time Arctic tropospheric ozone depletion events, *Dissertation*, Purdue University, West Lafayette, IN., 2010.
- Knepp, T. N., Bottenheim, J., Carlsen, M., Carlson, D., Donohoue, D., Friederich, G., Matrai, P. A., Netcheva, S., Perovich, D. K., Santini, R., Shepson, P. B., Simpson, W., Valentic, T., Williams, C. and Wyss, P. J.: Development of an autonomous sea ice tethered buoy for the study of ocean-atmosphere-sea ice-snow pack interactions: the O-buoy, *Atmos Meas Tech*, 3(1), 249–261, doi:10.5194/amt-3-249-2010, 2010.
- Knipping, E. M., Lakin, M. J., Foster, K. L., Jungwirth, P., Tobias, D. J., Gerber, R. B., Dabdub, D. and Finlayson-Pitts, B. J.: Experiments and Simulations of Ion-Enhanced Interfacial Chemistry on Aqueous NaCl Aerosols, *Science*, 288(5464), 301–306, doi:10.1126/science.288.5464.301, 2000.
- Koo, J.-H., Wang, Y., Kurosu, T. P., Chance, K., Rozanov, A., Richter, A., Oltmans, S. J., Thompson, A. M., Hair, J. W., Fenn, M. A., Weinheimer, A. J., Ryerson, T. B., Solberg, S., Huey, L. G., Liao, J., Dibb, J. E., Neuman, J. A., Nowak, J. B., Pierce, R. B., Natarajan, M. and Al-Saadi, J.: Characteristics of tropospheric ozone depletion events in the Arctic spring: analysis of the ARCTAS, ARCPAC, and ARCIONS measurements and satellite BrO observations, *Atmos Chem Phys*, 12(20), 9909–9922, doi:10.5194/acp-12-9909-2012, 2012.
- Koop, T., Luo, B., Tsias, A. and Peter, T.: Water activity as the determinant for homogeneous ice nucleation in aqueous solutions, *Nature*, 406(6796), 611–614, doi:10.1038/35020537, 2000.

- Krishfield, R. A., Proshutinsky, A., Tateyama, K., Williams, W. J., Carmack, E. C., McLaughlin, F. A. and Timmermans, M.-L.: Deterioration of perennial sea ice in the Beaufort Gyre from 2003 to 2012 and its impact on the oceanic freshwater cycle, *J. Geophys. Res. Oceans*, 119(2), 1271–1305, doi:10.1002/2013JC008999, 2014.
- Krnavek, L., Simpson, W. R., Carlson, D., Domine, F., Douglas, T. A. and Sturm, M.: The chemical composition of surface snow in the Arctic: Examining marine, terrestrial, and atmospheric influences, *Atmos. Environ.*, 50, 349–359, doi:10.1016/j.atmosenv.2011.11.033, 2012.
- Kumar, P. and Sharan, M.: Parameterization of the eddy diffusivity in a dispersion model over homogeneous terrain in the atmospheric boundary layer, *Atmospheric Res.*, 106, 30–43, doi:10.1016/j.atmosres.2011.10.020, 2012.
- Kuo, M. H., Moussa, S. G. and McNeill, V. F.: Modeling interfacial liquid layers on environmental ices, *Atmos Chem Phys*, 11(18), 9971–9982, doi:10.5194/acp-11-9971-2011, 2011.
- Küpper, F. C., Schweigert, N., Gall, E. A., Legendre, J.-M., Vilter, H. and Kloareg, B.: Iodine uptake in Laminariales involves extracellular, haloperoxidase-mediated oxidation of iodide, *Planta*, 207(2), 163–171, doi:10.1007/s004250050469, 1998.
- Kwok, R., Cunningham, G. F., Wensnahan, M., Rigor, I., Zwally, H. J. and Yi, D.: Thinning and volume loss of the Arctic Ocean sea ice cover: 2003–2008, *J. Geophys. Res.*, 114(C7), doi:10.1029/2009JC005312, 2009.
- Le Bras, G. and Platt, U.: A possible mechanism for combined chlorine and bromine catalyzed destruction of tropospheric ozone in the Arctic, *Geophys. Res. Lett.*, 22(5), 599–602, doi:10.1029/94GL03334, 1995.
- Leaitch, W. R., Barrie, L. A., Bottenheim, J. W., Li, S. M., Shepson, P. B., Muthuramu, K. and Yokouchi, Y.: Airborne observations related to ozone depletion at polar sunrise, *J. Geophys. Res. Atmospheres*, 99(D12), 25499–25517, doi:10.1029/94JD02750, 1994.
- Lehrer, E., Hönninger, G. and Platt, U.: A one dimensional model study of the mechanism of halogen liberation and vertical transport in the polar troposphere, *Atmos Chem Phys*, 4(11/12), 2427–2440, doi:10.5194/acp-4-2427-2004, 2004.
- Levanon, H. and Navon, G.: Spectrum and stability of oxygen iodide charge-transfer complex, *J. Phys. Chem.*, 73(6), 1861–1868, doi:10.1021/j100726a038, 1969.
- Li, S.-M., Yokouchi, Y., Barrie, L. A., Muthuramu, K., Shepson, P. B., Bottenheim, J. W., Sturges, W. T. and Landsberger, S.: Organic and inorganic bromine compounds and their composition in the Arctic troposphere during polar sunrise, *J. Geophys. Res. Atmospheres*, 99(D12), 25415–25428, doi:10.1029/93JD03343, 1994.

Liao, J., Sihler, H., Huey, L. G., Neuman, J. A., Tanner, D. J., Friess, U., Platt, U., Flocke, F. M., Orlando, J. J., Shepson, P. B., Beine, H. J., Weinheimer, A. J., Sjostedt, S. J., Nowak, J. B., Knapp, D. J., Staebler, R. M., Zheng, W., Sander, R., Hall, S. R. and Ullmann, K.: A comparison of Arctic BrO measurements by chemical ionization mass spectrometry and long path-differential optical absorption spectroscopy, *J. Geophys. Res. Atmospheres*, 116(D14), D00R02, doi:10.1029/2010JD014788, 2011.

Liao, J., Huey, L. G., Tanner, D. J., Flocke, F. M., Orlando, J. J., Neuman, J. A., Nowak, J. B., Weinheimer, A. J., Hall, S. R., Smith, J. N., Fried, A., Staebler, R. M., Wang, Y., Koo, J.-H., Cantrell, C. A., Weibring, P., Walega, J., Knapp, D. J., Shepson, P. B. and Stephens, C. R.: Observations of inorganic bromine (HOBr, BrO, and Br<sub>2</sub>) speciation at Barrow, Alaska, in spring 2009, *J. Geophys. Res. Atmospheres*, 117(D14), D00R16, doi:10.1029/2011JD016641, 2012a.

Liao, J., Huey, L. G., Tanner, D. J., Flocke, F. M., Orlando, J. J., Neuman, J. A., Nowak, J. B., Weinheimer, A. J., Hall, S. R., Smith, J. N., Fried, A., Staebler, R. M., Wang, Y., Koo, J.-H., Cantrell, C. A., Weibring, P., Walega, J., Knapp, D. J., Shepson, P. B. and Stephens, C. R.: Observations of inorganic bromine (HOBr, BrO, and Br<sub>2</sub>) speciation at Barrow, Alaska, in spring 2009, *J. Geophys. Res.*, 117(D14), D00R16, doi:10.1029/2011JD016641, 2012b.

Liao, J., Huey, L. G., Liu, Z., Tanner, D. J., Cantrell, C. A., Orlando, J. J., Flocke, F. M., Shepson, P. B., Weinheimer, A. J., Hall, S. R., Ullmann, K., Beine, H. J., Wang, Y., Ingall, E. D., Stephens, C. R., Hornbrook, R. S., Apel, E. C., Riemer, D., Fried, A., Mauldin III, R. L., Smith, J. N., Staebler, R. M., Neuman, J. A. and Nowak, J. B.: High levels of molecular chlorine in the Arctic atmosphere, *Nat. Geosci.*, 7(2), 91–94, doi:10.1038/ngeo2046, 2014.

Liu, Q., Schurter, L. M., Muller, C. E., Aloisio, S., Francisco, J. S. and Margerum, D. W.: Kinetics and Mechanisms of Aqueous Ozone Reactions with Bromide, Sulfite, Hydrogen Sulfite, Iodide, and Nitrite Ions, *Inorg. Chem.*, 40(17), 4436–4442, doi:10.1021/ic000919j, 2001.

Ma, Y., Xie, Z., Yang, H., Möller, A., Halsall, C., Cai, M., Sturm, R. and Ebinghaus, R.: Deposition of polycyclic aromatic hydrocarbons in the North Pacific and the Arctic: AIR-SEA EXCHANGE OF PAHS IN THE ARCTIC, *J. Geophys. Res. Atmospheres*, 118(11), 5822–5829, doi:10.1002/jgrd.50473, 2013.

Malicet, J., Daumont, D., Charbonnier, J., Parisse, C., Chakir, A. and Brion, J.: Ozone UV spectroscopy. II. Absorption cross-sections and temperature dependence, *J. Atmospheric Chem.*, 21(3), 263–273, doi:10.1007/BF00696758, 1995.

Marengo, A., Gouget, H., Nédélec, P., Pagés, J.-P. and Karcher, F.: Evidence of a long-term increase in tropospheric ozone from Pic du Midi data series: Consequences: Positive radiative forcing, *J. Geophys. Res. Atmospheres*, 99(D8), 16617–16632, doi:10.1029/94JD00021, 1994.

Martinez, M., Arnold, T. and Perner, D.: The role of bromine and chlorine chemistry for arctic ozone depletion events in Ny-Ålesund and comparison with model calculations, *Ann. Geophys.*, 17(7), 941–956, doi:10.1007/s00585-999-0941-4, 1999.

McConnell, J. C., Henderson, G. S., Barrie, L., Bottenheim, J., Niki, H., Langford, C. H. and Templeton, E. M. J.: Photochemical bromine production implicated in Arctic boundary-layer ozone depletion, *Nature*, 355(6356), 150–152, doi:10.1038/355150a0, 1992.

Melling, H., Riedel, D. A. and Gedalof, Z.: Trends in the draft and extent of seasonal pack ice, Canadian Beaufort Sea, *Geophys. Res. Lett.*, 32(24), L24501, doi:10.1029/2005GL024483, 2005.

Michalowski, B. A., Francisco, J. S., Li, S.-M., Barrie, L. A., Bottenheim, J. W. and Shepson, P. B.: A computer model study of multiphase chemistry in the Arctic boundary layer during polar sunrise, *J. Geophys. Res. Atmospheres*, 105(D12), 15131–15145, doi:10.1029/2000JD900004, 2000.

Mickley, L. J., Murti, P. P., Jacob, D. J., Logan, J. A., Koch, D. M. and Rind, D.: Radiative forcing from tropospheric ozone calculated with a unified chemistry-climate model, *J. Geophys. Res. Atmospheres*, 104(D23), 30153–30172, doi:10.1029/1999JD900439, 1999.

Miller, H. L., Weaver, A., Sanders, R. W., Arpag, K. and Solomon, S.: Measurements of arctic sunrise surface ozone depletion events at Kangerlussuaq, Greenland (67°N, 51°W), *Tellus B*, 49(5), 496–509, doi:10.1034/j.1600-0889.49.issue5.6.x, 1997.

Molina, L. T. and Molina, M. J.: Absolute absorption cross sections of ozone in the 185- to 350-nm wavelength range, *J. Geophys. Res. Atmospheres*, 91(D13), 14501–14508, doi:10.1029/JD091iD13p14501, 1986.

Molina, M. J. and Rowland, F. S.: Stratospheric sink for chlorofluoromethanes: chlorine atom-catalysed destruction of ozone, *Nature*, 249(5460), 810–812, doi:10.1038/249810a0, 1974.

Moore, C. W., Obrist, D., Steffen, A., Staebler, R. M., Douglas, T. A., Richter, A. and Nghiem, S. V.: Convective forcing of mercury and ozone in the Arctic boundary layer induced by leads in sea ice, *Nature*, 506(7486), 81–84, doi:10.1038/nature12924, 2014.

Morin, S., Hönninger, G., Staebler, R. M. and Bottenheim, J. W.: A high time resolution study of boundary layer ozone chemistry and dynamics over the Arctic Ocean near Alert, Nunavut, *Geophys. Res. Lett.*, 32(8), L08809, doi:10.1029/2004GL022098, 2005.

Morin, S., Savarino, J., Bekki, S., Gong, S. and Bottenheim, J. W.: Signature of Arctic surface ozone depletion events in the isotope anomaly ( $\Delta^{17}\text{O}$ ) of atmospheric nitrate, *Atmos Chem Phys*, 7(5), 1451–1469, doi:10.5194/acp-7-1451-2007, 2007.

- Morin, S., Erbland, J., Savarino, J., Domine, F., Bock, J., Friess, U., Jacobi, H.-W., Sihler, H. and Martins, J. M. F.: An isotopic view on the connection between photolytic emissions of NO<sub>x</sub> from the Arctic snowpack and its oxidation by reactive halogens, *J. Geophys. Res. Atmospheres*, 117(D14), D00R08, doi:10.1029/2011JD016618, 2012.
- Myhre, G., Shindell, D., Bréon, F.-M., Collins, W., Fuglestvedt, J., Huang, J., Koch, D., Lamarque, J.-F., Lee, D., Mendoza, B., Nakajima, T., Robock, A., Stephens, G., Takemura, T. and Zhang, H.: Anthropogenic and Natural Radiative Forcing, in *Climate Change 2013: The Physical Science Basis. Contribution of Working Group I to the Fifth Assessment Report of the Intergovernmental Panel on Climate Change*, edited by T. F. Stocker, D. Qin, G.-K. Plattner, M. Tignor, S. K. Allen, J. Boschung, A. Nauels, Y. Xia, V. Bex, and P. M. Midgley, pp. 659–740, Cambridge University Press, Cambridge, United Kingdom and New York, NY, USA. [online] Available from: [www.climatechange2013.org](http://www.climatechange2013.org), 2013.
- Neuman, J. A., Nowak, J. B., Huey, L. G., Burkholder, J. B., Dibb, J. E., Holloway, J. S., Liao, J., Peischl, J., Roberts, J. M., Ryerson, T. B., Scheuer, E., Stark, H., Stickel, R. E., Tanner, D. J. and Weinheimer, A.: Bromine measurements in ozone depleted air over the Arctic Ocean, *Atmos Chem Phys*, 10(14), 6503–6514, doi:10.5194/acp-10-6503-2010, 2010.
- Nghiem, S. V., Rigor, I. G., Richter, A., Burrows, J. P., Shepson, P. B., Bottenheim, J., Barber, D. G., Steffen, A., Latonas, J., Wang, F., Stern, G., Clemente-Colón, P., Martin, S., Hall, D. K., Kaleschke, L., Tackett, P., Neumann, G. and Asplin, M. G.: Field and satellite observations of the formation and distribution of Arctic atmospheric bromine above a rejuvenated sea ice cover, *J. Geophys. Res. Atmospheres*, 117(D17), D00S05, doi:10.1029/2011JD016268, 2012a.
- Nghiem, S. V., Hall, D. K., Mote, T. L., Tedesco, M., Albert, M. R., Keegan, K., Shuman, C. A., DiGirolamo, N. E. and Neumann, G.: The extreme melt across the Greenland ice sheet in 2012, *Geophys. Res. Lett.*, 39(20), L20502, doi:10.1029/2012GL053611, 2012b.
- Nghiem, S. V., Clemente-Colón, P., Douglas, T., Moore, C., Obrist, D., Perovich, D. K., Pratt, K. A., Rigor, I. G., Simpson, W., Shepson, P. B., Steffen, A. and Woods, J.: Studying Bromine, Ozone, and Mercury Chemistry in the Arctic, *Eos Trans. Am. Geophys. Union*, 94(33), 289–291, doi:10.1002/2013EO330002, 2013.
- O'Driscoll, P., Lang, K., Minogue, N. and Sodeau, J.: Freezing Halide Ion Solutions and the Release of Interhalogens to the Atmosphere, *J. Phys. Chem. A*, 110(14), 4615–4618, doi:10.1021/jp060491v, 2006.
- O'Driscoll, P., Minogue, N., Takenaka, N. and Sodeau, J.: Release of Nitric Oxide and Iodine to the Atmosphere from the Freezing of Sea-Salt Aerosol Components, *J. Phys. Chem. A*, 112(8), 1677–1682, doi:10.1021/jp710464c, 2008.



Oldridge, N. W. and Abbatt, J. P. D.: Formation of Gas-Phase Bromine from Interaction of Ozone with Frozen and Liquid NaCl/NaBr Solutions: Quantitative Separation of Surficial Chemistry from Bulk-Phase Reaction, *J. Phys. Chem. A*, 115(12), 2590–2598, doi:10.1021/jp200074u, 2011.

Oltmans, S. J. and Komhyr, W. D.: Surface ozone distributions and variations from 1973–1984: Measurements at the NOAA Geophysical Monitoring for Climatic Change Baseline Observatories, *J. Geophys. Res. Atmospheres*, 91(D4), 5229–5236, doi:10.1029/JD091iD04p05229, 1986.

Oltmans, S. J. and Levy, H.: Surface ozone measurements from a global network, *Atmos. Environ.*, 28(1), 9–24, doi:10.1016/1352-2310(94)90019-1, 1994.

Oltmans, S. J., Schnell, R. C., Sheridan, P. J., Peterson, R. E., Li, S.-M., Winchester, J. W., Tans, P. P., Sturges, W. T., Kahl, J. D. and Barrie, L. A.: Arctic Air Chemistry Seasonal surface ozone and filterable bromine relationship in the high Arctic, *Atmospheric Environ.* 1967, 23(11), 2431–2441, doi:10.1016/0004-6981(89)90254-0, 1989.

Oltmans, S. J., Johnson, B. J. and Harris, J. M.: Springtime boundary layer ozone depletion at Barrow, Alaska: Meteorological influence, year-to-year variation, and long-term change, *J. Geophys. Res. Atmospheres*, 117(D14), D00R18, doi:10.1029/2011JD016889, 2012.

Orlando, F., Waldner, A., Bartels-Rausch, T., Birrer, M., Kato, S., Lee, M.-T., Proff, C., Huthwelker, T., Kleibert, A., Bokhoven, J. van and Ammann, M.: The Environmental Photochemistry of Oxide Surfaces and the Nature of Frozen Salt Solutions: A New in Situ XPS Approach, *Top. Catal.*, 1–14, doi:10.1007/s11244-015-0515-5, 2016.

O’Sullivan, D. and Sodeau, J. R.: Freeze-Induced Reactions: Formation of Iodine–Bromine Interhalogen Species from Aqueous Halide Ion Solutions, *J. Phys. Chem. A*, 114(46), 12208–12215, doi:10.1021/jp104910p, 2010.

Oum, K. W., Lakin, M. J. and Finlayson-Pitts, B. J.: Bromine activation in the troposphere by the dark reaction of O<sub>3</sub> with seawater ice, *Geophys. Res. Lett.*, 25(21), 3923–3926, doi:10.1029/1998GL900078, 1998a.

Oum, K. W., Lakin, M. J., DeHaan, D. O., Brauers, T. and Finlayson-Pitts, B. J.: Formation of Molecular Chlorine from the Photolysis of Ozone and Aqueous Sea-Salt Particles, *Science*, 279(5347), 74–76, doi:10.1126/science.279.5347.74, 1998b.

Overland, J., Hanna, E., Hanssen-Bauer, I., Kim, S.-J., Walsh, J. E., Wang, M., Bhatt, U. S. and Thoman, R. L.: Arctic Report Card - Surface Air Temperature, [online] Available from: [http://www.arctic.noaa.gov/reportcard/air\\_temperature.html](http://www.arctic.noaa.gov/reportcard/air_temperature.html) (Accessed 5 June 2016), 2015.

- Parrish, D. D. and Zhu, T.: Clean Air for Megacities, *Science*, 326(5953), 674–675, doi:10.1126/science.1176064, 2009.
- Perovich, D. K. and Polashenski, C.: Albedo evolution of seasonal Arctic sea ice: ALEDO EVOLUTION OF SEASONAL SEA ICE, *Geophys. Res. Lett.*, 39(8), n/a-n/a, doi:10.1029/2012GL051432, 2012.
- Peterson, P. K.: Examining the role of sea ice and meteorology in Arctic boundary layer halogen chemistry, Dissertation, University of Alaska Fairbanks, Fairbanks, AK., 2015.
- Peterson, P. K., Pratt, K. A., Simpson, W. R., Nghiem, S. V., Pérez Pérez, L. X., Boone, E. J., Pöhler, D., Zielcke, J., General, S., Shepson, P. B., Frieß, U., Platt, U. and Stirm, B. H.: The role of open lead interactions in atmospheric ozone variability between Arctic coastal and inland sites, *Elem. Sci. Anthr.*, 4, 109, doi:10.12952/journal.elementa.000109, 2016a.
- Peterson, P. K., Simpson, W. R. and Nghiem, S. V.: Variability of bromine monoxide at Barrow, Alaska, over four halogen activation (March–May) seasons and at two on-ice locations, *J. Geophys. Res. Atmospheres*, 121(3), 2015JD024094, doi:10.1002/2015JD024094, 2016b.
- Phibbs, M. K. and Giguère, P. A.: Hydrogen Peroxide and Its Analogues: Iii. Absorption Spectrum of Hydrogen and Deuterium Peroxides in the Near Ultraviolet, *Can. J. Chem.*, 29(6), 490–493, doi:10.1139/v51-058, 1951.
- Piot, M. and von Glasow, R.: The potential importance of frost flowers, recycling on snow, and open leads for ozone depletion events, *Atmos Chem Phys*, 8(9), 2437–2467, doi:10.5194/acp-8-2437-2008, 2008.
- Piot, M. and von Glasow, R.: Modelling the multiphase near-surface chemistry related to ozone depletions in polar spring, *J. Atmospheric Chem.*, 64(2–3), 77–105, doi:10.1007/s10874-010-9170-1, 2009.
- Platt, U. and Hönninger, G.: The role of halogen species in the troposphere, *Chemosphere*, 52(2), 325–338, doi:10.1016/S0045-6535(03)00216-9, 2003.
- Platt, U. and Janssen, C.: Observation and role of the free radicals NO<sub>3</sub>, ClO, BrO and IO in the troposphere, *Faraday Discuss.*, 100(0), 175–198, doi:10.1039/FD9950000175, 1995.
- Pöhler, D., Vogel, L., Frieß, U. and Platt, U.: Observation of halogen species in the Amundsen Gulf, Arctic, by active long-path differential optical absorption spectroscopy, *Proc. Natl. Acad. Sci.*, 107(15), 6582–6587, doi:10.1073/pnas.0912231107, 2010.
- Post, E., Bhatt, U. S., Bitz, C. M., Brodie, J. F., Fulton, T. L., Hebblewhite, M., Kerby, J., Kutz, S. J., Stirling, I. and Walker, D. A.: Ecological Consequences of Sea-Ice Decline, *Science*, 341(6145), 519–524, doi:10.1126/science.1235225, 2013.

- Pratt, K. A., Custard, K. D., Shepson, P. B., Douglas, T. A., Pöhler, D., General, S., Zielcke, J., Simpson, W. R., Platt, U., Tanner, D. J., Gregory Huey, L., Carlsen, M. and Stirm, B. H.: Photochemical production of molecular bromine in Arctic surface snowpacks, *Nat. Geosci.*, 6(5), 351–356, doi:10.1038/ngeo1779, 2013.
- Raga, G. B. and Raga, A. C.: On the formation of an elevated ozone peak in Mexico City, *Atmos. Environ.*, 34(24), 4097–4102, doi:10.1016/S1352-2310(00)00070-4, 2000.
- Raso, A., Custard, K. D., Pratt, K. A., Tanner, D. J., Huey, L. G. and Shepson, P. B.: Active molecular iodine snowpack photochemistry in the Arctic, *J. Geophys. Res.*, (submitted), 2016.
- Read, K. A., Mahajan, A. S., Carpenter, L. J., Evans, M. J., Faria, B. V. E., Heard, D. E., Hopkins, J. R., Lee, J. D., Moller, S. J., Lewis, A. C., Mendes, L., McQuaid, J. B., Oetjen, H., Saiz-Lopez, A., Pilling, M. J. and Plane, J. M. C.: Extensive halogen-mediated ozone destruction over the tropical Atlantic Ocean, *Nature*, 453(7199), 1232–1235, doi:10.1038/nature07035, 2008.
- Richter, A., Wittrock, F., Eisinger, M. and Burrows, J. P.: GOME observations of tropospheric BrO in northern hemispheric spring and summer 1997, *Geophys. Res. Lett.*, 25(14), 2683–2686, doi:10.1029/98GL52016, 1998.
- Ridley, B., Walega, J., Montzka, D., Grahek, F., Atlas, E., Flocke, F., Stroud, V., Deary, J., Gallant, A., Boudries, H., Bottenheim, J., Anlauf, K., Worthy, D., Sumner, A. L., Splawn, B. and Shepson, P.: Is the Arctic Surface Layer a Source and Sink of NO<sub>x</sub> in Winter/Spring?, *J. Atmospheric Chem.*, 36(1), 1–22, doi:10.1023/A:1006301029874, 2000.
- Ridley, B. A. and Orlando, J. J.: Active Nitrogen in Surface Ozone Depletion Events at Alert during Spring 1998, *J. Atmospheric Chem.*, 44(1), 1–22, doi:10.1023/A:1022188822920, 2003.
- Ridley, B. A., Madronich, S., Chatfield, R. B., Walega, J. G., Shetter, R. E., Carroll, M. A. and Montzka, D. D.: Measurements and model simulations of the photostationary state during the Mauna Loa Observatory Photochemistry Experiment: Implications for radical concentrations and ozone production and loss rates, *J. Geophys. Res. Atmospheres*, 97(D10), 10375–10388, doi:10.1029/91JD02287, 1992.
- Ridley, B. A., Atlas, E. L., Montzka, D. D., Browell, E. V., Cantrell, C. A., Blake, D. R., Blake, N. J., Cinquini, L., Coffey, M. T., Emmons, L. K., Cohen, R. C., DeYoung, R. J., Dibb, J. E., Eisele, F. L., Flocke, F. M., Fried, A., Grahek, F. E., Grant, W. B., Hair, J. W., Hannigan, J. W., Heikes, B. J., Lefer, B. L., Mauldin, R. L., Moody, J. L., Shetter, R. E., Snow, J. A., Talbot, R. W., Thornton, J. A., Walega, J. G., Weinheimer, A. J., Wert, B. P. and Wimmers, A. J.: Ozone depletion events observed in the high latitude surface layer during the TOPSE aircraft program, *J. Geophys. Res. Atmospheres*, 108(D4), 8356, doi:10.1029/2001JD001507, 2003.

- Roberts, J. M., Osthoff, H. D., Brown, S. S. and Ravishankara, A. R.: N<sub>2</sub>O<sub>5</sub> Oxidizes Chloride to Cl<sub>2</sub> in Acidic Atmospheric Aerosol, *Science*, 321(5892), 1059–1059, doi:10.1126/science.1158777, 2008.
- Rodgers, C. D.: Inverse methods for atmospheric sounding: theory and practice, World Scientific Publishing., 2000.
- Röhrs, J. and Kaleschke, L.: An algorithm to detect sea ice leads by using AMSR-E passive microwave imagery, *The Cryosphere*, 6(2), 343–352, doi:10.5194/tc-6-343-2012, 2012.
- Roazanov, A., Bovensmann, H., Bracher, A., Hrechanyy, S., Roazanov, V., Sinnhuber, M., Stroh, F. and Burrows, J. P.: NO<sub>2</sub> and BrO vertical profile retrieval from SCIAMACHY limb measurements: Sensitivity studies, *Adv. Space Res.*, 36(5), 846–854, doi:10.1016/j.asr.2005.03.013, 2005.
- Saiz-Lopez, A. and von Glasow, R.: Reactive halogen chemistry in the troposphere, *Chem. Soc. Rev.*, 41(19), 6448–6472, doi:10.1039/C2CS35208G, 2012.
- Saiz-Lopez, A., Mahajan, A. S., Salmon, R. A., Bauguitte, S. J.-B., Jones, A. E., Roscoe, H. K. and Plane, J. M. C.: Boundary Layer Halogens in Coastal Antarctica, *Science*, 317(5836), 348–351, doi:10.1126/science.1141408, 2007.
- Salawitch, R. J., Canty, T., Kurosu, T., Chance, K., Liang, Q., da Silva, A., Pawson, S., Nielsen, J. E., Rodriguez, J. M., Bhartia, P. K., Liu, X., Huey, L. G., Liao, J., Stickel, R. E., Tanner, D. J., Dibb, J. E., Simpson, W. R., Donohoue, D., Weinheimer, A., Flocke, F., Knapp, D., Montzka, D., Neuman, J. A., Nowak, J. B., Ryerson, T. B., Oltmans, S., Blake, D. R., Atlas, E. L., Kinnison, D. E., Tilmes, S., Pan, L. L., Hendrick, F., Van Roozendaal, M., Kreher, K., Johnston, P. V., Gao, R. S., Johnson, B., Bui, T. P., Chen, G., Pierce, R. B., Crawford, J. H. and Jacob, D. J.: A new interpretation of total column BrO during Arctic spring, *Geophys. Res. Lett.*, 37(21), L21805, doi:10.1029/2010GL043798, 2010.
- Sander, S. P., Abbatt, J. P. D., Barker, J. R., Burkholder, J. B., Friedl, R. R., Golden, D. M., Huie, R. E., Kolb, C. E., Kurylo, M. J., Moortgat, G. K., Orkin, V. L. and Wine, P. H.: Chemical Kinetics and Photochemical Data for Use in Atmospheric Studies, Evaluation No. 17", Jet Propulsion Laboratory, Pasadena, CA. [online] Available from: <http://jpldataeval.jpl.nasa.gov>, 2011.
- Schultz, M. G., Akimoto, H., Bottenheim, J., Buchmann, B., Galbally, I. E., Gilge, S., Helmig, D., Koide, H., Lewis, A. C., Novelli, P. C., Plass-Dülmer, C., Ryerson, T. B., Steinbacher, M., Steinbrecher, R., Tarasova, O., Tørseth, K., Thouret, V. and Zellweger, C.: The Global Atmosphere Watch reactive gases measurement network, *Elem. Sci. Anthr.*, 3, 67, doi:10.12952/journal.elementa.000067, 2015.

Seabrook, J. A., Whiteway, J., Staebler, R. M., Bottenheim, J. W., Komguem, L., Gray, L. H., Barber, D. and Asplin, M.: LIDAR measurements of Arctic boundary layer ozone depletion events over the frozen Arctic Ocean, *J. Geophys. Res. Atmospheres*, 116(D17), D00S02, doi:10.1029/2011JD016335, 2011.

Seabrook, J. A., Whiteway, J. A., Gray, L. H., Staebler, R. and Herber, A.: Airborne lidar measurements of surface ozone depletion over Arctic sea ice, *Atmos Chem Phys*, 13(12), 6023–6029, doi:10.5194/acp-13-6023-2013, 2013.

Seinfeld, J. H. and Pandis, S. N.: *Atmospheric Chemistry and Physics: From Air Pollution to Climate Change*, John Wiley & Sons., 2012.

Shaw, M. D. and Carpenter, L. J.: Modification of Ozone Deposition and I<sub>2</sub> Emissions at the Air–Aqueous Interface by Dissolved Organic Carbon of Marine Origin, *Environ. Sci. Technol.*, 47(19), 10947–10954, doi:10.1021/es4011459, 2013.

Sheridan, P. J., Schnell, R. C., Zoller, W. H., Carlson, N. D., Rasmussen, R. A., Harris, J. M. and Sievering, H.: Arctic air, snow and ice chemistry Composition of Br-containing aerosols and gases related to boundary layer ozone destruction in the arctic, *Atmospheric Environ. Part Gen. Top.*, 27(17), 2839–2849, doi:10.1016/0960-1686(93)90315-P, 1993.

Simpson, W. R., Alvarez-Aviles, L., Douglas, T. A., Sturm, M. and Domine, F.: Halogens in the coastal snow pack near Barrow, Alaska: Evidence for active bromine air-snow chemistry during springtime, *Geophys. Res. Lett.*, 32(4), L04811, doi:10.1029/2004GL021748, 2005.

Simpson, W. R., Carlson, D., Hönninger, G., Douglas, T. A., Sturm, M., Perovich, D. and Platt, U.: First-year sea-ice contact predicts bromine monoxide (BrO) levels at Barrow, Alaska better than potential frost flower contact, *Atmos Chem Phys*, 7(3), 621–627, doi:10.5194/acp-7-621-2007, 2007a.

Simpson, W. R., von Glasow, R., Riedel, K., Anderson, P., Ariya, P., Bottenheim, J., Burrows, J., Carpenter, L. J., Frieß, U., Goodsite, M. E., Heard, D., Hutterli, M., Jacobi, H.-W., Kaleschke, L., Neff, B., Plane, J., Platt, U., Richter, A., Roscoe, H., Sander, R., Shepson, P., Sodeau, J., Steffen, A., Wagner, T. and Wolff, E.: Halogens and their role in polar boundary-layer ozone depletion, *Atmos Chem Phys*, 7(16), 4375–4418, doi:10.5194/acp-7-4375-2007, 2007b.

Simpson, W. R., Brown, S. S., Saiz-Lopez, A., Thornton, J. A. and Glasow, R. von: Tropospheric Halogen Chemistry: Sources, Cycling, and Impacts, *Chem. Rev.*, 115(10), 4035–4062, doi:10.1021/cr5006638, 2015.

Solberg, S., Schmidbauer, N., Semb, A., Stordal, F. and Hov, Ø.: Boundary-layer ozone depletion as seen in the Norwegian Arctic in spring, *J. Atmospheric Chem.*, 23(3), 301–332, doi:10.1007/BF00055158, 1996.

Solomon, S.: Stratospheric ozone depletion: A review of concepts and history, *Rev. Geophys.*, 37(3), 275–316, doi:10.1029/1999RG900008, 1999.

Solomon, S., Intergovernmental Panel on Climate Change and Intergovernmental Panel on Climate Change, Eds.: *Climate change 2007: the physical science basis: contribution of Working Group I to the Fourth Assessment Report of the Intergovernmental Panel on Climate Change*, Cambridge University Press, Cambridge ; New York., 2007.

Spicer, C. W., Plastridge, R. A., Foster, K. L., Finlayson-Pitts, B. J., Bottenheim, J. W., Grannas, A. M. and Shepson, P. B.: Molecular halogens before and during ozone depletion events in the Arctic at polar sunrise: concentrations and sources, *Atmos. Environ.*, 36(15–16), 2721–2731, doi:10.1016/S1352-2310(02)00125-5, 2002.

Steffen, A., Douglas, T., Amyot, M., Ariya, P., Aspmo, K., Berg, T., Bottenheim, J., Brooks, S., Cobbett, F., Dastoor, A., Dommergue, A., Ebinghaus, R., Ferrari, C., Gardfeldt, K., Goodsite, M. E., Lean, D., Poulain, A. J., Scherz, C., Skov, H., Sommar, J. and Temme, C.: A synthesis of atmospheric mercury depletion event chemistry in the atmosphere and snow, *Atmospheric Chem. Phys.*, 8(6), 1445–1482, doi:10.5194/acp-8-1445-2008, 2008.

Steffen, A., Bottenheim, J., Cole, A., Ebinghaus, R., Lawson, G. and Leitch, W. R.: Atmospheric mercury speciation and mercury in snow over time at Alert, Canada, *Atmos Chem Phys*, 14(5), 2219–2231, doi:10.5194/acp-14-2219-2014, 2014.

Stephens, C. R.: *Studies of tropospheric halogen radical chemistry during ozone and mercury depletion events in the Arctic*, Dissertation, Purdue University, West Lafayette, IN., 2012.

Stephens, C. R., Shepson, P. B., Steffen, A., Bottenheim, J. W., Liao, J., Huey, L. G., Apel, E., Weinheimer, A., Hall, S. R., Cantrell, C., Sive, B. C., Knapp, D. J., Montzka, D. D. and Hornbrook, R. S.: The relative importance of chlorine and bromine radicals in the oxidation of atmospheric mercury at Barrow, Alaska: MERCURY OXIDATION IN THE ARCTIC, *J. Geophys. Res. Atmospheres*, 117(D14), n/a-n/a, doi:10.1029/2011JD016649, 2012.

Strong, C., Fuentes, J. D., Davis, R. E. and Bottenheim, J. W.: Thermodynamic attributes of Arctic boundary layer ozone depletion, *Atmos. Environ.*, 36(15–16), 2641–2652, doi:10.1016/S1352-2310(02)00114-0, 2002.

Stull, R. B.: *An Introduction to Boundary Layer Meteorology*, Springer Netherlands, Dordrecht. [online] Available from: <http://dx.doi.org/10.1007/978-94-009-3027-8> (Accessed 4 May 2016), 1988.

Sturges, W. T. and Barrie, L. A.: Chlorine, Bromine AND Iodine in arctic aerosols, *Atmospheric Environ.* 1967, 22(6), 1179–1194, doi:10.1016/0004-6981(88)90349-6, 1988.

- Sumner, A. ., Shepson, P. ., Grannas, A. ., Bottenheim, J. ., Anlauf, K. ., Worthy, D., Schroeder, W. ., Steffen, A., Dominé, F., Perrier, S. and Houdier, S.: Atmospheric chemistry of formaldehyde in the Arctic troposphere at Polar Sunrise, and the influence of the snowpack, *Atmos. Environ.*, 36(15–16), 2553–2562, doi:10.1016/S1352-2310(02)00105-X, 2002.
- Sumner, A. L. and Shepson, P. B.: Snowpack production of formaldehyde and its effect on the Arctic troposphere, *Nature*, 398(6724), 230–233, doi:10.1038/18423, 1999.
- Tackett, P. J., Cavender, A. E., Keil, A. D., Shepson, P. B., Bottenheim, J. W., Morin, S., Deary, J., Steffen, A. and Doerge, C.: A study of the vertical scale of halogen chemistry in the Arctic troposphere during Polar Sunrise at Barrow, Alaska, *J. Geophys. Res. Atmospheres*, 112(D7), D07306, doi:10.1029/2006JD007785, 2007.
- Tang, T. and McConnell, J. C.: Autocatalytic release of bromine from Arctic snow pack during polar sunrise, *Geophys. Res. Lett.*, 23(19), 2633–2636, doi:10.1029/96GL02572, 1996.
- Tarasick, D. W. and Bottenheim, J. W.: Surface ozone depletion episodes in the Arctic and Antarctic from historical ozonesonde records, *Atmos Chem Phys*, 2(3), 197–205, doi:10.5194/acp-2-197-2002, 2002.
- Theys, N., Van Roozendael, M., Errera, Q., Hendrick, F., Daerden, F., Chabrillat, S., Dorf, M., Pfeilsticker, K., Rozanov, A., Lotz, W., Burrows, J. P., Lambert, J.-C., Goutail, F., Roscoe, H. K. and De Mazière, M.: A global stratospheric bromine monoxide climatology based on the BASCOE chemical transport model, *Atmos Chem Phys*, 9(3), 831–848, doi:10.5194/acp-9-831-2009, 2009.
- Theys, N., Van Roozendael, M., Hendrick, F., Yang, X., De Smedt, I., Richter, A., Begoin, M., Errera, Q., Johnston, P. V., Kreher, K. and De Mazière, M.: Global observations of tropospheric BrO columns using GOME-2 satellite data, *Atmos Chem Phys*, 11(4), 1791–1811, doi:10.5194/acp-11-1791-2011, 2011.
- Thompson, A. M.: The Oxidizing Capacity of the Earth's Atmosphere: Probable Past and Future Changes, *Science*, 256(5060), 1157–1165, doi:10.1126/science.256.5060.1157, 1992.
- Thompson, C. R., Shepson, P. B., Liao, J., Huey, L. G., Apel, E. C., Cantrell, C. A., Flocke, F., Orlando, J., Fried, A., Hall, S. R., Hornbrook, R. S., Knapp, D. J., Mauldin III, R. L., Montzka, D. D., Sive, B. C., Ullmann, K., Weibring, P. and Weinheimer, A.: Interactions of bromine, chlorine, and iodine photochemistry during ozone depletions in Barrow, Alaska, *Atmospheric Chem. Phys.*, 15(16), 9651–9679, doi:10.5194/acp-15-9651-2015, 2015.

- Thompson, C. R., Shepson, P. B., Liao, J., Huey, L. G., Cantrell, C., Flocke, F. and Orlando, J.: Bromine atom production and chain propagation during springtime Arctic ozone depletion events in Barrow, Alaska, *Atmospheric Chem. Phys. Discuss.*, 1–42, doi:10.5194/acp-2015-1039, 2016.
- Toyota, K., McConnell, J. C., Lupu, A., Neary, L., McLinden, C. A., Richter, A., Kwok, R., Semeniuk, K., Kaminski, J. W., Gong, S.-L., Jarosz, J., Chipperfield, M. P. and Sioris, C. E.: Analysis of reactive bromine production and ozone depletion in the Arctic boundary layer using 3-D simulations with GEM-AQ: inference from synoptic-scale patterns, *Atmospheric Chem. Phys.*, 11(8), 3949–3979, doi:10.5194/acp-11-3949-2011, 2011.
- Tsunogai, S. and Sase, T.: Formation of iodide-iodine in the ocean, *Deep Sea Res. Oceanogr. Abstr.*, 16(5), 489–496, doi:10.1016/0011-7471(69)90037-0, 1969.
- Tuckermann, M., Ackermann, R., Gölz, C., Lorenzen-Schmidt, H., Senne, T., Stutz, J., Trost, B., Unold, W. and Platt, U.: DOAS-observation of halogen radical-catalysed arctic boundary layer ozone destruction during the ARCTOC-campaigns 1995 and 1996 in Ny-Ålesund, Spitsbergen, *Tellus B*, 49(5), 533–555, doi:10.1034/j.1600-0889.49.issue5.9.x, 1997.
- Vandaele, A. C., Hermans, C., Simon, P. C., Carleer, M., Colin, R., Fally, S., Mérienne, M. F., Jenouvrier, A. and Coquart, B.: Atmospheric Spectroscopy Applications 96 Measurements of the NO<sub>2</sub> absorption cross-section from 42 000 cm<sup>-1</sup> to 10 000 cm<sup>-1</sup> (238–1000 nm) at 220 K and 294 K, *J. Quant. Spectrosc. Radiat. Transf.*, 59(3), 171–184, doi:10.1016/S0022-4073(97)00168-4, 1998.
- Vogt, R., Crutzen, P. J. and Sander, R.: A mechanism for halogen release from sea-salt aerosol in the remote marine boundary layer, *Nature*, 383(6598), 327–330, doi:10.1038/383327a0, 1996.
- Vogt, R., Sander, R., Glasow, R. von and Crutzen, P. J.: Iodine Chemistry and its Role in Halogen Activation and Ozone Loss in the Marine Boundary Layer: A Model Study, *J. Atmospheric Chem.*, 32(3), 375–395, doi:10.1023/A:1006179901037, 1999.
- Volz, A. and Kley, D.: Evaluation of the Montsouris series of ozone measurements made in the nineteenth century, *Nature*, 332(6161), 240–242, doi:10.1038/332240a0, 1988.
- Wallace, J. M. and Hobbs, P. V.: *Atmospheric Science: An Introductory Survey*, Academic Press., 2006.
- Weaver, J. R.: Birck Nanotechnology Center Technical Overview, edited by Purdue University Office of Research and Partnerships, [online] Available from: <http://docs.lib.purdue.edu/gendes/5> (Accessed 28 January 2016), 2015.



- Webster, M. A., Rigor, I. G., Nghiem, S. V., Kurtz, N. T., Farrell, S. L., Perovich, D. K. and Sturm, M.: Interdecadal changes in snow depth on Arctic sea ice, *J. Geophys. Res. Oceans*, 119(8), 5395–5406, doi:10.1002/2014JC009985, 2014.
- Wennberg, P.: Atmospheric chemistry: Bromine explosion, *Nature*, 397(6717), 299–301, doi:10.1038/16805, 1999a.
- Wennberg, P.: Atmospheric chemistry: Bromine explosion, *Nature*, 397(6717), 299–301, doi:10.1038/16805, 1999b.
- Wilmouth, D. M., Hanisco, T. F., Donahue, N. M. and Anderson, J. G.: Fourier Transform Ultraviolet Spectroscopy of the  $A\ 2\Pi_{3/2} \leftarrow X\ 2\Pi_{3/2}$  Transition of BrO, *J. Phys. Chem. A*, 103(45), 8935–8945, doi:10.1021/jp991651o, 1999.
- Worthy, D. E. J., Trivett, N. B. A., Hopper, J. F., Bottenheim, J. W. and Levin, I.: Analysis of long-range transport events at Alert, Northwest Territories, during the Polar Sunrise Experiment, *J. Geophys. Res. Atmospheres*, 99(D12), 25329–25344, doi:10.1029/94JD01209, 1994.
- Wren, S. N. and Donaldson, D. J.: Laboratory Study of pH at the Air–Ice Interface, *J. Phys. Chem. C*, 116(18), 10171–10180, doi:10.1021/jp3021936, 2012.
- Wren, S. N., Donaldson, D. J. and Abbatt, J. P. D.: Photochemical chlorine and bromine activation from artificial saline snow, *Atmos Chem Phys*, 13(19), 9789–9800, doi:10.5194/acp-13-9789-2013, 2013.
- Yang, X., Pyle, J. A. and Cox, R. A.: Sea salt aerosol production and bromine release: Role of snow on sea ice, *Geophys. Res. Lett.*, 35(16), doi:10.1029/2008GL034536, 2008.
- Yang, X., Pyle, J. A., Cox, R. A., Theys, N. and Van Roozendael, M.: Snow-sourced bromine and its implications for polar tropospheric ozone, *Atmospheric Chem. Phys.*, 10(16), 7763–7773, doi:10.5194/acp-10-7763-2010, 2010.
- Zeng, T., Wang, Y., Chance, K., Browell, E. V., Ridley, B. A. and Atlas, E. L.: Widespread persistent near-surface ozone depletion at northern high latitudes in spring: OZONE DEPLETION AT NORTHERN HIGH LATITUDES, *Geophys. Res. Lett.*, 30(24), doi:10.1029/2003GL018587, 2003.
- Zhou, X., Beine, H. J., Honrath, R. E., Fuentes, J. D., Simpson, W., Shepson, P. B. and Bottenheim, J. W.: Snowpack photochemical production of HONO: A major source of OH in the Arctic boundary layer in springtime, *Geophys. Res. Lett.*, 28(21), 4087–4090, doi:10.1029/2001GL013531, 2001.
- Zielcke, J.: Observations of reactive bromine, iodine and chlorine species in the Arctic and Antarctic with Differential Optical Absorption Spectroscopy, Dissertation, University of Heidelberg, Germany., 2015.

VITA

## VITA


John Weston Halfacre was born in Louisville, KY, on July 17, 1988. As a boy, he enjoyed learning he had an aptitude for school work, and always made time for his studies to please his parents. In 2006, he graduated from Floyd Central High School in Floyds Knobs, IN. Wes then chose to attend Indiana University Southeast as a chemistry major, remaining close to his home surrounded by the rolling hills of southern Indiana. While performing research as a junior, his advisor took his group to Indiana University Bloomington and gave Wes a romantic vision of what graduate school could be. The thought of being able to perform science and listen to music all day every day was very enticing to him. When it came time to make a decision, he chose to attend Purdue University with hopes of working with Paul Shepson to perform exciting Arctic-based research. After obtaining his Bachelor's degree in 2010, Wes immediately moved to West Lafayette to begin work with Prof. Shepson. While at Purdue, Wes learned more about himself, the world, and science than he could have anticipated. Most importantly, though, he learned he still has much more learning to do. Wes will return home to Indiana University Southeast to pursue this endeavor as an Assistant Professor of Chemistry, where he will drink more coffee, play more banjo, and convince undergraduates to do the same.

PUBLICATION

Atmos. Chem. Phys., 14, 4875–4894, 2014  
 www.atmos-chem-phys.net/14/4875/2014/  
 doi:10.5194/acp-14-4875-2014  
 © Author(s) 2014. CC Attribution 3.0 License.



Atmospheric  
 Chemistry  
 and Physics  
 Open Access



## Temporal and spatial characteristics of ozone depletion events from measurements in the Arctic

J. W. Halfacre<sup>1,\*</sup>, T. N. Knepp<sup>1,\*</sup>, P. B. Shepson<sup>1,2</sup>, C. R. Thompson<sup>1,\*\*</sup>, K. A. Pratt<sup>1,\*\*\*</sup>, B. Li<sup>3,\*\*\*\*</sup>, P. K. Peterson<sup>4</sup>, S. J. Walsh<sup>4</sup>, W. R. Simpson<sup>4</sup>, P. A. Matrai<sup>5</sup>, J. W. Bottenheim<sup>6</sup>, S. Netcheva<sup>7</sup>, D. K. Perovich<sup>8</sup>, and A. Richter<sup>9</sup>

<sup>1</sup>Department of Chemistry, Purdue University, West Lafayette, Indiana, USA

<sup>2</sup>Department of Earth, Atmospheric, and Planetary Sciences, Purdue University, West Lafayette, Indiana, USA

<sup>3</sup>Department of Statistics, Purdue University, West Lafayette, Indiana, USA

<sup>4</sup>Department of Chemistry, University of Alaska, Fairbanks, Alaska, USA

<sup>5</sup>Bigelow Laboratory for Ocean Sciences, East Boothbay, Maine, USA

<sup>6</sup>Air Quality Research Division, Environment Canada, Toronto, Ontario, Canada

<sup>7</sup>Air Quality Processes Research Section, Environment Canada, Toronto, Ontario, Canada

<sup>8</sup>US Army Cold Regions Research and Engineering Laboratory, Fairbanks, Alaska, USA

<sup>9</sup>Institute of Environmental Physics, University of Bremen, Bremen, Germany

\*now at: Science Systems and Applications, Inc., Hampton, Virginia, USA

\*\*now at: Institute of Arctic and Alpine Research, University of Colorado at Boulder, Boulder, Colorado, USA

\*\*\*now at: Department of Chemistry, University of Michigan, Ann Arbor, Michigan, USA

\*\*\*\*now at: Department of Statistics, University Illinois at Urbana-Champaign, Urbana, Illinois, USA

Correspondence to: J. W. Halfacre (jhalfacr@purdue.edu)

Received: 9 October 2013 – Published in Atmos. Chem. Phys. Discuss.: 19 November 2013

Revised: 24 February 2014 – Accepted: 21 March 2014 – Published: 20 May 2014

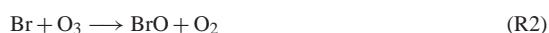
**Abstract.** Following polar sunrise in the Arctic springtime, tropospheric ozone episodically decreases rapidly to near-zero levels during ozone depletion events (ODEs). Many uncertainties remain in our understanding of ODE characteristics, including the temporal and spatial scales, as well as environmental drivers. Measurements of ozone, bromine monoxide (BrO), and meteorology were obtained during several deployments of autonomous, ice-tethered buoys (O-Buoys) from both coastal sites and over the Arctic Ocean; these data were used to characterize observed ODEs. Detected decreases in surface ozone levels during the onset of ODEs corresponded to a median estimated apparent ozone depletion timescale (based on both chemistry and the advection of O<sub>3</sub>-depleted air) of 11 h. If assumed to be dominated by chemical mechanisms, these timescales would correspond to larger-than-observed BrO mole fractions based on known chemistry and assumed other radical levels. Using backward air mass trajectories and an assumption that transport mechanisms dominate observations, the spatial scales for ODEs (defined by time periods in which ozone lev-

els  $\leq 15 \text{ nmol mol}^{-1}$ ) were estimated to be 877 km (median), while areas estimated to represent major ozone depletions ( $< 10 \text{ nmol mol}^{-1}$ ) had dimensions of 282 km (median). These observations point to a heterogeneous boundary layer with localized regions of active, ozone-destroying halogen chemistry, interspersed among larger regions of previously depleted air that retain reduced ozone levels through hindered atmospheric mixing. Based on the estimated size distribution, Monte Carlo simulations showed it was statistically possible that all ODEs observed could have originated upwind, followed by transport to the measurement site. Local wind speed averages were low during most ODEs (median of  $\sim 3.6 \text{ m s}^{-1}$ ), and there was no apparent dependence on local temperature.

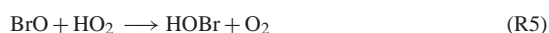
## 1 Introduction

Global tropospheric oxidation is generally controlled by ozone (O<sub>3</sub>), a major greenhouse gas (Gauss et al., 2006) and the most important precursor to the primary atmospheric oxidant, hydroxyl radical (OH) (Seinfeld and Pandis, 2006; Thompson, 1992). When the sun rises in the Arctic spring-time (typically around mid-March), boundary layer O<sub>3</sub> often drops precipitously from background mole fractions of ~40 nmol mol<sup>-1</sup> (ppbv, parts per billion by volume) to near zero levels for periods of hours, or even days, before recovering (Anlauf et al., 1994; Barrie et al., 1988; Bottenheim et al., 1986, 2002). During these ozone depletion events (ODEs), the prominent regional tropospheric oxidation pathways for hydrocarbons at the surface are driven by species other than OH radicals, notably Cl and Br atoms (Cavender et al., 2008; Jobson et al., 1994).

ODEs are considered to start by the reaction of O<sub>3</sub> with photolytically active halogens, particularly bromine (R1, R2) (Simpson et al., 2007b).



O<sub>3</sub> is removed in Reaction (R2) by Br to produce bromine monoxide (BrO). However, BrO is photolabile and can reproduce O<sub>3</sub> and Br in a null cycle. Therefore, the rate at which O<sub>3</sub> is destroyed is ultimately limited by the rate at which BrO reacts with another species to not reform O<sub>3</sub>, such as in Reactions (R3–R5).



Note that BrO + ClO (Reaction R4) can also produce OClO + Br; however, this pathway is not listed above since OClO primarily regenerates O<sub>3</sub> in a null cycle via photolysis. Ozone destruction is propagated by the regeneration of reactive halogen species. In the gas phase, Reactions (R3) and (R4) are believed to dominate at high halogen-oxide concentrations, while R5 is believed to play a larger role at smaller BrO levels (Le Bras and Platt, 1995; Piot and von Glasow, 2008). Reactions (R3) and (R4) directly reproduce reactive Br atoms, while the HOBr formed by Reaction (R5) must first undergo photolysis (Simpson et al., 2007b, and references therein). Additionally, Reaction (R5) is involved in a series of heterogeneous, autocatalytic reactions referred to as the “bromine explosion”, which are believed to supply net atmospheric reactive bromine (Fan and Jacob, 1992; Tang and McConnell, 1996; Vogt et al., 1996; Wennberg, 1999). The “bromine explosion” involves the production of

HOBr as above (R5), or through halogen reactions with oxidized nitrogen species (e.g., Aguzzi and Rossi, 2002; Hanson and Ravishankara, 1995). Uptake of this HOBr onto acidic, bromide-containing frozen surfaces produces Br<sub>2</sub> (Adams et al., 2002; Huff and Abbatt, 2002), which can then undergo the O<sub>3</sub>-destroying reactions once photolyzed (R1). This series of reactions will exponentially increase Br<sub>2</sub> levels until some required reagent runs out.

Hypothesized sources of reactive halogens include saline frozen surfaces found across the Arctic Ocean, such as the snowpack, blowing snow, and sea salt-derived aerosols (Abbatt et al., 2012; Fan and Jacob, 1992; Frieß et al., 2011; Jones et al., 2009; Simpson et al., 2005; Yang et al., 2008). Recent in situ experiments showed that saline, acidic surface snowpacks (above sea ice or tundra) can act as efficient sources of Br<sub>2</sub>, and that the “bromine explosion” can occur within the interstitial air of the snowpack, followed by release of reactive bromine into the boundary layer via wind pumping and diffusion (Pratt et al., 2013).

Despite our increasing understanding of the role of halogens in ODEs, basic ODE characteristics, such as their temporal and spatial scales, remain uncertain (Jacobi et al., 2010; Simpson et al., 2007b; Zeng et al., 2003). Current knowledge of the aforementioned O<sub>3</sub> depletion chemical mechanisms (CM) and the corresponding kinetics estimate the timescale for O<sub>3</sub> destruction to be on the order of days (Hausmann and Platt, 1994; Jobson et al., 1994; Piot and von Glasow, 2008, 2009; Tuckermann et al., 1997). However, there are only a few reports of Arctic ODEs that are assumed/known to have been observed primarily as a result of local-scale CM (Boudries and Bottenheim, 2000; Jacobi et al., 2006). ODEs can also be observed primarily due to air mass transport mechanisms (TM) in which air masses depleted of O<sub>3</sub> (via CM upwind) advect over the measurement site (Morin et al., 2005; Simpson et al., 2007b) and are detected as “ozone depletion events”. Given that the Arctic Ocean surface is sunlit, stable against vertical mixing, and ice-covered during the spring (Lehrer et al., 2004), it has been hypothesized that O<sub>3</sub>-depleted surface air could be the norm in the Arctic boundary layer during this time, and that O<sub>3</sub> is only observed at the surface due to turbulent vertical mixing in an otherwise stable boundary layer. This vertical mixing can temporarily transport free tropospheric O<sub>3</sub> from aloft to the surface, raising the surface-level mole fractions to between 30 and 40 nmol mol<sup>-1</sup> (Bottenheim et al., 2009; Hopper et al., 1998; Jacobi et al., 2010; Moore et al., 2014; Strong et al., 2002; Zeng et al., 2003). Regarding the spatial scales of individual O<sub>3</sub>-depleted air masses, Ridley et al. (2003) reported Arctic ODEs extending between 600 and 900 km in length from flights during the Tropospheric Ozone Production about the Spring Equinox experiment. Recently, Jones et al. (2013) reported the observation of multiple ODEs from a network of 10 O<sub>3</sub> monitors spread over the Droning Maud Land sector of Antarctica, some of which extended at least 1200 km in horizontal dimension. However, no such network of O<sub>3</sub> monitors

has yet been established in the Arctic to make analogous observations.

In a study of long-term Arctic coastal measurements, Tarasick and Bottenheim (2002) observed that ODEs most often occurred at temperatures of less than 253 K, leading to the proposal that such low temperatures could be necessary for the initiation of ozone depletion. This hypothesis was strengthened by Adams et al. (2002), who reported that frozen NaCl/NaBr surfaces efficiently uptake and react with HOBr to both form and release gas phase Br<sub>2</sub> at temperatures below 253 K. This observation has been hypothesized to occur due to the precipitation of NaCl · 2H<sub>2</sub>O at temperatures less than 252 K, which then requires a greater concentration of Br<sup>-</sup> to maintain the surface brine layer (Cho et al., 2002); when Cl<sup>-</sup> precipitates, the volume of the brine water must decrease to maintain the ionic concentration needed for the appropriate freezing point depression. Boundary-layer BrO enhancements have been correlated with low temperatures (Nghiem et al., 2012; Zeng et al., 2003), and apparently linear increases in maximum BrO concentrations have been observed with decreasing temperatures, below 258 K (Pöhler et al., 2010). Further, strong positive correlations between O<sub>3</sub> concentration and potential temperature have been reported (Seabrook et al., 2011; Strong et al., 2002). However, Bottenheim et al. (2009) and Neuman et al. (2010) observed ODEs at temperatures as high as 267 K, emphasizing uncertainty in the temperatures required for the observation of an O<sub>3</sub>-depleted air mass.

ODEs have often been associated with a calm, stable boundary layer. Events observed under high wind speeds (faster than 10 m s<sup>-1</sup>) are generally attributed to TM (Simpson et al., 2007b). Yang et al. (2008) hypothesized that saline snow atop sea ice could disperse during periods of high wind and become a source of both sea-salt aerosol and bromine, consequently initiating ODEs. Indeed, there have been coastal-based studies in which increased BrO and aerosol were observed during periods of elevated wind speeds (> 5 m s<sup>-1</sup>), and O<sub>3</sub> depletion sometimes, but not always, followed (Frieß et al., 2011; Jones et al., 2009). Alternatively, higher wind speeds could also lead to better ventilation of the snowpack in which Br<sub>2</sub> is produced (Albert et al., 2002; Foster et al., 2001; Michalowski et al., 2000; Pratt et al., 2013; Toyota et al., 2011). Michalowski et al. (2000) discussed that the rate at which HOBr reacts with Br<sup>-</sup> during Br<sub>2</sub> production in the “bromine explosion” was dependent on the timescale for turbulent diffusive transport of HOBr to the snowpack surface, which would be wind-speed dependent. However, due to few coincident observations of wind speeds, aerosol, O<sub>3</sub>, and BrO, the dependence of ODEs on wind speed remains unclear.

Arctic air masses depleted in O<sub>3</sub> typically spend a significant amount of time over the Arctic Ocean before arriving at coastal measurement sites, suggesting that the ice-covered ocean is the most probable site of ODE initiation (Bottenheim and Chan, 2006; Gilman et al., 2010; Jacobi et al.,



**Figure 1.** Map of locations at which various O-Buoys (abbreviated OB) were deployed between 2009 and 2011. For the coordinates, see Table 1. Sea ice extent image is for the month of March 2011. Map courtesy of Google Earth, and sea ice image courtesy of the National Snow and Ice Data Center.

2006; Simpson et al., 2007a). In situ chemical and meteorological data from the Arctic Ocean are, however, sparse. Most long-term Arctic tropospheric O<sub>3</sub> measurements have been made at coastal sites, and thus most observed ODEs have been attributed to TM. Attempts to study ODEs over the Arctic Ocean have been conducted on ice floes (e.g., Hopper et al., 1994; Hopper et al., 1998), aircraft (e.g., Jaeschke et al., 1999; Leitch et al., 1994; Neuman et al., 2010; Ridley et al., 2003; Seabrook et al., 2013; Sheridan et al., 1993), and ships (e.g., Bottenheim et al., 2009; Gilman et al., 2010; Jacobi et al., 2006; Nghiem et al., 2012; Pöhler et al., 2010; Seabrook et al., 2011). However, few of these studies have produced the long-term data required for in-depth studies of the temporal and spatial scales of ODEs.

Recently, a series of ice-tethered buoys were deployed as part of the Arctic Observing Network program to observe ODEs over the Arctic Ocean (Knepp et al., 2010). The buoys have been installed in sea ice for automated, continuous, several-month surface measurements of O<sub>3</sub>, BrO (Carlson et al., 2010), carbon dioxide, and local meteorological conditions. The data generated by the O-Buoys represent the first long-term measurements of these chemical species directly over the surface of the ice-covered Arctic Ocean. Using this unique data set, we estimate the timescales of O<sub>3</sub> depletion, examine the state of our understanding of the chemistry involved, and estimate the spatial extents and meteorological conditions supporting O<sub>3</sub>-depleted air masses.

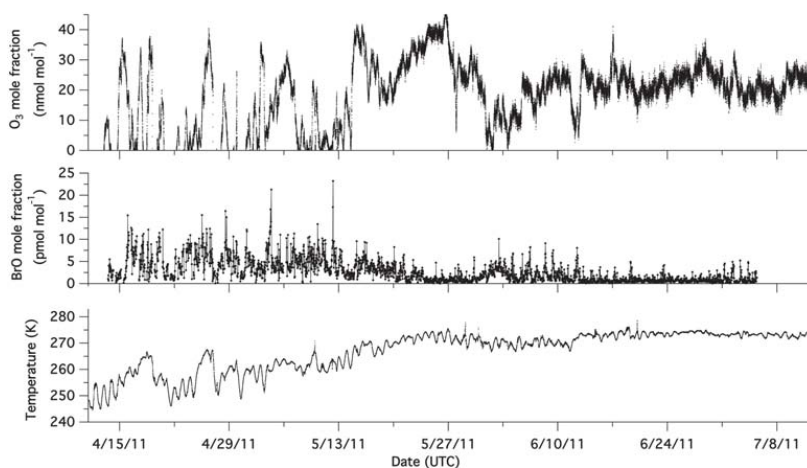


**Figure 2.** Example time series of  $O_3$ , BrO, and temperature from O-Buoy2 during its deployment in the Beaufort Sea.

## 2 Experimental

### 2.1 Instrumentation

Surface  $O_3$  and meteorology measurements discussed herein were collected during five separate deployments of O-Buoys (Table 1). Buoy deployment locations are shown in Fig. 1. Details of the O-Buoy design and operation are discussed extensively by Knepp et al. (2010), but a brief description of the meteorological,  $O_3$ , and BrO instruments are given herein. At the time of data analysis, BrO data were available from both O-Buoy1 (Barrow, Alaska, 2009 deployment) and O-Buoy2 (Beaufort Sea, 2010–2011 deployment) to compare with  $O_3$  depletion timescales. The O-Buoy2 time series, including  $O_3$ , BrO, and temperature, is presented in Fig. 2. During winter months, O-Buoys are set to operate on an abbreviated sampling schedule to conserve power, typically sampling for a total of 4 h once every 1–3 days. The O-Buoys were switched to daily 24 h sampling close to the time of polar sunrise, typically near the end of February or early March. The MAX-DOAS (multi-axis differential optical absorption spectroscopy) instrument was an exception to this sampling schedule as it was kept unpowered during the winter months, and turned on during the springtime switch to 24 h sampling. Though the O-Buoys are also active during fall, winter, and late summer months, we focus mostly on springtime and early summer data herein (dates presented in Table 1).

Temperature was measured using a Vaisala model HMP45C temperature and relative humidity probe. Wind speed was measured using a RM Young Model 05103 anemometer. The range of wind speeds observed across the four O-Buoys deployed was 0–15 m s<sup>-1</sup>. It was observed during the 2009 Barrow, Alaska, O-Buoy1 deployment, how-

ever, that the anemometer was susceptible to icing, which would impede its ability to spin freely and provide accurate measurements. This effect was most prominent during the same deployment, in which wind speed fell from a mean of about 2 to 0 m s<sup>-1</sup> for a period of 4 days. To mitigate the impact of this effect on the interpretation of the results, wind data were not utilized in our analysis when wind speed was measured as 0 m s<sup>-1</sup>. While there is reason to believe that wind speeds are indeed low during these periods, the actual wind speed is unknown. Thus, if the average wind speed calculated during an ODE contained > 50 % of such values, the wind data for that event were not included in the data analysis. We also acknowledge that an icing effect could create a measurement bias toward lower values. However, as discussed in the text (Sect. 3.3), on average this appears to be a minor issue in terms of our use of the anemometer data (e.g., to calculate ODE spatial scales) as we find effectively equivalent results using our anemometer wind speeds and those estimated using the HYSPLIT backwards trajectory model (Sect. 2.3).

Ozone was measured using custom-built 2B Technologies model 205 dual-beam  $O_3$  monitors. Customizations include one backup pump, one backup  $O_3$  scrubber, a lamp heater, and modified firmware to control the instrument remotely. The instrument inlet was located on the mast of the buoy 2 m above the sea ice and contained a 90 mm quartz fiber filter (Pall Life Sciences) to prevent intake of large particles. The instrument itself is located inside the hull of the buoy beneath the sea ice such that it operates under a near constant temperature ( $\sim -1.5^\circ\text{C}$ ). The  $O_3$  instrument did not display a temperature dependence during laboratory, pre-deployment  $O_3$  calibrations as long as the cell temperature of the instrument was stable; cell temperature stabilization generally occurred



**Table 1.** O-Buoy deployment locations and time periods of continuous measurements focused on herein.

O-Buoy number	Latitude	Longitude	General area	Dates of continuous measurements	Number of ODEs observed
1	71° N	156° W	Barrow, Alaska	2 Mar 2009–19 May 2009	13
1	77° N	135° W	Beaufort Sea	22 Mar 2010–14 Jul 2010	13
2	74° N	142° W	Beaufort Sea	11 Apr 2011–22 Jul 2011	6
3	60° N	90° W	Hudson Bay	22 Feb 2010–27 Mar 2010	3
4	78° N	112° W	Borden Island, Nunavut, Canada	04 Apr 2010–30 Apr 2010	3

**Table 2.** Cross sections used in spectral analysis. Each cross section is convolved using an instrument function determined by the 334 nm Hg peak.

Species	Cross section reference
BrO (228 K)	Wilmouth et al. (1999)
O <sub>3</sub> (243 K)	Malicet et al. (1995)
NO <sub>2</sub> (220 K)	Vandaele et al. (1998)
O <sub>4</sub>	Hermans et al. (2001)
Ring	Determined from zenith spectra using Chance and Spurr (1997)

after 20–30 min, and the first 30 min of O<sub>3</sub> data during these warm-up periods were excluded from data analysis. The instrument has a manufacturer specified limit of detection of 1 nmol mol<sup>-1</sup>, and individual measurement uncertainty was calculated to range from 2.1 to 3.5 nmol mol<sup>-1</sup>. Ozone monitor averaging times differed between buoy deployments: O-Buoy1 used 10 s averages, O-Buoy3 used 2 s averages, and both O-Buoy2 and O-Buoy4 used 1 min averages. For analysis, all data were smoothed to 5 min moving averages.

BrO was detected using a MAX-DOAS instrument. The scan head telescope, located at the top of the buoy mast, collects scattered radiation and sends it through a fiber optic cable to the computer/spectrometer module, which consists of a single board computer (Technologic Systems TS-7260), a stepper motor driver (Stepperboard BC2D15), interface electronics, and a miniature spectrometer (Ocean Optics HR2000, 318–455 nm). The scan elevation angle is controlled by the O-Buoy's supervisory computer and observes light at angles of 90 (zenith), 20, 10, 5, 2, and 1° over a period of 30 min (Carlson et al., 2010). The zenith spectrum from a 30 min data measurement period was used as the reference spectrum for the lower elevation angle spectra, which minimizes the differential absorption by stratospheric species. To obtain differential slant column densities (dSCD), the QDOAS software was used (Fayt et al., 2011) to fit both the logarithm of the ratio of each low elevation spectra and zenith spectra in the wavelength region 346–364 nm (convolved absorber cross sections detailed in Table 2), as well as a third-order polynomial to account for broadband features and a spectral offset to account for stray light. Fit residuals for both

O-Buoy1 and O-Buoy2 were less than  $1 \times 10^{-3}$  resulting in BrO dSCD errors of less than  $4 \times 10^{13}$  molecules cm<sup>-2</sup> and O<sub>4</sub> dSCD errors of less than  $1 \times 10^{42}$  molecules<sup>2</sup> cm<sup>-5</sup>. Retrieval of BrO mole fractions from dSCD data is a two-step inverse problem. First, the aerosol profile is determined from O<sub>4</sub> dSCDs using both the SCIATRAN radiative transfer model as a forward model, and the estimation techniques detailed in Frieß et al. (2006). Then, a vertical profile of BrO mole fractions from the ground to 2 km (100 m intervals) was obtained using both the radiative transfer model McArtim (Deutschmann et al., 2011) as a forward model, and similar optimal estimation techniques detailed in Frieß et al. (2011). Because we are only considering surface O<sub>3</sub> measurements, only the average BrO mole fractions in the lowest 100 m were used in subsequent portions of this study.

The BrO detection limit is a function of the geometry of the observation and the state of the atmosphere at the time of the measurement. We estimated a range for the detection limit ( $2\sigma$ ) from  $3.7 \times 10^{12}$  (clear sky) to  $1.5 \times 10^{13}$  mol cm<sup>-2</sup> (impaired visibility) for the total integrated column BrO through 2 km (VCD<sub>2km</sub>) by looking at the distribution of VCD<sub>2km</sub> values over a month in late summer where no BrO was observed. To evaluate the error associated with the retrieved surface mole fractions, it is necessary to consider both dSCD measurement error and smoothing error (Rodgers, 2000). Smoothing error calculations quantify the error resulting from the inability of the instrument to observe fine structure in the vertical profile. The smoothing error was estimated through considering the mean of an ensemble of profiles retrieved in late summer ( $\bar{x}$ ) when the dSCD measurements indicated no measurable BrO. This allowed us to assume the actual profile ( $x_a$ ) is given by 0 pmol mol<sup>-1</sup> (pptv, parts per trillion by volume) BrO through 2 km. The average surface mole fraction smoothing errors ( $\epsilon_s$ ) for the entire O-Buoy2 campaign were estimated using Eq. 1, where  $A$  represents the averaging kernel matrix and  $I$  is the identity matrix (Rodgers, 2000).

$$\epsilon_s = (A - I)(\bar{x} - x_a) \quad (1)$$

Individual surface mole fraction errors due to smoothing error averaged 0.3 pmol mol<sup>-1</sup> for the O-Buoy2 campaign. Including individual mole fraction errors due to propagated dSCD measurement error, total surface mole fraction errors

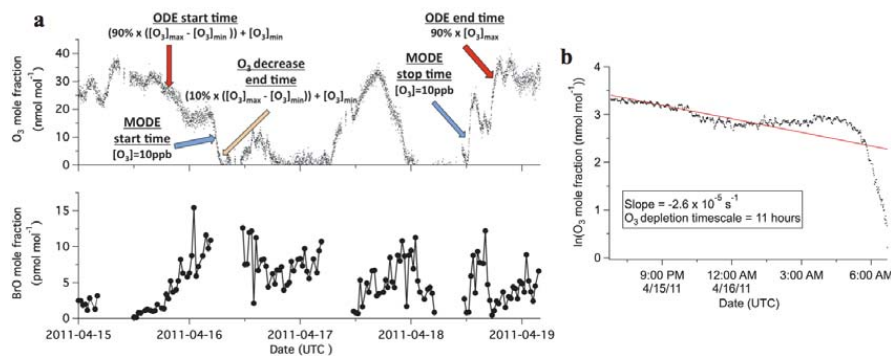


**Figure 3.** (a) Example ODE from O-Buoy2 deployment in the Beaufort Sea with ODE definitions illustrated. The brief resurgence of  $O_3$  on 17 April does not rise above  $25 \text{ nmol mol}^{-1}$  for longer than 12 h and is thus not considered as separating two ODEs. Error bars are not displayed to more clearly show the time series. As discussed in Sect. 2.1, individual measurement errors for  $O_3$  ranged from 2.1 to  $3.5 \text{ nmol mol}^{-1}$ , and BrO measurement errors ranged from 0.7 to  $6.9 \text{ pmol mol}^{-1}$  (median and average error  $\sim 3 \text{ pmol mol}^{-1}$ ). (b) Example of  $O_3$  depletion timescale calculation based on the depletion range (ODE start time –  $O_3$  decrease end time) from (a). The natural logarithm of the  $O_3$  values is plotted against time, and the inverse slope of this plot represents the  $O_3$  depletion timescale.

range from 0.7 to  $6.9 \text{ pmol mol}^{-1}$ , with average and median errors corresponding to  $\sim 3.0$  and  $3.3 \text{ pmol mol}^{-1}$  respectively. Due to the timing of the O-Buoy1 deployment at Barrow, we were unable to estimate smoothing error in the manner described above. Therefore, only errors due to propagated dSCD measurement error were considered. For O-Buoy1, total surface mole fraction errors range from 0.7 to  $4.5 \text{ pmol mol}^{-1}$ , with average and median errors corresponding to  $\sim 2.5$  and  $2.6 \text{ pmol mol}^{-1}$  respectively.

## 2.2 ODE definition

Ozone depletion events and “major” ozone depletion events (MODEs) are defined when  $O_3$  drops below 15 and  $10 \text{ nmol mol}^{-1}$ , respectively, for longer than 1 h. The MODE acronym was also utilized by Ridley et al. (2003), and we emphasize that our definition differs from theirs (a larger discussion of ODE definitions in the scientific literature is presented in the Supplement). The ODE start time is the time at which  $O_3$  falls from background ( $O_3$  mole fraction  $> 25 \text{ nmol mol}^{-1}$  for at least 12 h) to below the 90 % value of the mole fraction range during depletion. The ODE stop time is defined by the time when  $O_3$  recovers to 90 % of the local maximum  $O_3$  mole fraction after rising above  $25 \text{ nmol mol}^{-1}$  (if background concentrations will ultimately be reestablished). For MODEs, the start time is the time at which  $O_3$  falls below  $10 \text{ nmol mol}^{-1}$ , and the stop time is the time when  $O_3$  rises above  $10 \text{ nmol mol}^{-1}$  (if the  $O_3$  mole fraction will stay above  $10 \text{ nmol mol}^{-1}$  for at least 12 h). Finally, for the calculation of the  $O_3$  depletion timescale, an  $O_3$  decrease stop time was defined as the time at which  $O_3$  first

reached 10 % of the  $O_3$  mole fraction range during  $O_3$  depletion. These definitions are illustrated by Fig. 3a, and are further discussed in the Supplement. It should be noted that the increase in  $O_3$  mole fraction on 17 April 2011 seen in Fig. 3 does not recover above  $25 \text{ nmol mol}^{-1}$  for longer than 12 h, and its subsequent decrease does not represent a new ODE.

## 2.3 Air mass trajectory analysis

The NOAA HYSPLIT (Hybrid Single Particle Lagrangian Integrated Trajectory) air mass trajectory model (Draxler and Hess, 1997, 1998; Draxler, 1999) was utilized to examine backward trajectories during  $O_3$ -depleted conditions, as defined in Sect. 2.2. Backward air mass trajectories were calculated starting from a height of 10 m above ground level using the ODE stop time as the start time of the model (note that three events, one from each O-Buoy2, 3, and 4, did not have well-defined ODE stop times, and thus could not undergo this analysis). Isobaric trajectories were chosen because the stable surface air in which the ODEs occur is typically well isolated from the air aloft (Oltmans et al., 2012; Seabrook et al., 2013); as long as  $O_3$  is in ODE conditions, the air is likely to be surface layer air. The trajectory run lengths were defined by the ODE durations (ODE stop time – ODE start time; see Fig. S1 in the Supplement for the distribution of ODE time lengths), such that the final point of the backward trajectories corresponded to the defined ODE start times. ODE spatial scales were defined as the maximum distance between any two points of the backward air mass trajectory, as this would represent an upper limit to an event’s

spatial size (illustrated visually in Fig. 4). This analysis was performed for both the broader ODE definition and MODEs. Of the ODE air masses modeled isobarically, all but one remained near the surface (below 200 m above ground level) throughout the course of the trajectory. The outlying ODE air mass, occurring during O-Buoy1 2009 at Barrow, AK, rose above 800 m and likely did not represent surface layer air; this event was therefore excluded from HYSPLIT analyses. For comparison, we also estimated the ODE spatial scales by the same method using isentropic back trajectories (starting height of 10 m above ground level); by determining the distance between the start and end points for each isobaric trajectory; and by using Eq. (2):

$$D_{\text{ODE}} = v_{\text{wind}} \times t_{\text{ODE}}, \quad (2)$$

where  $D_{\text{ODE}}$  is the ODE diameter,  $v_{\text{wind}}$  is the average local wind speed from the anemometer, and  $t_{\text{ODE}}$  is the duration of the ODE.

The HYSPLIT model was also used to estimate some meteorological parameters at each position along the isobaric backward trajectories. For this analysis, the average and minimum air temperatures along each trajectory were compared with the temperatures recorded by the O-Buoy during each ODE. The path lengths and time lengths of individual trajectories were used to estimate the average wind speeds of the air masses, which were compared with the wind speeds obtained from the O-Buoy anemometer. Wind rose plots were created based on the quadrant in which the air mass trajectory spent the most time during a given ODE (north (315–45°), south (135–225°), east (45–135°), and west (225–315°)). Only four quadrants were used in the wind rose plots because there is a large level of uncertainty associated with using a back trajectory model for this purpose (Kahl, 1993). The angles used were obtained by calculating the bearing between the O-Buoy and each point along each back trajectory for each ODE.

#### 2.4 Monte Carlo experiment

A Monte Carlo experiment was performed to determine whether it was statistically possible that the observed ODEs resulted primarily from TM, given the estimated size distribution. In the limit of an ODE as large as the Arctic Ocean, the ODE would be observed at the O-Buoy primarily due to local CM. Thus, for some ODE size limit, it is not feasible for all ODE observations to result from TM. For this simulation experiment, we estimated the probability that assumed circular depletion regions overlap with a point of interest (an O-Buoy) when randomly placed about a defined area represented by the ice-covered Arctic Ocean. The diameters of the circles were defined by the ODE size distribution estimated from Beaufort Sea (O-Buoy1 and O-Buoy2) observations (Sect. 2.3); these particular ODEs were chosen for this exercise because of the similar locations and drift trajectories of the buoys, providing the needed statistics for the analy-



**Figure 4.** Example HYSPLIT backward air mass trajectory. The HYSPLIT model was run backward starting from the ODE end time until the ODE start time. ODE spatial dimensions were determined by calculating the maximum great circle distance between any two points along the trajectory.

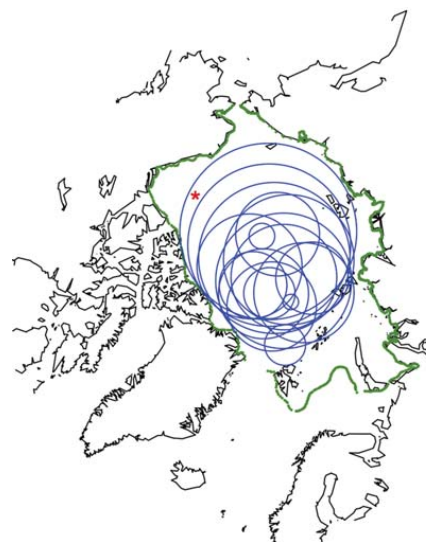


**Figure 5.** Visualization of one iteration out of 2000 of the Monte Carlo experiments. The area of interest within the Arctic is defined by the green outline. Blue circles represent ODE air masses. The red star represents the average location of the O-Buoy between O-Buoys 1 and 2. Seventeen different-sized air masses were randomly placed simultaneously within the area of interest.

sis. Nineteen ODEs were observed between the two deployments (in 2010 and 2011), with ODE sizes ranging from 210 to 3532 km (Supplemental Information Fig. S2). The circles, with sizes taken from the observed size distribution, were simultaneously and randomly placed in an area defined by the

average sea ice extent of the Arctic Ocean between March 2010 and 2011 (Fig. 5), as reported by the National Snow & Ice Data Center (<http://www.nsidc.org/>). We note, however, two O-Buoy2 events were excluded from this analysis. The first was removed due to an undefined ODE spatial scale (discussed in Sect. 2.3). The other ODE size excluded (diameter of 3532 km) was estimated to be larger than the defined area. Thus, a total of 17 circles were used in these simulations. The number of circles that overlapped with the location of the buoy (assumed to be 74.75° N, 142° W, an approximate location of both O-Buoy 1 and 2) was determined for multiple iterations of the experiments. Figure 5 represents one iteration of the experiment, which was repeated 2000 times in order to obtain a statistical distribution of the number of overlaps. Additionally, a sequence of similar Monte Carlo experiments was repeated for individual ODE sizes 1000 times to obtain the probability that each circle size overlaps with the location of the buoy. This simulation experiment was conducted to examine the relationship between ODE size and the probability that the ODE would only be observed due to TM.

### 3 Results and discussion

#### 3.1 Ozone depletion timescale

For O-Buoys 1–4, a total of 38 ODEs were observed between the months of February and June (see Table 1 for breakdown of each O-Buoy). On the assumption that O<sub>3</sub> decrease is an exponential decay process, and to express the observed depletion timescales in an objective manner, the apparent O<sub>3</sub> depletion timescale ( $\tau_{O_3}$ ) at the beginning of an ODE was estimated as the reciprocal of the slope of  $\ln[O_3]$  versus time (during the period ODE start time – O<sub>3</sub> decrease stop time, as discussed in Sect. 2.2; Fig. 3b). This timescale is observed due to a combination of both CM and TM, though the extent to which each factor affects  $\tau_{O_3}$  is unknown. Because we are analyzing the slopes, this analysis is mostly insensitive to the ODE start/depletion stop times as long as the depletion range of the plot constitutes the majority of the defined time frame. As seen in Fig. 6a,  $\tau_{O_3}$  ranged from 30 min to longer than 50 h (maximum of 14 days), with the majority (76 %) shorter than 24 h (median  $\tau_{O_3}$  of 11 h). These timescales correspond to O<sub>3</sub> decrease rates ( $-\frac{d[O_3]}{dt}$ ) that range between 0.02 and 30 nmol mol<sup>-1</sup> h<sup>-1</sup> (average and standard deviation:  $3.5 \pm 5.4$  nmol mol<sup>-1</sup> h<sup>-1</sup>). By comparison, Tuckermann et al. (1997) reported O<sub>3</sub> decrease rates ranging from 0.24 to 7 nmol mol<sup>-1</sup> h<sup>-1</sup> from their measurements in Ny-Ålesund, Spitsbergen. Removing coastal site data (O-Buoy1 2009, deployed in Barrow, AK) from the histogram did not significantly alter the  $\tau_{O_3}$  distribution. For the six ODEs with  $\tau_{O_3}$  equal to 50 h or longer, two cases occurred in June after changes in O<sub>3</sub> levels had become much more gradual, relative to the sporadic and episodic nature of the preceding months (February–May). Apart from these two events, which

occurred at higher temperatures, there was no clear difference in the local average wind speeds or temperatures that was unique to the remaining four of these six events. However, a likely cause for these extended events is poor vertical mixing in the absence of frontal passages. Recent work by Moore et al. (2014) provides evidence of coastal O<sub>3</sub> recovery to background levels when air passes over open leads. This recovery is hypothesized to occur due to increased convective mixing and downward transport of ozone from aloft. Thus, a longer depletion timescale may also imply a large-scale ice-covered surface.

If the observed ODEs were indeed dominated by the CM at the location of the O-Buoys (i.e., TM is minimized in the apparent  $\tau_{O_3}$ ), it is surprising that the majority of cases featured such short apparent timescales of O<sub>3</sub> depletion ( $\tau_{O_3} < 12$  h). As discussed in Sect. 1, most previous model estimates of O<sub>3</sub> depletion timescales due to chemistry are on the order of days (Hausmann and Platt, 1994; Jobson et al., 1994; Piot and von Glasow, 2008, 2009; Tuckermann et al., 1997). Generally, fast  $\tau_{O_3}$  observed at coastal sites have been attributed to TM. In these cases, O<sub>3</sub> has been hypothesized to be chemically destroyed upwind (i.e., over the Arctic Ocean), and the apparent  $\tau_{O_3}$  is a function of both the rate at which the O<sub>3</sub>-depleted air mass travels across the measurement site and the horizontal concentration gradient at the edges of those air masses. For example, Morin et al. (2005) observed O<sub>3</sub> levels to fall from mole fractions of  $\sim 30$  nmol mol<sup>-1</sup> to less than 5 nmol mol<sup>-1</sup> in around 3 min from over the Arctic Ocean, 6 km off the coast of Alert, Canada. However, fast O<sub>3</sub> depletion attributed to local chemistry has been previously reported: using measurements from aboard the icebreaker RV *Polarstern* in the Arctic Ocean, Jacobi et al. (2006) observed a decrease in O<sub>3</sub> from 40 to  $< 1$  nmol mol<sup>-1</sup> in less than 7 h.

To interpret the results from the O-Buoys, we first explore the extent to which known chemical mechanisms could account for the observed  $\tau_{O_3}$  values (i.e., the CM dominates while the TM is minimal). Rates of O<sub>3</sub> loss during ODEs have been previously thought to be limited by Reactions (R3, R4) at high BrO levels, estimated by Eq. (3) below (Le Bras and Platt, 1995; Platt and Janssen, 1995).

$$\left(-\frac{d[O_3]}{dt}\right) = 2k_{BrO+BrO}[BrO]^2 + 2k_{BrO+ClO}[BrO][ClO] \quad (3)$$

Recently, Liao et al. (2012) and Liao et al. (2014) report that (R3) and (R4) only account for around 40 % of the total O<sub>3</sub> depletion chemistry during the 2009 OASIS field campaign. Thompson et al. (2014), using a 0-D model constrained by chemical data collected during the same campaign, found that Br-atom destruction of O<sub>3</sub> has a low homogeneous gas phase radical propagation chain length (close to 1). Because of this small chain length, the dominant source of Br atoms that destroy O<sub>3</sub> appears to be the photolysis of Br<sub>2</sub> and BrCl emitted from the surface or aerosols (Thompson et al., 2014), and thus most of the BrO that is produced terminates via reaction with HO<sub>2</sub> (Reaction R5) (or NO<sub>2</sub> for more polluted

areas, such as Barrow, AK). Indeed, estimating the rate using Eq. (3) assumes that all Br atoms are produced from Reactions (R3) and (R4), which is inconsistent with the observed, often large concentrations of Br<sub>2</sub> (Liao et al., 2012). The BrO termination pathways would result in more heterogeneous recycling of Br atoms. They then compared  $\frac{d[\text{O}_3]}{dt}$  as calculated by both Eq. (3) and by the net chemical O<sub>3</sub>-destruction rate (Eq. 4).

$$\left(-\frac{d[\text{O}_3]}{dt}\right) = k[\text{Br}][\text{O}_3] + k[\text{Cl}][\text{O}_3] + k[\text{O}({}^1\text{D})][\text{H}_2\text{O}] + k[\text{OH}][\text{O}_3] + k[\text{HO}_2][\text{O}_3] - k[\text{BrO}][\text{NO}] - J[\text{BrO}] - k[\text{ClO}][\text{NO}] - J[\text{ClO}] \quad (4)$$

In calculating  $\frac{d[\text{O}_3]}{dt}$ , a regression between the rates showed that using only Eq. (3) underestimates the net  $\frac{d[\text{O}_3]}{dt}$  (from Eq. 4) by a factor of 4.1 on average by neglecting other chemical pathways (Thompson et al., 2014). Therefore, we estimate the BrO mole fractions required to cause the observed  $\tau_{\text{O}_3}$  according to Eqs. (5) and (6) below. These equations include the factor of 4.1 that accounts for the production of bromine atoms via Br<sub>2</sub> and BrCl photolysis, two molecular halogens derived from heterogeneous recycling of species such as HOBr and BrONO<sub>2</sub> on halide-containing aerosols or the saline snowpack (Abbatt et al., 2012; Simpson et al., 2007b). A constant ClO concentration of  $1.7 \times 10^8$  molecules cm<sup>-3</sup> (6 pmol mol<sup>-1</sup> at 248 K and atmospheric pressure) was assumed based on average concentrations measured during the 2009 OASIS campaign (Stephens, 2012).

$$\left(-\frac{d[\text{O}_3]}{dt}\right) = 4.1 \times (2k_{\text{BrO}+\text{BrO}}[\text{BrO}]^2 + 2k_{\text{BrO}+\text{ClO}}[\text{BrO}][\text{ClO}]) \quad (5)$$

$$\tau_{\text{O}_3} = \frac{[\text{O}_3]_{\text{avg}}}{4.1 \times (2k[\text{BrO}]^2 + 2k[\text{BrO}][\text{ClO}])} \quad (6)$$

Because Thompson et al. (2014) utilized a temperature of 248 K in their model, consistent with average local temperatures at Arctic coastal sites in the springtime, we also use this temperature for our BrO mole fraction estimations. The rate constants  $k_{\text{BrO}+\text{BrO}} = 3.8 \times 10^{-12}$  cm<sup>3</sup> molecules<sup>-1</sup> s<sup>-1</sup> and  $k_{\text{BrO}+\text{ClO}} = 8.2 \times 10^{-12}$  cm<sup>3</sup> molecules<sup>-1</sup> s<sup>-1</sup> were calculated based on Sander et al. (2011) and Atkinson et al. (2007), respectively. However, it should be noted that the rate constants change by only ~7–8% when calculated at 273 K ( $k_{\text{BrO}+\text{BrO}} = 3.5 \times 10^{-12}$  cm<sup>3</sup> molecules<sup>-1</sup> s<sup>-1</sup> and  $k_{\text{BrO}+\text{ClO}} = 7.6 \times 10^{-12}$  cm<sup>3</sup> molecules<sup>-1</sup> s<sup>-1</sup>). We also note that  $k_{\text{BrO}+\text{ClO}}$  includes the rate constants for both Reaction (R4a) and (R4b). The calculated BrO mole fractions corresponding to the estimated  $\tau_{\text{O}_3}$  range from ~1 ( $\tau_{\text{O}_3} = 356$  h) to 115 pmol mol<sup>-1</sup> ( $\tau_{\text{O}_3} = 28$  min), with a median of

16 pmol mol<sup>-1</sup> (Fig. 6b). The majority of the calculated distribution of BrO required is fairly comparable to previously reported enhanced surface BrO mole fraction ranges, which often peak around 20–40 pmol mol<sup>-1</sup> (Hausmann and Platt, 1994; Hönninger et al., 2004b; Pöhler et al., 2010; Tuckermann et al., 1997). Indeed, 32 out of 38 events were calculated to require less than 40 pmol mol<sup>-1</sup> of BrO for O<sub>3</sub> depletion. If, however, the expected BrO were calculated based on Eq. (6) without the factor of 4.1 (i.e., expected BrO based Reactions (R3) and (R4)), this number decreases to 20 out of 38 events. For the O-Buoy1 (Barrow, AK) and O-Buoy2 deployments, MAX-DOAS BrO data are available for comparison with the calculated BrO estimations (Fig 6b, c; Table 3). Though these observed BrO mole fractions exhibit maxima higher than 20 pmol mol<sup>-1</sup> (ex. Fig. 2), the average BrO mole fractions during periods of O<sub>3</sub> decrease (ODE start time – O<sub>3</sub> decrease stop time; Sect. 2.2) were found to be much less than 20 pmol mol<sup>-1</sup> (Table 3).

The amount of BrO data available was dependent on the length of daylight, as the MAX-DOAS is a passive instrument (Carlson et al., 2010). In the case of O-Buoy1 at Barrow, there were not enough BrO data available for most periods of O<sub>3</sub> decrease to produce solid conclusions. However, observed BrO levels for three events were not inconsistent with the calculated BrO levels required for the observed  $\tau_{\text{O}_3}$  (see Table S1 and Fig. S3 in the Supplement). While these three events do not have enough BrO data to merit an in-depth discussion, they are discussed in more detail in the Supplement. For the remaining O-Buoy1 and all O-Buoy2 cases in which there were enough BrO data to make comparisons, observed BrO levels were found to be lower than the calculated BrO required by Eqs. (5) and (6), even when considering the propagated measurement error (Table 3; described in Sect. 2.1). Indeed, in two of the O-Buoy2 cases, the observed BrO levels are less than a tenth of that required. This result is surprising since the Arctic Ocean is the assumed originating site for ODEs. At least for O-Buoy2, the observed BrO, assumed 6 pmol mol<sup>-1</sup> ClO, and factor of 4.1 (Thompson et al., 2014) cannot account for the apparent  $\tau_{\text{O}_3}$ .

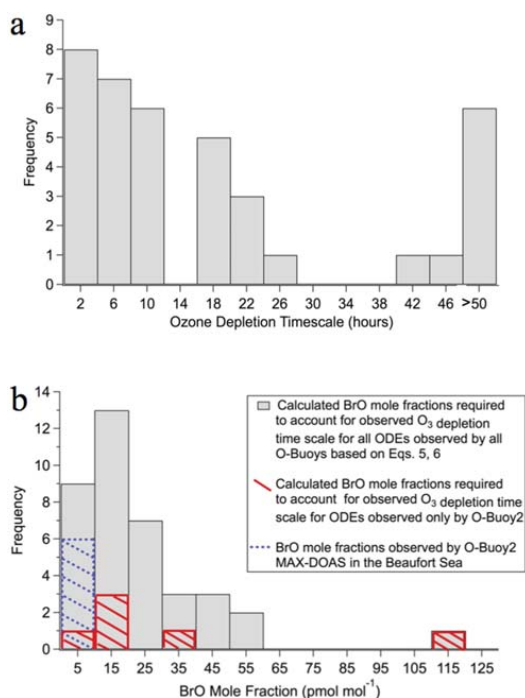
Possible reasons for the observed small  $\tau_{\text{O}_3}$  values can be summarized by the following two hypotheses:

1. There are chemical mechanisms for O<sub>3</sub> destruction that are currently not being considered, or other radical levels (e.g., IO, ClO, HO<sub>2</sub>) are higher than assumed here.
2. Most ODEs chemically initiate upwind of the O-Buoys such that the observed  $\tau_{\text{O}_3}$  largely result from TM, as discussed above.

Concerning the first hypothesis, iodine radical chemistry has been observed in Antarctica (Saiz-Lopez et al., 2007) and in the sub-Arctic at Hudson Bay (Mahajan et al., 2010). Models have shown that iodine chemistry has the potential to have a significant impact on O<sub>3</sub> destruction chemistry due to the very fast rate constant for IO reaction with BrO

**Table 3.** Average BrO mole fractions during periods of O<sub>3</sub> decrease from O-Buoy2 MAX-DOAS, the corresponding propagated errors, and the estimated BrO required for the observed O<sub>3</sub> depletion timescales based on Eq. (6) (Sect. 3.1; UTC – Coordinated Universal Time).

ODE start time (UTC)	O <sub>3</sub> decrease stop time (UTC)	Observed $\tau_{\text{O}_3}$ (hours)	Average observed BrO (pmol mol <sup>-1</sup> )	Measurement uncertainty (pmol mol <sup>-1</sup> )	Estimated BrO required from observed $\tau_{\text{O}_3}$ (pmol mol <sup>-1</sup> )
15 Apr 2011 18:47	16 Apr 2011 06:41	10.5	7.2	3.5	17.5
19 Apr 2011 04:15	19 Apr 2011 04:53	0.5	5.4	3.5	114.7
26 Apr 2011 14:46	26 Apr 2011 22:29	16.2	5.2	3.2	14.8
3 May 2011 11:37	3 May 2011 14:50	1.6	2.6	2.3	33.5
6 May 2011 12:58	7 May 2011 21:32	11.8	5	3.5	15.1
26 May 2011 21:22	28 May 2011 00:59	40.6	0.9	3.2	9.7

**Figure 6.** (a) Histogram of the calculated O<sub>3</sub> depletion timescale distribution during ODEs. To more clearly show the majority of events, the six events with  $\tau_{\text{O}_3}$  greater than 50 h are grouped together on the histogram. (b) Calculated BrO concentrations are shown for the observed ODEs. These values were calculated using Eq. (6) with an assumed ClO mole fraction of 6 pmol mol<sup>-1</sup> and other O<sub>3</sub> destruction pathways (discussed in Sect. 3.1). The calculated BrO mole fraction mode is 15 pmol mol<sup>-1</sup>. Measured BrO for O-Buoy2 is shown as the blue hatched bar, and the corresponding BrO required to account for the observed ozone depletion rates for O-Buoy2 events are shown as solid red diagonal bars.

(~32 times faster than Reaction (R3)) (Calvert and Lindberg, 2004; Atkinson et al., 2007). In a photochemical box model, Saiz-Lopez et al. (2007) found the ozone loss rate increased by a factor of four when iodine was included with bromine chemistry to destroy ozone (via IO + BrO,  $k_{\text{IO} + \text{BrO}} = 1.2 \times 10^{-10} \text{ cm}^3 \text{ molecule}^{-1} \text{ s}^{-1}$  at 248 K). Though previous studies have indicated the presence of active iodine chemistry through enhanced levels of total iodine (Martinez et al., 1999) and filterable iodine (Barrie et al., 1994; Schall and Heumann, 1993), there are currently no measurements of IO in the high Arctic above long-path DOAS limits of detection as low as 0.3 pmol mol<sup>-1</sup> (Pöhler et al., 2010), nor are there estimates of I<sub>2</sub> mole fractions for the Arctic Ocean region. Thus, this possible mechanism remains speculative. Additionally, the enhanced salinity of first year ice could be a reason for enhanced chlorine radical production as compared to coastal (e.g., Barrow) observations, or snowpack sources of HO<sub>x</sub> (HONO (Zhou et al., 2001), HCHO (Sumner and Shepson, 1999; Sumner et al., 2002), or H<sub>2</sub>O<sub>2</sub> (Hutterli et al., 2001; Jacobi et al., 2002)) could enhance HO<sub>2</sub> levels and thus reactivity.

We can potentially test for O<sub>3</sub> depletion chemistry missing from Eqs. (4–6) by examining the distribution of the ozone tendency,  $(\frac{d[\text{O}_3]}{dt})$ , with and without the calculated component from the chemistry included in Eq. (5). First, the observed short-term ozone tendency was calculated for values of  $dt$  between consecutive BrO measurements (currently O-Buoy1 at Barrow, and O-Buoy2 in the Beaufort Sea) and plotted in Fig. 7a and b. Both distributions are zero centered (average Barrow: 0.15 nmol mol<sup>-1</sup> h<sup>-1</sup>; average Beaufort: 0.01 nmol mol<sup>-1</sup> h<sup>-1</sup>) with heavy tails on each side. Then,  $\frac{d[\text{O}_3]}{dt}$  was calculated using Eq. (5), as above (Fig. 7c, d); this represents the component of the observed  $\frac{d[\text{O}_3]}{dt}$  resulting from O<sub>3</sub> depletion chemistry. By subtracting these two results, we obtain the distribution of ozone tendencies not accounted for by the considered chemical mechanisms (Fig. 7e, f). These two distributions (representing all observations, and those with known chemistry removed) do differ significantly after this subtraction at the 95 % confidence level according to the Kolmogorov-Smirnov test ( $p$  value =  $4.9 \times 10^{-4}$  and  $1.4 \times 10^{-6}$  for the O-Buoy1 and 2 results, respectively). Both distribution averages become more shifted

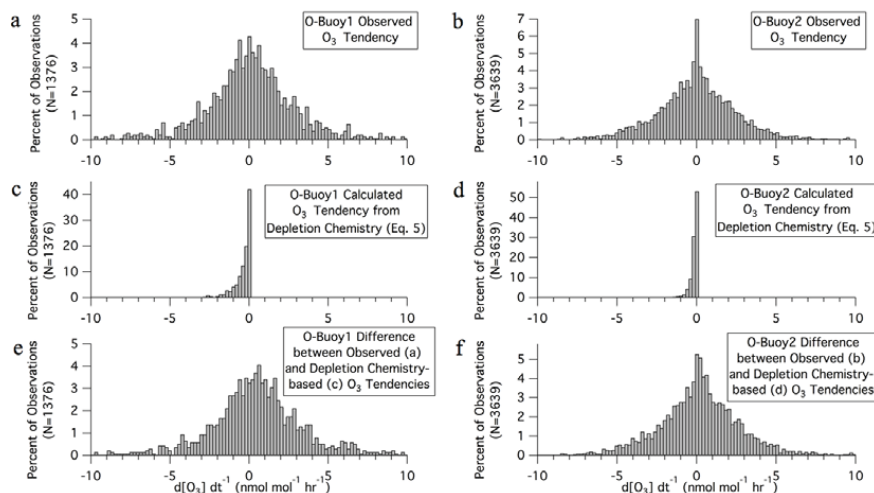


**Figure 7.** Histogram of the O<sub>3</sub> tendency for observations from O-Buoy1 at Barrow, AK (a, c, e), and O-Buoy2 in the Beaufort Sea (b, d, f). (a, b) show the distributions of observed O<sub>3</sub> tendencies between consecutive BrO measurement points. Middle plots (c, d) represent the O<sub>3</sub> tendency distribution based on the depletion chemistry accounted for by Eq. (5). (e, f) result from the difference of the observed O<sub>3</sub> tendency (a, b) and the contributions of the chemistry accounted for by Eq. (5) (c, d).

from zero, with an average  $\frac{d[O_3]}{dt}$  of  $-0.43 \text{ nmol mol}^{-1} \text{ h}^{-1}$  for O-Buoy1, and  $-0.18 \text{ nmol mol}^{-1} \text{ h}^{-1}$  for O-Buoy2. However, it can be shown that the overall symmetry does slightly improve after subtraction by calculating skewness (Eq. 7):

$$\text{skewness} = \frac{\sum_{i=1}^N (x_i - \bar{x})^3}{(N-1)s^3}, \quad (7)$$

where  $N$  represents the number of measurements and  $s$  represents the standard deviation of a sample. Skewness decreases in magnitude from  $-0.38$  to  $-0.25$  for the O-Buoy1 at Barrow case, and from  $-0.82$  to  $-0.80$  in the O-Buoy2 in the Beaufort Sea case. Springtime chemical O<sub>3</sub> production in the Arctic boundary layer has been found to be essentially negligible (Helmig et al., 2009; Helmig et al., 2012), and so it is likely the positive portions of these distributions result from air mass transport and vertical mixing. This analysis then produces a result not inconsistent with the idea that the remainder of the negative  $\frac{d[O_3]}{dt}$  represents air mass transport.

Hypothesis two, in which the TM dominates the observed  $\tau_{O_3}$ , is in line with those of many previous studies (e.g., Botenheimer et al., 2009; Hausmann and Platt, 1994; Jacobi et al., 2010; Morin et al., 2005). As discussed in these studies, fast O<sub>3</sub> depletion can often be attributed to changes in air mass flow, and surface O<sub>3</sub> mole fractions can return to background levels upon the passage of low-pressure systems, with associated enhanced vertical mixing. The idea that most of the negative side of the ozone tendency distribution results from transport and not local chemistry is statistically possible only

if the average spatial scale of an ODE region is below some critical size (discussed below in Sect. 3.2).

### 3.2 ODE spatial scales

To estimate the spatial scales of ODEs, we combined O-Buoy observations with backward air mass trajectory model (Sect. 2.3). This analysis assumes O<sub>3</sub> depletes within an air mass upwind via CM, and this air mass subsequently roams across the measurement site; the size of this O<sub>3</sub>-depleted air mass can be estimated from the length of time O<sub>3</sub> is depleted and the wind speed (i.e., TM dominates the CM at the observation site). We emphasize, however, that the observations likely involve some combination of both TM and in situ CM, given O-Buoy measurements of BrO levels greater than  $0 \text{ pmol mol}^{-1}$  (indicative of active O<sub>3</sub> depletion chemistry). It is of course conceptually possible that other transport scenarios exist; for instance, conditions could exist in some region upwind that result in the continuous depletion of O<sub>3</sub>-containing air masses that pass over this region. This depleted air may then pass over the buoy. If the depleted air remains intact, however, the spatial-scale calculations would still apply.

As shown in Fig. 8, the median of the one-dimensional length for the ODEs was 877 km. While the estimated size distribution of the MODEs ( $O_3 < 10 \text{ nmol mol}^{-1}$ ) showed no clear mode, it is clear that the distribution contains mostly (relatively) smaller events, with a median size of 282 km. The distribution of results is also consistent with observations by Jones et al. (2013) and Ridley et al. (2003), who

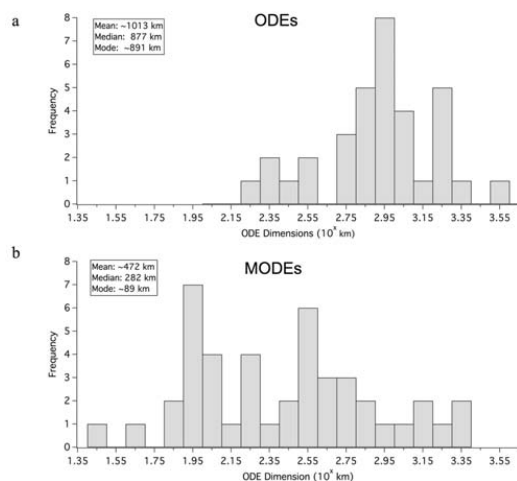


**Figure 8.** (a) Histogram of ODE dimensions for all ODEs. The median of the distribution is 877 km. (b) Histogram of dimensions of MODEs. The median of the distribution is 282 km.

both reported ODEs of spatial dimensions of at least 1200 km and between 600 and 900 km, respectively. The results presented here strongly suggest that large areas of the Arctic are at least partially depleted during Arctic springtime with local embedded areas that are more depleted. While these isobaric trajectories likely represent the near-surface transport path of depleted air (Seabrook et al., 2013), we also estimated the ODE spatial scales using isentropic back trajectories (starting at 10 m above ground level) and the local wind speeds using the O-Buoy anemometer (Eq. 2). The means for the isobaric ( $1013 \pm 379$  km), isentropic ( $1260 \pm 279$  km), and local wind-speed-based ( $1154 \pm 341$  km) spatial-scale distributions were statistically similar at the 95 % confidence level (confidence intervals reported here). Additionally, spatial-scale estimation using the distance between the isobaric trajectory start and end points yielded comparable results (mean  $947 \pm 238$  km).

As discussed in Sect. 3.1, known chemical mechanisms with reasonable levels of other radicals could not account for the observed  $\tau_{\text{O}_3}$  values, suggesting these fast  $\tau_{\text{O}_3}$  values were due in large part to TM. A Monte Carlo simulation experiment was conducted with the aim of examining the statistical possibility that all observed ODEs, based on the general ODE definition ( $\text{O}_3 \leq 15 \text{ nmol mol}^{-1}$ ), could have occurred upwind of the buoy and were observed because of TM. As described in Sect. 2.4, the simulations were conducted by randomly placing circles (hypothetical ODEs/source regions) across an area the size of the Arctic Ocean sea ice. These circles were defined using the distribution of ODE spatial scales determined from the 17 events observed by the O-Buoy1 and O-Buoy2 deployments (Fig. S2), which observed

$\text{O}_3$ -depleted air  $\sim 60$  % of the time between late March and May 2010 and  $\sim 65$  % of the time between mid April and May 2011, respectively. We note that assuming circular regions for ODEs could underestimate the ODE size since it assumes the center of the event passes over the buoy, when in fact a secant is more likely. Additionally, the area could be overestimated if the true ODE shapes are actually elliptical or irregular in shape. For this statistical exercise, we made the assumptions that the circles could appear (initiate) anywhere across the Arctic Ocean, and that the circles could also represent possible sizes of ODE source regions. While there is evidence to suggest the existence of specific source regions favorable to ODE formation (Bottenheim and Chan, 2006; Bottenheim et al., 2009; Koo et al., 2012; Simpson et al., 2007a; Theys et al., 2011), no definitive conclusions have yet been made from in situ observations regarding either the locations or the sizes of such regions. We also assume that the circle must be contained wholly within the bounds shown in Fig. 5 in order to equally represent all sizes from the distribution. We acknowledge that this assumption could overestimate the frequency with which ODEs overlap with the buoy, as ODEs have been observed in sub-Arctic regions, such as Kangerlussuaq, Greenland ( $67^\circ \text{ N}$ ,  $51^\circ \text{ W}$ ; Miller et al., 1997), and Hudson Bay ( $55^\circ \text{ N}$ ,  $75^\circ \text{ W}$ ; Hönninger et al., 2004a). However, this approach could also underestimate the frequency of overlap, as ODEs that initiate remotely from the buoy would be less likely to be part of the observed distribution of events; in other words, it is also possible that the study region for the Monte Carlo simulation could be too large. It is also assumed that the circles represent fully formed  $\text{O}_3$ -depleted air masses or source regions, and that a circle overlapping with the buoy represents “local” ODE initiation relative to the O-Buoy.

The Monte Carlo simulations show that the randomly placed circles most often do not overlap with the measurement site (Fig. 9a). In fact, only very large sizes (larger than  $\sim 1750$  km) were likely to intercept the O-buoy location with a significant probability ( $> 10$  %), as shown in Fig. 9b. Specifically, none of the 17 circles overlapped with the O-Buoy site in 58 % of the 2000 simulation iterations, and only one circle (in 17) overlapped with the O-Buoy site in 33 % of iterations. For the median ODE size, the probability of any individual event overlapping the Buoy was less than 1 %, as shown in Fig. 9b. Therefore, the spatial statistics exercise supports the possibility that the overwhelming majority of ODEs observed by the O-Buoys in the Beaufort Sea could have been observed primarily due to TM, and ODEs initiated upwind. We emphasize that this Monte Carlo exercise does not prove that this is the case, only that this hypothesis is not inconsistent with the observed ODE spatial scales. The practical question is then raised as to how many buoys (observation sites) must be present to increase the probability of observing an ODE primarily due to local chemistry (with the assumption of equal probability of initiation across the Arctic Ocean and that ODE sizes represent source regions,



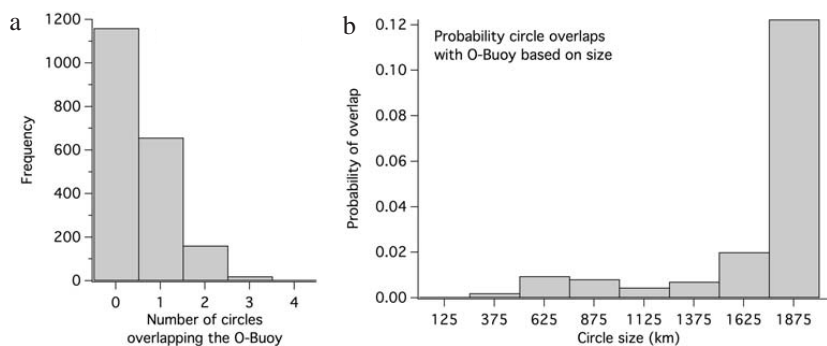


**Figure 9.** Results from Monte Carlo simulation experiment. **(a)** Based on the size distribution as defined by the ODE definition ( $O_3 \leq 15 \text{ pmol mol}^{-1}$ ), circular areas were shown to not overlap with the site of the O-Buoy 58 % of the time (mode=0), followed by an overlap of one circle 33 % of the time. **(b)** Plot of the probability that an individual circle overlaps with the measurement site vs. the size of the circle.

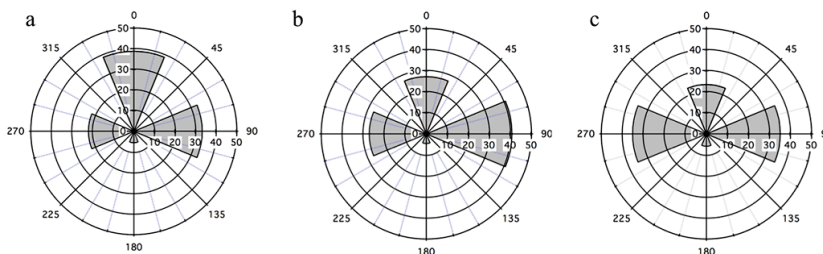


**Figure 10.** Wind rose plots based on the HYSPLIT backward air mass trajectories showing measured wind direction (degrees) and frequency (%), for **(a)** ODEs, **(b)** MODEs, and **(c)** non-ODEs observed during the two O-Buoy Beaufort Sea deployments (see Fig. 1; Table 1).

as assumed for the Monte Carlo experiment). If, for example, two additional O-Buoys were deployed at the North Pole ( $86^\circ \text{ N}$ ,  $54^\circ \text{ W}$ ) and in the East Siberian Sea ( $75^\circ \text{ N}$ ,  $170^\circ \text{ E}$ ), both potential sites of future O-Buoy deployments, repeating the simulations showed that five out of 17 circles overlapped with at least one measurement site, with no simulation iterations resulting in zero circle overlaps (Fig. S4). This result emphasizes the need for multiple, simultaneous deployments of O-Buoys across different geographical regions to ensure that local-scale chemistry is observed within one deployment season.

To examine if there is a consistent upwind region from which ODEs travel, wind rose plots were constructed for the ODEs observed by O-Buoy1 (2010 deployment) and O-Buoy2 in the Beaufort Sea, as shown in Fig. 10. As above, the O-Buoys deployed in the Beaufort Sea were chosen because of their similar locations and drift trajectories, providing the needed statistics for the analysis. During ODEs (Fig. 10a), air masses most commonly traveled from the north ( $\sim 39\%$  of cases), followed by those from the east ( $\sim 33\%$  of cases) and the west ( $\sim 22\%$  of cases). For the MODE air masses, the trajectories most often originated from the eastern sec-

tor ( $\sim 41\%$  of cases; Fig. 10b), and the northern and western sectors accounted for  $\sim 27\%$  of cases each. Finally for cases in which  $O_3$  was not depleted (non-ODE cases; Fig. 10c), the eastern and western sectors each accounted for 35 % of cases, and the north accounted for 24 %. Only one event in each case showed an air mass originating from the south, toward the Alaskan and Canadian coasts. The results presented are consistent with a hypothesis that all regions that are sea-ice covered can support ODE chemistry. Notably, the region to the east of the buoys (i.e., from the Canadian archipelago and eastern Beaufort Sea) features sea ice that historically contains a high fraction of multiyear ice (Kwok et al., 2009), and GOME satellite imagery has previously shown large amounts of BrO to be present in this region (Choi et al., 2012; Koo et al., 2012; Richter et al., 1998; Salawitch et al., 2010). Using backward air mass trajectories originating from the coastal sites of Alert, Canada, and Zeppelinfjellet, Svalbard, Bottenheim and Chan (2006) suggested that ODE air mass source regions could be in the East Siberian Sea, an area to the northwest of the O-Buoys that features first-year ice that breaks up in spring. It should be noted, however, that Bottenheim and Chan (2006) only reported trends during the month of

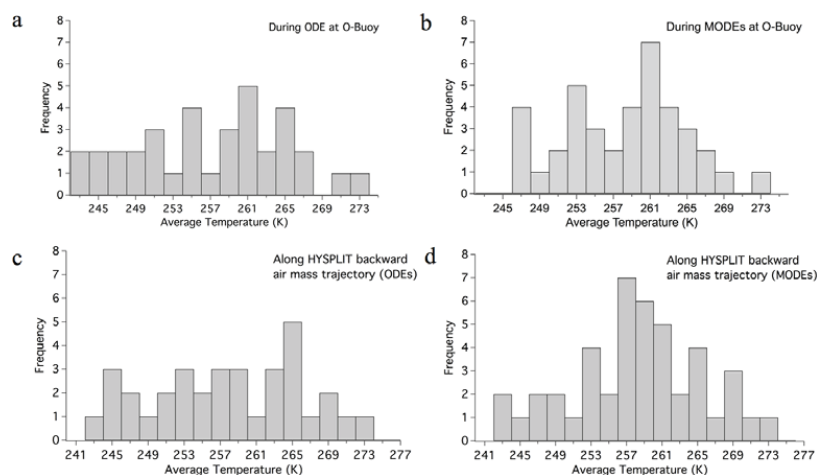


**Figure 11.** Histograms of the average ambient temperature measured by the O-Buoys during (a) ODEs and (b) MODEs. Histograms of the average temperature along the HYSPLIT backward air mass trajectories for (c) ODEs and (d) MODEs.

April, as opposed to this study that examined ODEs from as early as February to as late as June (Table 1 and Fig. 2). Unfortunately, there were not enough events per month here to observe any clear monthly source region trends. Additionally, while the ODE and MODE cases show slight preferences for northern or eastern winds, respectively, the non-ODE cases do not appear to differ significantly from the ODE and MODE cases. As recently presented by Moore et al. (2014), it is also possible that  $O_3$  recovers when air passes over open sea ice leads due to convective mixing, and air that passed over unbroken ice was more often  $O_3$ -depleted, and thus local sea ice conditions could have a more direct impact on  $O_3$  levels than the wind direction.

### 3.3 Temperature and wind speed during ODEs

Figure 11 shows the distribution of average temperatures that applied during the ODEs in this study. Local average temperatures during ODEs ranged between 243 and 273 K (Fig. 11a; median 257 K). The apparent mode of the distribution (261 K) is 8 K warmer than the hypothesized required upper limit temperature for rapid ozone depletion (253 K). Indeed,  $\sim 66\%$  of the ODEs occurred at average temperatures greater than 253 K. An illustrative event is shown in Fig. 2; the O-Buoy2 ODE occurring in early June shows a noticeable increase in BrO while temperatures average around 270 K. The temperatures for MODEs resulted in a similar distribution (Fig. 11b). If, however, ODEs most often originate upwind from the site of O-Buoys, the local temperatures could be irrelevant, as the actual depletion chemistry may have taken place at a location where the temperature was much lower. To examine this, the isobaric HYSPLIT

backward air mass trajectories were utilized to estimate the average temperatures experienced by the observed air mass upwind. In Fig. 11c and d, we present histograms of the average temperatures from each air mass trajectory for both ODEs and MODEs, which were observed to be very similar (medians:  $\sim 258$  and  $257$  K for ODE and MODE, respectively) and not significantly different from those measured at the O-Buoys. As with the local observations, approximately two-thirds of the trajectory temperature averages were above 253 K, though we acknowledge that there is a high level of uncertainty associated with using an air mass back trajectory model for such a purpose in a data sparse region (Kahl, 1993). Additionally, we analyzed the minimum temperatures observed by the O-Buoy and from HYSPLIT trajectories during the same depletion periods. The median minimum temperatures observed at the O-Buoy are 251 and 253 K for the ODE and MODE cases, respectively. Similarly, the median minimum temperatures obtained from HYSPLIT trajectories are 250 and 254 K for the ODE and MODE cases, respectively. In both cases, it is interesting that only about half of the events were observed with minimum temperatures less than the eutectic temperature of NaCl (252 K), consistent with the results above. This analysis reveals no apparent temperature dependence for  $O_3$  depletion and shows that temperatures below 253 K were not necessary to observe ozone-depleted air masses, corroborating the conclusions of Bottenheim et al. (2009) and Jacobi et al. (2010).

Recent reports discuss the possibility that ODEs can be initiated after blowing snow events (Frieß et al., 2011; Jones et al., 2009; Yang et al., 2008; Yang et al., 2010), which presumably produce the availability of new saline surfaces, whether in suspended aerosol form, or through

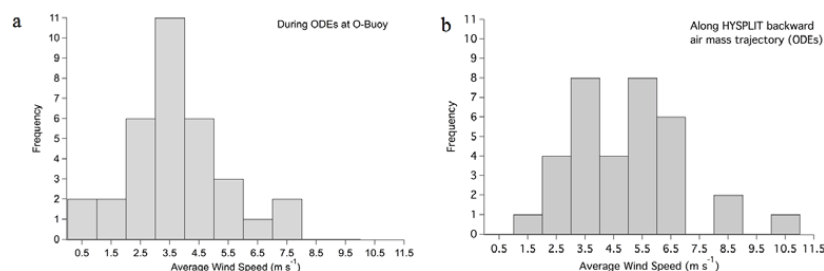


**Figure 12.** (a) Histogram of the average wind speed measured by the O-Buoys during ODEs. (b) Histogram of average wind speeds from O<sub>3</sub>-depleted air masses, as determined from the HYSPLIT backward air mass trajectories.

redeposition of sea salt aerosol to the physical surface. Blowing snow events occur during periods of higher wind speeds ( $> 8 \text{ m s}^{-1}$ ) (Frieß et al., 2011), implying that there might be a relationship between wind speed and ODEs. We thus performed an analysis for wind speeds analogous to the temperatures using both local O-Buoy data and HYSPLIT backward trajectories. Figure 12a shows that ODEs observed at the O-Buoy were characterized by low measured wind speeds (median of  $3.6 \text{ m s}^{-1}$  and a mode of  $3.5 \text{ m s}^{-1}$ ), relative to what is needed for blowing snow. However, there is also a difficulty in this analysis in that, under these circumstances, when the air is most of the time at least partly depleted, such a histogram may reflect, at least in part, the normal distribution of wind speeds found in the Arctic troposphere. Therefore, for comparison, periods when O<sub>3</sub> was not depleted (non-ODEs) were examined (see Supplement). As shown in Fig. S5, there was no apparent difference in the modes for non-ODEs relative to the depleted cases. We reiterate that the O-Buoy wind speed measurements reported here could be biased low (see Sect. 2.1); thus, we compare this distribution to one determined by the HYSPLIT method (described in the Supplement) below.

The distribution of average wind speeds along the HYSPLIT trajectories (Fig. 12b) reveals a faster median wind speed of  $4.9 \text{ m s}^{-1}$ , potentially consistent with ODEs occurring at somewhat higher wind speeds. However, the distribution showed no clear preference for higher wind speeds for ODEs. During non-ODE periods, we found the majority of wind speeds to be between 3 and  $6 \text{ m s}^{-1}$ , similar to that for the ODE cases (Fig. S5b in the Supplement), showing that the wind speeds characterizing the upwind air masses observed for ODEs are not different from those for non-depleted conditions. From this analysis, we found that elevated wind speed appeared to be neither a prerequisite, nor a defining characteristic for ODEs, as also found by Helmig et al. (2012) and Solberg et al. (1996).

#### 4 Conclusions

The O-Buoy was developed in part to enable the observation of ODEs at the hypothesized location of their initiation, the frozen Arctic Ocean surface. Surface measurements of ambient O<sub>3</sub>, BrO, temperature, and wind speed from five separate O-Buoy deployments were utilized to gain insights into the characteristics of ODEs observed over the Arctic Ocean.

The apparent timescales of O<sub>3</sub> depletion during ODEs, based on both CM and TM, were calculated to be shorter (median of 11 h) than previous modeled chemical estimates (e.g., Hausmann and Platt, 1994) by a factor of two or more. This observation suggests the O<sub>3</sub> depletion timescales are dominated by TM, accelerated chemical mechanisms involving higher radical levels, or novel chemical mechanisms. If TM are assumed to dominate local observations, spatially, the majority of the Arctic Ocean marine boundary layer is likely at least partially depleted in O<sub>3</sub> during spring, suggesting that O<sub>3</sub>-depleted air masses remain intact for long periods of time after halogen chemistry has subsided. Regions of MODEs ( $\text{O}_3 < 10 \text{ nmol mol}^{-1}$ ) were, on average, smaller, with a median of 282 km, compared to a median of 877 km for ODEs ( $\text{O}_3 \leq 15 \text{ nmol mol}^{-1}$ ). An expanded network of O<sub>3</sub> monitors across the Arctic Ocean is required to effectively capture the spatial extent of the small, actively O<sub>3</sub>-depleting air masses, as well as that of the larger, depleted air masses. Monte Carlo simulations supported the possibility that these spatial ODE sizes are consistent with depletion upwind of the O-Buoy, followed by air mass transport to the buoy. However, the degree to which process dominates local observations of ODEs (TM vs. CM) is unknown, as O-Buoy observations of BrO indicate that there is generally always some degree of chemistry involved. Thus, to further address the question of the O<sub>3</sub> depletion timescales, more long-term O<sub>3</sub> and halogen measurements over the Arctic Ocean sea ice are necessary, particularly in locations such as the East Siberian and Chukchi seas.

There was no apparent temperature dependence observed for the presence of an ODE, and low temperatures (i.e., less than 253 K) were not required for the observation of an

ODE. The distribution of wind speeds local to the O-Buoy was moderately low during ODEs (mode of  $\sim 3.5 \text{ m s}^{-1}$ ), showing that ODEs were primarily observed under relatively calm conditions. While higher average wind speeds (median  $\sim 5 \text{ m s}^{-1}$ ) were estimated for the course of the backward air mass trajectory, we did not observe a clear preference for ODEs occurring during higher wind speeds. Concurrent measurements of blowing snow, sea salt aerosol, ozone, and halogens, in addition to wind speed, are required to better understand the relationship between wind speed and ODEs.

**The Supplement related to this article is available online at doi:10.5194/acp-14-4875-2014-supplement.**

*Acknowledgements.* The authors thank the NSF for the funding of both the development and deployments of the O-Buoys (grants ARC-0612331, ARC-0611992, ARC-0612047, and ARC-0612457 to P. A. Matrai, D. K. Perovich, P. B. Shepson, and W. R. Simpson, respectively), as well as for the NSF Postdoctoral Fellowship for Polar Regions Research for K. A. Pratt. Additionally, we are thankful for additional funding for O-Buoys provided by the Government of Canada Program for the International Polar Year, as part of OASIS-CANADA (Project no. MD065). We would like to also thank U. Frieß and J. Zielke at the University of Heidelberg for assistance with the inversion of the MAX-DOAS data. The authors gratefully thank the NOAA Air Resources Laboratory (ARL) for the provision of the HYSPLIT transport and dispersion model used in this publication, as well as the National Snow and Ice Data Center for providing access to monthly sea ice extent data. The authors are grateful to the O-Buoy\* team, without whom this project would not have been possible. \*The current O-Buoy team includes M. Carlsen, F. Chavez, M. Everly, G. Friederich, P. Joyce, R. Oglesbee, C. Rauschenberg, A. Sheppard, R. Stehle, B. Tupper, T. Valentic, C. Wahl, C. Williams, P. Wyss, and J. Zimmerman.

Edited by: R. Sander

## References

- Abbatt, J. P. D., Thomas, J. L., Abrahamsson, K., Boxe, C., Granfors, A., Jones, A. E., King, M. D., Saiz-Lopez, A., Shepson, P. B., Sodeau, J., Toohey, D. W., Toubin, C., von Glasow, R., Wren, S. N., and Yang, X.: Halogen activation via interactions with environmental ice and snow in the polar lower troposphere and other regions, *Atmos. Chem. Phys.*, 12, 6237–6271, doi:10.5194/acp-12-6237-2012, 2012.
- Adams, J. W., Holmes, N. S., and Crowley, J. N.: Uptake and reaction of HOBr on frozen and dry NaCl/NaBr surfaces between 253 and 233 K, *Atmos. Chem. Phys.*, 2, 79–91, doi:10.5194/acp-2-79-2002, 2002.
- Aguzzi, A. and Rossi, M. J.: Heterogeneous hydrolysis and reaction of BrONO<sub>2</sub> and Br<sub>2</sub>O on pure ice and ice doped with HBr, *J. Phys. Chem. A*, 106, 5891–5901, doi:10.1021/Jp014383e, 2002.
- Albert, M. R., Grannas, A. M., Bottenheim, J., Shepson, P. B., and Perron, F. E.: Processes and properties of snow–air transfer in the high Arctic with application to interstitial ozone at Alert, Canada, *Atmos. Environ.*, 36, 2779–2787, doi:10.1016/s1352-2310(02)00118-8, 2002.
- Anlauf, K. G., Mickle, R. E., and Trivett, N. B. A.: Measurement of Ozone during Polar Sunrise Experiment 1992, *J. Geophys. Res.*, 99, 25345–25353, doi:10.1029/94jd01312, 1994.
- Atkinson, R., Baulch, D. L., Cox, R. A., Crowley, J. N., Hampson, R. F., Hynes, R. G., Jenkin, M. E., Rossi, M. J., and Troe, J.: Evaluated kinetic and photochemical data for atmospheric chemistry: Volume III – gas phase reactions of inorganic halogens, *Atmos. Chem. Phys.*, 7, 981–1191, doi:10.5194/acp-7-981-2007, 2007.
- Barrie, L. A., Bottenheim, J. W., Schnell, R. C., Crutzen, P. J., and Rasmussen, R. A.: Ozone Destruction and Photochemical Reactions at Polar Sunrise in the Lower Arctic Atmosphere, *Nature*, 334, 138–141, 1988.
- Barrie, L. A., Staebler, R., Toom, D., Georgi, B., Denhartog, G., Landsberger, S., and Wu, D.: Arctic Aerosol Size-Segregated Chemical Observations in Relation to Ozone Depletion during Polar Sunrise Experiment 1992, *J. Geophys. Res.*, 99, 25439–25451, doi:10.1029/94jd01514, 1994.
- Bottenheim, J. W., Gallant, A. G., and Brice, K. A.: Measurements of NO<sub>y</sub> species and O<sub>3</sub> at 82° N latitude, *Geophys. Res. Lett.*, 13, 113–116, doi:10.1029/GL013i002p00113, 1986.
- Bottenheim, J. W., Fuentes, J. D., Tarasick, D. W., and Anlauf, K. G.: Ozone in the Arctic lower troposphere during winter and spring 2000 (ALERT2000), *Atmos. Environ.*, 36, 2535–2544, doi:10.1016/s1352-2310(02)00121-8, 2002.
- Bottenheim, J. W. and Chan, E.: A trajectory study into the origin of spring time Arctic boundary layer ozone depletion, *J. Geophys. Res.*, 111, D19301, doi:10.1029/2006jd007055, 2006.
- Bottenheim, J. W., Netcheva, S., Morin, S., and Nghiem, S. V.: Ozone in the boundary layer air over the Arctic Ocean: measurements during the TARA transpolar drift 2006–2008, *Atmos. Chem. Phys.*, 9, 4545–4557, doi:10.5194/acp-9-4545-2009, 2009.
- Boudries, H. and Bottenheim, J. W.: Cl and Br atom concentrations during a surface boundary layer ozone depletion event in the Canadian high Arctic, *Geophys. Res. Lett.*, 27, 517–520, doi:10.1029/1999gl011025, 2000.
- Calvert, J. G. and Lindberg, S. E.: Potential influence of iodine-containing compounds on the chemistry of the troposphere in the polar spring. I. Ozone depletion, *Atmos. Environ.*, 38, 5087–5104, doi:10.1016/j.atmosenv.2004.05.049, 2004.
- Carlson, D., Donohoue, D., Platt, U., and Simpson, W. R.: A low power automated MAX-DOAS instrument for the Arctic and other remote unmanned locations, *Atmos. Meas. Tech.*, 3, 429–439, doi:10.5194/amt-3-429-2010, 2010.
- Cavender, A. E., Biesenthal, T. A., Bottenheim, J. W., and Shepson, P. B.: Volatile organic compound ratios as probes of halogen atom chemistry in the Arctic, *Atmos. Chem. Phys.*, 8, 1737–1750, doi:10.5194/acp-8-1737-2008, 2008.
- Cho, H., Shepson, P. B., Barrie, L. A., Cowin, J. P., and Zaveri, R.: NMR investigation of the quasi-brine layer in ice/brine mixtures, *J. Phys. Chem. B*, 106, 11226–11232, doi:10.1021/Jp020449, 2002.
- Choi, S., Wang, Y., Salawitch, R. J., Canty, T., Joiner, J., Zeng, T., Kurosu, T. P., Chance, K., Richter, A., Huey, L. G., Liao, J., Neuman, J. A., Nowak, J. B., Dibb, J. E., Weinheimer, A. J., Diskin, G., Ryerson, T. B., da Silva, A., Curry, J., Kinnison, D., Tilmes, S., and Levelt, P. F.: Analysis of satellite-derived Arctic tropo-

- spheric BrO columns in conjunction with aircraft measurements during ARCTAS and ARCPAC, *Atmos. Chem. Phys.*, 12, 1255–1285, doi:10.5194/acp-12-1255-2012, 2012.
- Deutschmann, T., Beirle, S., Frieß, U., Grzegorski, M., Kern, C., Kritten, L., Platt, U., Prados-Román, C., Puķīte, J., Wagner, T., Werner, B., and Pfeilsticker, K.: The Monte Carlo atmospheric radiative transfer model McArtim: Introduction and validation of Jacobians and 3D features, *J. Quant. Spectrosc. Radiat. Transfer*, 112, 1119–1137, 2011.
- Draxler, R. R. and Hess, G. D.: Description of the HYSPLIT 4 modeling system. NOAA Tech. Memo. ERL ARL-224, NOAA Air Resources Laboratory, Silver Spring, MD, 1997.
- Draxler, R. R. and Hess, G. D.: An overview of the HYSPLIT 4 modeling system of trajectories, dispersion, and deposition, *Aust. Meteor. Mag.*, 47, 295–308, 1998.
- Draxler, R. R.: HYSPLIT 4 users's guide, U.S. Dept. of Commerce, National Oceanic and Atmospheric Administration, Environmental Research Laboratories, Air Resources Laboratory, Silver Spring, MD, 1–209, 1999.
- Fan, S. M. and Jacob, D. J.: Surface Ozone Depletion in Arctic Spring Sustained by Bromine Reactions on Aerosols, *Nature*, 359, 522–524, doi:10.1038/359522a0, 1992.
- Fayt, C., De Smedt, I., Letocart, V., Merlaud, A., Pinardi, G., and Van Roozendaal, M.: QDOAS Software User Manual, Belgian Institute for Space Aeronomy, 2011.
- Foster, K. L., Plastringer, R. A., Bottenheim, J. W., Shepson, P. B., Finlayson-Pitts, B. J., and Spicer, C. W.: The role of Br<sub>2</sub> and BrCl in surface ozone destruction at polar sunrise, *Science*, 291, 471–474, doi:10.1126/science.291.5503.471, 2001.
- Frieß, U., Monks, P. S., Remedios, J. J., Rozanov, A., Sinreich, R., Wagner, T., and Platt, U.: MAX-DOAS O<sub>4</sub> measurements: A new technique to derive information on atmospheric aerosols: 2. Modeling studies, *J. Geophys. Res.*, 111, D14203, doi:10.1029/2005JD006618, 2006.
- Frieß, U., Sihler, H., Sander, R., Pöhler, D., Yilmaz, S., and Platt, U.: The vertical distribution of BrO and aerosols in the Arctic: Measurements by active and passive differential optical absorption spectroscopy, *J. Geophys. Res.*, 116, D00R04, doi:10.1029/2011JD015938, 2011.
- Gauss, M., Myhre, G., Isaksen, I. S. A., Grewe, V., Pitari, G., Wild, O., Collins, W. J., Dentener, F. J., Ellingsen, K., Gohar, L. K., Hauglustaine, D. A., Iachetti, D., Lamarque, J. F., Mancini, E., Mickley, L. J., Prather, M. J., Pyle, J. A., Sanderson, M. G., Shine, K. P., Stevenson, D. S., Sudo, K., Szopa, S., and Zeng, G.: Radiative forcing since preindustrial times due to ozone change in the troposphere and the lower stratosphere, *Atmos. Chem. Phys.*, 6, 575–599, doi:10.5194/acp-6-575-2006, 2006.
- Gilman, J. B., Burkhardt, J. F., Lerner, B. M., Williams, E. J., Kuster, W. C., Goldan, P. D., Murphy, P. C., Warneke, C., Fowler, C., Montzka, S. A., Miller, B. R., Miller, L., Oltmans, S. J., Ryerson, T. B., Cooper, O. R., Stohl, A., and de Gouw, J. A.: Ozone variability and halogen oxidation within the Arctic and sub-Arctic springtime boundary layer, *Atmos. Chem. Phys.*, 10, 10223–10236, doi:10.5194/acp-10-10223-2010, 2010.
- Hanson, D. R. and Ravishankara, A. R.: Heterogeneous Chemistry of Bromine Species in Sulfuric-Acid under Stratospheric Conditions, *Geophys. Res. Lett.*, 22, 385–388, doi:10.1029/94GL03379, 1995.
- Hausmann, M. and Platt, U.: Spectroscopic measurement of bromine oxide and ozone in the high Arctic during Polar Sunrise Experiment 1992, *J. Geophys. Res.*, 99, 25399–25413, doi:10.1029/94jd01314, 1994.
- Helmig, D., Cohen, L. D., Bocquet, F., Oltmans, S., Grachev, A., and Neff, W.: Spring and summertime diurnal surface ozone fluxes over the polar snow at Summit, Greenland, *Geophys. Res. Lett.*, 36, L08809, doi:10.1029/2008GL036549, 2009.
- Helmig, D., Boylan, P., Johnson, B., Oltmans, S., Fairall, C., Staebler, R., Weinheimer, A., Orlando, J., Knapp, D. J., Montzka, D. D., Flocke, F., Frieß, U., Sihler, H., and Shepson, P. B.: Ozone dynamics and snow-atmosphere exchanges during ozone depletion events at Barrow, Alaska, *J. Geophys. Res.*, 117, D20303, doi:10.1029/2012jd017531, 2012.
- Hönninger, G., Leser, H., Sebastián, O., and Platt, U.: Ground-based measurements of halogen oxides at the Hudson Bay by active longpath DOAS and passive MAX-DOAS, *Geophys. Res. Lett.*, 31, L04111, doi:10.1029/2003GL018982, 2004a.
- Hönninger, G., von Friedeburg, C., and Platt, U.: Multi axis differential optical absorption spectroscopy (MAX-DOAS), *Atmos. Chem. Phys.*, 4, 231–254, doi:10.5194/acp-4-231-2004, 2004b.
- Hopper, J. F., Peters, B., Yokouchi, Y., Niki, H., Jobson, B. T., Shepson, P. B., and Muthuramu, K.: Chemical and Meteorological Observations at Ice Camp Swan during Polar Sunrise Experiment 1992, *J. Geophys. Res.*, 99, 25489–25498, doi:10.1029/94JD02303, 1994.
- Hopper, J. F., Barrie, L. A., Silis, A., Hart, W., Gallant, A. J., and Dryfhout, H.: Ozone and meteorology during the 1994 Polar Sunrise Experiment, *J. Geophys. Res.*, 103, 1481–1492, 1998.
- Huff, A. K., and Abbatt, J. P. D.: Kinetics and product yields in the heterogeneous reactions of HOBr with ice surfaces containing NaBr and NaCl, *J. Phys. Chem. A*, 106, 5279–5287, doi:10.1021/Jp014296m, 2002.
- Hutterli, M. A., McConnell, J. R., Stewart, R. W., Jacobi, H. W., and Bales, R. C.: Impact of temperature-driven cycling of hydrogen peroxide (H<sub>2</sub>O<sub>2</sub>) between air and snow on the planetary boundary layer, *J. Geophys. Res.*, 106, 15395–15404, doi:10.1029/2001jd900102, 2001.
- Jacobi, H. W., Frey, M. M., Hutterli, M. A., Bales, R. C., Schrems, O., Cullen, N. J., Steffen, K., and Koehler, C.: Measurements of hydrogen peroxide and formaldehyde exchange between the atmosphere and surface snow at Summit, Greenland, *Atmos. Environ.*, 36, 2619–2628, doi:10.1016/S1352-2310(02)00106-1, 2002.
- Jacobi, H. W., Kaleschke, L., Richter, A., Rozanov, A., and Burrows, J. P.: Observation of a fast ozone loss in the marginal ice zone of the Arctic Ocean, *J. Geophys. Res.*, 111, D15309, doi:10.1029/2005jd006715, 2006.
- Jacobi, H. W., Morin, S., and Bottenheim, J. W.: Observation of widespread depletion of ozone in the springtime boundary layer of the central Arctic linked to mesoscale synoptic conditions, *J. Geophys. Res.*, 115, D17302, doi:10.1029/2010jd013940, 2010.
- Jaeschke, W., Salkowski, T., Dierssen, J. P., Trumbach, J. V., Krischke, U., and Günther, A.: Measurements of trace substances in the Arctic troposphere as potential precursors and constituents of Arctic haze, *J. Atmos. Chem.*, 34, 291–319, 1999.
- Jobson, B. T., Niki, H., Yokouchi, Y., Bottenheim, J., Hopper, F., and Leitch, R.: Measurements of C<sub>2</sub>–C<sub>6</sub> Hydrocarbons during the Polar Sunrise 1992 Experiment – Evidence for Cl atom

- and Br atom Chemistry, *J. Geophys. Res.*, 99, 25355–25368, doi:10.1029/94JD01243, 1994.
- Jones, A. E., Anderson, P. S., Begoin, M., Brough, N., Hutterli, M. A., Marshall, G. J., Richter, A., Roscoe, H. K., and Wolff, E. W.: BrO, blizzards, and drivers of polar tropospheric ozone depletion events, *Atmos. Chem. Phys.*, 9, 4639–4652, doi:10.5194/acp-9-4639-2009, 2009.
- Jones, A. E., Wolff, E. W., Brough, N., Bauguitte, S. J. B., Weller, R., Yela, M., Navarro-Comas, M., Ochoa, H. A., and Theys, N.: The spatial scale of ozone depletion events derived from an autonomous surface ozone network in coastal Antarctica, *Atmos. Chem. Phys.*, 13, 1457–1467, doi:10.5194/acp-13-1457-2013, 2013.
- Kahl, J. D.: A Cautionary Note on the Use of Air Trajectories in Interpreting Atmospheric Chemistry Measurements, *Atmos. Environ., Part A*, 27, 3037–3038, 1993.
- Knepp, T. N., Bottenheim, J., Carlsen, M., Carlson, D., Donohoue, D., Friederich, G., Matrai, P. A., Netcheva, S., Perovich, D. K., Santini, R., Shepson, P. B., Simpson, W., Valentic, T., Williams, C., and Wyss, P. J.: Development of an autonomous sea ice tethered buoy for the study of ocean-atmosphere-sea ice-snow pack interactions: the O-buoy, *Atmos. Meas. Tech.*, 3, 249–261, doi:10.5194/amt-3-249-2012, 2010.
- Koo, J. H., Wang, Y., Kurosu, T. P., Chance, K., Rozanov, A., Richter, A., Oltmans, S. J., Thompson, A. M., Hair, J. W., Fenn, M. A., Weinheimer, A. J., Ryerson, T. B., Solberg, S., Huey, L. G., Liao, J., Dibb, J. E., Neuman, J. A., Nowak, J. B., Pierce, R. B., Natarajan, M., and Al-Saadi, J.: Characteristics of tropospheric ozone depletion events in the Arctic spring: analysis of the ARCTAS, ARCPAC, and ARCIONS measurements and satellite BrO observations, *Atmos. Chem. Phys.*, 12, 9909–9922, doi:10.5194/acp-12-9909-2012, 2012.
- Kwok, R., Cunningham, G. F., Wensnahan, M., Rigor, I., Zwally, H. J., and Yi, D.: Thinning and volume loss of the Arctic Ocean sea ice cover: 2003–2008, *J. Geophys. Res.*, 114, C07005, doi:10.1029/2009JC005312, 2009.
- Le Bras, G. and Platt, U.: A Possible Mechanism for Combined Chlorine and Bromine Catalyzed Destruction of Tropospheric Ozone in the Arctic, *Geophys. Res. Lett.*, 22, 599–602, doi:10.1029/94GL03334, 1995.
- Leaith, W. R., Barrie, L. A., Bottenheim, J. W., Li, S. M., Shepson, P. B., Muthuramu, K., and Yokouchi, Y.: Airborne Observations Related to Ozone Depletion at Polar Sunrise, *J. Geophys. Res.*, 99, 25499–25517, 1994.
- Lehrer, E., Hönninger, G., and Platt, U.: A one dimensional model study of the mechanism of halogen liberation and vertical transport in the polar troposphere, *Atmos. Chem. Phys.*, 4, 2427–2440, doi:10.5194/acp-4-2427-2004, 2004.
- Liao, J., Huey, L. G., Tanner, D. J., Flocke, F. M., Orlando, J. J., Neuman, J. A., Nowak, J. B., Weinheimer, A. J., Hall, S. R., Smith, J. N., Fried, A., Staebler, R. M., Wang, Y., Koo, J. H., Cantrell, C. A., Weibring, P., Walega, J., Knapp, D. J., Shepson, P. B., and Stephens, C. R.: Observations of inorganic bromine (HOBr, BrO, and Br<sub>2</sub>) speciation at Barrow, Alaska, in spring 2009, *J. Geophys. Res.*, 117, D00R16, doi:10.1029/2011JD016641, 2012.
- Liao, J., Huey, L. G., Liu, Z., Tanner, D. J., Cantrell, C. A., Orlando, J. J., Flocke, F. M., Shepson, P. B., Weinheimer, A. J., Hall, S. R., Ullmann, K., Beine, H. J., Wang, Y., Ingall, E. D., Stephens, C. R., Hornbrook, R. S., Apel, E. C., Riemer, D., Fried, A., Mauldin III, R. L., Smith, J. N., Staebler, R. M., Neuman, J. A., and Nowak, J. B.: High levels of molecular chlorine in the Arctic atmosphere, *Nature Geosci.*, 7, 91–94, doi:10.1038/ngeo2046, 2014.
- Mahajan, A. S., Shaw, M., Oetjen, H., Hornsby, K. E., Carpenter, L. J., Kaleschke, L., Tian-Kunze, X., Lee, J. D., Moller, S. J., Edwards, P., Commane, R., Ingham, T., Heard, D. E., and Plane, J. M. C.: Evidence of reactive iodine chemistry in the Arctic boundary layer, *J. Geophys. Res.*, 115, D20303, doi:10.1029/2009JD013665, 2010.
- Martinez, M., Arnold, T., and Perner, D.: The role of bromine and chlorine chemistry for arctic ozone depletion events in Ny-Ålesund and comparison with model calculations, *Ann. Geophys.*, 17, 941–956, doi:10.1007/s00585-999-0941-4, 1999.
- Michalowski, B. A., Francisco, J. S., Li, S.-M., Barrie, L. A., Bottenheim, J. W., and Shepson, P. B.: A computer model study of multiphase chemistry in the Arctic boundary layer during polar sunrise, *J. Geophys. Res.*, 105, 15131–15145, doi:10.1029/2000JD900004, 2000.
- Miller, H. L., Weaver, A., Sanders, R. W., Arpag, K., and Solomon, S.: Measurements of arctic sunrise surface ozone depletion events at Kangerlussuaq, Greenland (67° N, 51° W), *Tellus B*, 49, 496–509, doi:10.1034/j.1600-0889.49.issue5.6.x, 1997.
- Moore, C. W., Obrist, D., Steffen, A., Staebler, R. M., Douglas, T. A., Richter, A., and Nghiem, S. V.: Convective forcing of mercury and ozone in the Arctic boundary layer induced by leads in sea ice, *Nature*, 506, 81–84, doi:10.1038/nature12924, 2014.
- Morin, S., Hönninger, G. H., Staebler, R. M., and Bottenheim, J. W.: A high time resolution study of boundary layer ozone chemistry and dynamics over the Arctic Ocean near Alert, Nunavut, *Geophys. Res. Lett.*, 32, L08809, doi:10.1029/2004GL022098, 2005.
- Neuman, J. A., Nowak, J. B., Huey, L. G., Burkholder, J. B., Dibb, J. E., Holloway, J. S., Liao, J., Peischl, J., Roberts, J. M., Ryerson, T. B., Scheuer, E., Stark, H., Stickel, R. E., Tanner, D. J., and Weinheimer, A.: Bromine measurements in ozone depleted air over the Arctic Ocean, *Atmos. Chem. Phys.*, 10, 6503–6514, doi:10.5194/acp-10-6503-2010, 2010.
- Nghiem, S. V., Rigor, I. G., Richter, A., Burrows, J. P., Shepson, P. B., Bottenheim, J., Barber, D. G., Steffen, A., Latonas, J., Wang, F. Y., Stern, G., Clemente-Colon, P., Martin, S., Hall, D. K., Kaleschke, L., Tackett, P., Neumann, G., and Asplin, M. G.: Field and satellite observations of the formation and distribution of Arctic atmospheric bromine above a rejuvenated sea ice cover, *J. Geophys. Res.*, 117, D00S05, doi:10.1029/2011JD016268, 2012.
- Oltmans, S. J., Johnson, B. J., and Harris, J. M.: Springtime boundary layer ozone depletion at Barrow, Alaska: Meteorological influence, year-to-year variation, and long-term change, *J. Geophys. Res.*, 117, D00R18, doi:10.1029/2011JD016889, 2012.
- Piot, M. and von Glasow, R.: The potential importance of frost flowers, recycling on snow, and open leads for ozone depletion events, *Atmos. Chem. Phys.*, 8, 2437–2467, doi:10.5194/acp-8-2437-2008, 2008.
- Piot, M. and von Glasow, R.: Modelling the multiphase near-surface chemistry related to ozone depletions in polar spring, *J. Atmos. Chem.*, 64, 77–105, doi:10.1007/s10874-010-9170-1, 2009.
- Pöhler, D., Vogel, L., Frieß, U., and Platt, U.: Observation of halogen species in the Amundsen Gulf, Arctic, by active long-path

- differential optical absorption spectroscopy, *Prog. Natl. Acad. Sci.*, 107, 6582–6587, doi:10.1073/pnas.0912231107, 2010.
- Pratt, K. A., Custard, K. D., Shepson, P. B., Douglas, T. A., Pöhler, D., General, S., Zielcke, J., Simpson, W. R., Platt, U., Tanner, D. J., Huey, G. L., Carlsen, M., and Stirm, B. H.: Photochemical production of molecular bromine in Arctic surface snowpacks, *Nature Geosci.*, 6, 351–356, doi:10.1038/ngeo1779, 2013.
- Richter, A., Wittrock, F., Eisinger, M., and Burrows, J. P.: GOME observations of tropospheric BrO in northern hemispheric spring and summer 1997, *Geophys. Res. Lett.*, 25, 2683–2686, 1998.
- Ridley, B. A., Atlas, E. L., Montzka, D. D., Browell, E. V., Cantrell, C. A., Blake, D. R., Blake, N. J., Cinquini, L., Coffey, M. T., Emmmons, L. K., Cohen, R. C., DeYoung, R. J., Dibb, J. E., Eisele, F. L., Flocke, F. M., Fried, A., Grahek, F. E., Grant, W. B., Hair, J. W., Hannigan, J. W., Heikes, B. J., Lefer, B. L., Mauldin, R. L., Moody, J. L., Shetter, R. E., Snow, J. A., Talbot, R. W., Thornton, J. A., Walega, J. G., Weinheimer, A. J., Wert, B. P., and Wimmers, A. J.: Ozone depletion events observed in the high latitude surface layer during the TOPSE aircraft program, *J. Geophys. Res.*, 108, 8356, doi:10.1029/2001JD001507, 2003.
- Rodgers, C. D.: *Inverse Methods for Atmospheric Sounding: Theory and Practice*, Series on Atmospheric, Oceanic, and Planetary Physics, edited by: Taylor, F. W., World Scientific Publishing, 46–50, 2000.
- Saiz-Lopez, A., Mahajan, A. S., Salmon, R. A., Bauguitte, S. J. B., Jones, A. E., Roscoe, H. K., and Plane, J. M. C.: Boundary layer halogens in coastal Antarctica, *Science*, 317, 348–351, doi:10.1126/Science.1141408, 2007.
- Salawitch, R. J., Canty, T., Kurosu, T., Chance, K., Liang, Q., da Silva, A., Pawson, S., Nielsen, J. E., Rodriguez, J. M., Bhartia, P. K., Liu, X., Huey, L. G., Liao, J., Stickel, R. E., Tanner, D. J., Dibb, J. E., Simpson, W. R., Donohoue, D., Weinheimer, A., Flocke, F., Knapp, D., Montzka, D., Neuman, J. A., Nowak, J. B., Ryerson, T. B., Oltmans, S., Blake, D. R., Atlas, E. L., Kinnison, D. E., Tilmes, S., Pan, L. L., Hendrick, F., Van Roozendael, M., Kreher, K., Johnston, P. V., Gao, R. S., Johnson, B., Bui, T. P., Chen, G., Pierce, R. B., Crawford, J. H., and Jacob, D. J.: A new interpretation of total column BrO during Arctic spring, *Geophys. Res. Lett.*, 37, L21805, doi:10.1029/2010GL043798, 2010.
- Schall, C. and Heumann, K. G.: GC determination of volatile organoiodine and organobromine compounds in Arctic seawater and air samples, *Fresenius. J. Anal. Chem.*, 346, 717–722, doi:10.1007/bf00321279, 1993.
- Seabrook, J. A., Whiteway, J., Staebler, R. M., Bottenheim, J. W., Komguem, L., Gray, L. H., Barber, D., and Asplin, M.: LIDAR measurements of Arctic boundary layer ozone depletion events over the frozen Arctic Ocean, *J. Geophys. Res.*, 116, D00S02, doi:10.1029/2011JD016335, 2011.
- Seabrook, J. A., Whiteway, J. A., Gray, L. H., Staebler, R., and Herber, A.: Airborne lidar measurements of surface ozone depletion over Arctic sea ice, *Atmos. Chem. Phys.*, 13, 6023–6029, doi:10.5194/acp-13-6023-2013, 2013.
- Sheridan, P. J., Schnell, R. C., Zoller, W. H., Carlson, N. D., Rasmussen, R. A., Harris, J. M., and Sievering, H.: Composition of Br-Containing Aerosols and Cases Related to Boundary-Layer Ozone Destruction in the Arctic, *Atmos. Environ., Part A*, 27, 2839–2849, 1993.
- Simpson, W. R., Alvarez-Aviles, L., Douglas, T. A., Sturm, M., and Dominé, F.: Halogens in the coastal snow pack near Barrow, Alaska: Evidence for active bromine air-snow chemistry during springtime, *Geophys. Res. Lett.*, 32, L04811, doi:10.1029/2004GL021748, 2005.
- Simpson, W. R., Carlson, D., Hönninger, G., Douglas, T. A., Sturm, M., Perovich, D., and Platt, U.: First-year sea-ice contact predicts bromine monoxide (BrO) levels at Barrow, Alaska better than potential frost flower contact, *Atmos. Chem. Phys.*, 7, 621–627, doi:10.5194/acp-7-621-2007, 2007a.
- Simpson, W. R., von Glasow, R., Riedel, K., Anderson, P., Ariya, P., Bottenheim, J., Burrows, J., Carpenter, L. J., Frieß, U., Goodsite, M. E., Heard, D., Hutterli, M., Jacobi, H. W., Kaleschke, L., Neff, B., Plane, J., Platt, U., Richter, A., Roscoe, H., Sander, R., Shepson, P., Sodeau, J., Steffen, A., Wagner, T., and Wolff, E.: Halogens and their role in polar boundary-layer ozone depletion, *Atmos. Chem. Phys.*, 7, 4375–4418, doi:10.5194/acp-7-4375-2007, 2007b.
- Solberg, S., Schmidbauer, N., Semb, A., Stordal, F., and Hov, O.: Boundary-layer ozone depletion as seen in the Norwegian Arctic in Spring, *J. Atmos. Chem.*, 23, 301–332, doi:10.1007/Bf00055158, 1996.
- Stephens, C. R.: *Studies of tropospheric halogen radical chemistry during ozone and mercury depletion events in the Arctic*, Ph.D., Chemistry, Purdue University, West Lafayette, IN, 356 pp., 2012.
- Strong, C., Fuentes, J. D., Davis, R. E., and Bottenheim, J. W.: Thermodynamic attributes of Arctic boundary layer ozone depletion, *Atmos. Environ.*, 36, 2641–2652, 2002.
- Sumner, A. L., and Shepson, P. B.: Snowpack production of formaldehyde and its effect on the Arctic troposphere, *Nature*, 398, 230–233, 1999.
- Sumner, A. L., Shepson, P. B., Grannas, A. M., Bottenheim, J. W., Anlauf, K. G., Worthy, D., Schroeder, W. H., Steffen, A., Dominé, F., Perrier, S., and Houdier, S.: Atmospheric chemistry of formaldehyde in the Arctic troposphere at Polar Sunrise, and the influence of the snowpack, *Atmos. Environ.*, 36, 2553–2562, doi:10.1016/S1352-2310(02)00105-X, 2002.
- Tang, T., and McConnell, J. C.: Autocatalytic release of bromine from Arctic snow pack during polar sunrise, *Geophys. Res. Lett.*, 23, 2633–2636, doi:10.1029/96GL02572, 1996.
- Tarasick, D. W. and Bottenheim, J. W.: Surface ozone depletion episodes in the Arctic and Antarctic from historical ozonesonde records, *Atmos. Chem. Phys.*, 2, 197–205, doi:10.5194/acp-2-197-2002, 2002.
- Theys, N., Van Roozendael, M., Hendrick, F., Yang, X., De Smedt, I., Richter, A., Begoin, M., Errera, Q., Johnston, P. V., Kreher, K., and De Mazière, M.: Global observations of tropospheric BrO columns using GOME-2 satellite data, *Atmos. Chem. Phys.*, 11, 1791–1811, doi:10.5194/acp-11-1791-2011, 2011.
- Thompson, A. M.: The Oxidizing Capacity of the Earth's Atmosphere - Probable Past and Future Changes, *Science*, 256, 1157–1165, 1992.
- Thompson, C. R., Shepson, P. B., Liao, J., Huey, L. G., and Cantrell, C.: Bromine atom production and chain propagation during springtime Arctic ozone depletion events in Barrow, Alaska, in preparation, 2014.
- Toyota, K., McConnell, J. C., Lupu, A., Neary, L., McLinden, C. A., Richter, A., Kwok, R., Semeniuk, K., Kaminski, J. W., Gong, S.-L., Jarosz, J., Chipperfield, M. P., and Sioris, C. E.: Analy-

- sis of reactive bromine production and ozone depletion in the Arctic boundary layer using 3-D simulations with GEM-AQ: inference from synoptic-scale patterns, *Atmos. Chem. Phys.*, 11, 3949–3979, doi:10.5194/acp-11-3949-2011, 2011.
- Tuckermann, M., Ackermann, R., Götz, C., Lorenzen-Schmidt, H., Senne, T., Stutz, J., Trost, B., Unold, W., and Platt, U.: DOAS-observation of halogen radical-catalysed arctic boundary layer ozone destruction during the ARCTOC-campaigns 1995 and 1996 in Ny-Ålesund, Spitsbergen, *Tellus B*, 49, 533–555, 1997.
- Vogt, R., Crutzen, P. J., and Sander, R.: A mechanism for halogen release from sea-salt aerosol in the remote marine boundary layer, *Nature*, 383, 327–330, 1996.
- Wennberg, P.: Atmospheric chemistry – Bromine explosion, *Nature*, 397, 299–301, doi:10.1038/16805, 1999.
- Yang, X., Pyle, J. A., and Cox, R. A.: Sea salt aerosol production and bromine release: Role of snow on sea ice, *Geophys. Res. Lett.*, 35, L16815, doi:10.1029/2008gl034536, 2008.
- Yang, X., Pyle, J. A., Cox, R. A., Theys, N., and Van Roozendaal, M.: Snow-sourced bromine and its implications for polar tropospheric ozone, *Atmos. Chem. Phys.*, 10, 7763–7773, doi:10.5194/acp-10-7763-2010, 2010.
- Zeng, T., Wang, Y. H., Chance, K., Browell, E. V., Ridley, B. A., and Atlas, E. L.: Widespread persistent near-surface ozone depletion at northern high latitudes in spring, *Geophys. Res. Lett.*, 30, 2298, doi:10.1029/2003GL018587, 2003.
- Zhou, X. L., Beine, H. J., Honrath, R. E., Fuentes, J. D., Simpson, W., Shepson, P. B., and Bottenheim, J. W.: Snowpack photochemical production of HONO: a major source of OH in the Arctic boundary layer in springtime, *Geophys. Res. Lett.*, 28, 4087–4090, doi:10.1029/2001gl013531, 2001.